UNIVERSITEIT VAN PRETORIA
UNIVERSITY OF PRETORIA
YUNIBESITHI YA PRETORIA
Denkleiers • Leading Minds • Dikgopolo tša Dihlalefi

ABS braking on rough terrain

by

Herman Adendorff Hamersma

Submitted in partial fulfilment of the requirements for the degree

Philosophiae Doctor (Mechanical Engineering)

in the

Faculty of Engineering, Built Environment and Information Technology (EBIT)
University of Pretoria

July 2017

The financial assistance of the National Research Foundation (DAAD-NRF) towards this research is hereby acknowledged. Opinions expressed and conclusions arrived at, are those of the author, and are not necessarily to be attributed to the DAAD-NRF.

Thesis Summary

Title: ABS braking on rough terrain
Author: Herman Adendorff Hamersma
Promotor: Prof P.S. Els
Department: Department of Mechanical and Aeronautical Engineering
Degree: Philosophiae Doctor (Mechanical Engineering)

Keywords: Off-road vehicle dynamics; off-road ABS braking; Rolling radius; Semi-active suspension; Wheel hop estimation; Suspension force prediction

This aim of this project may be condensed to the following question:

Is there an improvement achievable in the braking performance of a vehicle on a rough road?

Several follow-up questions arise from the above problem statement:

a) *What are the causes of the unsatisfactory stopping time and distance when braking on a rough road and how can they be addressed?*
b) *Can the off-road braking of a vehicle be modelled mathematically?*
c) *What are the criteria used to evaluate the on-road braking performance of a vehicle and can the off-road braking performance of a vehicle be evaluated using the same criteria?*
d) *Can the off-road braking performance be improved without compromising the on-road performance?*

An extensive literature survey is done on existing research addressing these four questions. It is found that, although the literature acknowledges that the braking performance of a vehicle deteriorates under off-road conditions, very little has been done to address it. Two main factors influencing the braking performance are identified, namely the ABS algorithm inputs and tyre force generation characteristics. An experimentally validated vehicle model is developed that serves as the basis from which the research question will be addressed. An FTire model is parameterised and used as the tyre model throughout this study. Three measured off-road terrain profiles are used.

The first step in addressing the research question is developing a performance evaluation technique that can easily, quantifiably and visually compare the braking performance of several ABS systems on any road surface, in any condition. The performance evaluation technique considers the stopping distance, longitudinal deceleration, lateral path offset error, and yaw rate error as metrics.

The second step is investigating one of the common assumptions found in ABS algorithms, namely that the roll radius is constant. This is investigated experimentally and it is concluded that the assumption is valid on smooth and rough road surfaces when using the kinematic definition of the roll radius, but invalid when using the kinetic definition of the roll radius.

Investigation of the influence of the tyre force generation characteristics on the braking performance is the third step. It is found that the tyre normal force variation and corresponding suspension force variation correlates closely with the braking performance. A higher suspension force variation is associated with longer stopping distances.

The final step is the development of a three step control strategy that aims to reduce the suspension force variation. This is done by estimating the wheel hop using easy to measure states, predicting the suspension force variation based on these estimates, and finally selecting the ideal suspension configuration.

The control strategy, called the WiSDoM algorithm, was evaluated by doing several simulations on the three off-road road profiles, with different braking points as the only changed variable. The WiSDoM algorithm's performance was compared with the baseline vehicle performance and found to decrease the stopping distance on all three off-road road profiles, without negatively affecting the stability of the vehicle. The WiSDoM algorithm did not have a significant influence on the braking performance on a smooth road.

Proefskrifopsomming

Titel: Anti-sluitremstelsel rem op rowwe terrein
Outeur: Herman Adendorff Hamersma
Promotor: Prof P.S. Els
Departement: Departement van Meganiese en Lugvaartkundige Ingenieurswese
Graad: Philosophiae Doctor (Meganiese Ingenieurswese)

Sleutelwoorde: veldvoertuigdinamika; veld anti-sluitremstelsels; rolradius; semi-aktiewe suspensiestelsels; wielhopskatting; suspensiekragvoorspelling

Die doel van hierdie projek kan in die volgende navorsingsvraag saamgevat word:

Kan die remvermoë van 'n voertuig, wat op 'n rowwe terrein ry, verbeter word?

Verskeie opvolg vrae kan na aanleiding van die bostaande navorsingsvraag geformuleer word:

a) *Wat is die oorsake van die onbevredigende stoptyd en stopafstand wanneer daar op 'n rowwe terrein gerem word en hoe kan dit aangespreek word?*
b) *Kan die remvertoning van 'n voertuig wat nie op 'n gelyke pad ry nie wiskundig gemodelleer word?*
c) *Wat is die kriteria wat gebruik word om die remvermoë van 'n voertuig op 'n gelyke pad te beoordeel en is hierdie kriteria van toepassing wanneer die remvermoë op 'n rowwe terrein beoordeel word?*
d) *Kan die remvermoë op rowwe terrein verbeter word sonder om die remvermoë op gelyke paaie nadelig te beïnvloed?*

'n Literatuurstudie van bestaande navorsing is van stapel gestuur wat hierdie vier vrae aanspreek. Daar is gevind dat, alhoewel die literatuur erken dat die rowwe terrein remvermoë van voertuie veel te wense laat, daar bittermin gedoen is om die verskynsel aan te spreek. Twee faktore wat die remvermoë dramaties beïnvloed is geïdentifiseer, naamlik die anti-sluit remstelselalgoritme se insette en die ontwikkeling van bandkragte in die band-padkoppelvlak. 'n Eksperimenteel gevalideerde voertuigmodel is ontwikkel wat die basis vorm waaruit die navorsingsvrae geadresseer word. 'n FTire bandmodel is geparameteriseer en deurgaans gebruik as die bandmodel in hierdie studie. Drie gemeete padprofiele is ook gebruik.

Die eerste stap om die navorsingsvrae te beantwoord is die ontwikkeling van 'n remvertoningevalueringstegniek wat gebruik kan word om die vertoning van verskeie anti-sluit resmtelsels, op enige terrein, maklik, kwantifiseerbaar en visueel met mekaar te vergelyk. Die remvertoning evalueringstegniek neem die stopafstand, longitudinale versnelling, laterale padafwyking en giersnelheidfout in ag.

Die tweede stap is om een van die aannames wat in anti-sluit remstelselalgoritmes gevind word te ondersoek. Dit is die aanname dat die rolradius konstant is. Dit is eksperimenteel ondersoek en daar is gevind dat die aanname geldig is op beide gelyke en rowwe terreine, mits die kinematiese definisie van die rolradius gebruik word. Die aanname is egter ongeldig wanneer die kinetiese definisie van die rolradius gebruik word.

Die ondersoek na die invloed van bandkragopwekking op die remvertoning is die derde stap in die aanspreek van die navorsingsvrae. Daar is gevind dat die bandnormaalkragvariasie en die ooreenstemmende suspensiekragvariasie korelleer met die rowwe terrein remvertoning van ‘n voertuig. ‘n Hoër suspensiekragvariasie word met langer stopafstande geassosieer.

Die laaste stap in die aanspreek van die navorsingsvrae is die ontwikkeling van ‘n drievoudige beheerstrategie wat ten doel het om, wanneer daar op ‘n rowwe terrein gerem word, die suspensiekragvariasie te verminder. Dit word gedoen deur die wielhop te skat, die geskatte wielhop te gebruik om die suspensiekragte te voorspel en dan die ideale suspensiekonfigurasie te kies vanuit die voorspelde suspensiekragte.

Die beheerstrategie is evalueer deur verskeie simulasies uit te voer op die drie rowwe padprofiele, met die rempunt die enigste verandering. Die beheerstrategie se vertoning is vergelyk met die basislynvoertuig se remvertoning en daar is gevind dat die beheerstrategie die stopafstand verminder op al drie padprofiele. Die beheerstrategie het nie ‘n noemenswaardige invloed op die remvertoning op ‘n gelyke pad gehad nie.

Acknowledgements

I would like to extend my gratitude and appreciation to the following people, without whom successful completion of this project would have been neither a dream nor a possibility:

- Prof Schalk Els, for his mentorship, guidance, and friendship, not only with the completion of this project, but throughout my academic career.

- My wife Anneke, for her unconditional love, support, understanding, acceptance, and encouragement. For being there through the highest of highs and the lowest of lows, for time spent apart when we yearned to be close, my never-ending love and gratitude is but scant return for what you have sacrificed during this undertaking.

- My mother Susan and Charles, for their earnest concern and unwavering support. For lending a kind ear and a caring heart when frustrations ran deep and rampant.

- My grandfather Kris for being the role model and example that provided me with the inspiration that resulted in the audacity to attempt this project and gave me the longevity to see it through.

- My grandmother Riekie for reminding me that family comes first.

- Dr Theunis Botha, for acting as a soundboard for many ideas and hypotheses.

- The Vehicle Dynamics Group at the University of Pretoria for their eagerness to help whenever extra hands were required, their enthusiasm and curiosity to investigate the world of vehicle dynamics and the friendly advice, questions, arguments and observations, and the entertaining banter during coffee sessions.

- Prof Valentin Ivanov and his team at the Technische Universität Ilmenau for inspiring this project during my initial visit to their facilities in April 2013 and for the subsequent hospitality during secondments in 2015 and 2016.

- The financial assistance of the National Research Foundation (DAAD-NRF) towards this research is hereby acknowledged. Opinions expressed and conclusions arrived at, are those of the author, and are not necessarily to be attributed to the DAAD-NRF.

Soli Deo Gloria

Table of Contents

List of Figures

Chapter 3 Modelling the vehicle and its subsystems

Chapter 4 Braking performance evaluation

Chapter 5 ABS algorithm inputs

Chapter 6 The influence of tyre force generation on the braking performance

Chapter 7 Improving the braking performance: The WiSDoM algorithm

Appendix A The tyre test trailer ADAMS model

List of Tables

List of Symbols

Alpha-numeric symbols

Lowercase

SYMBOL	DESCRIPTION	UNIT
$\bar{a}_{ABS}$	Mean deceleration of vehicle with ABS active	[m/s^2]
$\bar{a}_{no\ ABS}$	Mean deceleration of vehicle with ABS inactive	[m/s^2]
$a_0, a_1, \dots a_{13}$	Lateral force coefficients (Magic Formula tyre model)	[-]
$b_0, b_1, \dots b_{10}$	Longitudinal force coefficients (Magic Formula tyre model)	[-]
c_f	Front damping coefficient	[N.s/m]
c_r	Rear damping coefficient	[N.s/m]
$c_0, c_1, \dots c_{17}$	Self-aligning moment coefficients (Magic Formula tyre model)	[-]
f	Brake friction coefficient	[-]
$f_{4S_{4_{front}}}$	Function describing 4S$_4$ front suspension force	[N]
$f_{4S_{rear}}$	Function describing 4S$_4$ rear suspension force	[N]
h	Height of centre of gravity	[m]
h_{PC}	Distance from pitch centre to centre of gravity	[m]
j_x	Longitudinal vehicle jerk	[m/s^3]
k_f	Front spring stiffness	[N/m]
k_r	Rear spring stiffness	[N/m]
l_f	Distance from vehicle CG to front wheels	[m]
l_r	Distance from vehicle CG to rear wheels	[m]
m	Number of metrics being compared	[-]
m_s	Sprung mass	[kg]
m_u	Unsprung mass	[kg]
n	Number of tests being compared	[-]
p_a	Brake actuation pressure	[Pa]
r_e	Equivalent radius for brake torque calculation	[m]
r_{eff}	Effective roll radius	[m]
r_{eo}	Original effective roll radius	[m]
r_i	Inner brake pad radius	[m]
$r_{kinematic}$	Kinematic roll radius	[m]
r_{kineic}	Kinetic roll radius	[m]
r_o	Outer brake pad radius	[m]
r_{stat}	Static roll radius	[m]
t	Time	[s]
t_{hold}	Maximum hold time in ABS control cycle	[s]
t_{up}	Maximum pressure build time in ABS control cycle	[s]
Δt	Change in time	[s]
$\vec{\boldsymbol{u}}_k$	KF control vector	[-]
v	Vehicle speed	[m/s]
v_{CP}	Tyre tangential speed at contact patch	[m/s]
$\boldsymbol{v}_k$	Observation noise at time step *k*	[-]
$v_{sliding}$	Sliding velocity	[m/s]
$\boldsymbol{w}_k$	Process noise at time step *k*	[-]
x	Independent variable in Pacejka tyre model; Comparison matrix	[-]

SYMBOL	DESCRIPTION	UNIT
$\ddot{x}$	Longitudinal acceleration	[m/s^2]
$x_{i,\dots}$	ith row of comparison matrix	[-]
x_{ij}	ith metric of jth manoeuvre	[-]
$x_{ij,norm}$	Normalised ith metric of jth manoeuvre	[-]
x_m	Position on horizontal axis where peak value occurs (Magic Formula tyre model)	[angle or slip%]
$\vec{\boldsymbol{x}}_k$	State vector at time step *k*	[-]
$\hat{\boldsymbol{x}}_{k\|k-1}$	*A priori* state estimate at time step k using information from previous time steps up to time step k-1	[-]
y	Magic Formula force output without vertical shift	[N]
$\tilde{\boldsymbol{y}}_k$	Measurement residual at time step *k*	[-]
z_f	Front suspension relative displacement	[m]
$\dot{z}_f$	Front suspension relative velocity	[m/s]
$\vec{\boldsymbol{z}}_k$	Observation vector at time step *k*	[-]
z_r	Rear suspension relative displacement	[m]
$\dot{z}_r$	Rear suspension relative velocity	[m/s]
z_1	Front unsprung mass vertical translation	[m]
z_{1_UKF}	Front unsprung mass vertical translation estimated by UKF	[m]
$\dot{z}_1$	Front unsprung mass vertical velocity	[m/s]
$\dot{z}_{1\_UKF}$	Front unsprung mass vertical velocity estimated by UKF	[m/s]
$\ddot{z}_1$	Front unsprung mass vertical acceleration	[m/s^2]
z_2	Rear unsprung mass vertical translation	[m]
z_{2_UKF}	Rear unsprung mass vertical translation estimated by UKF	[m]
$\dot{z}_2$	Rear unsprung mass vertical velocity	[m/s]
$\dot{z}_{2\_UKF}$	Rear unsprung mass vertical velocity estimated by UKF	[m/s]
$\ddot{z}_2$	Rear unsprung mass vertical acceleration	[m/s^2]
z_3	Sprung mass vertical translation	[m]
$\dot{z}_3$	Sprung mass vertical velocity	[m/s]
$\ddot{z}_3$	Sprung mass vertical acceleration	[m/s^2]

Uppercase

SYMBOL	DESCRIPTION	UNIT
A	Upper wheel angular acceleration threshold	[rad/s^2]
A_i	ith value in sample A	[-]
$\bar{A}$	Mean of sample A	[-]
B	Stiffness factor (Magic Formula coefficient)	[-]
$\boldsymbol{B}$	Control input matrix	[-]
C	Shape factor (Magic Formula coefficient)	[-]
D	Peak value (Magic Formula coefficient)	[-]
E	Curvature factor (Magic Formula coefficient)	[-]
$\boldsymbol{F}$	State transition model	[-]
F_{act}	Brake actuating force	[N]
$F_{i,front}$	Front suspension force of ith value of sample	[N]
$F_{i,rear}$	Rear suspension force of ith value of sample	[N]
F_x	Longitudinal force	[N]
F_y	Lateral force	[N]
F_z	Vertical force	[N]
$\bar{F}_{front}$	Mean suspension force on front axle	[N]
$\bar{F}_{rear}$	Mean suspension force on rear axle	[N]
$\bar{F}_{susp}$	Mean suspension force	[N]
F_{susp_front}	Front 4S$_4$ suspension force	[N]
F_{susp_rear}	Rear 4S$_4$ suspension force	[N]
$\bar{F}_{weighted}$	Weighted mean suspension force	[N]

SYMBOL	DESCRIPTION	UNIT
$\boldsymbol{H}$	Observation model	[-]
$\boldsymbol{I}$	Identity matrix	[-]
I_O	Moment of inertia about point O	[kg.m^2]
I_y	Moment of inertia about y-y axis	[kg.m^2]
$\boldsymbol{K}_k$	Kalman gain at time step *k*	[-]
L	Wheelbase	[m]
M_O	Moment about point O	[N.m]
M_y	Moment about y-axis	[N.m]
M_z	Moment about z-axis	[N.m]
N	Sample size	[-]
$\boldsymbol{P}_{k\|k-1}$	Predicted error covariance matrix with time steps up to time step k-1 taken into account	[-]
$\boldsymbol{Q}_k$	Process noise covariance at time step *k*	[-]
$\boldsymbol{R}_k$	Measurement noise covariance at time step *k*	[-]
S_h	Horizontal shift (Magic Formula coefficient)	[-]
$\boldsymbol{S}_k$	Residual covariance at time step *k*	[-]
S_v	Vertical shift (Magic Formula coefficient)	[-]
T_{brake}	Brake torque	[N.m]
W_d	Dynamic load transfer due to braking	[N]
X	Independent variable (Magic Formula tyre model)	[angle or slip%]
Y	Dependent variable (Magic Formula tyre model)	[N or N.m]

Greek symbols

SYMBOL	DESCRIPTION	UNIT
α	Angular acceleration	[rad/s^2]
α_{max}	Upper wheel angular acceleration threshold	[rad/s^2]
α_{min}	Lower wheel angular acceleration threshold	[rad/s^2]
γ	Camber angle	[rad]
θ	Angle	[rad]
θ_y	Pitch angle	[rad]
$\dot{\theta}_y$	Pitch rate	[rad/s]
$\ddot{\theta}_y$	Pitch angular acceleration	[rad/s^2]
θ_1	Disc brake contact angle smaller value	[rad]
θ_2	Disc brake contact angle larger value	[rad]
λ	Longitudinal wheel slip	[-]
λ_{max}	Longitudinal wheel slip upper threshold	[-]
μ	Coefficient of friction	[-]
μ_x	Longitudinal tyre friction	[-]
μ_y	Lateral tyre friction	[-]
ρ	Tyre deflection	[m]
ρ_{rr}	Pneumatic trail	[m]
σ	Suspension strut force standard deviation	[N]
$\sigma_{weighted}$	Weighted suspension strut force standard deviation	[N]
φ	Front/rear axle weighting	[-]
ω	Angular velocity	[rad/s]
ω_{max}	Maximum wheel speed	[rad/s]
ω_{min}	Minimum wheel speed	[rad/s]
ω_{peak}	Peak-to-peak wheel speed percentage	[%]

Abbreviations and acronyms

ACRONYM	DESCRIPTION
ABS	Antilock Brake System
ABSIP	ABS Index of Performance
ADAMS	Automatic Dynamic Analysis of Mechanical Systems
ADAS	Advanced Driver Assist Systems
BWR	Benedict-Webb-Rubin (authors of a real gas equation)
CG	Centre of Gravity
CTI	Cosin Tire Interface
DAQ	Data Acquisitioning system
DIC	Digital Image Correlation
DLC	Double Lane Change
DOF	Degree of Freedom
ECU	Electronic Control Unit
ESC	Electronic Stability Control
EOM	Equations of Motion
FL	Front Left
FR	Front Right
FFT	Fast Fourier Transform
FMVSS	Federal Motor Vehicle Safety Standard
GLONASS	Global Navigation Satellite System
GNSS/INS	Global Navigation Satellite System/Inertial Navigation System
GPS	Global Positioning System
HIL	Hardware-in-the-loop
INS	Inertial Navigation System
ITAE	Integral of the Time multiplied by the Absolute Error
KF	Kalman Filter
LVDT	Linear Variable Differential Transformer
MBS	Multi-body Dynamics Simulation
MF-SWIFT	Magic Formula – Short Wavelength Intermediate Frequency Tyre
MR	Magneto-Rheological
OEM	Original Equipment Manufacturer
PI	Proportional Integral
RANSAC	Random Sample Consensus
RL	Rear Left
RMS	Root Mean Square
RR	Rear Front
SAE	Society of Automotive Engineers
SIFT	Scale-Invariant Feature Transform
SUV	Sports Utility Vehicle
TC	Traction Control
WFT	Wheel Force Transducer
WiSDoM	Weighted Standard Deviation Minimisation
$4S_4$	Four state semi-active suspension system

Chapter 1

Introduction and problem statement

Newman's first law: It is useless to put on your brakes when you're upside down.

- Paul Newman (1925-2008), American actor

1.1 Introduction

Since the dawn of automobiles, accidents have been prone to happen. The first recorded instance of an automobile crash is rumoured to have occurred in 1771, when Nicolas-Joseph Cugnot's steam-powered vehicle (known as the *fardier à vapeur* or steam dray) collided with a wall at a speed of approximately 4km/h. Some historians however doubt that this event truly occurred due to a lack of documented evidence (Smallwood, 2013).

With the advent of the internal combustion engine (made practical by Nikolaus Otto in 1876), Karl Benz built what is widely regarded as the first automobile in 1886. Improvements in engine technology, such as increased compression ratios, the emergence of leaded fuel, overhead camshafts, turbochargers, multi-valve engines and fuel injection led to increasing highway speeds (Wan, 2000). Rapid deceleration from high speed became a necessity and led to an improvement of the brake technology. Benz's first automobile used a block of wood that pressed against the steel wheel when the driver applied the brake with a lever system. Karl Benz's wife invented brake lining during her infamous drive from Mannheim to Pforzheim in 1888 when she found the block of wood was inadequate and asked a shoemaker to add a strip of leather. Louis Renault invented the drum brake in 1902, although the brake was activated mechanically. Hydraulic brake actuation was developed in 1918 by Malcolm Loughead (who later changed his name to Lockheed) and was first used on the 1921 Duesenberg Straight Eight (also known as the Model A) and the first mass-produced car with hydraulic brake actuation was the 1924 Chrysler 70. William Lanchester patented the disk brake in 1902 and it was first implemented on the Chrysler Crown Imperial flagship model in 1949. The disk brake only became popular in the 1950s. Electronic brake control systems were originally used in the USA after the end of World War II using analogue switching technology.

Antilock braking systems (ABS) were conceived originally for trains in the early 1900s (SAE, 2014). These systems were first applied to passenger vehicles and light trucks by Bosch in 1936. The original Bosch system used an electric motor that controlled the opening and closing of an orifice on each brake circuit (SAE, 2014). Kelsey-Hayes began an automatic braking system development plan in 1957, concluding that the system should prevent loss of vehicle control and reduce stopping distance (SAE, 2014). The first commercial systems entered production in the 1960s and Bosch began supplying a hydraulic ABS system to Mercedes-Benz in October 1978. Subsequently, the prevalence of ABS on passenger and light commercial vehicles has increased significantly (SAE, 2014). Research on improving ABS systems continues today with the development of hybrid and full electric vehicles where regenerative braking may be used to recover some of the kinetic energy that would otherwise

be lost to heat due to the application of friction brakes (Savitski et al., 2016, Savitski et al., 2015, Ivanov et al., 2015a, Ivanov et al., 2015b).

According to SAE (2014), the goal of ABS application is:

"The application of ABS to a vehicle can provide improvements in the vehicle performance under braking compared to a conventional brake system. Improvement is typically sought in the areas of stability, steerability, and stopping distance … In addition to minimizing stopping distance, vehicle stability is another aspect to straight line braking that must be considered. For the case of straight line braking with the steering held fixed in the straight ahead position, the vehicle should brake in a straight line in the presence of external disturbances … Preservation of steering control and stability during braking are prime goals of the application of ABS to vehicles."

Early sports utility vehicles (SUVs) were derivatives of commercial and military vehicles such as the World War II Jeep and Land Rover. To be able to traverse rugged off-road terrain, SUVs typically need to have low ground pressure and large ground clearance. With the abovementioned increase in attainable vehicle speed through engine technology development, the speed of SUVs has also increased dramatically. The SUV designer is now faced with a problem: balancing the customer's demand for high speed and fast acceleration, combined with the ability to negotiate rough terrain, with the basic requirements of vehicle safety. As a result, advanced driver assist systems (ADAS) such as traction control (TC), electronic stability control (ESC), and ABS have become prevalent throughout the SUV industry (Breuer and Bill, 2008). Although these ADAS systems have been implemented successfully on passenger vehicles traversing paved roads and highways, the implementation of these systems on off-road vehicles driving on off-road terrains has left much to be desired (Penny and Els, 2016).

1.2 Initial experimental investigation

A 2013 year model Land Rover Defender 110 that is equipped with an OEM fitted ABS was used to experimentally investigate whether ABS is indeed detrimental to the braking performance of a vehicle on a rough road. Braking tests were performed by accelerating the vehicle to speed and then slamming on the brakes so that the wheels either locked (the ABS was disabled by removing the fuse) or the ABS activated. The tests were conducted on a flat concrete road and on the Belgian paving at Gerotek Test Facilities (Armscor Defence Institutes SOC, 2016). Table 1-1 shows the measurement equipment used during the brake tests and their locations on the vehicle body. Data was recorded on a Somat eDAQlite (HBM) at a sampling frequency of 1000Hz.

Table 1-1 Brake test measurement equipment

SENSOR	LOCATION
Differential GPS with base station	Vehicle roof (GPS)
Tri-axial accelerometer	Vehicle CG
3x gyroscopes	Vehicle CG

Figure 1-1 shows the Land Rover Defender braking on Gerotek Test Facilities' Belgian paving (Armscor Defence Institutes SOC, 2016) and Figure 1-2 shows the measured vehicle speed for several test runs. The measured stopping times and stopping distances are given in Figure 1-3.

Figure 1-3 shows that the stopping time and distance increased substantially when the vehicle was braked on the Belgian paving when comparing it to the stopping time and distance on the flat road. The stopping distance increased for both ABS on and ABS off tests on the Belgian paving.

Figure 1-1 Land Rover Defender braking on the Belgian paving at Gerotek Test Facilities (Armscor Defence Institutes SOC, 2016)

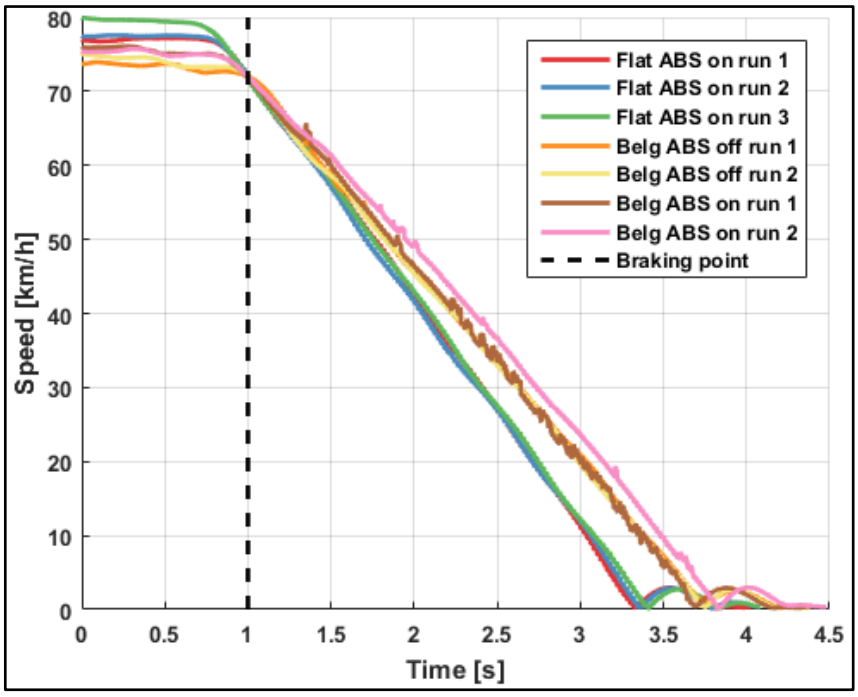

Figure 1-2 Measured vehicle speed during braking manoeuvres

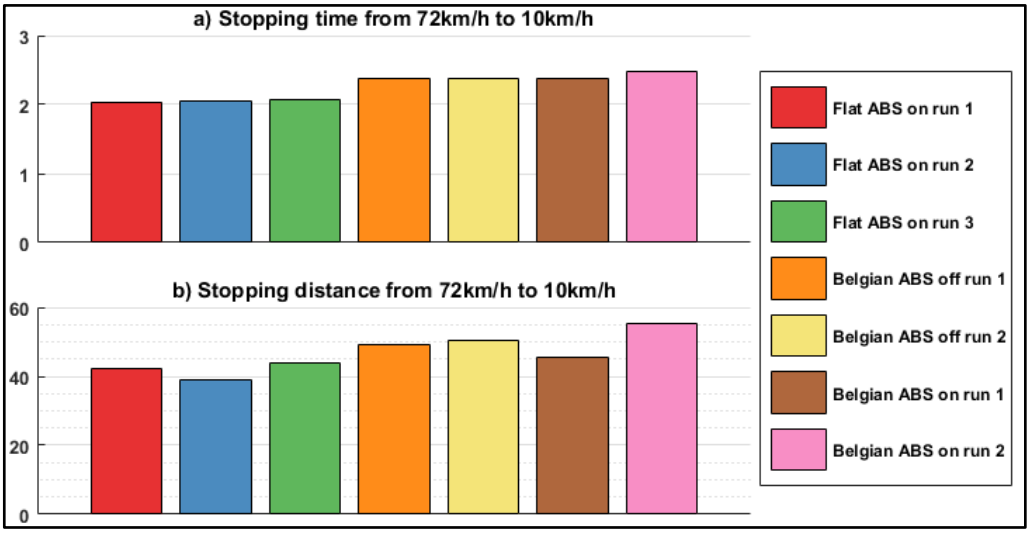

Figure 1-3 a) Measured stopping times and b) stopping distance from braking point as defined in Figure 1-2

The initial investigation of the braking performance of a vehicle and the degradation of this performance on a rough road leads to the main research question of this study. The research question is:

Is there an improvement achievable in the braking performance of a vehicle on a rough road?

This project will investigate this research question, based on the detailed literature review of Chapter 2.

Chapter 2

Literature review of factors influencing braking performance

If we knew what it was we were doing, it would not be called research, would it?

- Albert Einstein (1879–1955), German-born theoretical physicist

Two main factors influencing the braking performance have been identified, namely the force generation characteristics of tyres and the anti-lock braking systems and their control algorithms. Chapter 2 discusses these two factors and their relevance.

2.1 Tyre force generation

Tyre characteristics are of crucial importance for the dynamic behaviour of vehicles and form the foundation of the vehicle dynamics of a ground vehicle. The forces generated in the contact patches between the road and the tyre (the tyre-road interface) determine the way in which a vehicle accelerates, brakes, and corners.

The classical laws of dry friction (Coulomb friction) are not valid when applied to the mechanism of friction force generation of tyres due to the visco-elastic behaviour of rubber (Breuer and Bill, 2008). Two mechanisms are primarily responsible for friction force generation between the tyre and the road, namely adhesion and hysteresis (Gillespie, 1992). The adhesive component arises due to the intermolecular bonds between the tyre molecules and the road surface molecules. Adhesion accounts for the larger component of friction on dry, smooth roads, but degenerates significantly when the road surface is contaminated with water or ice (Blundell and Harty, 2004). The hysteresis component is due to the energy loss when the tyre deforms while sliding over tiny undulations and irregularities in the road surface. Hysteresis is not influenced significantly by water or ice being present on the road surface (Gillespie, 1992). The coefficient of friction is not constant, it depends on the tread compound and road surface friction pairing, the contact pressure (which is not uniform over the contact patch area (Gillespie, 1992)), the contact patch slip speed and the tyre and surface temperature (Breuer and Bill, 2008). All of these phenomena result in tyre characteristics being severely nonlinear.

2.1.1 *Longitudinal force characteristics*

The friction force development of a rolling wheel is only possible when relative movement between the tyre and the road is present. For the case of longitudinal friction force generation, the slip is defined as the ratio between the contact patch sliding velocity and the vehicle's velocity. The sliding velocity is defined as the difference between the vehicle velocity and the tangential tyre velocity (see Equation (2.1)). A rigid body assumption of the wheel is often made and the contact patch velocity is substituted as in Equation (2.2) (Breuer and Bill, 2008).

$$\lambda = \frac{|v_{sliding}|}{v} = \frac{|v - v_{CP}|}{v} \quad (2.1)$$

$$\lambda = \frac{|v - \omega r_{eff}|}{v} \quad (2.2)$$

Figure 2-1 shows a typical steady-state graph of longitudinal friction force as a function of tyre slip on smooth terrain and at constant vertical load. Tyre slip comprises two components, namely deformation and sliding. Deformation slip results from the translational deformation in the region of the contact patch that rotates under the influence of the tangential load (a torque applied to the wheel). The deformation slip determines the linear region of the longitudinal force vs. longitudinal slip curve. The deformation slip diminishes as slip values increase. As longitudinal slip increases, more sliding regions develop in the contact patch. Sliding initially starts at the trailing edge and gradually expands toward the leading edge of the contact patch as the applied tangential load increases. At 100 per cent slip, only sliding is present (Breuer and Bill, 2006). The effect of increasing slip in the contact patch is known as the relaxation length, or run-in effect. Figure 2-1 shows a typical longitudinal friction coefficient curve as a function of longitudinal tyre slip. Figure 2-2 illustrates the concept of longitudinal friction force development in the contact patch.

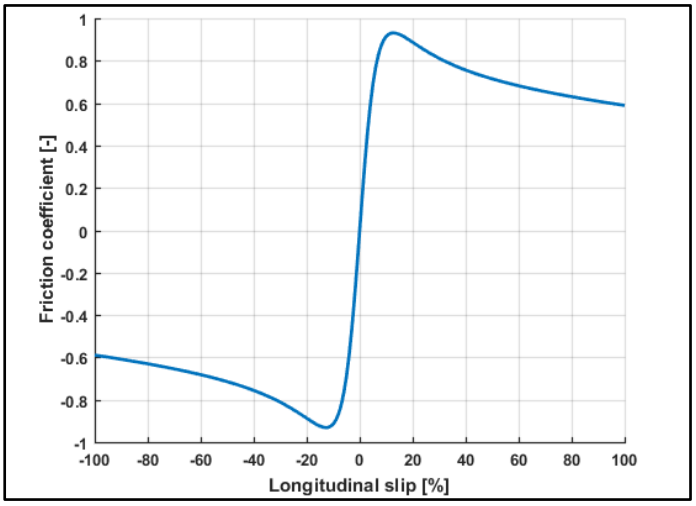

Figure 2-1 Longitudinal friction coefficient as a function of longitudinal tyre slip

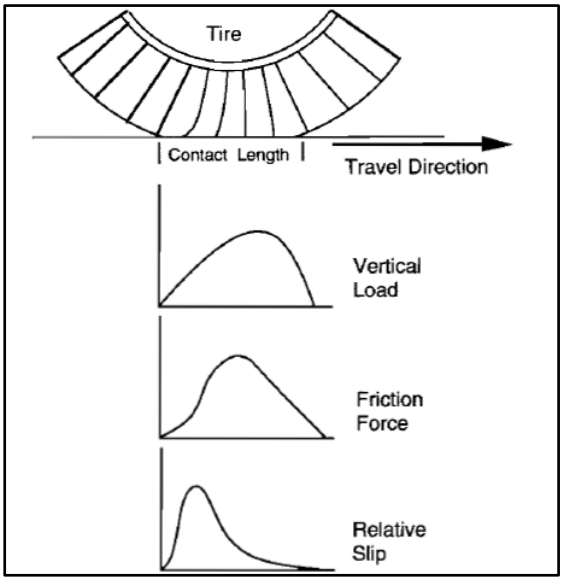

Figure 2-2 Distribution of vertical load, longitudinal friction force and longitudinal slip in the contact patch (Gillespie, 1992)

When the vertical load on a tyre suddenly increases (this may occur due to the vehicle's load transfer or due to the uneven road), the contact patch area is increased. This does not immediately result in increased longitudinal friction force generation because the contact patch was extended by non-deformed rubber. The tyre has to continue rolling before an increase in longitudinal friction force is generated due to the tyre's relaxation length effect (Breuer and Bill, 2008). Reducing the vertical load does not have the same result as increasing the load. While the vertical load is decreased, the rubber that is not in contact with the road anymore relaxes immediately. The comparatively slow increase of the longitudinal force due to loading of the tyre is thus opposed by a quick reduction of the longitudinal force during the unloading of the tyre. According to Breuer and Bill (2008) the intensity of these variations in longitudinal force generation is significantly influenced by:

- the type of suspension,
- the damper characteristics,
- the unsprung mass (wheel, tyre and parts of the suspension) and
- the vertical tyre stiffness.

2.1.2 *Lateral force characteristics*

The aim of ABS is to improve the stopping distance of the vehicle whilst still maintaining stability and some directional control. The development of lateral friction forces by the tyres is very important when considering the stability of a vehicle. The lateral forces not only develop forces when cornering or performing lane changes, they resist external disturbance forces, such as wind gusts and road side-slopes. Lateral forces are mainly generated by the tyre due to lateral slip of the tyre (sideslip angle) and lateral inclination of the tyre (camber angle) (Gillespie, 1992). While tyre camber angle is the main source of lateral force generation for motorcycles, it plays a minor role when applied to cars. The focus here is thus on lateral force generation through sideslip angle.

The sideslip angle is defined by Gillespie (1992) as the difference between the direction of heading of a tyre and the direction of travel. When the tyre elements meet the road they are not deflected and do not generate lateral force. As the wheel rolls along its direction of travel, the tyre elements in the contact patch remain in their original positions, thus deflecting sideways (see Figure 2-3). Since the tyre elements are now deflected, a force is generated. At the rear of the contact patch, the lateral force developed exceeds the available friction and slip occurs. Figure 2-4 shows a typical plot of lateral force as a function of slip angle.

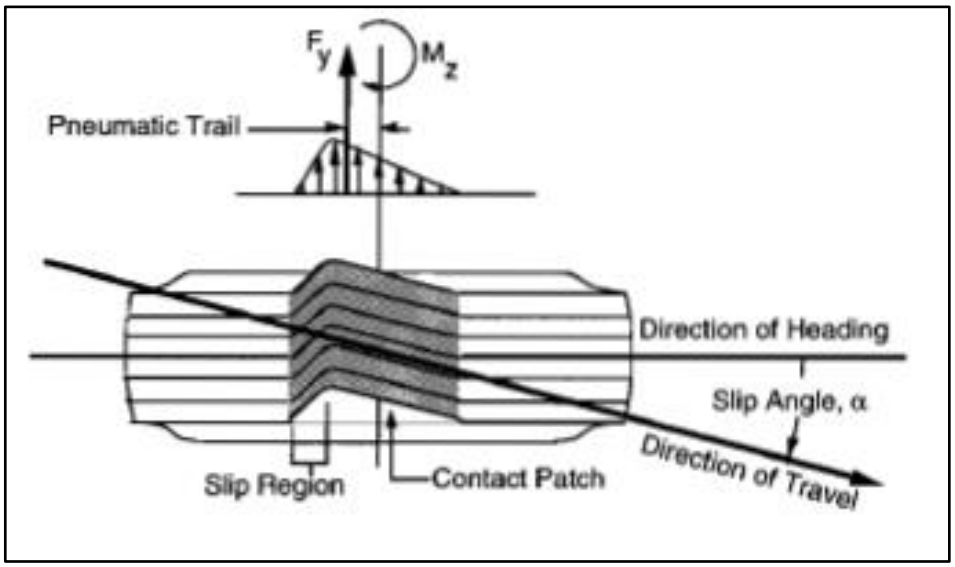

Figure 2-3 Tyre deformation due to a slip angle (Gillespie, 1992)

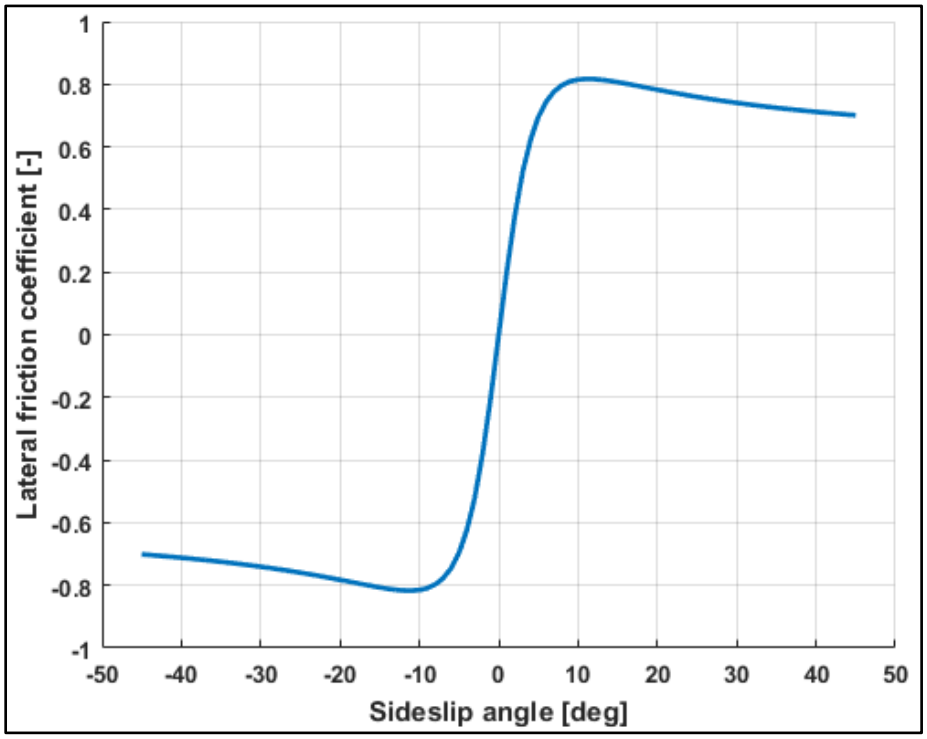

Figure 2-4 Lateral force as a function of tyre side slip angle

2.1.3 *Combined lateral and longitudinal force generation*

When a tyre is operated under conditions where longitudinal and lateral forces are developed simultaneously, the force characteristics depart significantly from those shown in Figure 2-1 and Figure 2-4. As the tyre generates longitudinal force, the lateral force that can be generated diminishes. Since the friction force generated by a tyre in any direction is limited by the friction coefficient multiplied with the normal load, it may be assumed that the maximum force developed in any direction is a constant (assuming that the contact patch is symmetric and the tyre is isotropic). This gives rise to the concept of the friction circle. The friction circle (a plot of lateral force as a function of longitudinal force at constant slip angle) is shown in

Figure 2-5. It may therefore be assumed that the magnitude of the vector sum of the lateral and longitudinal forces cannot exceed the friction limit, hence the limit being characterized by a circle on the plot of lateral force as a function of longitudinal force. The friction circle is a circle if the maximum longitudinal force and maximum lateral force is the same. If the magnitudes of the maxima differ, the friction circle will assume an elliptical shape (Gillespie, 1992).

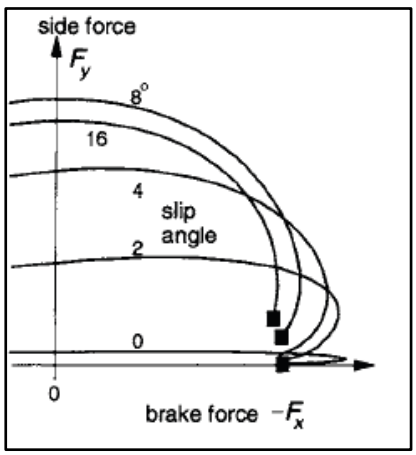

Figure 2-5 The friction circle (Abe, 2015)

2.1.4 *Tyre models*

Tyre modelling has stood at the centre of vehicle dynamics modelling since the dawn of vehicle dynamics research. Research into the behaviour of rubber tyres may be dated back to as early as 1931 (Bradley and Allen, 1931) and advances in the study of the cornering properties was published by Fiala (1954). The research done by Fiala (1954) was theoretically based and described the fundamental properties fairly accurately, especially the cornering properties, but not the self-aligning moment, generated during cornering. A breakthrough was made in modelling the dynamic properties of tyres with the landmark Pacejka Magic Formula semi-empirical tyre model published in 1989 (Bakker et al., 1989). The advantages of using a semi-empirical or curve-fit approach to tyre modelling was the high computational efficiency achievable, a limiting factor in the early days of multi-body dynamics simulation (MBS) run on the computers of the time.

Gillespie (1992) emphasises the importance of understanding the dynamic properties of tyres when he states that all the primary control and disturbance forces, with the exception of aerodynamic loads, are applied to the vehicle through the tyre-road interface (the contact patch). A thorough understanding of the resulting forces and moments is thus essential when modelling a vehicle, especially due to their nonlinear nature. There are four fundamental factors that influence the mathematical modelling of a tyre (Pacejka, 2005):

- Frictional properties in the tyre-road interface
- Distribution of the normal contact pressure
- Compliance of the tread rubber
- Compliance of the belt/carcass

Pacejka (2005) and Blundell and Harty (2004) concur that tyre models are usually developed for a specific application, with different approaches and resulting accuracy. Pacejka (2005) divides tyre models into two main categories, that of mathematical (or empirical) models that describe measured tyre characteristics, and physics-based models. Physics-based models are finite element based and are typically more complex and computationally expensive to implement. The design engineer is tasked with choosing a suitable tyre model that provides adequate accuracy while allowing simulation within a reasonable timeframe.

Blundell and Harty (2004) emphasise that it is often neglected that the resultant forces and moments generated by a tyre are as a product of integration of the forces over the contact patch area. Early tyre models neglected road irregularities, treating the road as an infinitely flat surface requiring only a vertical datum for definition. Advances in tyre modelling extended the road to two-dimensional models that allowed the road to be defined as a series of sections. This allowed for durability simulations, with the tyres encountering potholes, bumps and other obstacles. A typical current approach is to define the road as a three-dimensional object with geometry and frictional characteristics using a finite element based approach.

The most recent development in road profile modelling is to make use of Curved Regular Grid (CRG) road models or Regular Grid Roads (RGR). The CRG road model is open source code that was started by several OEMs in Germany in 2008. The CRG road model has a regular elevation grid with a curved centreline, providing high fidelity road models with compact storage (VIRES Simulationstechnologie GmbH, 2016). RGR road models were developed specifically to be used with FTire models and differs from CRG roads because it does not contain a centreline. An RGR road will have a square shape in the x-y road plane. The road centreline is described in a separate file as a 3D spline (MSC Software, 2016). CRG and RGR road property files are typically more compact than the corresponding RDF file of the same terrain.

2.1.4.1 The Fiala tyre model

The Fiala tyre model, developed in 1954, approximates the carcass deflection by a symmetric parabola. The Fiala model has the advantage that it only requires ten input parameters that are all physically related to the tyre properties. There are, however, several limitations to the model, namely:

- The model cannot represent combined loading.
- The influence of camber angle on the lateral force and self-aligning moment characteristics is not modelled.
- The variation in cornering stiffness at no slip angle due to varying vertical tyre load is not considered.
- The offsets in lateral force characteristics due tyre construction (conicity and ply) are not included (Blundell and Harty, 2004).

The Fiala model is rarely used nowadays in the literature.

2.1.4.2 The Magic Formula tyre model

The so-called Magic Formula tyre model was developed by Bakker et al. (1989) and has gone through numerous revisions and refinements (Pacejka, 2005). It is a semi-empirical model, initially developed only for smooth terrains, that is used to calculate steady-state tyre force and moment characteristics and is based on a series of curve-fits based on polynomials of a Fourier series. In their discussion of the Magic Formula model, Blundell and Harty (2004) laments on the disadvantage that the curve fit coefficients have no engineering significance in terms of the physical tyre properties. The Magic Formula tyre model was originally developed to relate (although the Magic Formula model now provides for a range of tyre properties):

- the lateral force F_y as a function of slip angle α,
- the aligning moment M_z as a function of slip angle α and
- the longitudinal force F_x as a function of longitudinal slip λ.

Data for these curves are obtained from steady state tyre testing, i.e. lateral force and self-aligning moment are measured during pure cornering, and longitudinal force is measured during pure braking. The general form of the model, as presented in Bakker et al. (1989), is given in Equation (2.3).

$$y(x) = D\sin[C\tan^{-1}\{Bx - E(Bx - \tan^{-1}Bx)\}]$$

where

$$Y(X) = y(x) + S_v \qquad x = X + S_h \tag{2.3}$$

In the case of Equation (2.3), Y is either side force F_y, the aligning moment M_z, or the longitudinal force F_x and X is either the slip angle α or the longitudinal slip λ. S_v and S_h are vertical and horizontal offsets arising from tyre construction features such as conicity and ply or added camber angle (in the case of lateral force). The coefficients B to D are illustrated in Figure 2-6. E is a curvature, given by Equation (2.4).

$$E = \frac{Bx_m - \tan(\pi/2C)}{Bx_m - \tan^{-1}(Bx_m)} \tag{2.4}$$

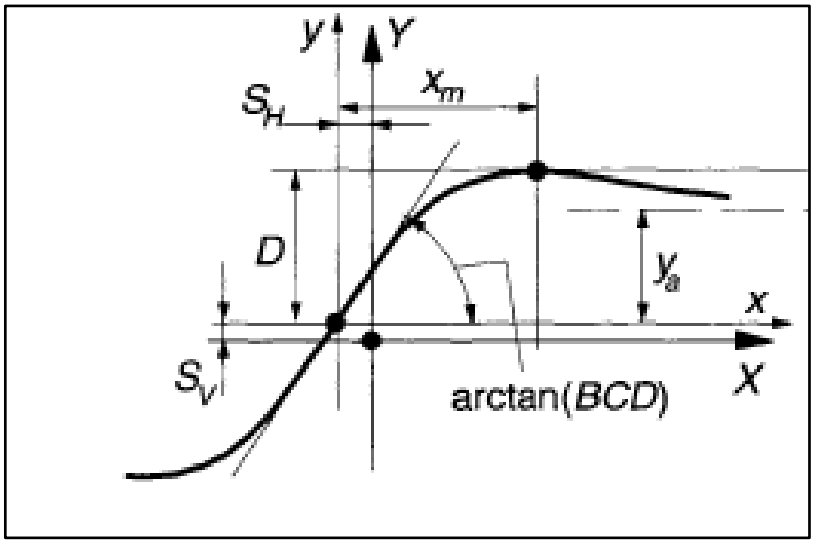

Figure 2-6 Coefficients used in the Magic Formula tyre model (Bakker *et al.*, 1989)

The Magic Formula model utilises a set of coefficients $a_0, a_1, a_2 \dots a_{13}$ (for lateral force), $b_0, b_1, b_2 \dots b_{10}$ (for longitudinal force) and $c_0, c_1, c_2 \dots c_{17}$(for self-aligning moment) that are used to formulate the curves characterising the tyre force characteristics. Equation (2.5) is an example of the quantity BCD (the slope, see Figure 2-6) for longitudinal force (Bakker et al., 1989). These coefficients are used as input to the simulation software.

$$BCD = (b_3 F_z^2 + b_4 F_z) exp(-b_5 F_z) \tag{2.5}$$

Pacejka (2005) provides a comparison between the Magic Formula model's computed characteristics and experimental data of a 195/65R15 tyre (the data was captured with Delft University's Delft Tyre Test Trailer). In general, there is good agreement between computed and measured curves, with the exception of self-aligning torque under braking conditions. Pacejka (2005) attributes the discrepancy to varying road camber variations and tyre non-uniformities.

The enveloping behaviour of the tyre when negotiating obstacles and road irregularities has to be simplified, because the Magic Formula model requires that the contact patch be reduced to a single point. Pacejka (2005) presented the enveloping behaviour of tyres when slowly rolled over various cleats at various axle heights. Figure 2-7 shows (from top row to bottom row): the shape of the cleat, the measured vertical force, the measured horizontal (longitudinal force) and the effective roll radius for a 205/60R15 tyre.

Changing the effective roll radius of a tyre due to varying vertical loads has the effect of moving the instantaneous centre of zero velocity. Pacejka (2005) identified three possible locations of the instantaneous centre of zero velocity, which is illustrated in Figure 2-8. For the case when the wheel load is zero, the instantaneous centre of zero velocity is level with, or slightly below, the road surface. A small wheel load results in some tyre deflection and may have the effect that the instantaneous centre of zero velocity is above the road surface. Finally, under large vertical loads the instantaneous centre of zero velocity is below the road surface.

It is thus of crucial importance that tyre models accurately define the effective roll radius, especially when the model is being used on an uneven road. The effective roll radius is determined in the simulation environment by the tyre-road contact model.

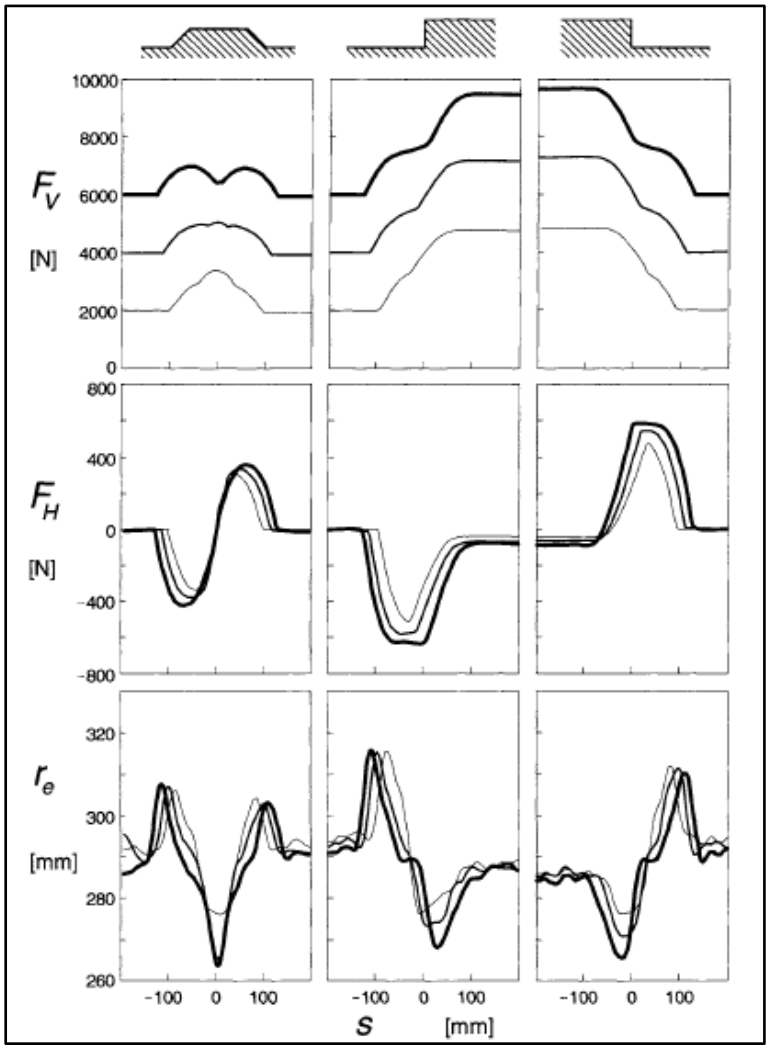

Figure 2-7 Effective roll radius variations for a tyre rolling over various cleats at varying axle heights (Pacejka, 2005)

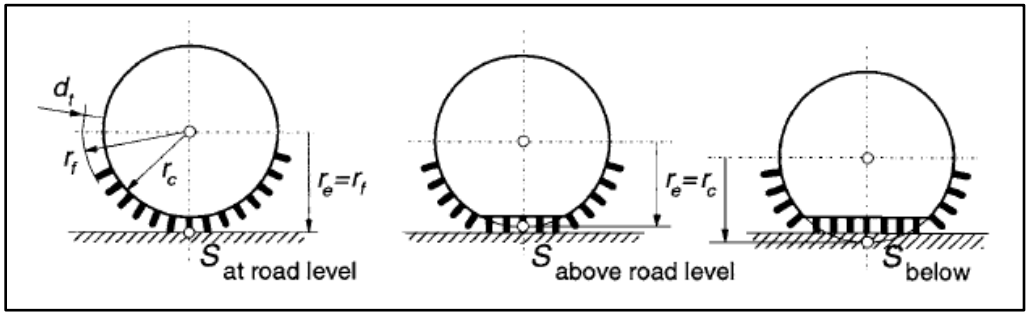

Figure 2-8 Location of instantaneous centre of zero velocity, from left to right: zero wheel load, a small wheel load, and a large wheel load (Pacejka, 2005)

MSC Software's (2016) ADAMS suite has four different contract methods that model the contact between the tyre model and the road, namely the one point follower contact, the 3D equivalent volume contact, the 3D enveloping contact, and the tyre cross-section profile contact method. The tyre cross-section profile contact method is intended for use with motorcycle tyres and is omitted from this investigation.

2.1.4.2.1 One point follower contact

The one point follower contact method is the default method used by ADAMS (MSC Software, 2016). This approach considers the tyre and rim as a disk and the contact point is the point on the wheel centre plane and the road tangent plane that has the shortest distance to the wheel centre. The single point follower contact method is only valid for smooth roads and

obstacles with a wavelength larger than the tyre's circumference. The contact method is illustrated in Figure 2-9. This method may be used with 2D road, 3D Spline Road, OpenCRG Road, and RGR Road road types (MSC Software, 2016).

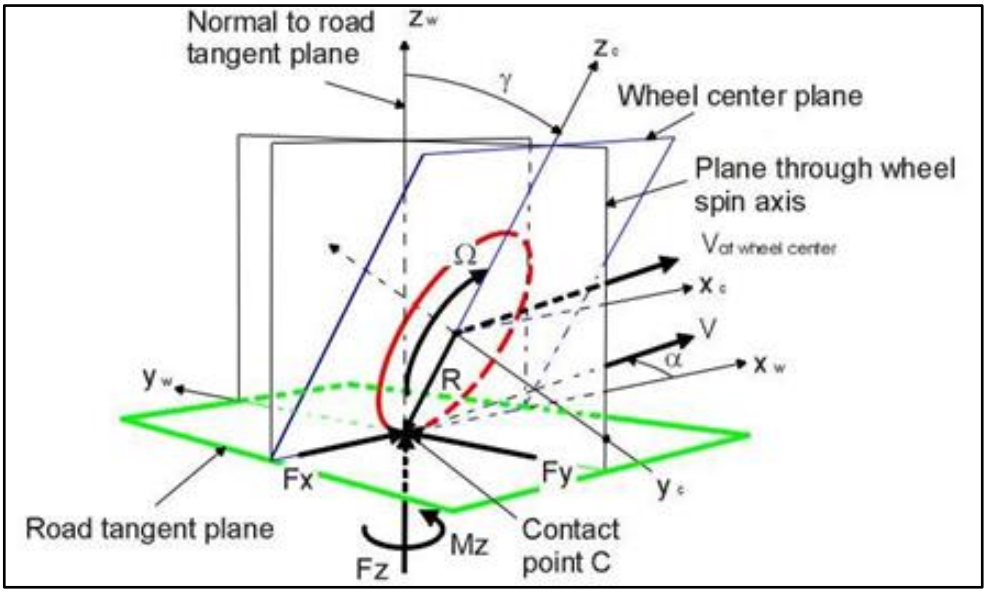

Figure 2-9 One point follower contact (MSC Software, 2016)

2.1.4.2.2 Three dimensional (3D) equivalent volume contact

The 3D equivalent volume contact method is used in ADAMS with 3D Shell Roads (MSC Software, 2016). This method utilises a three-dimensional tyre-to-road contact method that computes the volume of intersection between the road and the tyre. The road is modelled as a set of discrete triangles and the tyre as a set of cylinders. The width and shape (see Figure 2-10) of the tyre is used to determine the penetration of the tyre into the road and from this penetration, an effective contact point is determined. Similar to the one point follower contact method, this method is intended for use with smooth roads and obstacles with a wavelength larger than the tyre circumference (MSC Software, 2016).

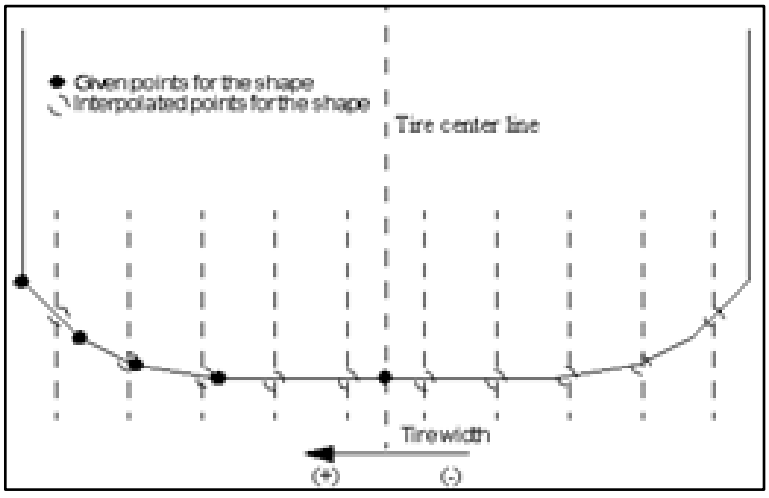

Figure 2-10 3D equivalent volume contact method (MSC Software, 2016)

2.1.4.2.3 Three dimensional (3D) enveloping contact

The 3D enveloping contact method is intended for use over undulating roads with wavelengths shorter than the tyre circumference. ADAMS uses the so-called 'tandem-egg' or 'tandem-cam' approach to model this enveloping effect. A series of connected elliptical cams are defined so that the outside shape corresponds to the tyre shape (see Figure 2-11). The contact of each cam is then determined during simulation (MSC Software, 2016).

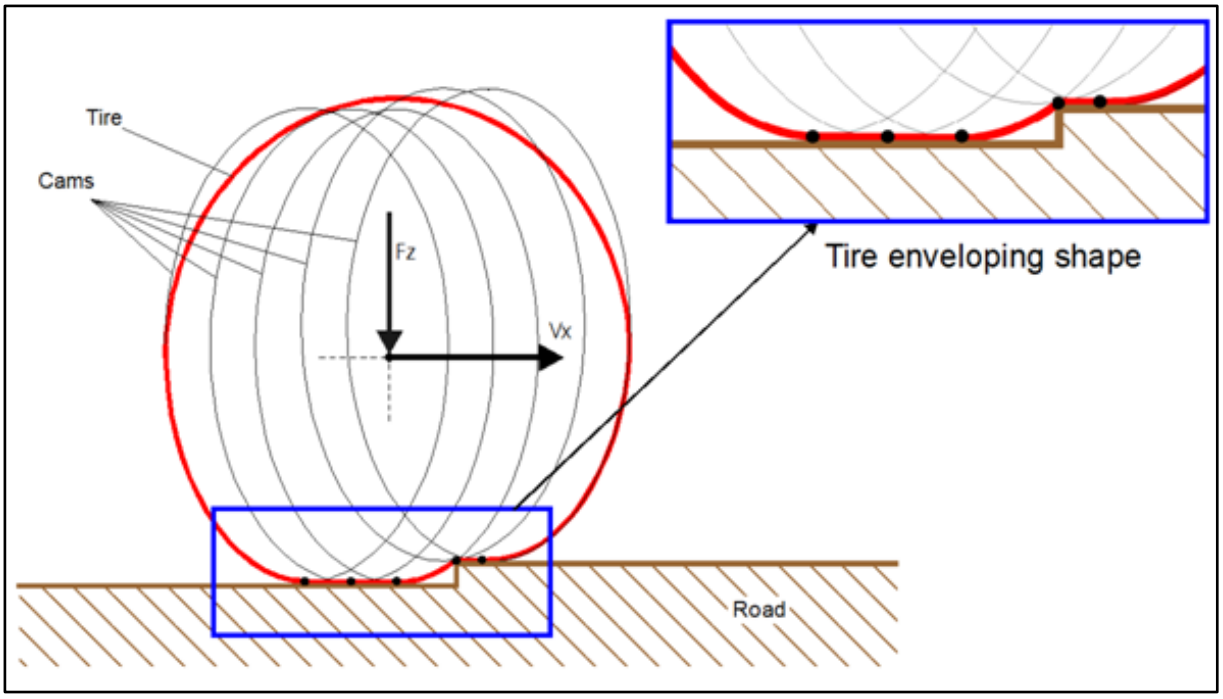

Figure 2-11 3D enveloping contact method (MSC Software, 2016)

2.1.4.3 The Brush model

Rather than being a single model, the Brush model should rather be classified as an approach to tyre modelling, as there are various different interpretations and implementations of the concept of the Brush model. The Brush modelling approach is discussed by Pacejka (2005). The premise on which the Brush model is based is that the tyre can be modelled as a row of elastic bristles that touch the road plane and can deflect in the horizontal direction (that is laterally and longitudinally). The bristles are called tread elements and their compliance represents the elasticity of the combination of carcass, belt, and actual tread elements of the real tyre. The Brush model thus falls in the theoretical tyre model category and is a rather simple physical model. As the tyre rolls, the tread elements entering the contact patch are not deflected and the element is assumed perpendicular to the road surface. As the tread element progresses through the contact patch, it deflects and a corresponding force is generated. The tip of the tread element stays in contact with the road in the same position as long as there is sufficient friction (adhesion). When the force exceeds the available adhesion, the tread element's tip starts to slide across the road surface. Figure 2-12 gives a representation of the Brush model.

Figure 2-12 shows the deflection of each tread element increases as it moves through the contact patch. The deflection varies linearly with distance from the leading edge of the contact patch. The maximum deflection is governed by the coefficient of friction, the vertical force distribution, and the stiffness of the tread elements. Numerous approaches to modelling the coefficient of friction, vertical force distribution and tread element stiffness gives rise to the various interpretations in the literature. The Brush model approach takes into account the effect of pure sideslip and pure longitudinal slip, as well as combined slip conditions. The effect of camber on lateral force and self-aligning moment and during combined loading is also considered (Pacejka, 2005).

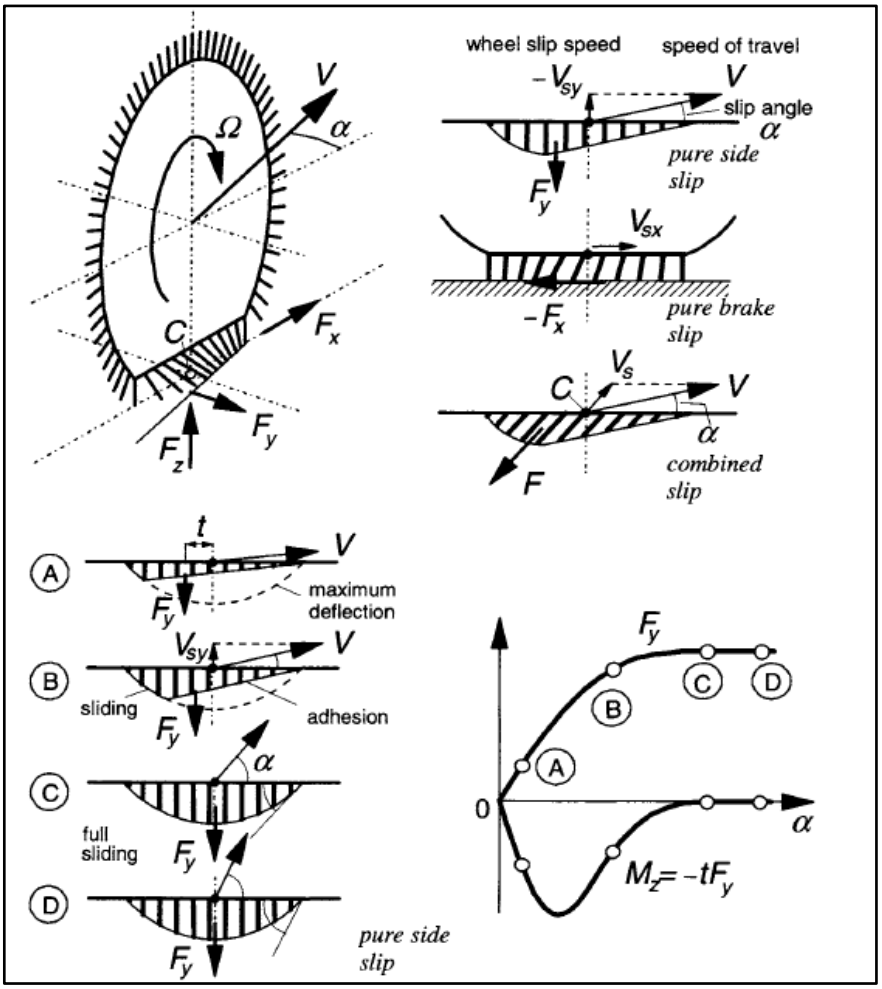

Figure 2-12 The Brush tyre model (Pacejka, 2005)

2.1.4.4 Rigid ring tyre model and MF-SWIFT

The rigid ring tyre model was originally developed by Zegelaar and Pacejka (1997) and models the tyre-wheel system with three components: the tyre tread-band (or ring), the rim and the sidewalls. The tread-band is modelled as a rigid circular ring with three degrees of freedom and the rim is modelled as a rigid body that rotates. The model thus has four degrees of freedom. The tread-band and the rim are connected via two translational springs and dampers and one rotational spring and damper, the springs and dampers representing the sidewall. A transient slip model is included in the rigid ring model that makes provision for the relaxation length (run-in) phenomenon. Figure 2-13 shows the basic tyre model.

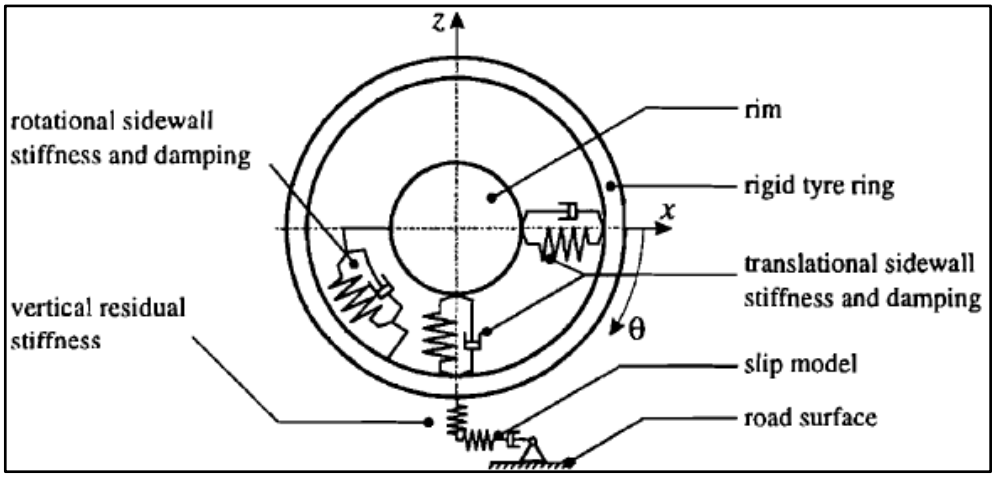

Figure 2-13 The rigid ring tyre model (Zegelaar and Pacejka, 1997)

A modal analysis is performed to parameterise the model. Frequency response functions are estimated by exciting the tyre with brake torque variations at various vertical loads. The rigid ring model approach was expanded by Delft University and TNO to the current MF-SWIFT model. MF-SWIFT is an acronym for Magic Formula – Short Wavelength Intermediate Frequency Tyre. It is intended to capture the dynamic tyre behaviour up to 60-100 Hz and has the capability to handle short wavelength obstacles, while incorporating the Magic Formula characteristics too. Some ability to use the model on uneven roads is also included (Schmeitz et al., 2007).

The contact patch slip model attempts to capture the delay caused by the relaxation length phenomenon by modelling it as a first-order differential equation. The largest drawback of the MF-SWIFT approach is that it still relies on reducing the contact patch to a single point where the forces characterised by the Magic Formula can be applied. The approach followed by the MF-SWIFT model is to determine an 'effective road surface', assuming that the quasi-static response of the single-point tyre-road interface is the same as the quasi-static response of a real tyre on a real uneven road surface. The tyre model's resulting response to regular obstacles, such as a step, sine, trapezium, and triangular bumps looks promising when compared to drum test experimental data (Schmeitz et al., 2007).

2.1.4.5 Flexible Ring Tire Model (FTire)

FTire is one of the more recently developed tyre models and is a 3-dimensional nonlinear vibration model that may be used for vehicle dynamics simulations on even and uneven roadways (Gipser, 2007). The tyre belt is represented by a slim ring that can be displaced and bent in arbitrary directions relative to the rim. The flexible belt ring is modelled with bending stiffness while elastically mounted on the rim, complete with radial, tangential, and lateral stiffness. This enables the ring to have in-plane and out-of-plane degrees of freedom. The ring is numerically approximated with a finite number of belt elements that are coupled with their direct neighbours with nonlinear springs and bending stiffness. Massless tread ribs are added to each belt element (similar to the tread elements in the Brush model). These ribs have nonlinear stiffness and damping properties in the radial, tangential, and lateral directions. The radial deflections of the ribs depend on the road profile, locus, and orientation of the belt element to which they are attached. The tangential and lateral deflections of the ribs are determined by the sliding velocity on the ground. The FTire model provides for all six forces and moments of the tyre by integrating the elastic forces in the belt (Gipser, 2007).

An advantage to using the FTire model is that it provides for the use of various road models and the traversing of obstacles in the rolling direction. Figure 2-14 depicts the FTire rolling over a Belgian paving along with the resulting instantaneous pressure distribution (Gipser, 2007). It is a high frequency, non-linear, physics-based model that takes the entire contact patch area into account.

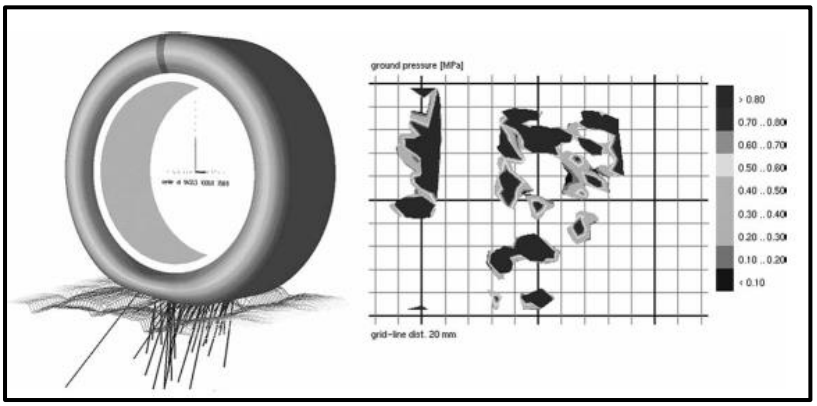

Figure 2-14 FTire rolling over a Belgian paving (Gipser, 2007)

Stallmann et al. (2014) compared the vertical response of the Magic Formula tyre model implementation in ADAMS (MSC Software, 2016) with that of the FTire model. They concluded that the FTire model gives significantly more accurate results.

2.1.4.6 Experimental validation of tyre models

A significant amount of research has been done with regard to the modelling of tyre characteristics. Some of these models are very complex and nonlinear, but in order to obtain meaningful simulation models, it is necessary to compare the models' characteristics with the actual characteristics of the tyres being simulated. Unfortunately, obtaining experimental data on tyres is a difficult process.

The University of Pretoria has a tyre test trailer designed to test tyres of various sizes, ranging from SUV tyres (with a free radius of approximately 400mm) to large military specification tyres with a diameter of 1.6m and even larger. The tyres are mounted on adjustable hubs that allow continuous slip angle adjustments and discrete camber angle adjustments. The hubs have commercial brake discs and callipers that may be used to brake the wheels to validate longitudinal force characteristics. Combined loading cases may also be tested. The measurement axle is fitted with an air suspension that allows the continuous adjustment of vertical force on the tyres.

Wheel force transducers (WFT) are used to measure the tyre forces and moments. This allows measurement of the six forces and moments generated by a tyre while it is mounted to a vehicle that is in transit. The Wheel Force Transducer has been calibrated and validated to prove that it measures accurately (Becker and Els, 2012).

In summary, the tyre tester may be used to capture all six force and moment components generated by the tyre due to varying slip and camber angles, and different applied brake pressures on real roads. An earlier version of the tyre tester was used successfully to capture the tyre characteristics of a Michelin XZL 16.00R20 tyre (Babulal et al., 2015, Stallmann and Els, 2014, Stallmann et al., 2014). The tyre tester is shown in Figure 2-15.

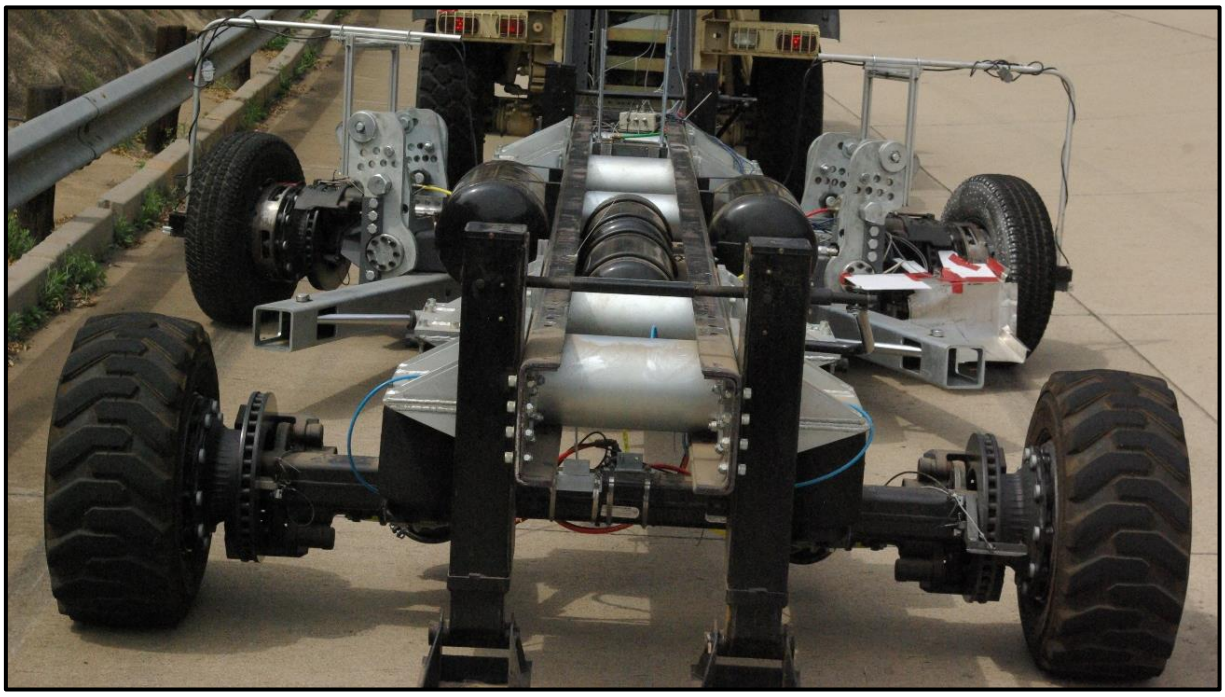

Figure 2-15 University of Pretoria tyre test trailer

2.1.5 *Tyre factors influencing braking performance*

Undulations in the road surface cause wheel and body motions that result in varying vertical wheel loads. Due to the nonlinear characteristics of tyres, it may result in decreased longitudinal forces generated at the tyre-road interface. This may have the effect of increased stopping distances on uneven or rough roads due to a loss in the longitudinal friction force. The rougher the road, the higher the loss of longitudinal friction force is. This phenomenon significantly complicates the modulation of brake pressure by an anti-lock braking system (Breuer and Bill, 2008).

Jaiswal et al. (2010) used a 14 degree of freedom (DOF) vehicle model to study the influence of tyre model transience on ABS braking. They used three, single-point contact transient tyre models, a stretched-string tyre model, a modified stretched-string tyre model, and a contact mass transient tyre model. Straight-line braking and brake-in-turn manoeuvres were simulated on smooth road surfaces. Different road surface conditions were simulated, namely a dry road, a wet road and a dry snowy road. Jaiswal et al. (2010) concluded that the accurate modelling of the tyre transient dynamics is crucial to the accurate simulation of ABS braking.

Adcox et al. (2013) investigated the effect of the tyre's torsional dynamics on the performance of ABS. A rigid-ring tyre model with a LuGre friction model was used in the simulation environment and a quarter-car test rig was built. Included in their investigation was a sensitivity analysis where low-pass filtering the wheel speed, the sensitivity to sidewall torsional stiffness and the sensitivity to wheel and tread ring inertia (of the rigid ring model) were considered. Their investigation showed that the low-pass filter's cut-off frequency had a significant effect on the braking distances achieved. The selection of the cut-off frequency was also tyre dependent and it influenced the robustness of the ABS performance to variations in tyre inertia and torsional stiffness.

2.2 Braking

The second main factor of cardinal importance to the braking performance of a vehicle is the braking system and its components. A driver operates a vehicle by accelerating, braking and steering in a closed loop. In this closed control loop, the vehicle may be seen as the controlled system, the driver the controller, and the environment in which the vehicle is located as a source of information and interferences. The driver, who makes decisions based on his/her experience and intuition and reacts to the vehicle's response, gives inputs to the vehicle. The vehicle then reacts to these inputs (Breuer and Bill, 2008).

Breuer and Bill (2008) divide the braking process into three categories:

1. Parking braking (preventing unwanted movement of a stationary vehicle)
2. Continuous braking (preventing unwanted acceleration while driving downhill)
3. Deceleration braking (reducing the speed of a vehicle)

Parking braking is a simple force balance. The applied brake force must prevent the vehicle from moving, be it by rolling downhill or by external applied forces on a level road. The engine via the transmission while travelling downhill often performs continuous braking. To prevent excessive heat dissipation in the friction brakes, retarders or engine braking is used. When the driver desires higher decelerations, the friction brakes are used to brake the wheels. For the vehicle to decelerate, friction forces must be generated in the tyre-road interface (Breuer and Bill, 2008).

2.2.1 *Load transfer during braking*

During braking, load transfers from the rear axle to the front. The dynamic axle load varies due to the centre of mass height, wheelbase, and the magnitude of the deceleration (Breuer and Bill, 2008). Gillespie (1992) describes this dynamic load transfer with Equation (2.6):

$$W_d = \frac{h_{PC}}{L} m_s \ddot{x} \tag{2.6}$$

Equation (2.6) shows that the load transfer is more pronounced when the vehicle centre of gravity is located far from the pitch centre, as is the case for SUVs. The maximum brake force on the front axle is thus dependent on the brake force on the rear axle through the deceleration and the associated load transfer from the rear brake action. The same effect is present on the rear axle. The relationship between the front and rear brake force for a typical passenger car on a surface with coefficient of friction of $\mu = 0.81$ is shown in Figure 2-16 (Gillespie, 1992). Because of the load transfer from the rear to the front axle, the front wheels see an increased normal force resulting in a corresponding increase in longitudinal force. This leads to the concept of brake proportioning and front disk brakes are typically larger with increased cooling to exploit the increased braking capability of the front wheels.

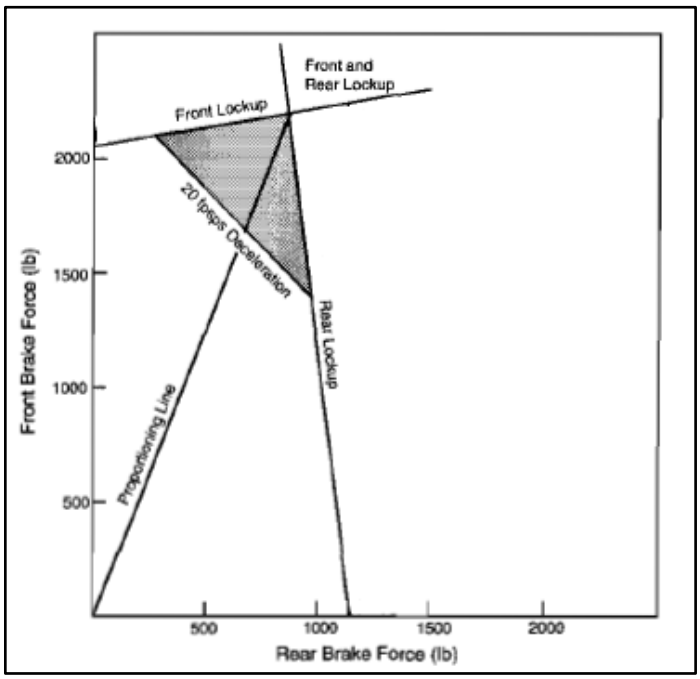

Figure 2-16 Maximum brake forces on front and rear axle (Gillespie, 1992)

2.2.2 *Vehicle stability during braking*

The forces generated by the tyres during braking significantly influence the vehicle dynamics. Vehicle deceleration performance cannot be separated from the vehicle's ability to remain stable during the braking process. Pitch and yaw motions may result from the braking process. In the United States of America, the Federal Motor Vehicle Safety Standard (FMVSS) 105 and 121 (FMVSS, 2013) establishes the braking performance requirements for vehicles with hydraulic and air brake systems, respectively. Gillespie (1992) summarises the requirements as follows:

a) A fully loaded passenger car with new, unburnished brakes (new brakes that have not been polished due to operation) must be able to stop from speeds of 50 and 100km/h in distances that correspond to average decelerations of 5.2 and 5.5m/s^2, respectively.

b) A fully loaded passenger car with burnished brakes must be able to stop from 50, 100, 130 and 160km/h in distances that correspond to average decelerations of 5.2, 5.8, 5.5 and 4.9m/s^2, respectively.
c) A lightly loaded passenger car with burnished brakes must be able to stop from 100km/h in a distance that corresponds to an average deceleration of 6.1m/s^2.
d) A lightly loaded and fully loaded car with a failure in the brake system must be able to stop from 100km/h in a distance that corresponds to an average deceleration of 2.6m/s^2.

The hydraulic brake standard (FMVSS 105) only has stopping requirements for dry, even surfaces (Gillespie, 1992). Due to the nonlinear, visco-elastic friction mechanism that generates forces at the tyre-road interface, a locked tyre (when the tyre is sliding with no rotation over the road surface) cannot generate any lateral forces. This may create an unstable situation in the lateral direction and about the vertical axis of the vehicle. A vehicle is considered stable when braking inputs do not induce any unwanted vehicle movements. It is permissible that the vehicle becomes unsteerable (i.e. the front wheels lock) as long as it remains on a straight course. Lateral swerving of the rear axle (which may occur when the rear wheels lock) is not permissible (Breuer and Bill, 2008). Gillespie (1992) asserts that it is desirable to lock up the front and rear wheels at the same time, but acknowledges that this is not possible over the complete range of operating conditions under which the vehicle must remain stable and controllable.

The shaded area in Figure 2-16 indicates the braking region during which decelerations greater than 6.1m/s^2 (20fpsps in Figure 2-16) will occur. The aim of brake proportioning is determining the slope of the proportioning line (see Figure 2-16) so that front wheel lockup will always occur before rear wheel lockup under all operating conditions. The limit of stability is reached if the brake force generated at the front and rear is the same. If this condition is met, the braking system is termed ideal and the result will be the shortest possible stopping distance (Breuer and Bill, 2008). The ideal brake proportioning line is shown in Figure 2-16.

In vehicles not equipped with ABS, brake force metering devices are implemented to ensure that the vehicle brakes along the ideal brake proportioning line up to a set deceleration magnitude. Once this magnitude is reached, the brake force at the rear axle is reduced and the front wheels subsequently lock before the rear wheels (Gillespie, 1992). Breuer and Bill (2008) condense the goal of a braking system to the following:

The highest goal for a good brake system design must be that a vehicle obtains a short braking distance, does not leave its track, and remains steerable.

This is in agreement with the SAE requirement of ABS:

"The application of ABS to a vehicle can provide improvements in the vehicle performance under braking compared to a conventional brake system. Improvement is typically sought in the areas of stability, steerability, and stopping distance … In addition to minimizing stopping distance, vehicle stability is another aspect to straight line braking that must be considered. For the case of straight line braking with the steering held fixed in the straight ahead position, the vehicle should brake in a straight line in the presence of external disturbances … Preservation of steering control and stability during braking are prime goals of the application of ABS to vehicles." (SAE, 2014).

2.2.3 *Anti-lock brake systems (ABS)*

The application of ABS in vehicles has eliminated the need to use brake proportioning, since each wheel is individually prevented from locking (Gillespie, 1992). Wheels tend to lock

almost instantaneously once the longitudinal slip exceeds the slip value at which peak longitudinal force is generated (Dukkipati et al., 2008).

Breuer and Bill (2008) list the requirements for ABS as:

- Brake control must allow for steerability and stability on all roads.
- ABS must fully exploit the maximum coefficient of friction between the tyres and the road.
- Brake control has to work at all vehicle speeds.
- Brake control must adapt quickly to changing friction coefficients and must be tolerant with respect to wear and tear.
- ABS must show full performance for environment temperatures ranging from -20°C to 120°C.
- The yaw moments induced by braking on roads with varying coefficients of friction at the wheels must increase slow enough to allow average drivers to counter steer.
- When braking in a turn, the car must remain steerable and stable and have minimum braking distance.
- On uneven roads, the requirements for steerability, stability, and minimum braking distance are still applicable.
- ABS must be tolerant of different tyres and tyre wear levels.
- Car vibrations may not be amplified by ABS control.
- The average of the brake pedal position may not change significantly during pedal oscillations.
- The maintenance of perfect performance must be guaranteed and in the case of failure, the system must be switched off.

ABS hardware consists of an electronic control unit (ECU), a solenoid valve for releasing and reapplying pressure to a brake circuit, a pump, and a wheel speed sensor. Each brake circuit has two solenoid valves, resulting in eight valves for a vehicle with four wheels. The solenoid valves and the pump are located in the ABS modulator.

Two advantages of implementing ABS are:

- The longitudinal friction force generated is maintained close to the peak due to the cycle of releasing and reapplying brake pressure (see Figure 2-17) (Dukkipati et al., 2008).
- During the release phase of ABS application, the wheel does not generate longitudinal force. This allows the wheel to generate lateral force, which in turn provides some control to the driver via steer input (Breuer and Bill, 2008).

There are several ABS control strategies available, making use of modern control techniques such as sliding mode control, gain scheduling and fuzzy logic control (Aly et al., 2011). The best-documented ABS algorithm was published by Robert Bosch GmbH in 1999 (Siegert et al., 1999), referred to as the Bosch algorithm henceforth. The Bosch algorithm is a bang-bang type, rule-based control strategy that uses three different pressure control modes to control the brake pressure at each wheel. These three pressure control modes are pump (increase pressure), dump (reduce pressure), and hold (maintain pressure). The Bosch algorithm combines these three pressure control modes in various configurations resulting in a repetitive ABS control cycle consisting of eight phases (Penny and Els, 2016).

The Bosch algorithm takes the wheel angular acceleration and longitudinal slip as inputs to the rule-based algorithm. Two upper and one lower threshold for the angular wheel acceleration and an upper longitudinal wheel slip threshold are defined *a priori* and different control phases are triggered when these thresholds are exceeded. Figure 2-18 shows a schematic representation of the Bosch algorithm.

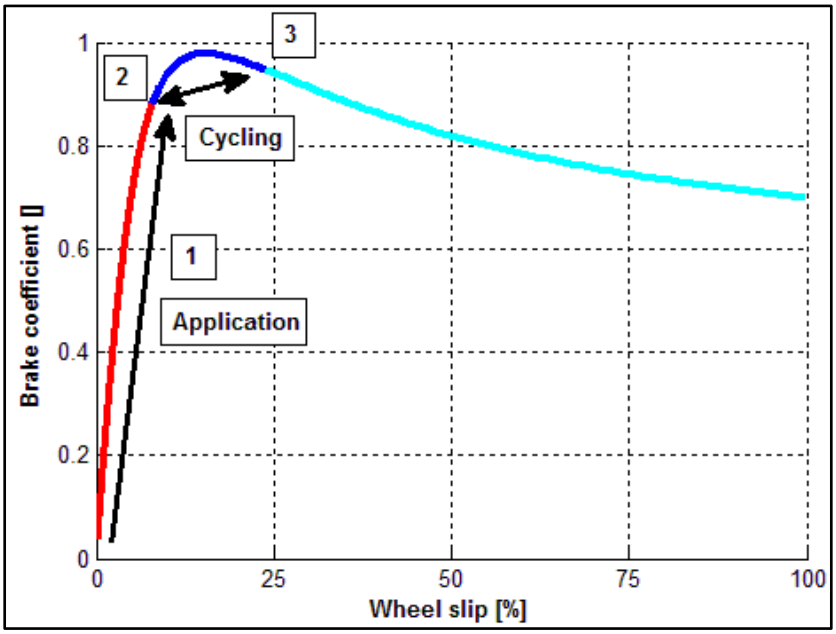

Figure 2-17 ABS operation: 1) Wheel is braked below peak friction coefficient 2) Peak friction coefficient is reached 3) Wheel starts to lock but brake pressure is released. Once wheel is up to speed, braking is resumed from point 1.

Phase 1 is the start of the control cycle, where the brake calliper pressure is the same as the master cylinder pressure. Once the wheel peripheral acceleration goes beyond the defined lower threshold, Phase 2 is triggered. During Phase 2 the brake pressure is held constant, as the wheel acceleration could have exceeded the lower acceleration threshold with the wheel slip still below the slip threshold. Phase 2 is time limited to prevent the cycle from remaining in a hold-phase and thus increasing braking distance. If the slip threshold is not exceeded during Phase 2, the control cycle returns to Phase 1. Brake pressure is thus gradually built up by cycling between Phase 1 and 2 until the slip threshold is exceeded. Once the slip threshold is exceeded, Phase 3 is initiated. Brake pressure is reduced during Phase 3 until the wheel acceleration is within the acceptable range, i.e. above the lower acceleration threshold. Phase 4 is a hold-phase where brake pressure is held constant until the wheel acceleration exceeds the higher of the two upper acceleration thresholds or a predefined time limit is exceeded (as in Phase 2, the cycle is prevented from remaining in a hold-phase for too long). Once the wheel acceleration exceeds the higher of the two upper acceleration thresholds, Phase 5 is begun. At this stage, the wheel is slightly under braked and brake pressure is increased as quickly as possible. Phase 6, a constant pressure phase, is started when the wheel acceleration drops below the higher of the two upper acceleration thresholds and is maintained until the wheel acceleration drops below the lower of the two upper acceleration thresholds. A time limit is applied to Phase 6 too, as is the case for all the hold phases. Pressure is built in stages in Phase 7, using a stepwise increase. The pump-hold stages are cycled at a predetermined rate. Phase 7 continues until the wheel acceleration drops below the lower acceleration threshold. Phase 8 is similar to Phase 3 and the control cycle is repeated. The Bosch algorithm is shown schematically in Figure 2-18.

In Figure 2-18, A and α_{max} denote the two upper angular wheel acceleration thresholds, α_{min} the lower angular acceleration threshold, and λ_{max} the upper slip threshold. A is typically chosen as $10\alpha_{max}$. t_{up} and t_{hold} are time limits used in the control cycle to prevent the algorithm from becoming stuck in a certain phase. t_{up} and t_{hold} are also used to gradually build pressure in Phase 7. Figure 2-19 shows the resulting brake line pressure for one cycle of the ABS algorithm. The values used for the acceleration and slip thresholds are given in Table 2-1. The thresholds were the same as those used by Penny and Els (2016)

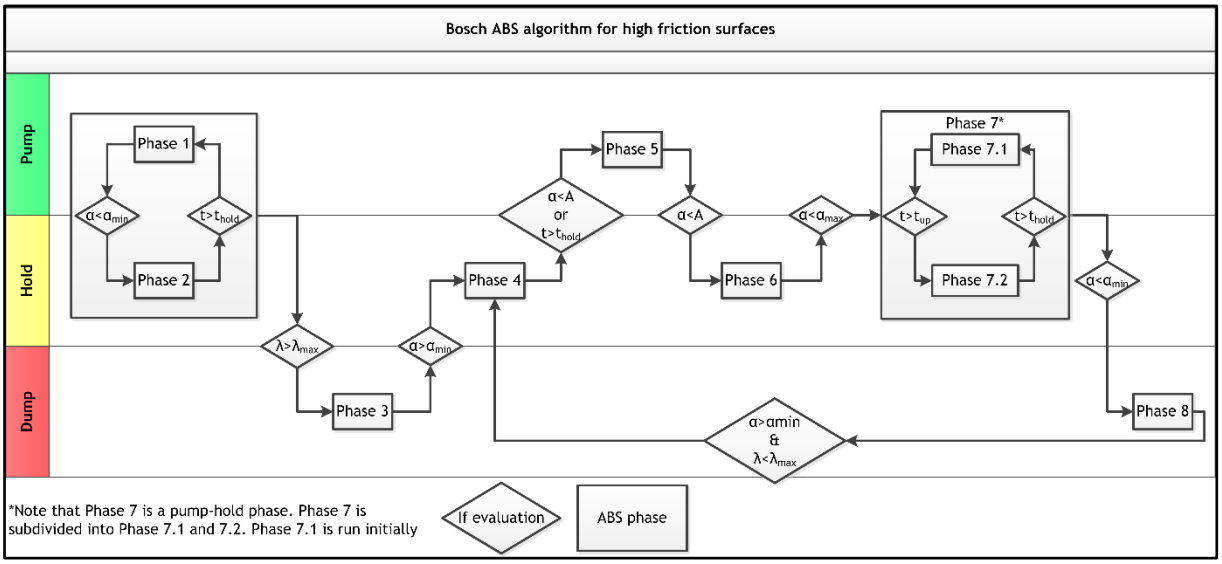

Figure 2-18 Schematic representation of Bosch ABS algorithm

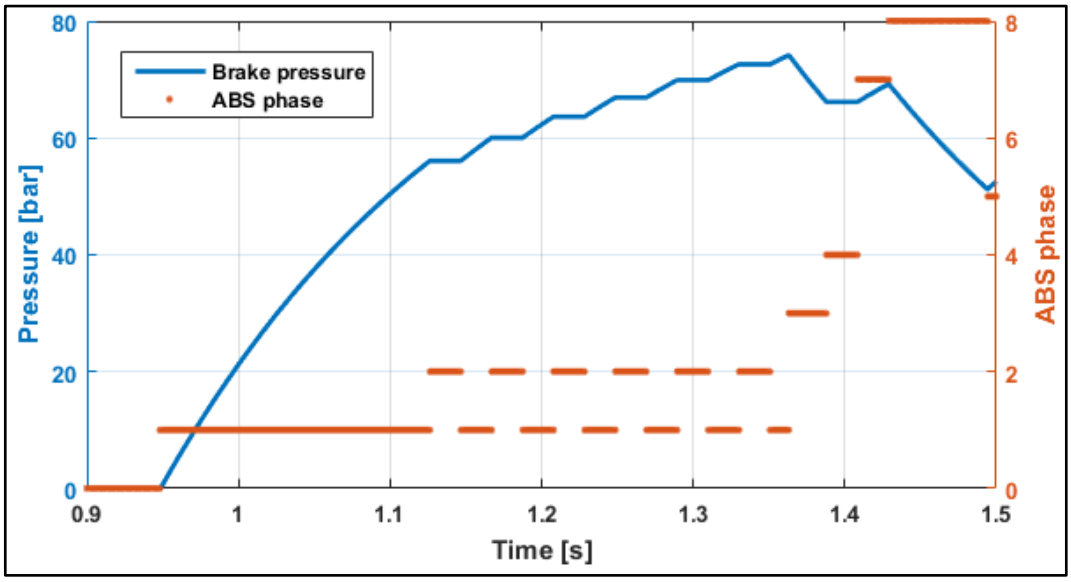

Figure 2-19 Brake pressure modulation for one cycle of the Bosch ABS algorithm

Table 2-1 ABS thresholds and step times (Penny and Els, 2016)

Threshold	Value	Unit
A	25	[rad/s^2]
α_{max}	5	[rad/s^2]
α_{min}	-100	[rad/s^2]
λ_{max}	0.2	[-]
t_{up}	20	[ms]
t_{hold}	20	[ms]

2.2.4 *Factors that influence ABS performance*

During the discussion of ABS and its control algorithm, it is noted that tyre longitudinal slip is used as input to the ABS algorithm. The longitudinal slip of a tyre is defined with Equation (2.2), which is repeated here for the sake of continuity:

$$\lambda = \frac{|v - \omega r_{eff}|}{v} \tag{2.7}$$

It is evident in Equation (2.7) that the definition of the tyre's rolling radius is important. The effective rolling radius in Equation (2.7) is often assumed to be constant (the rigid disc

assumption) and is defined under specified zero conditions. Two of the most common zero conditions are (Upadhyaya et al., 1988):

a) when there is a driving torque applied to propel the vehicle across a surface while delivering zero net traction, and
b) when the vehicle is pushed with zero axle torque. This is the condition under which the Society of Automotive Engineers (SAE) defines the effective radius (Miller et al., 2001)

The rolling radius defined in a) and b) is determined under quasi-static conditions and is assumed constant. Figure 2-20 shows a scenario where this assumption may be invalid as significant tyre deflection is present.

Figure 2-20 Tyre deformation when rolling over a cleat

Using the correct rolling radius when the tyre deflects dynamically is important, since this is the point at which it is assumed that the tyre forces are generated and applied in tyre models such as the Magic Formula model. As may be seen in Figure 2-20, this may be a complicated definition. In general, the effective rolling radius changes with tyre deflection, which may be due to varying vertical loads (due to load transfer between the front and rear axles of the vehicle during braking) or to uneven road surfaces, such as the case shown in Figure 2-20.

A significant amount of work was done specifically in the 1980s by Upadhyaya et al. (1988), specifically looking at the tractive performance of agricultural vehicles. These studies investigated the effect of the test procedure and the interpretation of rolling radius and motion resistance. The rolling radius used in these studies was defined under an explicitly stated zero-condition (either a) or b), as discussed above). The “true rolling radius” and “true slip” were then determined empirically and a nonlinear regression was used to fit a curve through the obtained test data.

Kiss (2003) investigated three radii of agricultural tyres, namely the distance between the bottom of the tyre and the wheel centre, the kinematic rolling radius defined by motion and

the kinetic rolling radius. His measurements were done at different tyre pressures on sandy loam soil. The reported measurements relied on the double integration of accelerometer measurements (to determine vertical wheel travel) and only the distance from the centre of the wheel to the road surface was considered as a dynamic radius. The kinematic rolling radius was defined as a function of slip and was defined with Equation (2.8) at different slip values. It is however unclear how the tyre slip was determined. The kinetic rolling radius was considered only under static conditions where the wheel's angular acceleration, the tyre dynamics and vibration modes were neglected and the longitudinal tyre force and the applied brake or driving torque are directly proportional, as shown in Equation (2.9). The kinetic rolling radius was reported as a function of inflation pressure.

$$r_{kinematic} = distance\ advanced/wheel\ rotation\ angle\ in\ radians \tag{2.8}$$

$$M_y = F_x r_{kinetic} \tag{2.9}$$

The shortcoming with these approaches to the rolling radius is the assumption that the rolling radius is a constant value that can be determined under quasi-static conditions (as done by Kiss (2003)) or a large amount of empirical data is needed to determine the "true rolling radius" or "true slip" as done by Upadhyaya et al. (1988). The nature of these studies was also limited to soft, deformable terrains where the dynamics of the manoeuvre is of lesser importance and the quasi-static approach used by Kiss (2003) may yield acceptable results.

2.2.5 *Brake models*

Brake models typically relate the brake line pressure as input and calculates the resulting output torque. The torque is a function of the actuating force, the coefficient of friction, and the geometry of the brake. Equation (2.10) relates the brake torque and the actuating force of a disc brake (Budynas and Nisbett, 2008):

$$T_{brake} = f F_{act} r_e \tag{2.10}$$

Two approaches are used to relate the brake torque and the actuating force, depending on the amount of wear of the brake pads. The first approach, known as the Uniform Wear approach, is applicable to worn in disc brakes. The actuating force and brake torque for the case of Uniform Wear is given by Budynas and Nisbett (2008) as:

$$\begin{aligned} F_{act} &= (\theta_2 - \theta_1) p_a r_i (r_o - r_i) \\ T_{brake} &= \frac{1}{2} f (\theta_2 - \theta_1) p_a r_i \left(r_o^2 - r_i^2\right) \end{aligned} \tag{2.11}$$

The second approach is known as the Uniform Pressure approach and is applicable to new disc brakes. The actuating force and brake torque for the case of Uniform Pressure is given by Equation (2.11) (Budynas and Nisbett, 2008). The angles and radii of Equation (2.11) and (2.12) are illustrated in Figure 2-21.

$$\begin{aligned} F_{act} &= \frac{1}{2} (\theta_2 - \theta_1) p_a \left(r_o^2 - r_i^2\right) \\ T_{brake} &= \frac{1}{3} f (\theta_2 - \theta_1) p_a r_i \left(r_o^3 - r_i^3\right) \end{aligned} \tag{2.12}$$

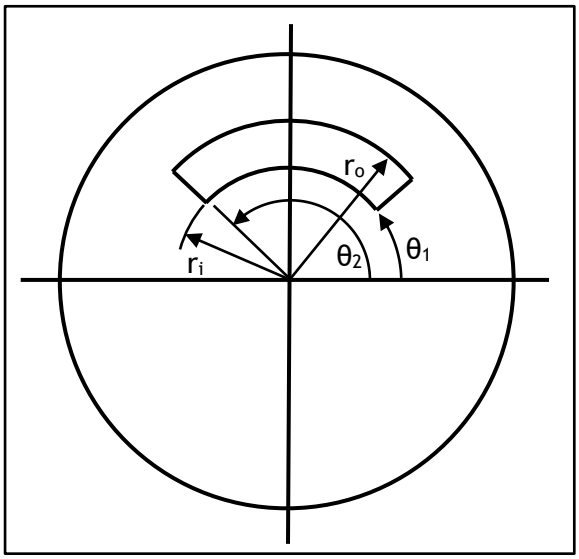

Figure 2-21 Illustration of disc brake parameters of Equation (2.11) and (2.12)

The advent of ABS systems has resulted in the need to model the brake system and its hydraulic losses, the ABS modulator and the pump accurately. This presents a problem, as the brake system on most vehicles is a complicated hydraulic circuit containing numerous valves, accumulators and other fittings and connections that are difficult to model analytically. Many researchers in the automotive field have resorted to hardware-in-the-loop (HIL) systems to avoid this additional modelling complexity. A typical example of using HIL to alleviate the problem of modelling the intricacies associated with a hydraulic brake system is shown schematically in Figure 2-22. The schematic shown in Figure 2-22 was developed by Heidrich et al. (2013).

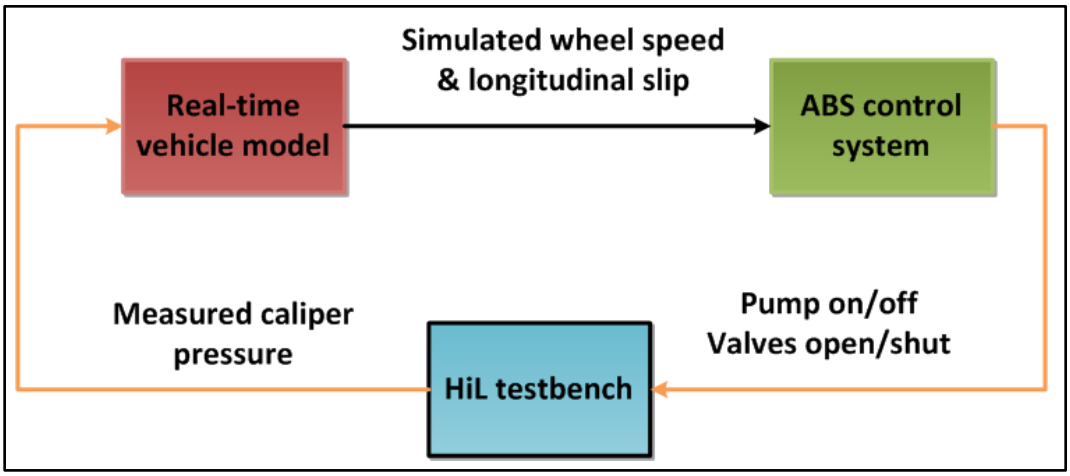

Figure 2-22 Schematic representation of hardware-in-the-loop brake system setup

The HIL setup of Figure 2-22 feeds the wheel speeds and longitudinal slip to the ABS algorithm. The angular wheel accelerations are derived from the wheel speeds and the brake pressure is modulated according to these inputs. Pressure transducers measure the brake line pressure at each brake calliper and feed measured values back into the real-time vehicle model. Equation (2.11) is then used to calculate the brake torque and the wheel speeds are updated and fed back to the ABS algorithm.

HIL adds the additional requirement that the vehicle models must be capable of running in real-time. To this end, simplified vehicle dynamics models have been developed to enable real-time solution of the equations of motion (EOM). These simplified vehicle dynamics models typically make use of lookup tables to bypass the solution of the kinematic constraints on the multi-body dynamics. Simplified tyre models are also typically used. Very

little experimental validation of these simplified, real-time vehicle models is available in the literature.

2.3 Research question and conclusion from literature review

The initial investigation of the braking performance, discussed in Section 1.2 of a vehicle and the degradation of this performance on a rough road leads to the main research question of this study. The research question is:

Is there an improvement achievable in the braking performance of a vehicle on a rough road?

Several follow-up questions arise from the above problem statement as a result of the literature review:

a) *What are the causes of the worsened stopping time and distance when braking on a rough road and how can they be addressed?*
b) *Can the off-road braking of a vehicle be modelled mathematically?*
c) *What are the criteria used to evaluate the on-road braking performance of a vehicle and can the off-road braking performance of a vehicle be evaluated using the same criteria?*
d) *Can the off-road braking performance be improved without compromising the on-road performance?*

Several phenomena influence the degradation of ABS performance on rough roads. These include the tyre force generation and the inputs given to the ABS control algorithm. To address the research questions posed in Section 2.3, the following must be considered:

- Load transfer on undulating roads may have a large influence on the braking performance. The presence of excitation of the sprung mass's pitch degree of freedom natural frequency due to wheel hop excitation, combined with the presence of load transfer during braking, may influence the braking performance. Large variations on the normal force of the tyre leads to worsened braking performance. Reducing the load transfer and lowering the tyre normal force variation may improve the braking performance on undulating roads.

- Addressing the degradation in braking performance on undulating roads will require accurate inputs to the ABS algorithm. The ABS algorithm makes its decisions based on angular wheel acceleration and longitudinal wheel slip. Important aspects to take note of include:
    - The angular wheel acceleration is derived from the measured angular wheel speed and low-pass filtering is used to remove excessive noise from the measured signals. The fidelity of the angular wheel acceleration given to the ABS control algorithm as input is crucially important to its successful operation.
    - Calculation of the longitudinal slip relies on accurate angular wheel speed measurements and knowledge of the effective rolling radius. The rolling radius is usually defined under quasi-static conditions and is assumed constant. The validity of this assumption must be tested.

- Modelling the braking of a vehicle equipped with ABS requires a complex tyre model that accurately captures the steady state and transient behaviour of the vehicle's tyres. A validated tyre model of the tyre being used on the test vehicle has to be developed. The developed tyre model must accurately capture the tyre's dynamic

properties in the horizontal (specifically longitudinal) and vertical directions on flat and rough roads. The tyre model must also include higher frequency dynamics, such as the rigid body mode shapes, which may occur due to high frequency excitation of the road surface and the ABS brake torque input. It is thus proposed to use the FTire tyre model.

The thesis is laid out as follows:

- Chapter 3 develops the vehicle model used in this study.
- A detailed assessment of braking performance and the associated performance evaluation thereof is established in Chapter 4.
- Chapter 5 looks at the inputs to ABS and improving these inputs on undulating roads.
- The influence of suspension stiffness and damping on the stopping distance on rough roads is the theme of Chapter 6.
- A control algorithm that attempts to improve the braking performance of a sports-utility-vehicle, equipped with a controllable suspension, is proposed in Chapter 7.

Finally, a conclusion is drawn in Chapter 8.

Chapter 3

Modelling the vehicle and its subsystems

Today's scientists have substituted mathematics for experiments, and they wander off through equation after equation, and eventually build a structure, which has no relation to reality

- Nikola Tesla (1856-1943), Serbian American inventor

3.1 Experimental vehicle

The vehicle used as the experimental platform for this study is a 1997 Land Rover Defender. It must be noted that this is a different vehicle from the one used for the initial experimental investigation of Section 1.2 (which was a 2013 year model). The 1997 Land Rover Defender was chosen as the research platform for the Vehicle Dynamics Group (VDG) at the University of Pretoria by Els (2006) because the vehicle:

- is a 'low technology' vehicle that simplifies modifications to the vehicle,
- has a ladder frame chassis that makes it possible to easily modify or add mounting points as needed,
- is spacious inside, allowing the integration of various sensors and actuators as needed for research purposes,
- has a high centre of gravity (typical of an off-road vehicle) which amplifies the challenges faced when dealing with vehicle dynamics and
- it is easy to fit a controllable suspension without changing the suspension kinematics.

The OEM suspension system of the Land Rover Defender has been removed and replaced with a hydro-pneumatic suspension system that is operated in a semi-active manner. The semi-active suspension enables switching between two discrete suspension force-displacement characteristics and two discrete damper characteristics. The suspension struts are fixed between the vehicle body and the two solid axles, replacing the traditional coil spring and damper. Each strut is connected to two gas accumulators via control valves and hydraulic damper valves. The basic circuit diagram is shown in Figure 3-1 (Els, 2006). The suspension system is called the four state semi-active suspension system, or $4S_4$.

The soft spring characteristic is achieved by opening both control valves and thus compressing the combined gas of the two accumulators. Closing control valve 2 (see Figure 3-1) seals off accumulator 2, a smaller gas volume is thus compressed and a higher spring characteristic is achieved. The two spring characteristics can be individually tailored by adjusting the accumulator gas volumes. The damping characteristics are selected by switching the damper pack bypass valves. Low damping is achieved by opening the bypass valve (valve 1). For high damping the bypass valve is closed and the hydraulic fluid is forced through the damper pack. Adding or subtracting oil from the struts results in ride height adjustment. The result is a semi-active suspension system that switches between two spring

characteristics and two damper characteristics, resulting in four possible combinations per strut. The $4S_4$ can switch between any of the settings within 50ms. The spring and damper characteristics of the $4S_4$ are shown in Figure 3-2. Els (2006) proposed using the soft spring in conjunction with low damping as a 'Ride Comfort' suspension mode and the hard spring with high damping as a 'Handling' suspension mode. Thoresson et al. (2009b) used a gradient-based optimisation algorithm to identify the optimal gas accumulator sizes and damping scale factors.

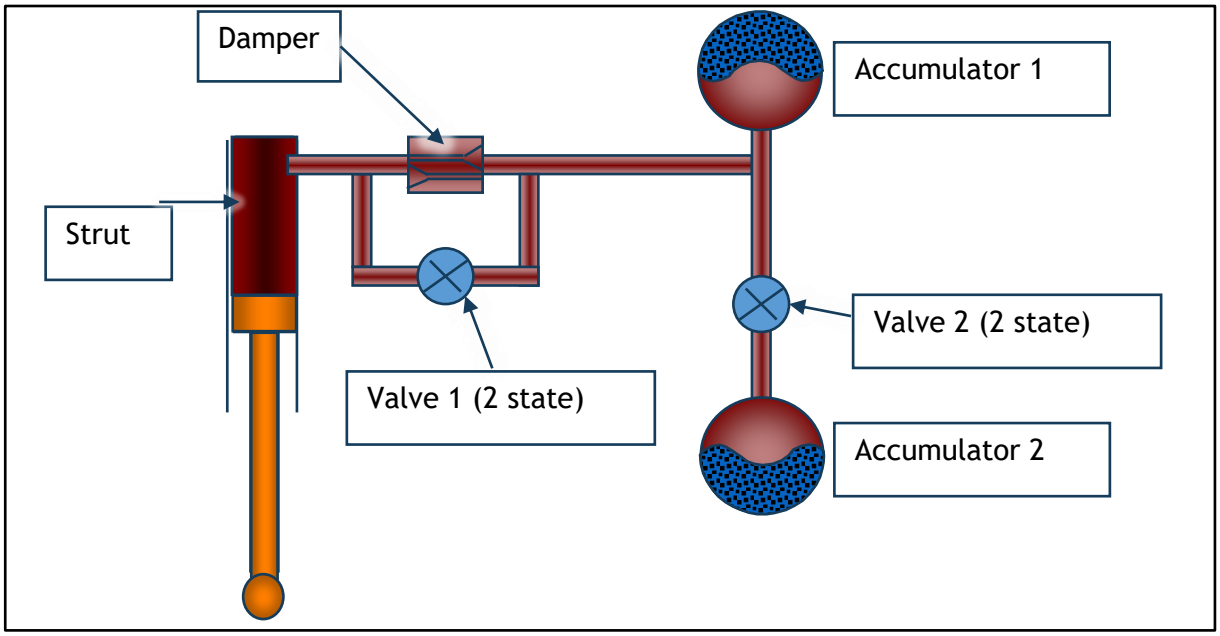

Figure 3-1 $4S_4$ hydro-pneumatic suspension system circuit diagram (Els, 2006)

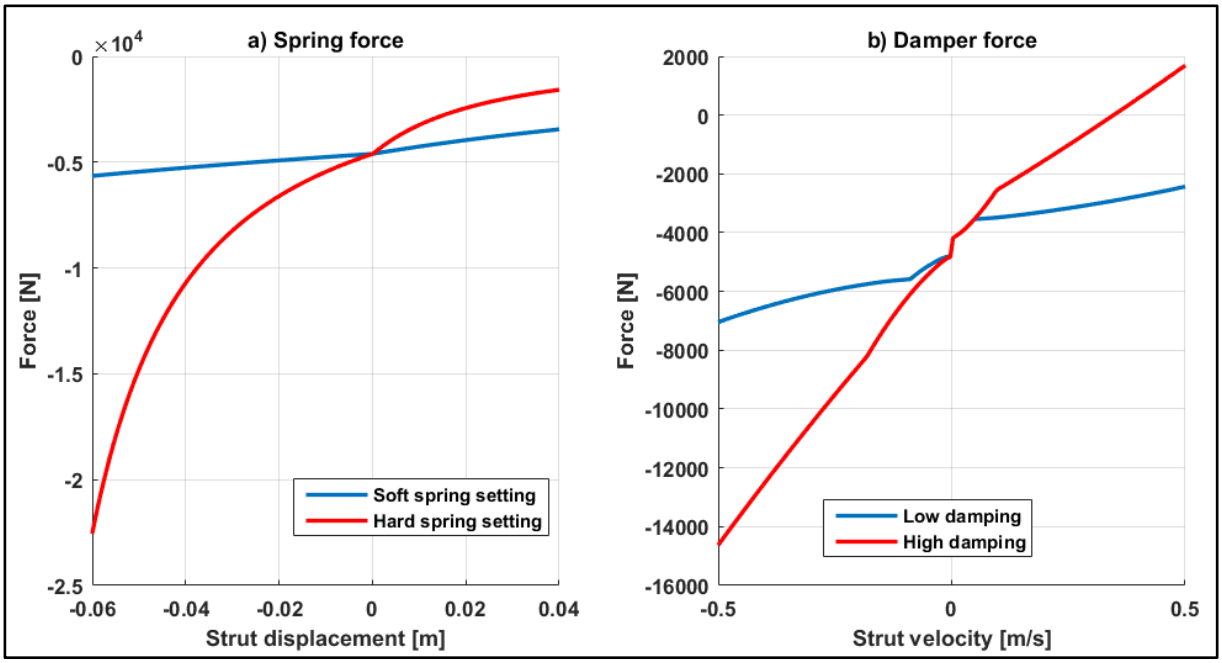

Figure 3-2 $4S_4$ spring force (a) and damper force characteristics (b). Negative displacement or velocity values indicate compression of the strut.

The vehicle is fitted with Michelin LTX A/T2 235/85R16 tyres. The Michelin LTX A/T2 is an all-terrain tyre with a large aspect ratio that is prevalent on SUVs and light trucks. The compound is designed to resist chipping and tearing, especially on off-road conditions. The OEM claims that these tyres have an upgraded tread compound for tough off-road endurance.

The tyre has two high tensile steel belts and a spiral nylon wrap beneath a rubber tread (Michelin, 2016).

3.2 Vehicle model

A fully nonlinear multi-body dynamics model, developed in MSC Software's ADAMS suite, is used as the basis of this study. It is important to define the coordinate system used throughout the study. Figure 3-3 illustrates what is known as the SAE Vehicle Axis System, with the degrees of freedom known as (Gillespie, 1992):

- X-translation: The longitudinal degree of freedom, positive in the forward direction.
- Y-translation: The lateral degree of freedom, positive to the right side of the vehicle.
- Z-translation: The vertical degree of freedom, positive downward.
- X-rotation: The roll degree of freedom.
- Y-rotation: The pitch degree of freedom.
- Z-rotation: The yaw degree of freedom.

All the rotational degrees of freedom are positive according to the right hand rule.

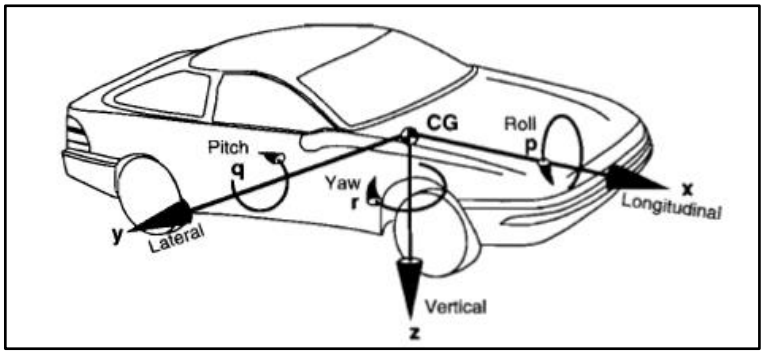

Figure 3-3 The SAE vehicle axis system (Gillespie, 1992)

Thoresson et al. (2009a) modelled the full vehicle in ADAMS (ADAMS, or Automatic Dynamic Analysis of Mechanical Systems, is a multi-body dynamics software package developed by MSC Software (2016)). The vehicle body was modelled as two rigid bodies that are connected along the roll axis at the chassis height by a revolute joint and a torsion spring. This was done to improve the model's accuracy due to body torsional flexibility in the roll DOF. The bump and rebound stops were modelled with nonlinear splines as force elements between the vehicle body and the axles. Splines were also used to model the suspension bushings and the rear anti-roll bar was modelled as a torsion spring acting between the two rear trailing arms (Thoresson et al., 2009a). Els et al. (2006) experimentally determined the mass and inertia properties needed for mathematical modelling of the vehicle and these were included by Thoresson et al. (2009a) in the ADAMS (MSC Software, 2016) model. The complete model consists of 15 unconstrained degrees of freedom and 16 moving parts. The degrees of freedom are listed in Table 3-1 and indicated schematically in Figure 3-4 and Figure 3-5. The parameters influencing the longitudinal response (i.e. the braking and aerodynamic drag) of the vehicle were modelled by Hamersma and Els (2014).

Table 3-1 Bodies, degrees of freedom and associated motions of the ADAMS (MSC Software, 2016) model of the Land Rover Defender (Thoresson *et al.*, 2009)

BODY	DOF	ASSOCIATED MOTIONS
Vehicle body (two rigid bodies)	7	Body torsion Longitudinal, Lateral, Vertical Roll, Pitch, Yaw
Front axle	2	Vertical, Roll
Rear axle	2	Vertical, Roll
Wheels (four off)	4	Rotation of each wheel

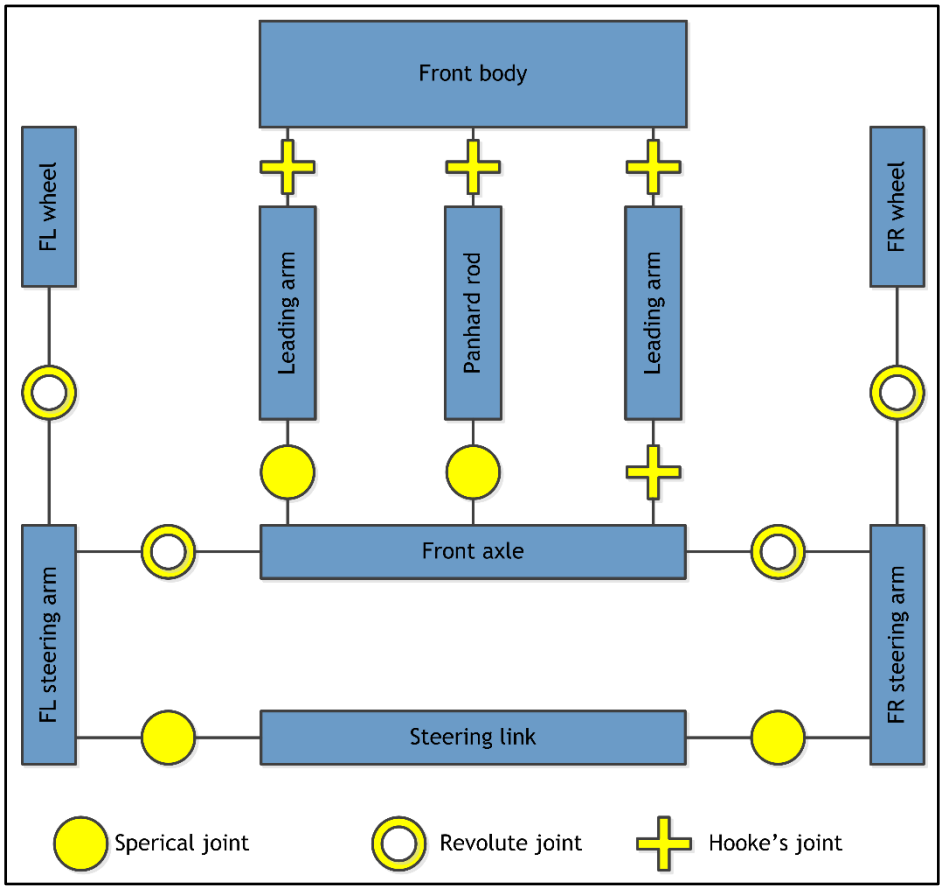

Figure 3-4 Schematic of Land Rover Defender front suspension kinematics

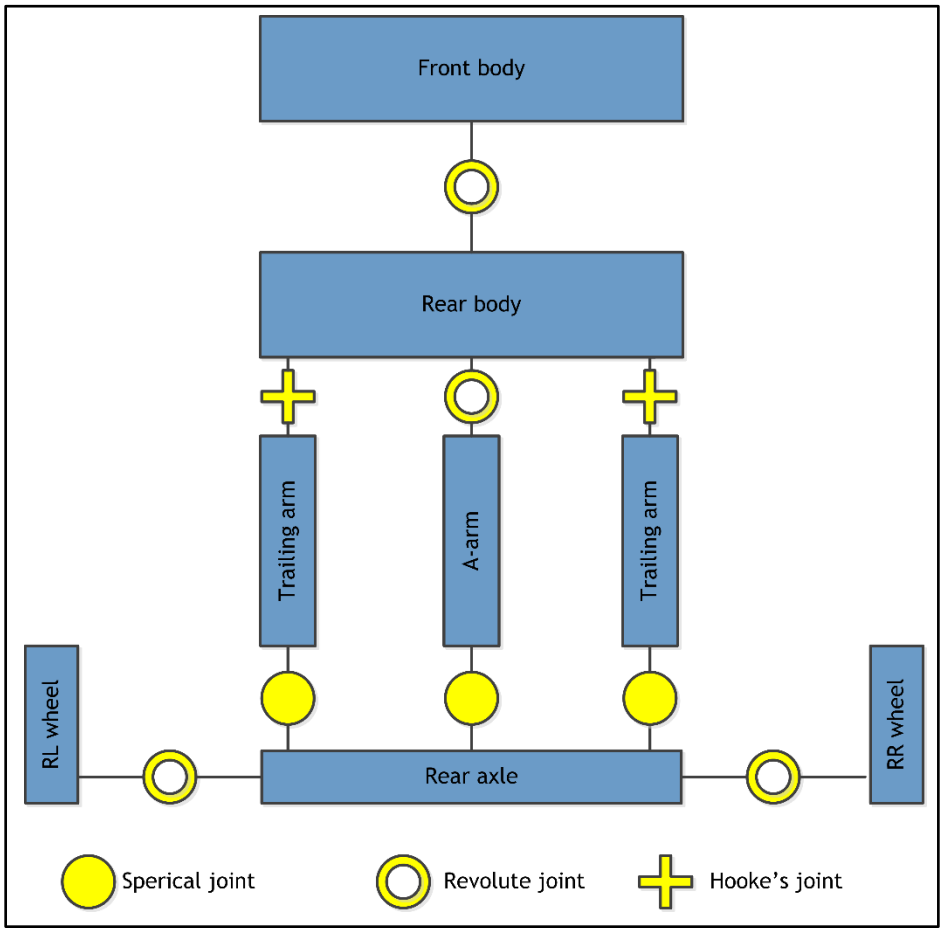

Figure 3-5 Schematic of Land Rover Defender rear suspension kinematics

The model is run in co-simulation with MATLAB/Simulink (MathWorks, 2016). The following subsystems were modelled in MATLAB/Simulink (MathWorks, 2016). They rely on feedback from the ADAMS (MSC Software, 2016) model to calculate their output:

- $4S_4$ suspension struts
- Brake system and ABS algorithm
- Path following driver model

The $4S_4$ hydropneumatic springs were modelled by Van der Westhuizen and Els (2015). They compared the accuracy of different gas models (ideal gas and real gas, both combined with the energy equation approach) to model the gas accumulators on the $4S_4$ strut. They found that the Benedict-Webb-Rubin (BWR) real gas equation combined with the energy equation gave the best results, but that the computational efficiency of the model using the BWR equation combined with the energy equation was significantly slower than that using an ideal gas approach. The adiabatic assumption of the ideal gas law gave sufficient accuracy at higher frequency excitations and this is the model used for the gas accumulators in this study. The damper was modelled by using a lookup table that was populated with experimental data by Thoresson (2007). The model takes the valve settings and relative suspension displacement and velocity as input and then calculates the corresponding strut force (the sum of spring and damping forces) as output.

The longitudinal demand forces, including the brake system, was modelled by Hamersma and Els (2014) and used extensively by Penny and Els (2016) to investigate the ABS braking performance of the vehicle on a rough road. The ABS algorithm is described in detail in Section 2.2.3 and was modelled using MATLAB/Simulink's StateFlow toolbox (MathWorks, 2016).

Path following is accomplished by a driver model developed by Thoresson et al. (2014) and refined by Botha (2011). The driver model takes the chassis lateral acceleration, yaw angle and rate, centre of gravity (CG) x and y position, and vehicle speed as input. The desired path is given as a series of x-y coordinates. These x-y coordinates are used to determine a path yaw angle. Two separate controllers are then used to follow the prescribed path, one to determine the desired yaw rate and one to correct the lateral path following error that may occur because of integration drift. These two controllers combine to give a steering rate that is integrated to obtain the steering angle. This steering angle is given as input to the ADAMS (MSC Software, 2016) model. It controls the kingpin angle and not the steering wheel angle and thus the steering system kinematics are not modelled explicitly.

3.2.1 *Road profiles*

The experimental work of this project will be conducted at Gerotek Test Facilities (Armscor Defence Institutes SOC, 2016). The Suspension Track at Gerotek Test Facilities (Armscor Defence Institutes SOC, 2016) has three road surfaces of interest to this study, namely the parallel corrugations, angled corrugations and Belgian paving.

All the above-mentioned tracks are concrete tracks with rigid undulations. The parallel corrugations track resembles a washboard road with discrete obstacles perpendicular to the direction of travel – the left and right wheels are excited simultaneously. The angled corrugations track is similar to the parallel corrugations track, with the exception that the periodic obstacles are set at an oblique angle to the direction of travel and the left and right wheels are excited out of phase. The Belgian paving track provides random excitation of the wheels.

Crucial to the accurate modelling of the vehicle response over the undulating tracks is the measurement of the road profile. The road profiles used throughout this study were measured experimentally by Becker and Els (2014). Upon closer inspection of the spatial

frequencies of the road profiles, Becker and Els (2014) found two distinct peaks in the spatial frequency domain when they measured the Belgian paving's road profile. These peaks correspond to the length of the blocks and the gaps between the blocks. The Belgian paving's excitation is thus not completely random. The Belgian paving may be classified as a Class D road, an extremely rough road when using the ISO8608:2016 classification (International Organisation of Standardisation, 2016). The road profiles have a spatial resolution of 6mm longitudinally by 42mm laterally. Figure 3-6 to Figure 3-8 shows portions of the measured road profiles.

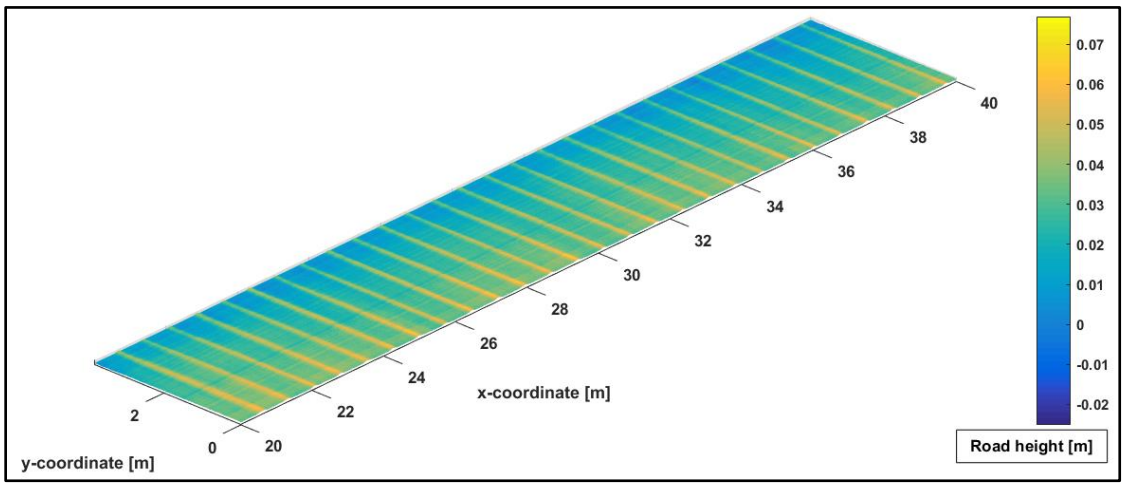

Figure 3-6 Measured road profile of parallel corrugations track

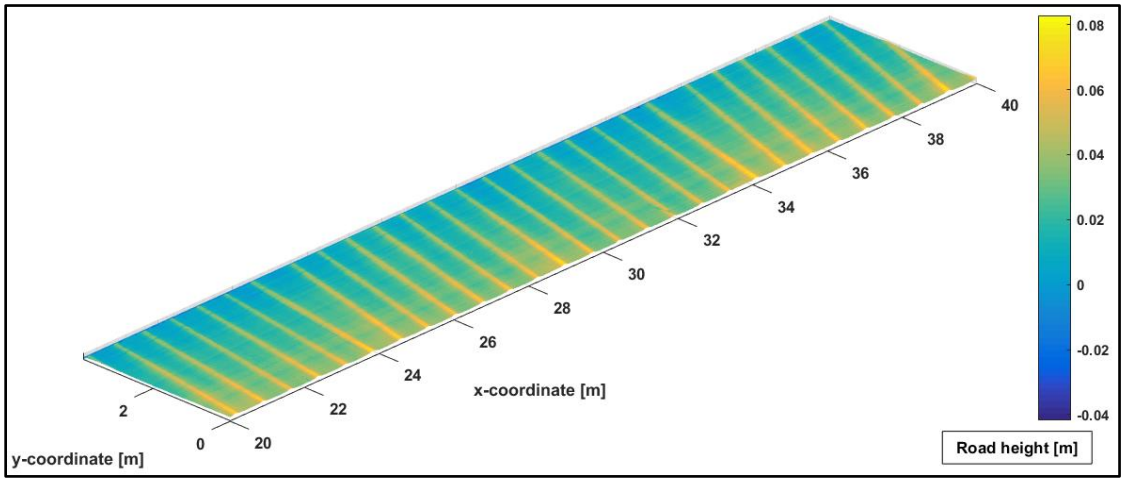

Figure 3-7 Measured road profile of angled corrugations track

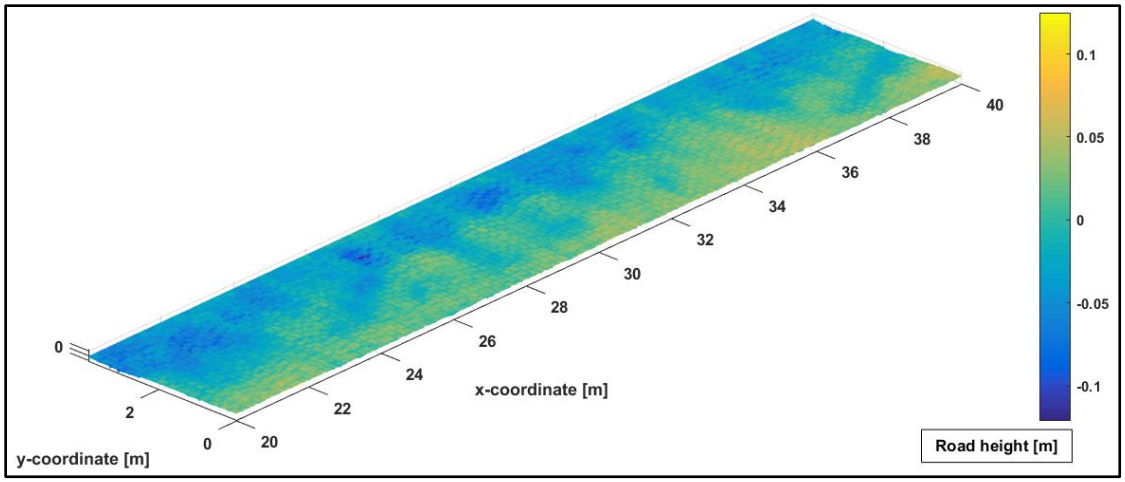

Figure 3-8 Measured road profile of Belgian paving

3.2.2 *Tyre model*

It was concluded in Section 2.3 that the accurate modelling of a vehicle braking performance on undulating roads with wavelengths shorter than the tyre circumference requires an FTire tyre model. Bosch et al. (2016) parameterised and validated an FTire model of the Michelin LTX A/T2 tyre (Michelin, 2016). The tyre model was validated experimentally in the field with the use of a tyre test trailer (see Section 2.1.4.6 for more information on the validation of tyre models). An ADAMS (MSC Software, 2016) model of the tyre test trailer was used to simulate the conducted field tests.

Figure 3-9 shows the response of the tyre when towed over a discrete object (in this case a 50mm square steel cleat). More excitation is present in the field measurement prior to the tyre encountering the cleat, this is due to small irregularities and seams between the concrete blocks of the test track. The tyre model's vertical response over the cleat accurately captures the actual response of the tyre. The tyre model exhibits higher vertical damping than measurements. This is due to the increased excitation of the field measurements that is present due to the small irregularities on the test track and movement of the towing vehicle.

The tyre test trailer was also towed over the Belgian paving at Gerotek Test Facilities (Armscor Defence Institutes SOC, 2016) while measuring the vertical tyre force. Figure 3-10 (a) shows the measured and simulated forces over the Belgian paving. It is difficult to ensure that the ADAMS (MSC Software, 2016) model of the tyre test trailer negotiates exactly the same path as the tyre test trailer in the field test. Even a slight discrepancy in speed and path may result in significant variation when comparing the simulation and experimental results in the time domain. Clearly a validation in the time domain will result in an unsatisfactorily correlation due to the deviation between the measured and simulated signals. Rather than comparing tests and simulations in the time domain, a probability theorem approach is considered which involves the analysis of random phenomena within a signal. This validation technique comprises of determining the probability that a certain vertical load is present in a validation test as well as the corresponding simulation data set (Bosch et al., 2016).

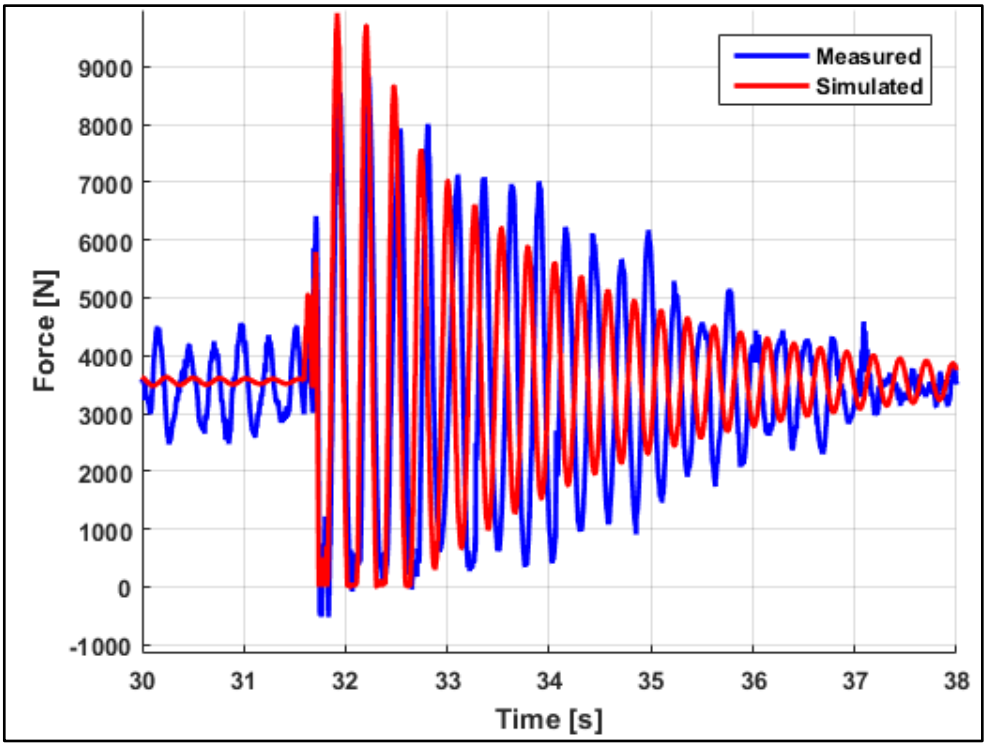

Figure 3-9 Vertical tyre force experimental validation

The mathematical probability theorem was applied as a validation method by Bosch et al. (2016) considering the Gaussian distribution of each of the validation test and simulation time signals. The Gaussian distribution accurately predicts the probability that any observation or signal will fall between any two real predefined limits. Figure 3-10 (b) depicts a histogram of the measured and simulated tyre's vertical force behaviour over the Belgian paving.

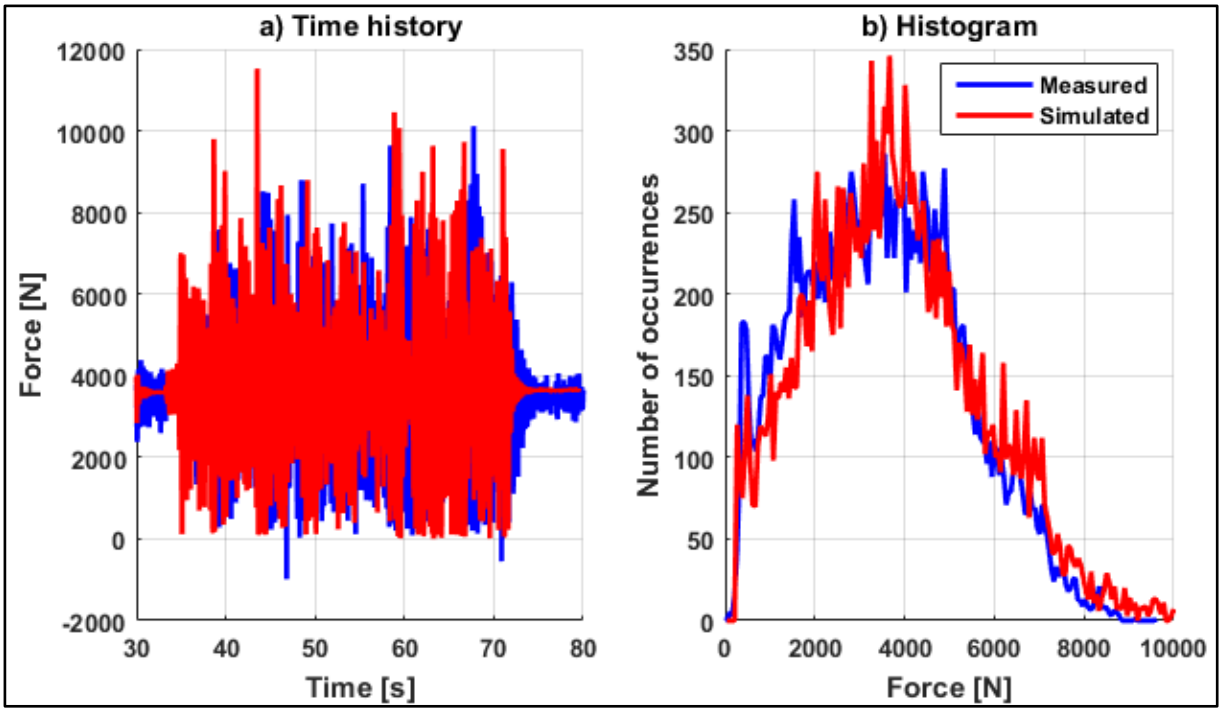

Figure 3-10 Vertical tyre force validation on the Belgian paving: a) Time history and b) histogram

The longitudinal and lateral force generation characteristics of the tyre model are validated experimentally with a tyre test trailer. The tyre test trailer's measurement axle can continuously vary the tyre slip angle at discretely adjustable camber angles. The axle is also fitted with a braking system that induces longitudinal slip. The lateral, longitudinal and combined (i.e. friction circle) characteristics of the tyre can thus be determined. The measurement axle is fitted with an air suspension typically found on truck trailers, allowing the continuous adjustment of vertical load. Tyre forces are measured with the WFTs discussed in Section 2.1.4.6. Figure 3-11 shows the tyre tester. The measurement axle is the one closest to the camera. Note the camber adjustment plates, brakes and slip angle adjustment arms.

Validation of the tyre friction characteristics was done by building an ADAMS (MSC Software, 2016) model of the measurement axle. The model is run in co-simulation with MATLAB/Simulink (MathWorks, 2016). The tyre tester ADAMS (MSC Software, 2016) model is discussed in more detail in Appendix A. Several experimentally measured states are given as input to the model to replicate the experiments. The inputs given to the model and outputs obtained from the model are given in Table 3-2.

The measured vertical tyre force is used to control the vertical tyre force in the simulation. This is to ensure that the simulated measurement conditions closely resemble the experimental conditions.

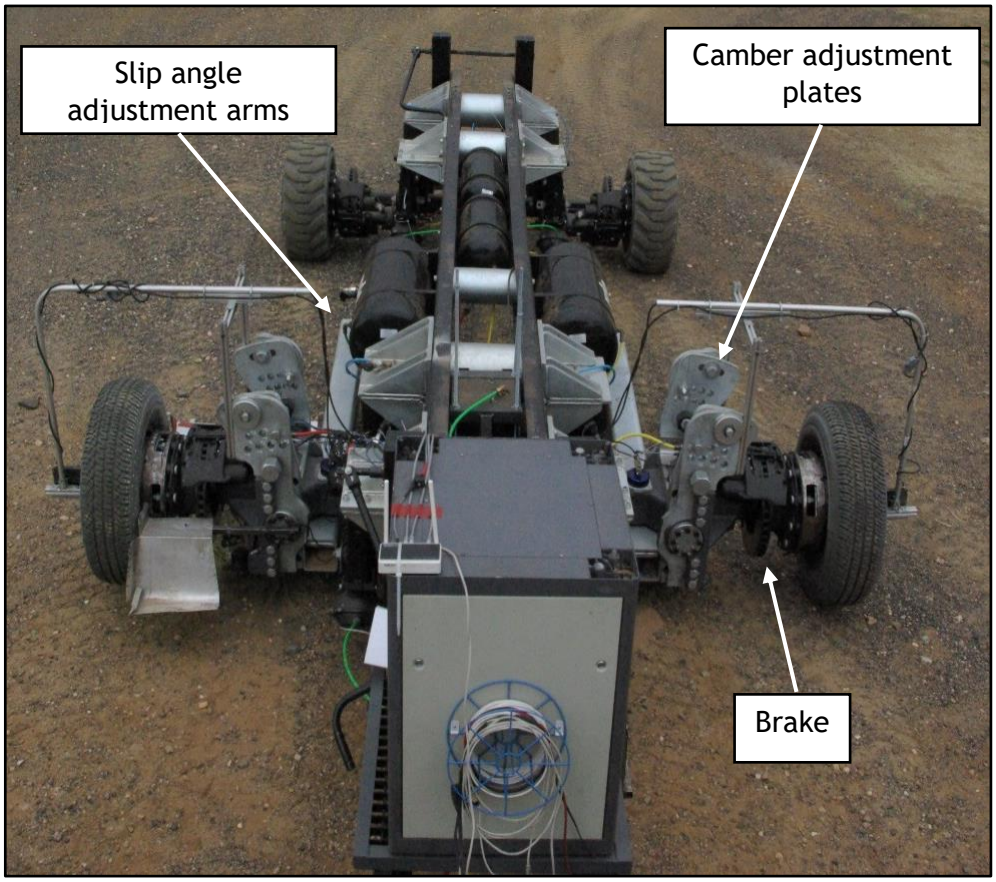

Figure 3-11 The tyre test trailer (photo taken from the towing vehicle).

Table 3-2 Tyre test trailer ADAMS (MSC Software, 2016) model inputs and outputs

INPUTS	OUTPUTS
Trailer longitudinal velocity	Tyre forces and moments
Camber angle	Tyre slip angle
Slip angle measured at slip angle pivot	Slip angle
Brake torque measured with WFT	Longitudinal slip
Vertical tyre force measured with WFT	Wheel speed

Lateral validation of the tyre model is done by changing the tyre slip angle while measuring the lateral tyre force. Figure 3-12 shows the measured and simulated lateral friction coefficient. Similarly, the longitudinal tyre model validation is done by braking the wheels while measuring wheel speed, trailer speed and longitudinal tyre force. Figure 3-13 shows the measured and simulated longitudinal friction coefficient.

Braking the wheels while they are at an angle is the procedure to validate the tyre model for the combined loading case. Figure 3-14 compares the measured and simulated results for the combined case. The data is shown in the time domain, as it makes the comparison easier. The results presented in Figure 3-14 show that the tyre model is accurate for the combined force generation case.

The FTire model captures the lateral and longitudinal tyre response accurately. The FTire model is evidently capable of accurately modelling the force generation characteristics of the Michelin LTX A/T2 235/85R16 on smooth and undulating road surfaces.

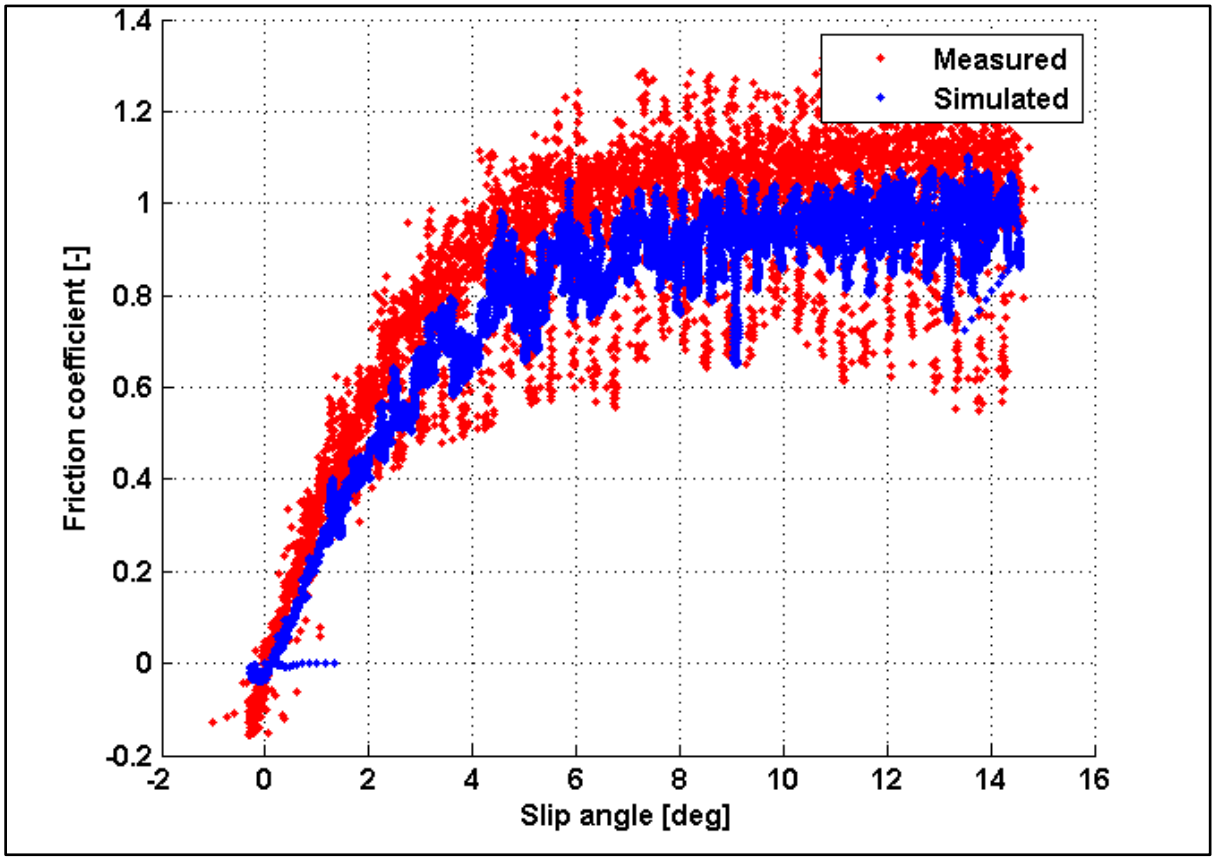

Figure 3-12 Lateral tyre force experimental validation

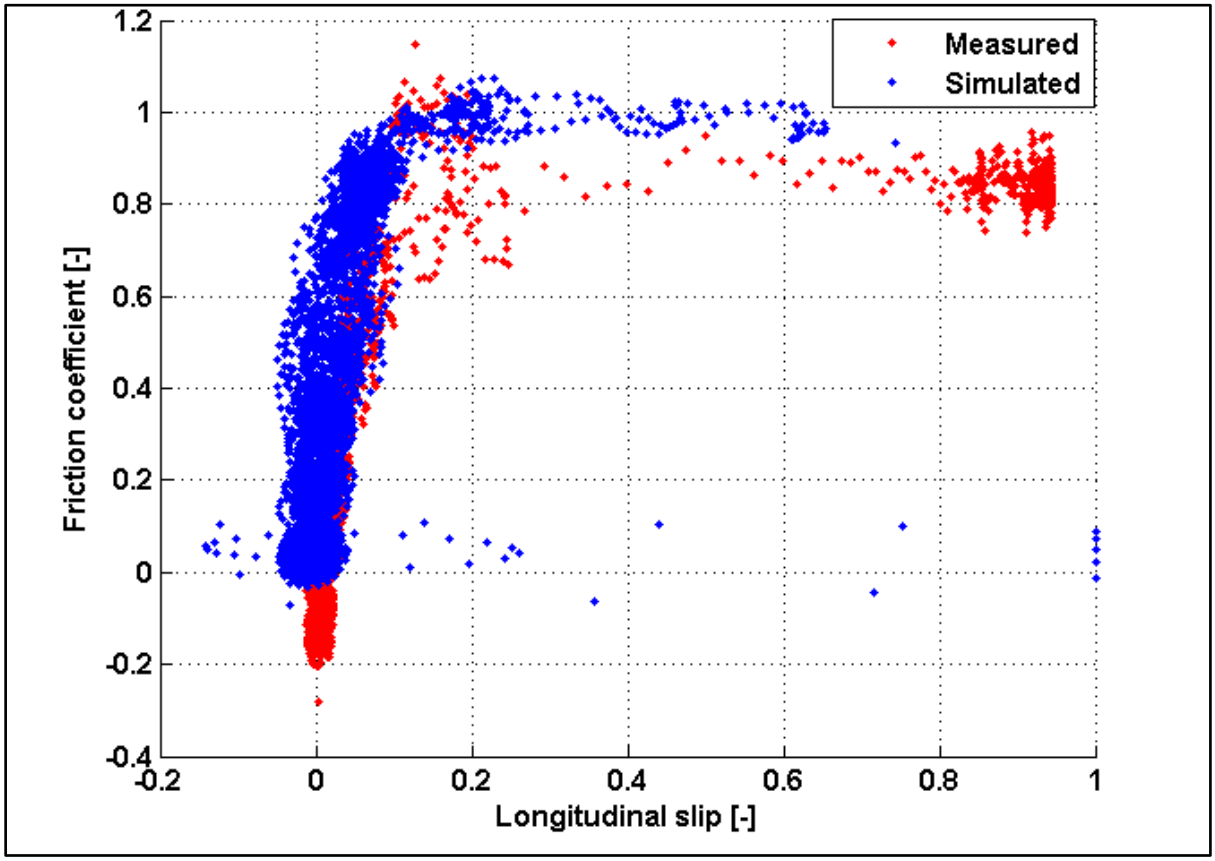

Figure 3-13 Longitudinal tyre force experimental validation

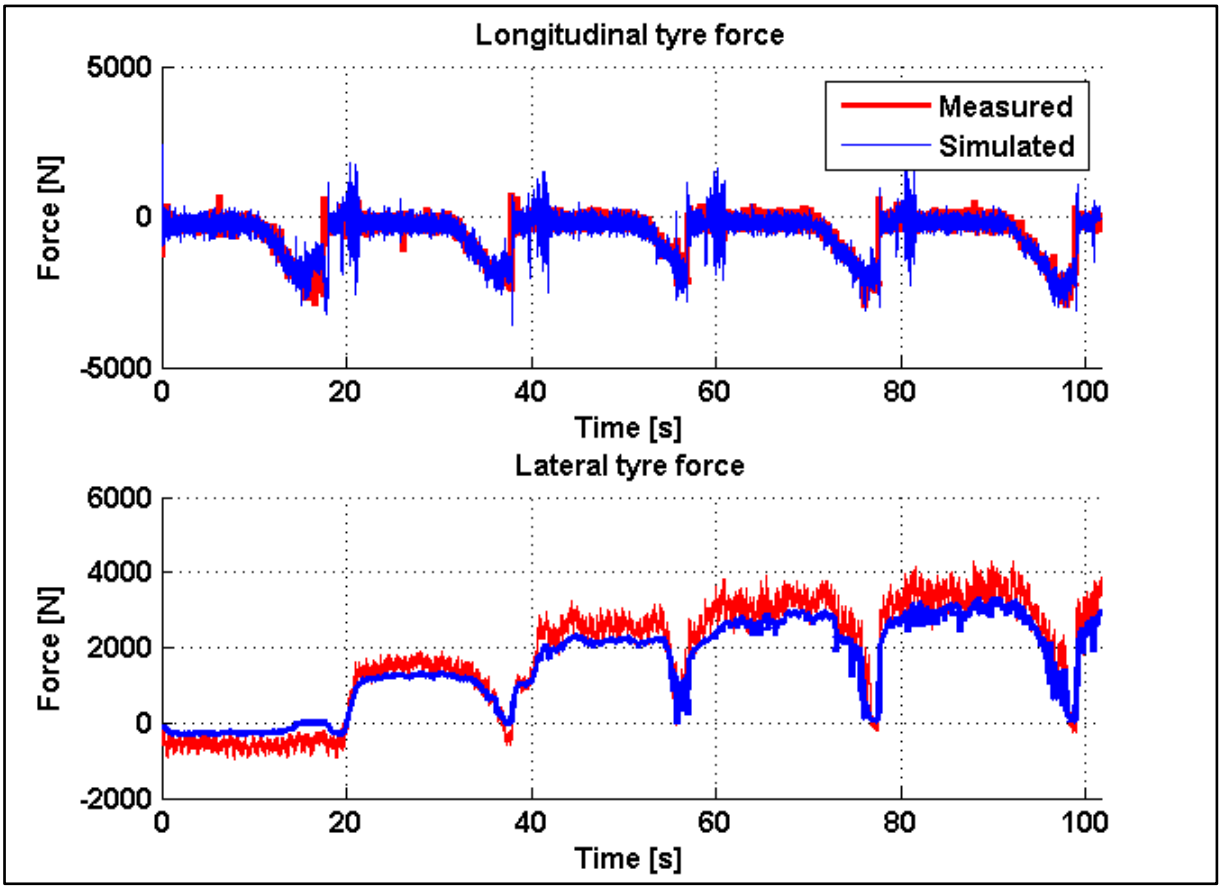

Figure 3-14 Combined longitudinal and lateral force experimental validation results

3.2.3 *Braking system*

The braking system of the Land Rover consists of two parts, namely the ABS algorithm and the hydraulic brake circuit. The ABS algorithm is discussed in detail in Section 2.2.3 and the ABS algorithm is shown schematically in Figure 2-18 (see page 23). The hydraulic circuit is responsible for converting the applied brake pressure to brake torque. The general equation for converting applied brake pressure to brake torque was discussed in Section 2.2.5. The brake torque calculated with Equation (2.11) is applied to the wheel carrier in ADAMS (MSC Software, 2016) in the opposite direction of wheel rotation.

The problem that may arise through this application of brake torque is that during wheel lockup, the wheels may actually start to rotate in the reverse direction. This is obviously not the case in a real-world scenario and provision must be made for such an occurrence in the simulation environment. Wheel lockup detection and the subsequent control of the wheel speed is thus crucially important.

Wheel lockup is detected using an if-statement. The logic flow detecting wheel lockup is shown schematically in Figure 3-15. Once wheel lockup is detected, a Proportional Integral (PI) controller is used to maintain the wheel speed at zero. Simultaneously, the wheel lockup detection is still running in the background. Once the brake torque reduces back to zero (indicating the brake is being released), the PI control maintaining the wheel speed at zero is terminated. The wheel then spins back up to speed. The PI gains were determined iteratively. It must be noted that the PI control of the wheel lockup condition is only applicable to the theoretical aspect of this project, as it aims to prevent the wheels from turning in reverse. It has no practical implementation, because the wheels will lock and slide in practice. It is a modelling technique used to avoid the complexities associated with friction modelling in brake systems.

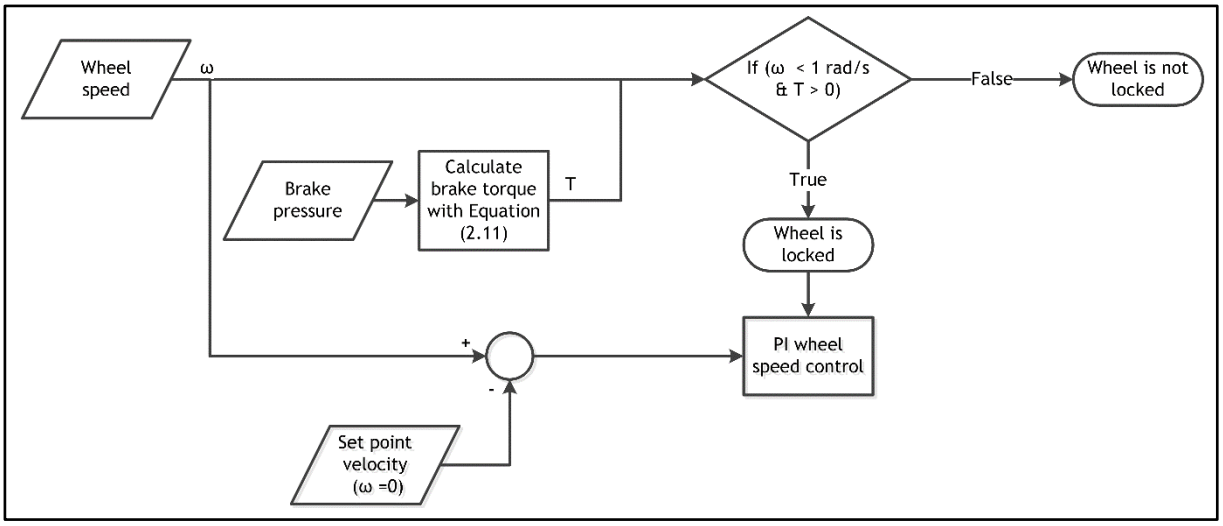

Figure 3-15 Wheel lockup detection and lockup control

3.2.4 *Experimental model validation*

The experimental validation of the ADAMS (MSC Software, 2016) model of the Land Rover Defender was done in the following five steps:

a) Validation of the vertical response of the vehicle when driving over a rough road.
b) Validation of the longitudinal response when braking on a smooth road. This includes evaluating the performance of the wheel lockup detection and wheel speed control when lockup is detected.
c) Validation of the longitudinal response when braking on a rough road.
d) Verification of the path following abilities of the driver model during a severe manoeuvre.

The ADAMS HASTIFF solver was used in the SI1 formulation with a modified corrector in all the validation simulations. According to the MSC ADAMS Solver information, the HASTIFF solver is used in conjunction with the SI1 formulation because it enables the HASTIFF integrator to monitor the integration of velocity variables that therefore results in highly accurate simulations (MSC Software, 2016). This formulation ensures that the velocities and accelerations that are calculated satisfy all first- and second-time derivatives. This is important, because the modelled forces are used for validation of some of the modelled parameters. According to Newton's Second Law, the acceleration is directly proportional to the force and hence the second-time derivative's accuracy is of utmost importance (MSC Software, 2016)

3.2.4.1 Vertical validation

The vertical response of the Land Rover Defender was determined by driving the vehicle over the suspension track at Gerotek Test Facilities (Armscor Defence Institutes SOC, 2016) at a constant speed with the $4S_4$ in the 'Ride Comfort' mode. The tests were repeated for two speeds on the Belgian paving, the parallel corrugations, and the angled corrugations. The measured data channels are given in Table 3-3.

Table 3-3 Vertical validation measurement channels

SENSOR	POSITION
Differential GPS with base station	Vehicle roof (GPS)
4g tri-axial accelerometer	Vehicle CG
Pressure transducers (4 off)	One at each suspension strut
Displacement transducers (4 off)	One at each suspension strut

The field tests were repeated in the simulation environment. A drive force located at the vehicle CG was used to drive the vehicle at the measured speed using a PI controller. The vertical acceleration at the vehicle CG, the suspension forces and displacements were used for validation.

The field tests and simulation results are compared in Figure 3-16 at 8.5m/s and Figure 3-17 at 15m/s. In both figures, a) shows the vehicle speeds, b) the vertical acceleration measured at the vehicle's centre of gravity and c) the magnitude of the scaled, single-sided Fast Fourier Transform (FFT) of the vertical acceleration. Up to approximately 15Hz extremely good correlation is obtained. Higher frequency excitation was present in the measured acceleration that was not captured by the simulation model.

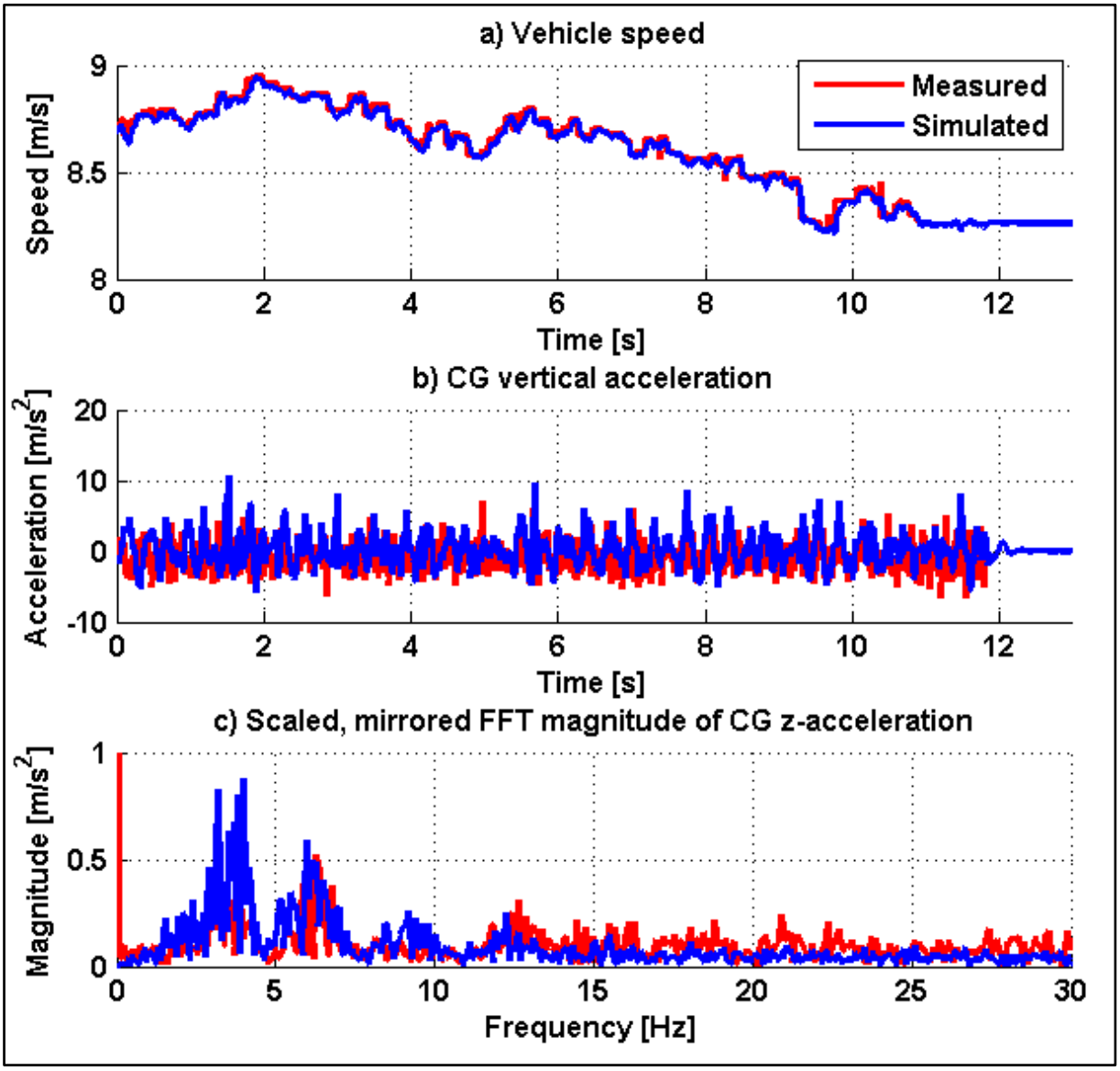

Figure 3-16 Validation of vehicle response over Belgian paving in Ride Comfort suspension mode at 8.5m/s

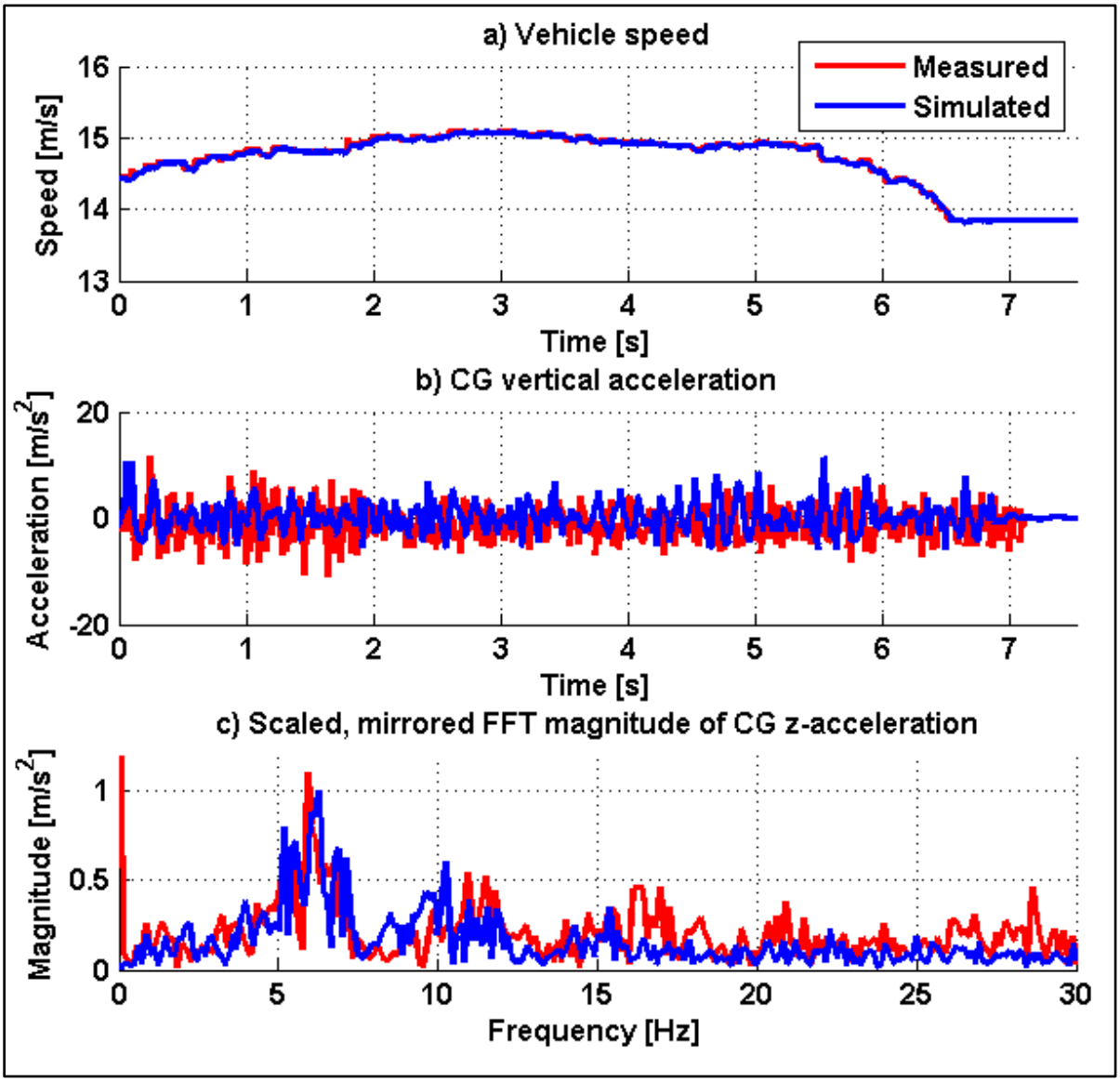

Figure 3-17 Validation of vehicle response over Belgian paving in 'Ride Comfort' suspension mode at 15m/s

3.2.4.2 Longitudinal validation

The braking performance of the Land Rover Defender was validated by braking in a straight line on a smooth concrete surface and by braking in a straight line on the Belgian paving at Gerotek Test Facilities (Armscor Defence Institutes SOC, 2016). The braking tests were conducted in dry conditions with the $4S_4$ in 'Ride Comfort' mode. The vehicle was braked from approximately 45km/h to standstill during the tests. The Land Rover Defender was instrumented with the WFT developed by Becker and Els (2012), as well as a proximity switch to measure wheel speed, and a NovAtel SPAN-CPT Single Enclosure GNSS/INS Receiver (NovAtel Inc., n.d.). The data was recorded on a Helios Single Board Computer (Diamond Systems Corporation, 2016) at a sampling frequency of 1000Hz. The smooth surface braking test results are shown in Figure 3-18 and the Belgian paving braking test results are shown in Figure 3-19.

The correlation between measured and modelled vehicle speeds is very good on both road surfaces, although some discrepancies are present when comparing the wheel speeds on the Belgian paving. The front left wheel locked up on the Belgian paving in the simulation, but not in the actual brake tests. An interesting observation is the variation in longitudinal force on the Belgian paving, even when the wheel has locked. This is not seen on the smooth road. This variation is thus due to the terrain input and the varying tyre normal force.

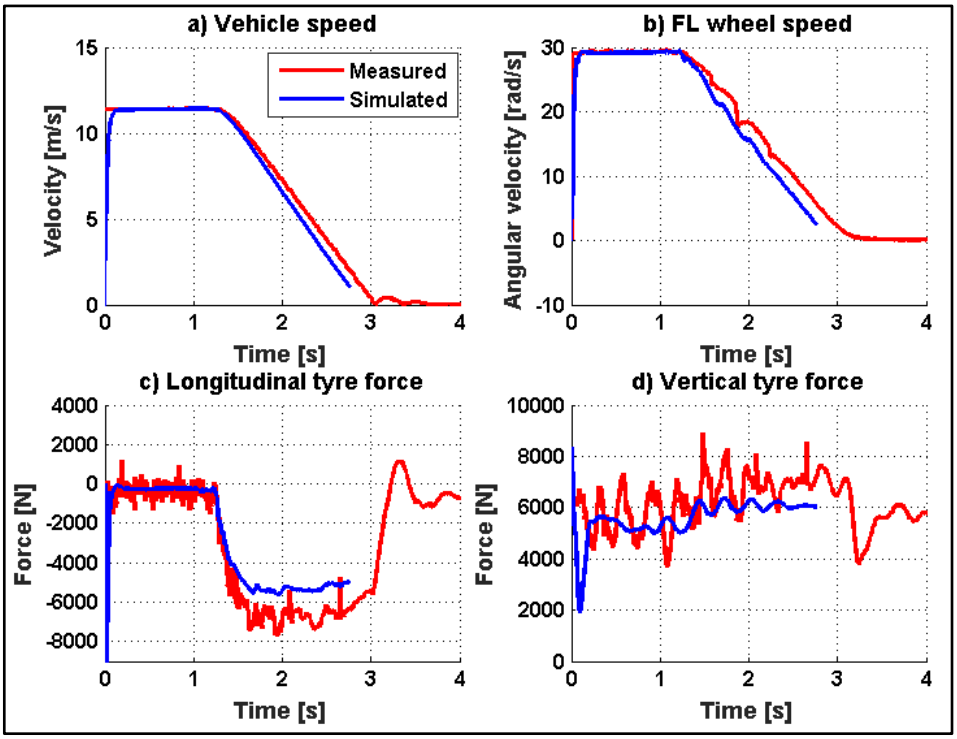

Figure 3-18 Comparison of braking performance on dry, smooth concrete surface

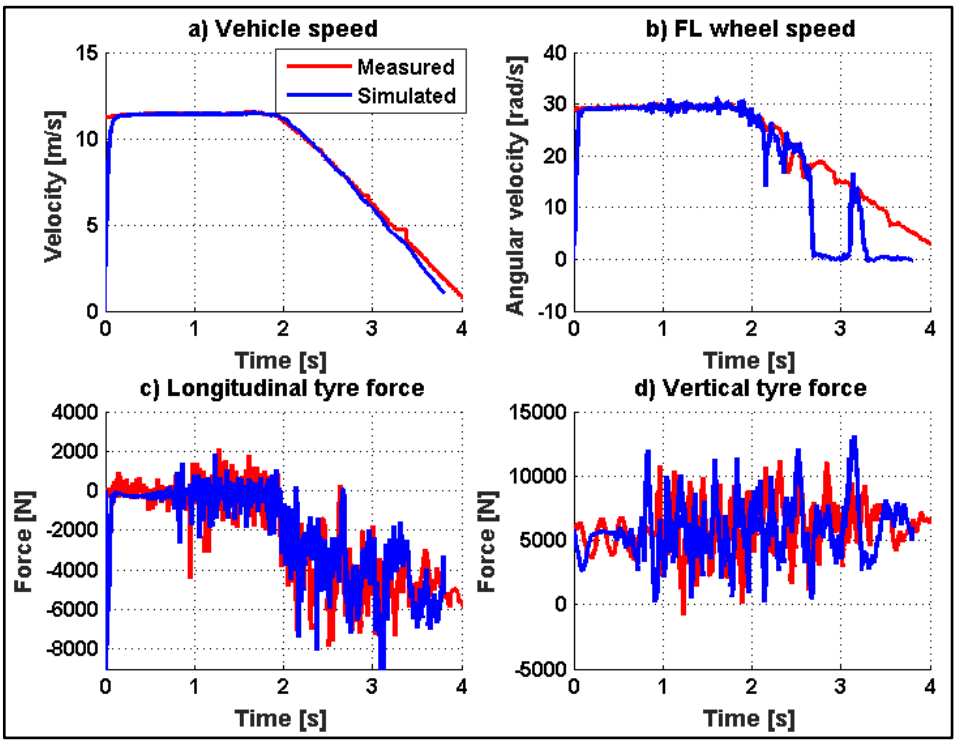

Figure 3-19 Comparison of braking performance on dry Belgian paving

The performance of the wheel lockup detection and subsequent wheel speed control was evaluated by giving a 15MPa brake pressure step input to the model after 1 second of simulation. After 0.5 seconds of braking, the brake pressure was reduced back to zero. The simulation results are indicated in Figure 3-20. The front left wheel locks almost immediately as indicated in Figure 3-20 b) once the brake pressure is increased. The wheel speed is kept in the locked state until the brake pressure is reduced. The wheel spins back up to speed and the vehicle then coasts along until the simulation is terminated after 4.5s of simulation time has elapsed. The deceleration seen once the brake is released is due to the aerodynamic drag.

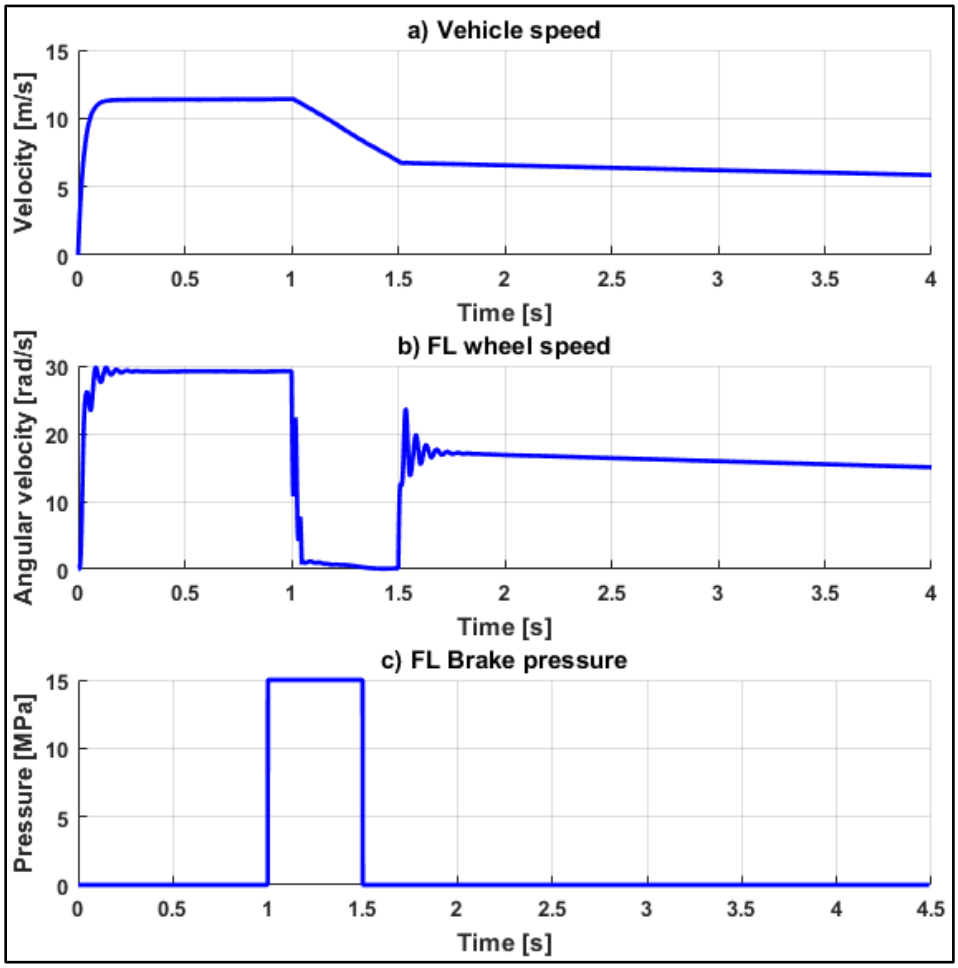

Figure 3-20 Brake lockup and release

3.2.4.3 Path following validation

The final validation step of the full multi-body dynamics model is validating its path following ability. The path following was validated by performing a severe lane change manoeuvre as described by ISO 3888-1:1999 (International Organisation of Standardisation, 1999). Both the 'Ride Comfort' and 'Handling' modes were simulated. The manoeuvres were performed at 70km/h. It must be noted that these are relatively high speeds for the Land Rover Defender to perform this severe manoeuvre.

The vehicle speed, path prescribed and followed during simulation and body roll angle as simulated and measured are indicated in Figure 3-21 and Figure 3-22 for the 'Ride Comfort' and 'Handling' suspension modes, respectively. The path following ability of the model is very good, even at severe body roll angles and high lateral acceleration. The lateral acceleration of the vehicle peaked at 6m/s^2 during the manoeuvres. Slight discrepancies between the measured and simulated roll angle is present. These discrepancies are attributable to the ideal gas model used to model the $4S_4$ air springs and slight variations in speed during the experimental measurements. Van der Westhuizen and Els (2015) obtained better results when using the Benedict-Webb-Rubin real gas model, but the correlation obtained with the ideal gas model is deemed adequate for the purpose of this study.

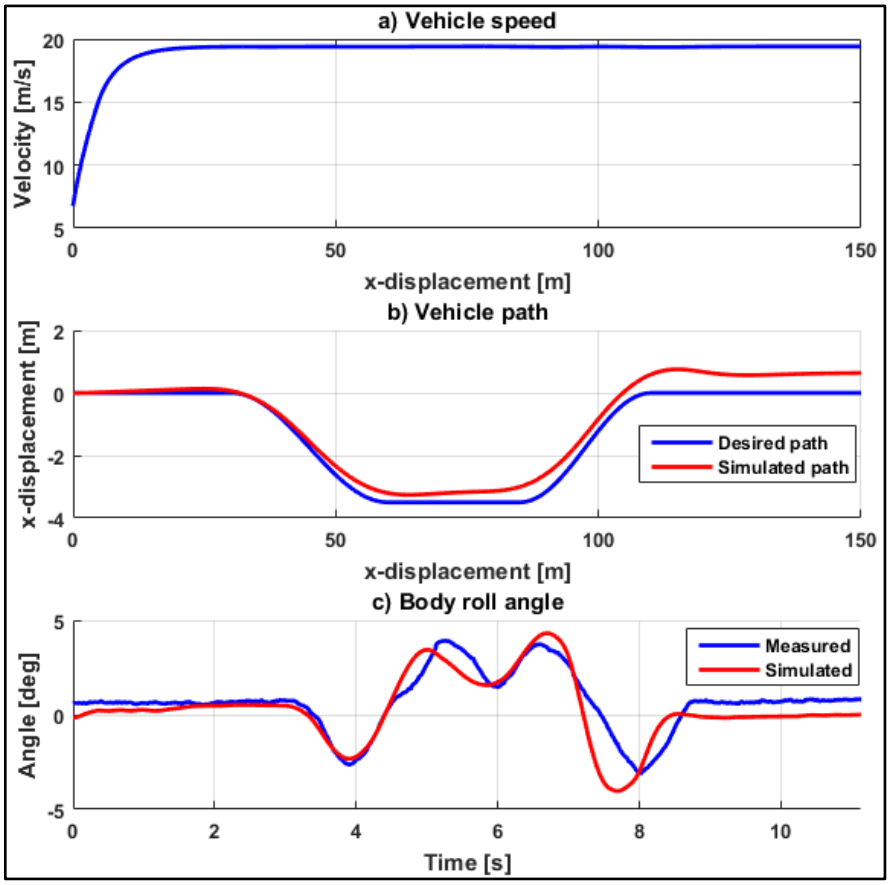

Figure 3-21 Severe lane change manoeuvre simulation and experimental results at 70km/h in Ride Comfort suspension mode

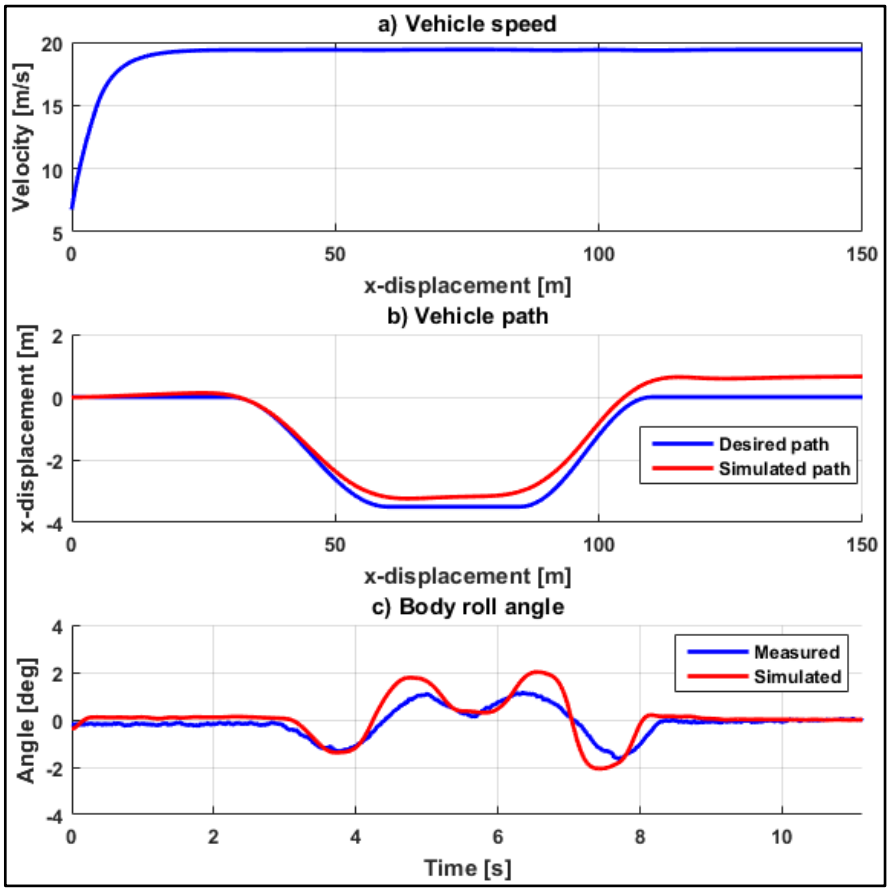

Figure 3-22 Severe lane change manoeuvre simulation and experimental results at 70km/h in Handling suspension mode

3.3 Conclusion and next steps

The full multi-body dynamics model of the experimental vehicle was developed in ADAMS (MSC Software, 2016). The tyres used on the experimental vehicle were modelled with the FTire physics-based tyre model. Extensive experimental validation tests and simulations were performed to ensure that the vehicle model accurately represents the experimental vehicle's response over rough terrain, specifically while braking. Research question (b) of Section 2.3 has thus been answered in the affirmative – the off-road braking of a vehicle can indeed be modelled mathematically.

A model-based design approach will be followed in this study to develop an algorithm that attempts to address the degradation of braking performance on an undulating road. The ADAMS model is the foundation on which the rest of this study will build on.

The next step in the study is formulating a performance evaluation metric that can be used to quantifiably compare the braking performance of vehicles.

Chapter 4

Braking performance evaluation

The key to good decision making is evaluating the available information - the data - and combining it with your own estimates of pluses and minuses.

- Emily Oster (1980-), American economist

4.1 Introduction

The third research question of Section 2.3 is (question (c)):

What are the criteria used to evaluate the smooth road braking performance of a vehicle and can the rough road braking performance of a vehicle be evaluated using the same criteria?

There are several test procedures described by the Society of Automotive Engineers (SAE, 2014) to evaluate the performance of ABS, namely:

a) straight line braking on high and low friction surfaces
b) stability and controllability in response to steering inputs
c) braking in a turn
d) split friction coefficient braking

The utilisation of the available friction force is a fundamental aspect of any brake system design. The yaw velocity (or yaw rate) response to steering may be used as a measure of both stability and steerability. For the case of braking in a turn, lateral load transfer occurs from the inside to the outside wheels. The ABS algorithm's control of the longitudinal slip on the inside and outside wheels at similar slip values usually results in a rigid body motion that increases the radius of the turn. The split coefficient braking scenarios typically occur when the road surface friction coefficients differ between left and right, a common scenario on roads in cold climates. Emergency stop manoeuvres under these conditions will exceed the friction available on the low coefficient side, once again resulting in imbalanced longitudinal forces. The resulting rigid body moment will tend to steer the vehicle to the higher coefficient surface (SAE, 2014).

Because there are so many scenarios, many of them with conflicting requirements, it is unavoidable that a compromise in the performance of ABS systems under each scenario will have to be made. ABS is also often closely interconnected with traction control and stability control. It thus becomes difficult to isolate the ABS effect. No single metric or evaluation method exists that compares the performance of different antilock brake systems with one another.

4.2 Exploiting the tyres' physics

As mentioned by the SAE in their review of antilock brake systems (SAE, 2014), there is an unavoidable trade-off between the different requirements of ABS. The ABS control algorithm has to balance the braking as well as the directional control requirements. This is inherently due to the longitudinal and lateral force generation characteristics of tyres. The tyre friction circle is the ideal tool to visualise this trade-off. Figure 4-1(a) shows a typical plot of the longitudinal friction as a function of longitudinal slip (negative friction indicates it is in the braking direction). Figure 4-1(b) indicates one quadrant of the friction circle. The trade-offs the ABS control system designer is faced with are indicated in Figure 4-1 as well. The first scenario indicated is where 100% braking is achieved. This occurs when the wheel slip is controlled so that the friction force is at its peak. In this case, the driver will not be able to steer and the vehicle may become unstable if a lateral disturbance is present. The second scenario is the case where no braking force is generated, but the maximum possible side force is achieved (this is indicated as 100% side force in Figure 4-1). A third scenario is also shown: the case where the wheel is locked – i.e. the longitudinal slip is at 100%. The aim of the ABS control system is to find an acceptable compromise between scenarios one and two.

Ideally, the ABS controller must be able to switch rapidly between 100% braking and 100% side force. In such an ideal case, the friction force will follow the black line (labelled as "Ideal ABS" in Figure 4-1(b). Physically, this relates to the speed at which brake pressure can be decreased and increased from 100% to 0% and back to 100%. If the ABS system is capable of doing this faster than the tyres can switch from 100% braking to 100% side force (due to the relaxation length effect of the tyres, see Maurice and Pacejka (1997)), the ABS performance will be limited by the tyre friction force generation characteristics. Further improvements to the ABS performance in such a case will be due to the fitment of tyres with a shorter relaxation length and not by tuning the ABS algorithm or updating the ABS hardware. In such an ideal case, the braking half of the friction circle (the negative μ_x and entire μ_y sector, i.e. quadrants three and four) will be available to the driver to exploit during an emergency manoeuvre.

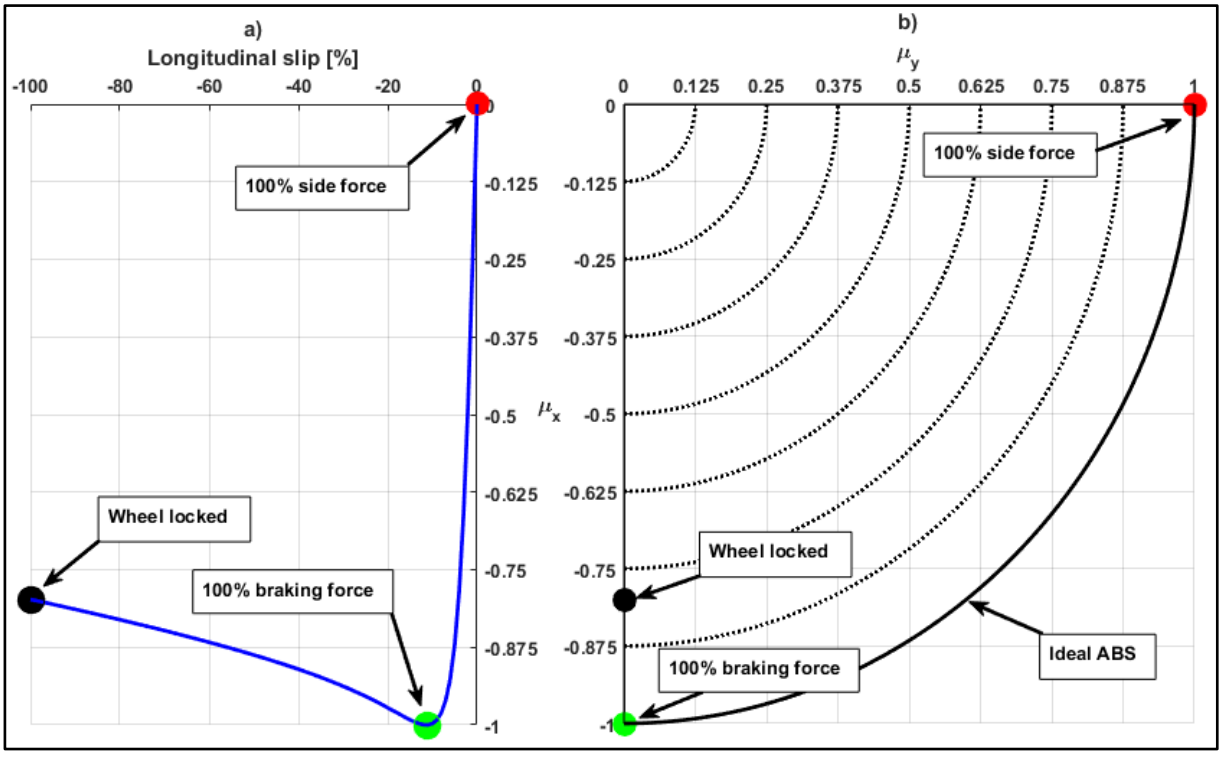

Figure 4-1 Tyre longitudinal friction (a) and tyre friction circle (b)

4.3 Existing ABS performance assessment criteria

Savitski et al. (2015) experimentally evaluated the performance of three ABS algorithms with straight line braking tests on a low friction surface. The experimental surface consisted of wet tiles with an average coefficient of friction of 0.2 (Ivanov et al., 2015a). They divided the assessment criteria into three categories, namely:

a) the braking performance
b) the ABS control performance
c) the driving comfort

The braking performance was evaluated using the brake distance, average deceleration and the ABS index of performance. The ABS index of performance, or ABSIP, shows the ratio between the average deceleration of the vehicle with ABS and without ABS. The ABSIP is given by:

$$ABSIP = \frac{\bar{a}_{ABS}}{\bar{a}_{no\ ABS}} \tag{4.1}$$

A value of one indicates that the ABS system does not improve the mean vehicle deceleration. Values larger than one indicate an improvement in the braking performance. The algorithms investigated by Savitski et al. (2015) resulted in ABSIPs in the range of 1.34 to 1.74, indicating significant improvements in the average vehicle deceleration. It is assumed that the driver of the non-ABS vehicle is passive and brakes with all the wheels locked, rather than a good driver reacting to the vehicle feedback and modulating the brakes (also known as cadence braking).

The ABS control system's response to differing wheel slip dynamics was evaluated by determining the amount of wheel lockup occurring before the control system was able to reduce brake pressure and thus reducing wheel slip. A peak-to-peak value was used to evaluate the performance for each wheel. The worst-case value for the left and right wheels on each axle was used to compare different ABS algorithms. The peak-to-peak value was determined with Equation (4.2):

$$\omega_{peak} = \frac{\omega_{max} - \omega_{min}}{\omega_{max}} \times 100\% \tag{4.2}$$

Typical values ranged from 6% to 57% for the front wheels and 8% to 36% for the rear wheels (a lower value indicates better performance). The average slip percentage was also used as an ABS control system performance assessment criteria. The best-case resulted in 14% for the front wheels and 8% for the rear wheels. In their study, it may be seen that the values are almost identical between the left and right wheels on the same axle; this indicates that there is very little lateral load transfer during the straight-line brake manoeuvres, as expected. There is however, a problem associated with using this metric to determine ABS performance. By tuning the ABS performance to reduce the peak overshoot or to minimise the variation in longitudinal slip, the designer is in effect approaching an optimal slip controller. Kienhöfer et al. (2008) developed a gain-scheduled slip controller that aims to control the longitudinal slip at the longitudinal friction force peak. Using the stopping distance and the ABS pressurised air consumption (their ABS was applied to a heavy vehicle) to evaluate their system's performance, their slip control resulted in an improvement on conventional rule-based ABS by 10% on stopping distance and 30% on air consumption. Kienhöfer et al. (2008) did however not take the yaw stability or steerability of the vehicle into account.

Apart from the safety-related performance criteria, comfort and refinement is becoming of greater importance in modern vehicles. The shock and vibration experienced on the vehicle

during ABS operation is therefore also becoming an important consideration, especially on top-end luxury vehicles. Savitski et al. (2015) postulated that jerk was a good indicator of driver perception. Lower jerk results in improved ABS performance in terms of comfort and driver perception. The integral of the time multiplied by the absolute error (ITAE) of the vehicle jerk in the longitudinal direction was determined with Equation (4.3):

$$Jerk\ ITAE = \int_{t_1}^{t_2} |j_x| t\ dt \tag{4.3}$$

The smallest ITAE value recorded during their experiments was 2.92m/s^2 and the largest 12.0 m/s^2.

To visualise their results, Savitski et al. (2015) normalised their assessment metrics (the test with the best score was normalised to 100%) and the resulting metrics were visualised on a radar plot, as shown in Figure 4-2. In the example of Figure 4-2, ABS system 1 (the blue dashed line) may be seen to be better than the alternatives.

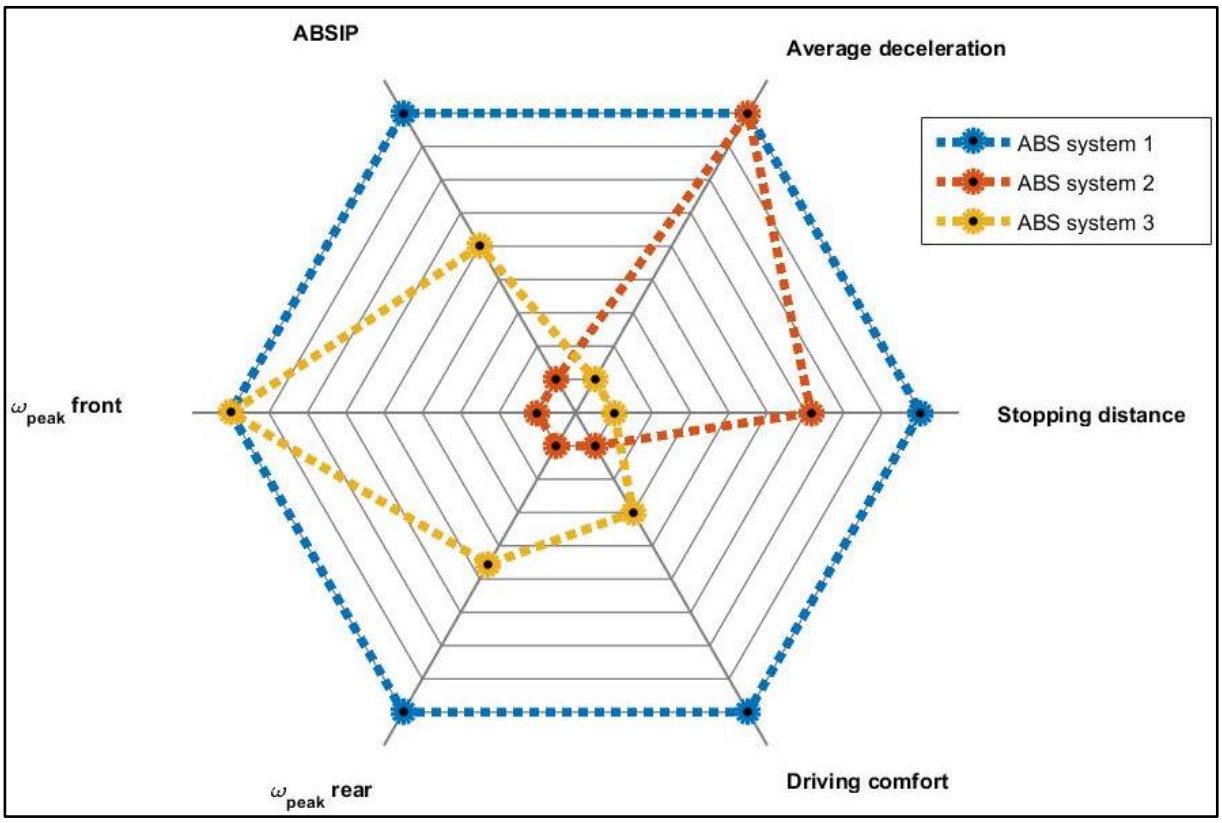

Figure 4-2 Radar plot used to compare ABS system performance as developed by Savitski et al. (2015)

The study by Savitski et al. (2015) was limited to straight line braking tests. The Antilock Brake System Review by the SAE (2014) specifically mentioned the contribution ABS makes towards a vehicle's stability when braking on split-mu road surfaces and when braking in a turn. Lee et al. (2003) evaluated the performance of a commercial ABS on split-mu roads. The road they tested on had a friction coefficient of 0.35 on the left and 0.6 on the right. The ABS braking performance was compared with the performance of a conventional braking system under these conditions. To compare the braking performance, they considered steering angle input, vehicle deceleration, vehicle yaw rate and the stopping distance. From their results, it may clearly be seen that the vehicle equipped with ABS stops in a shorter distance, the steering angle input by the driver required to keep the vehicle driving in a straight line is significantly smaller and the yaw rate indicates better stability when compared to the vehicle without ABS. All of their comparisons were done in the time domain.

Day and Roberts (2002) compared the braking performance of a vehicle with ABS and one without ABS when braking during a severe lane-change manoeuvre, as described by ISO 3888-1:1999 (International Organisation of Standardisation, 1999). The vehicle's ability to maintain the desired path was not described in detail, it was merely stated that the vehicle equipped with ABS stayed within the cones. The vehicle without ABS skidded straight ahead and was not able to stay within the cones (the steering input preceded the application of a force to the brake pedal).

The radar plot of Figure 4-2 may be less useful when evaluating the performance of the ABS under split-mu manoeuvres or when braking in a turn or during a lane change manoeuvre, because it merely compares averages and does not consider vehicle stability or steerability. The current investigation aims to formulate a method of comparing different ABS algorithms with one another that will guide the design engineer in selecting the most appropriate ABS for their application by taking into account all the requirements as discussed by SAE (2014).

4.4 Existing directional stability assessment criteria

Quantifying the straight line braking performance by limiting it to stopping distance and average deceleration is easy, but directional control is more challenging to define quantitatively. Directional control is often studied with the aim of developing a driver steering model to be used in conjunction with vehicle simulation models. Thoresson et al. (2014) and Kapp and Els (2015) controlled two vehicle states to develop such a driver model, namely the desired yaw acceleration and the lateral offset from the path. The desired yaw acceleration was related to the desired steering wheel input velocity (which is directly proportional to the yaw rate) and was used as the main path following controller. When using only the yaw rate to perform path following, a lateral offset from the desired path will eventually occur due to integration drift. To rectify this, the lateral path following error was controlled with a PID controller.

The use of both yaw rate variation and lateral path offset error is applicable to evaluating the performance of an ABS. The reasons for a driver to steer during braking is to avoid an obstacle or obstruction in the vehicle's path or to maintain the trajectory to prevent the vehicle from veering out of its lane. The average driver at this stage will not be too concerned with the yaw rate of the vehicle (unless the vehicle is spinning already) and will attempt to avoid the obstacle by changing the vehicle's lateral position. The driver attempts to do this by steering, which in turn generates a yaw acceleration and a corresponding change in the yaw rate. If the yaw acceleration is high enough, the vehicle will steer quickly enough to avoid the obstacle, but this "obstacle avoidance" is due to the lateral offset from the original path of the vehicle due to the induced yaw acceleration. It is highly unlikely that an average vehicle will be able to move from its trajectory laterally without generating a yaw acceleration (this is possible with four wheel steering, but there are few examples of four-wheel steer vehicles on the road). Similarly, the lateral path error cannot be considered separately from the yaw rate. The SAE's antilock braking system review mentions that it is not uncommon for a vehicle to spin about its yaw axis while the CG maintains a straight line when braking on a split-mu surface (SAE, 2014).

4.5 Proposed ABS performance evaluation technique

A suitable ABS performance evaluation technique must be able to objectively compare different possibilities and make it easier for the control system designer to identify the best ABS control system for the application. A compromise cannot be avoided, but the aim of the performance evaluation technique is to compare the braking performance from a practical vehicle dynamics point-of-view clearly and quantitatively. The literature discussed in the preceding sections highlighted the need for the ABS control system to minimise the

stopping distance while allowing the driver to maintain directional control. The proposed metrics to evaluate ABS performance are thus:

a) Stopping distance and its standard deviation (if more than one test is carried out for the same algorithm)
b) Mean and standard deviation of vehicle deceleration during the braking manoeuvre
c) Mean and standard deviation of absolute vehicle yaw rate error during the braking manoeuvre
d) Mean and standard deviation of absolute lateral path following error during the braking manoeuvre

When several runs of the same test are performed, the mean and standard deviation of each of these four metrics can be used. The mean value of each metric gives an indication of the performance of the brake system with regard to that metric and the standard deviation gives an indication of the system's stability (or repeatability).

The comfort effect discussed by Savitski et al. (2015) is excluded, as ABS is only active during emergency braking. The comfort requirement is thus of secondary importance when considering vehicle occupant safety. The proposed comparison technique does however provide room for the easy integration of additional requirements the control system designer may want to include.

The evaluation technique assigns a single value to each of the abovementioned metrics' means. A comparison matrix containing m rows and n number of columns, where m represents the number of metrics being used (the abovementioned four is recommended, but additional metrics can be added) and n represents the number of tests being compared, is assembled. Each row in the comparison matrix is normalised relative to the best value in the row. Two possible normalisations exist:

a) A higher value is better, for a case such as the mean deceleration during the braking manoeuvre. In such a case, the metric is normalised by:

$$x_{ij,norm} = \frac{x_{ij}}{\max(x_{i,\dots})} \times 100\%, i \in 1,2,3,\dots,m;\ j \in 1,2,3,\dots,n \tag{4.4}$$

b) A lower value is better, for cases such as stopping distance or absolute lateral path following error. In such a case, the metric is normalised by:

$$x_{ij,norm} = \frac{min(x_{i,\dots})}{x_{i,j}} \times 100\%, \qquad i \in 1,2,3,\dots,m;\ j \in 1,2,3,\dots,n \tag{4.5}$$

The standard deviation of each of the metrics during the braking manoeuvre is also taken into account. The standard deviation of each metric is also normalised using Equation (4.4), resulting in the worst-case scenario being assigned a value of 100%.

An illustration technique similar to the radar plot shown in Figure 4-2 is used to compare the ABS performance of different algorithms with each other. Additionally, the standard deviation of each metric is also illustrated. Figure 4-3 shows how two ABS algorithms using the proposed performance evaluation technique are compared. At the first glance, it may be seen that ABS algorithm 1 performs better than algorithm 2 in all four of the metrics when considering the mean values and when considering the standard deviation. This is the advantage of using the proposed evaluation technique, as it provides clear and quantifiable evidence to support the selection of an ABS algorithm to another. Additional metrics can be included by modifying the radar plot of Figure 4-3 with the addition of more axes.

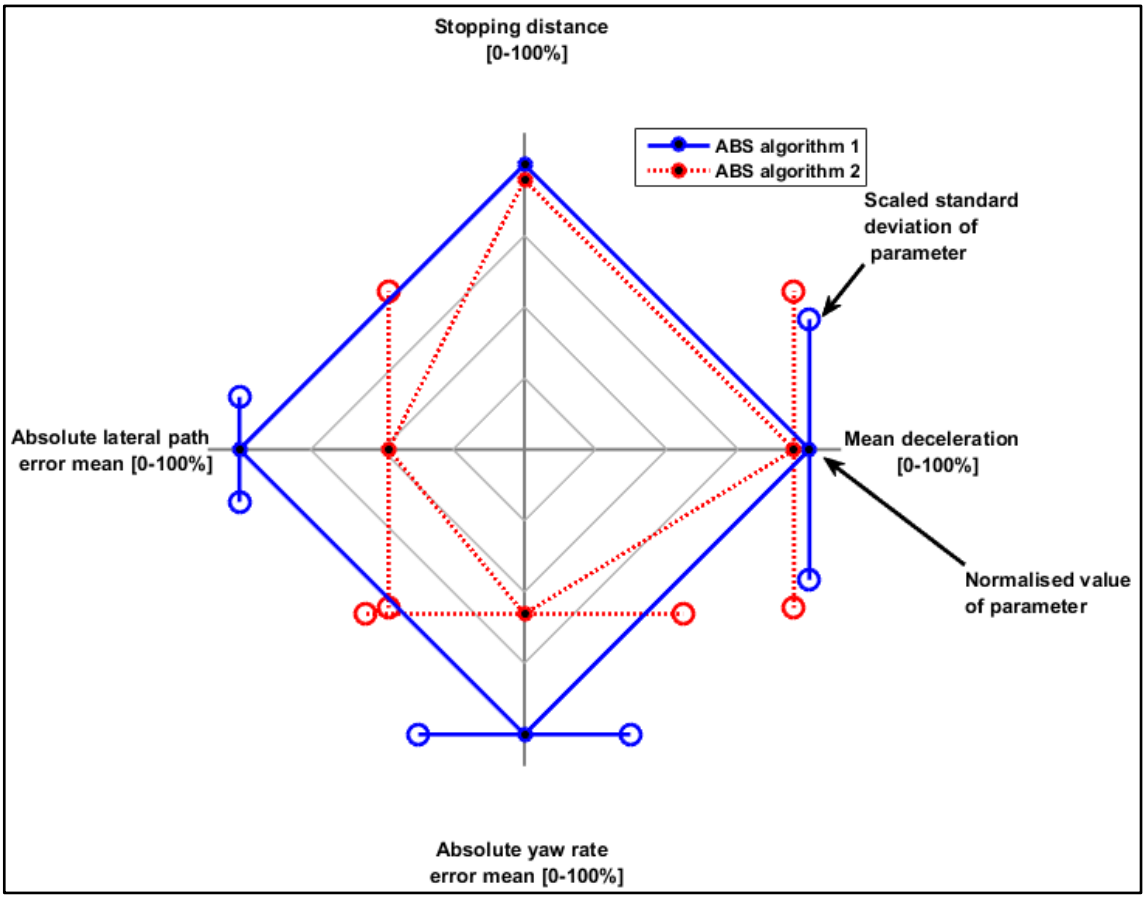

Figure 4-3 Comparing the performance of two ABS algorithms

4.6 Illustrating the ABS performance evaluation technique on smooth roads

Simulations are now used to illustrate the proposed ABS performance evaluation technique. The simulations were repeated for three different vehicle configurations: two different ABS algorithms and the vehicle without ABS. These are indicated as ABS 1, ABS 2, and No ABS in the figures throughout Chapter 4. The Bosch algorithm of Section 2.2.3 shown in Figure 2-18 was used as ABS algorithm 1. ABS algorithm 2 utilised the same algorithm, but time delays were introduced in the input signals to the ABS algorithm, possibly worsening its performance.

Five braking scenarios were simulated, as recommended by SAE (2014):

a) Braking in a straight line on a high friction surface.
b) Braking in a straight line on a low friction surface.
c) Braking in a turn on a high friction surface.
d) Braking in a turn on a low friction surface.
e) Braking in a straight line on a split-mu surface.

The straight-line braking manoeuvres were simulated with an initial speed of 80km/h. The brake-in-turn manoeuvre was simulated with an initial speed of 60km/h. The high friction surface had a friction coefficient of 1 and the low friction coefficient surface had a friction coefficient of 0.3. The high friction brake-in-turn simulation had a constant radius of 50m and the low friction surface a constant radius of 120m. The split-mu surface had a coefficient of friction of 0.8 under the left side and 0.3 under the right side of the vehicle. All of the simulations were terminated when the vehicle speed reached 15km/h, as typical ABS algorithms are only applied above 15km/h.

4.6.1 *Straight line braking results*

Figure 4-4 and Figure 4-5 show the straight line braking results on high (Figure 4-4) and low (Figure 4-5) friction surfaces. The differences are clearly visible, with the stopping time increasing from 2.2s to 7.3s for ABS algorithm 1. It is worth noting that on the high friction surface, the stopping time of the vehicle without ABS was better than that of ABS algorithm 2. On the low friction surface, however, the opposite was true. The lateral path error in both cases was very small, equivalent to approximately a tyre width on the high friction surface and even less on the low friction surface. The yaw rate deviated very little from the desired yaw rate, as is expected for a straight-line brake test on a constant friction surface.

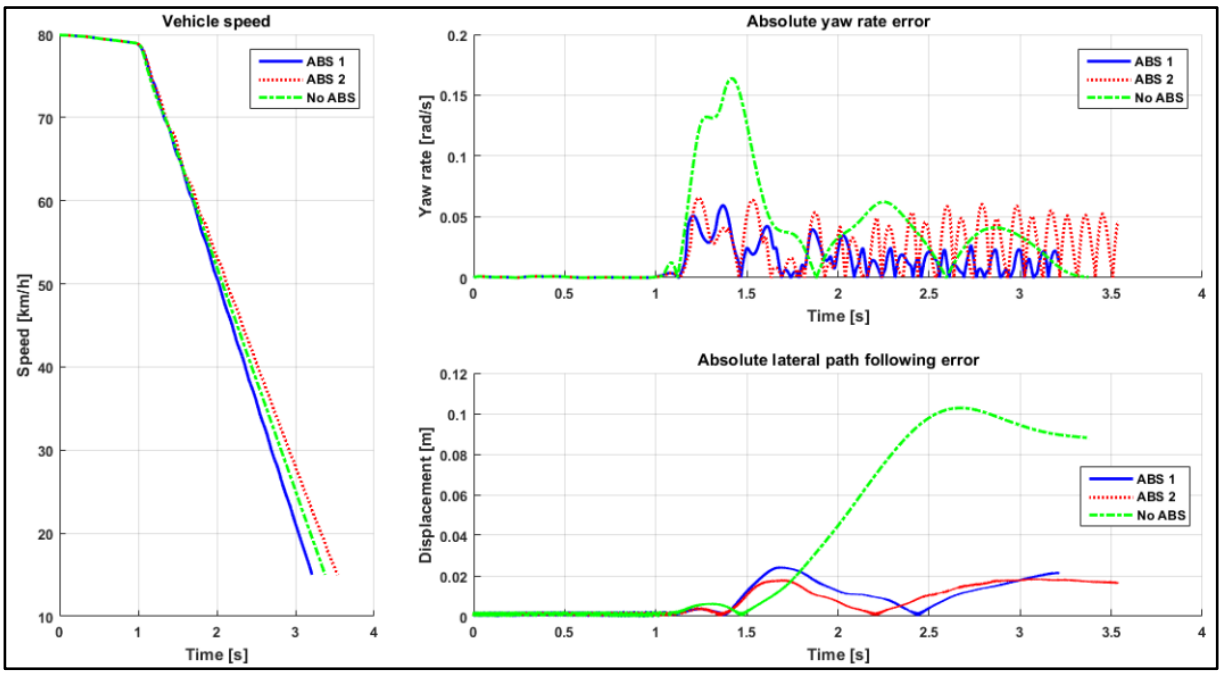

Figure 4-4 Straight-line, high friction braking simulation results

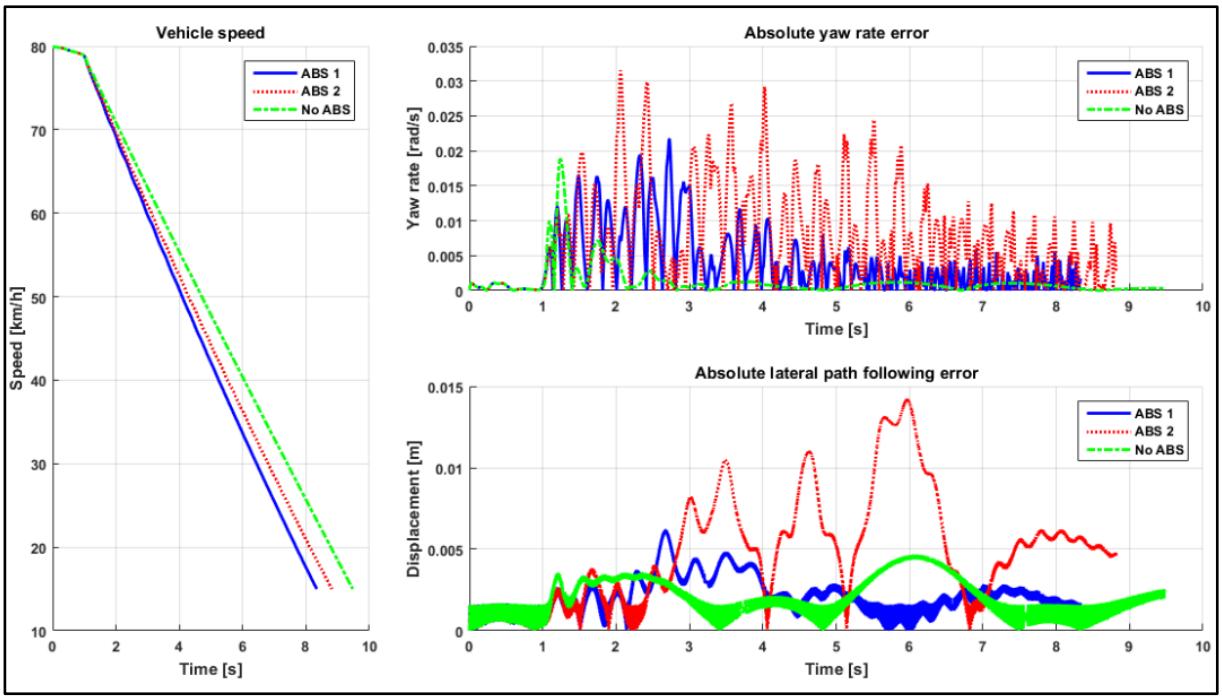

Figure 4-5 Straight-line, low friction braking simulation results

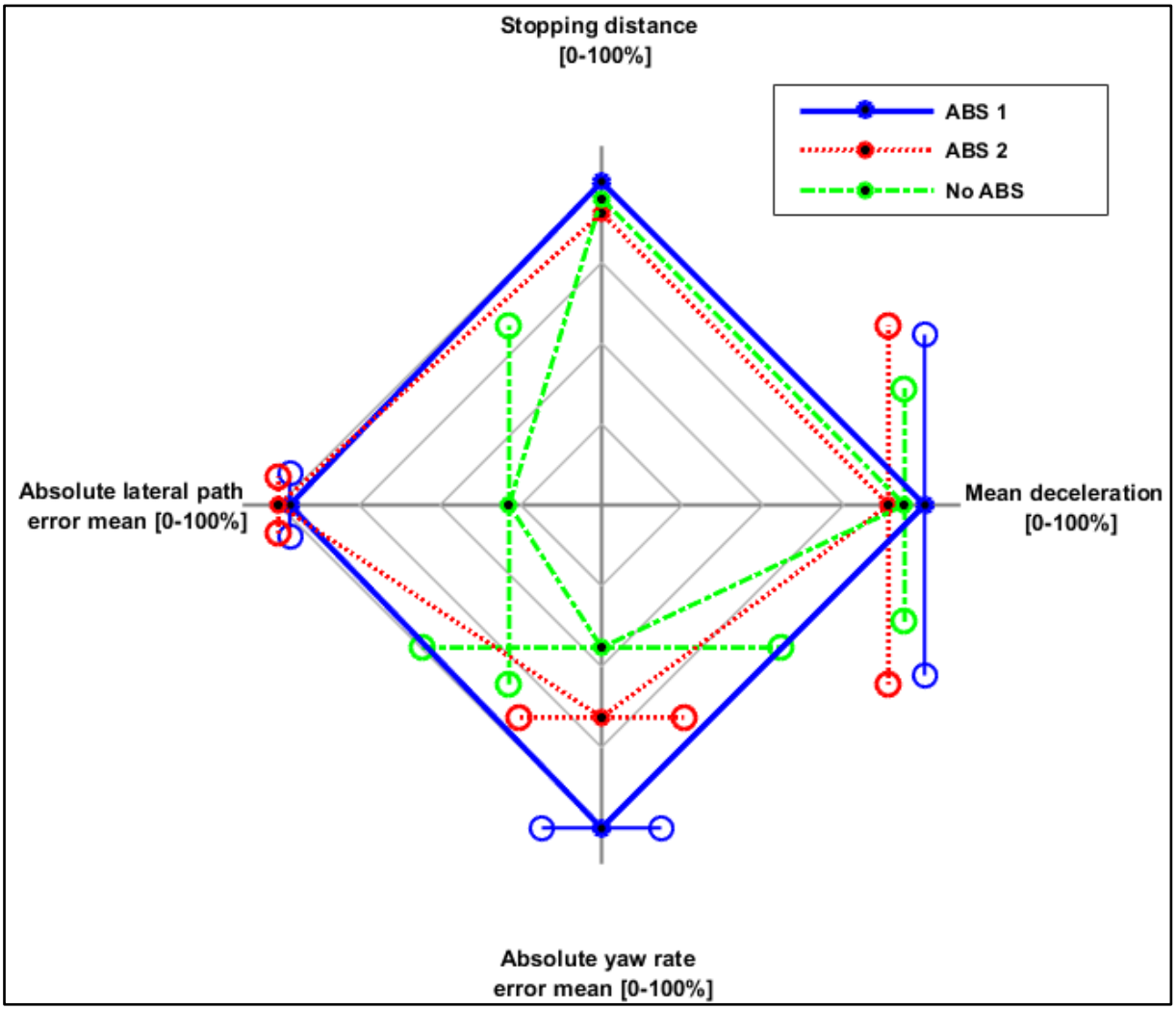

Figure 4-6 Comparing ABS performance for straight-line braking on high friction surface

The simulation results of ABS algorithm 1 and 2 and the conventional braking simulation are processed with the evaluation technique discussed in Section 4.5 and the results for the high friction surface are shown in Figure 4-6 and for the low friction surface in Figure 4-7. Figure 4-6 clearly shows that ABS algorithm 1 performed the best for the high friction surface straight-line brake tests. It scored the best for three of the four metrics considered, namely stopping distance, mean deceleration and absolute yaw rate mean error. ABS algorithm 2's performance was better than that of the conventional braking system when considering the directional stability of the vehicle, as may be seen with the better performance in the lateral path following mean error and in the absolute yaw rate mean error. There is however, very little to choose between all three simulations with regard to stopping distance and mean deceleration on the high friction surface. It may also be seen that the variation in the metrics used to evaluate the directional stability was significantly lower for the two simulations with ABS enabled.

Figure 4-7 shows some interesting results when comparing the low friction simulations' braking performance. Both the simulations with ABS active resulted in improved stopping distances and mean decelerations when compared to the conventional brake system. This indicates that the ABS enabled simulations utilised the longitudinal friction available to the driver better than the conventional brake system. The directional stability for these two ABS enabled cases was however worse than the directional stability of the simulation without ABS. This indicates that the simulation without ABS merely locked the wheels and the vehicle skidded to a halt, while the modulation of the brakes resulted in some directional stability issues. This may be attributed to the yaw moment generated by asymmetrically

modulating the left and right wheel's brakes or to the steering controller. Because the simulation is a straight-line brake test, the directional stability of the vehicle seemed to be improved when the ABS was deactivated. The steerability was however reduced significantly, as the wheels locked and skidded for the duration of the test. This illustrates the importance of using more than one scenario when evaluating the braking performance of a vehicle; limiting the analysis to straight-line, constant road friction tests is not sufficient to evaluate braking performance.

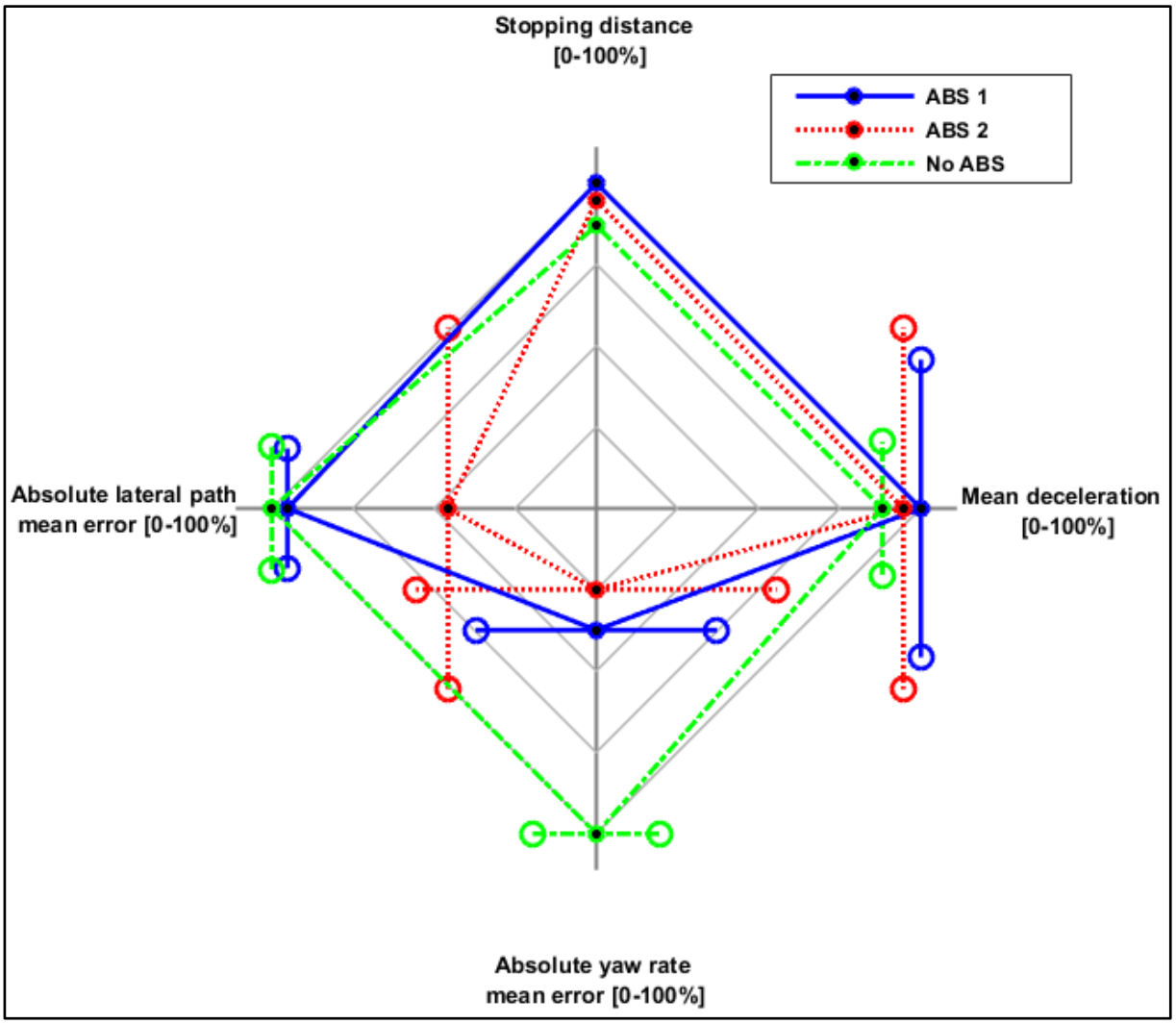

Figure 4-7 Comparing ABS performance for straight-line braking on low friction surface

4.6.2 *Brake-in-turn results*

The brake-in-turn simulation results are shown in Figure 4-8 and Figure 4-9. The brake-in-turn results clearly show the advantage of having an ABS equipped vehicle, specifically on the low friction surface in Figure 4-9. For the case of the high friction surface (Figure 4-8), the lateral path error made by the vehicle without ABS is significant. The lateral path error was 3.65m when the vehicle reaches 15km/h at the end of the simulation. However, when comparing the yaw rate error on the high friction surface, at first glance there seems to be little difference between the three simulations. This highlights the importance of including the lateral path error and not using the yaw rate on its own. Both the ABS equipped vehicles managed to track the desired yaw rate and path quite accurately, the only difference discernible is in the stopping distance. The ABS algorithm 2 vehicle's stopping distance was 17.1m, compared to 16.1m for ABS algorithm 1 vehicle's stopping distance.

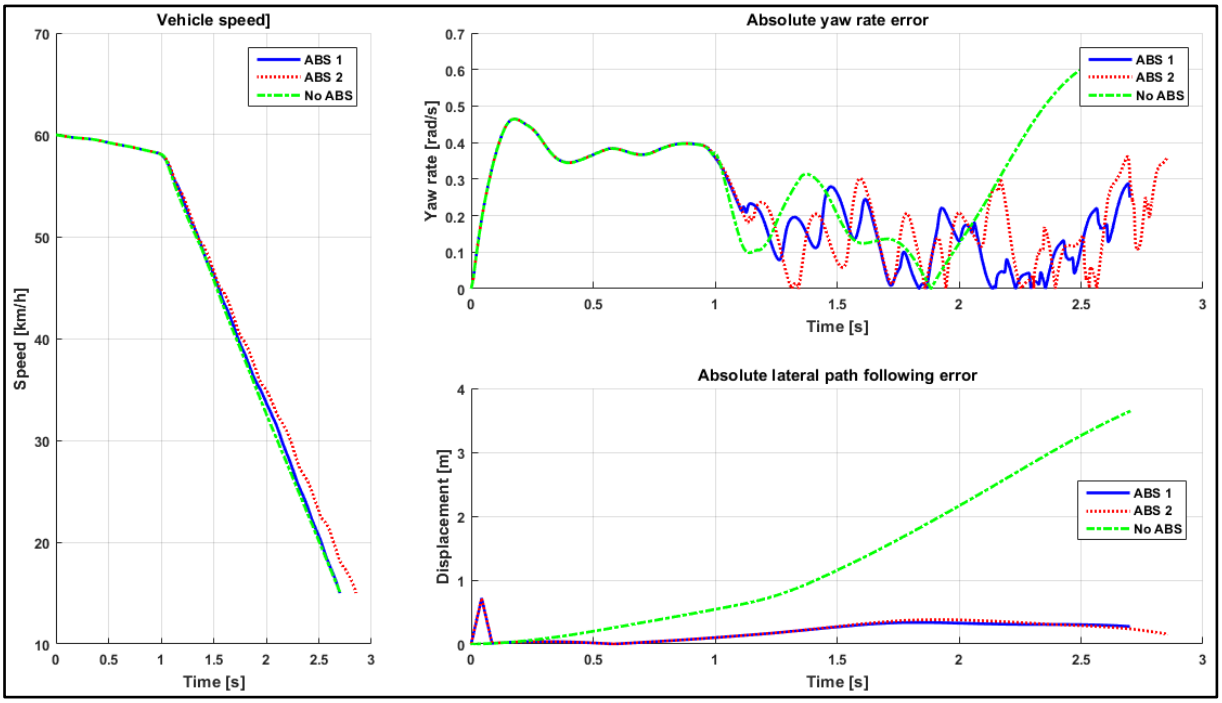

Figure 4-8 Brake-in-turn on high friction surface simulation results

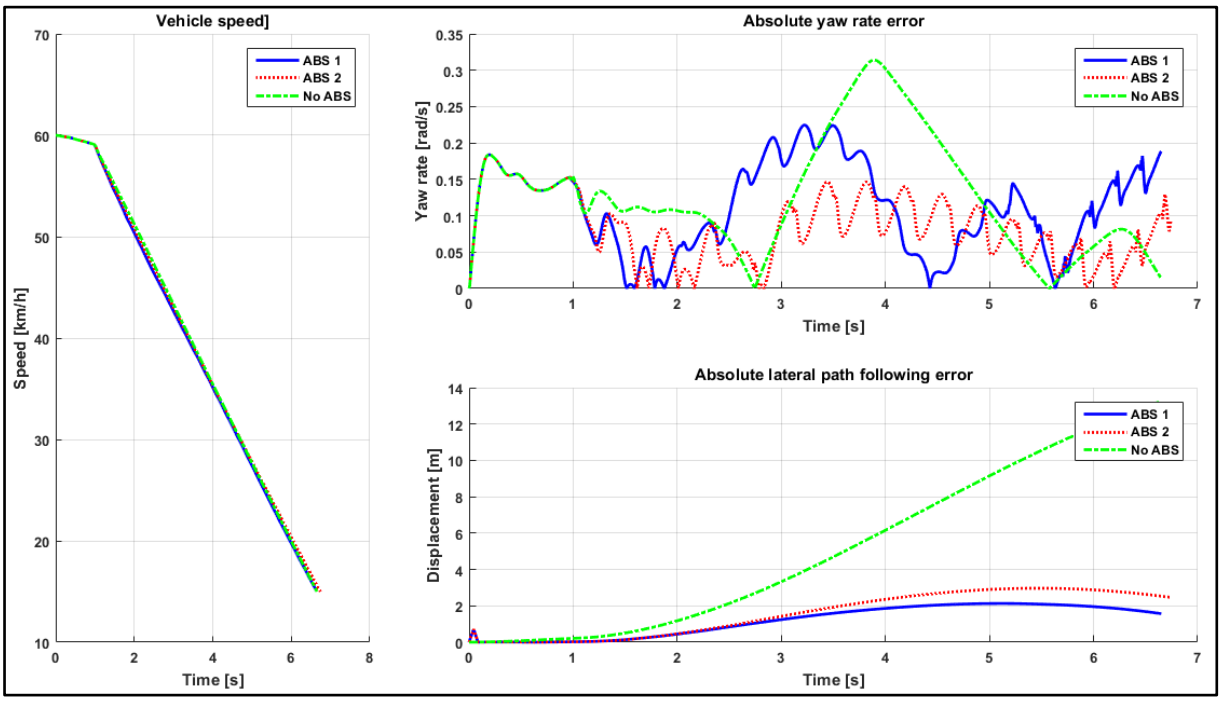

Figure 4-9 Brake-in-turn on low friction surface simulation results

Processing the simulation results with the steps outlined in Section 4.5 results in the radar plots of Figure 4-10 (for the high friction brake-in-turn manoeuvre) and Figure 4-11 for the low friction brake-in-turn manoeuvre. Similar to the high friction results of Section 4.6.1, the stopping distances and mean deceleration do not differ as significantly as the directional stability results. Both the ABS algorithms' directional stability during the brake-in-turn manoeuvres was significantly better than that of the conventional brake system. The low friction brake-in-turn manoeuvre gives similar results to that of the high friction brake-in-turn manoeuvre, with a slight discrepancy between the lateral path following and yaw rate tracking ability of the ABS enabled simulations.

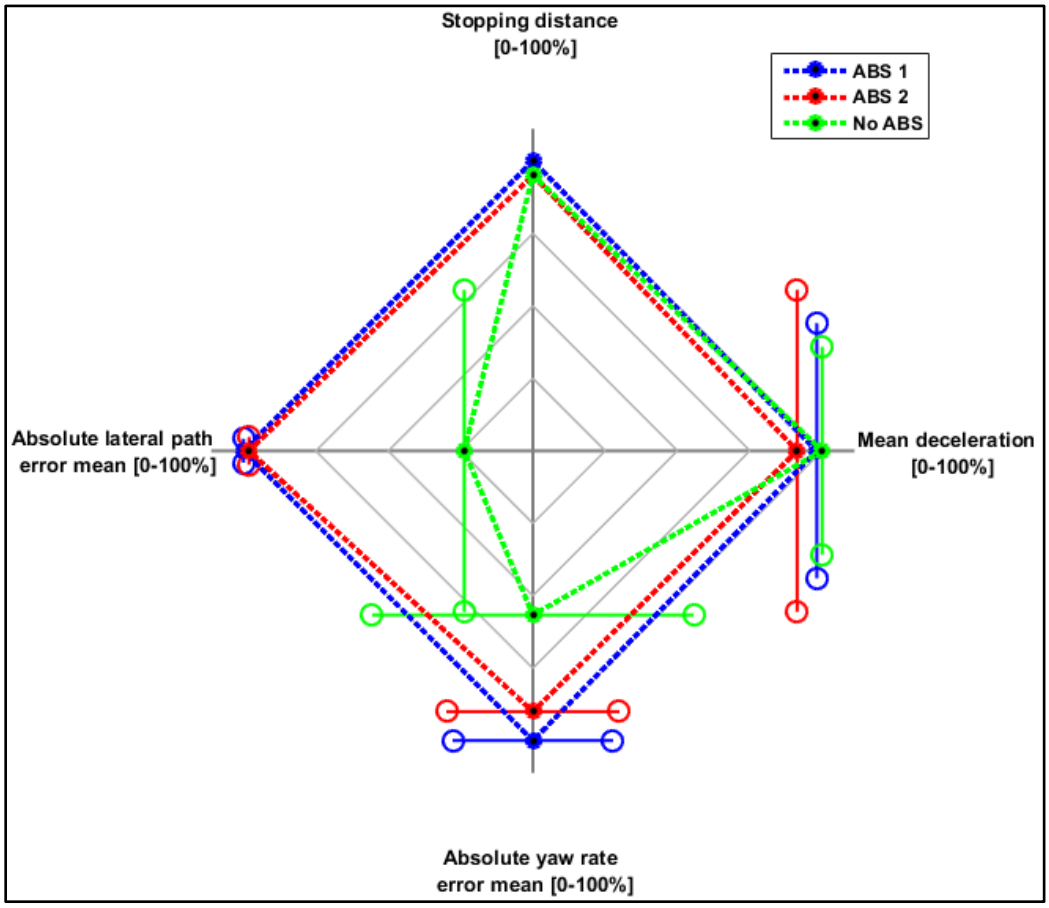

Figure 4-10 Comparing ABS performance for brake-in-turn on high friction surface

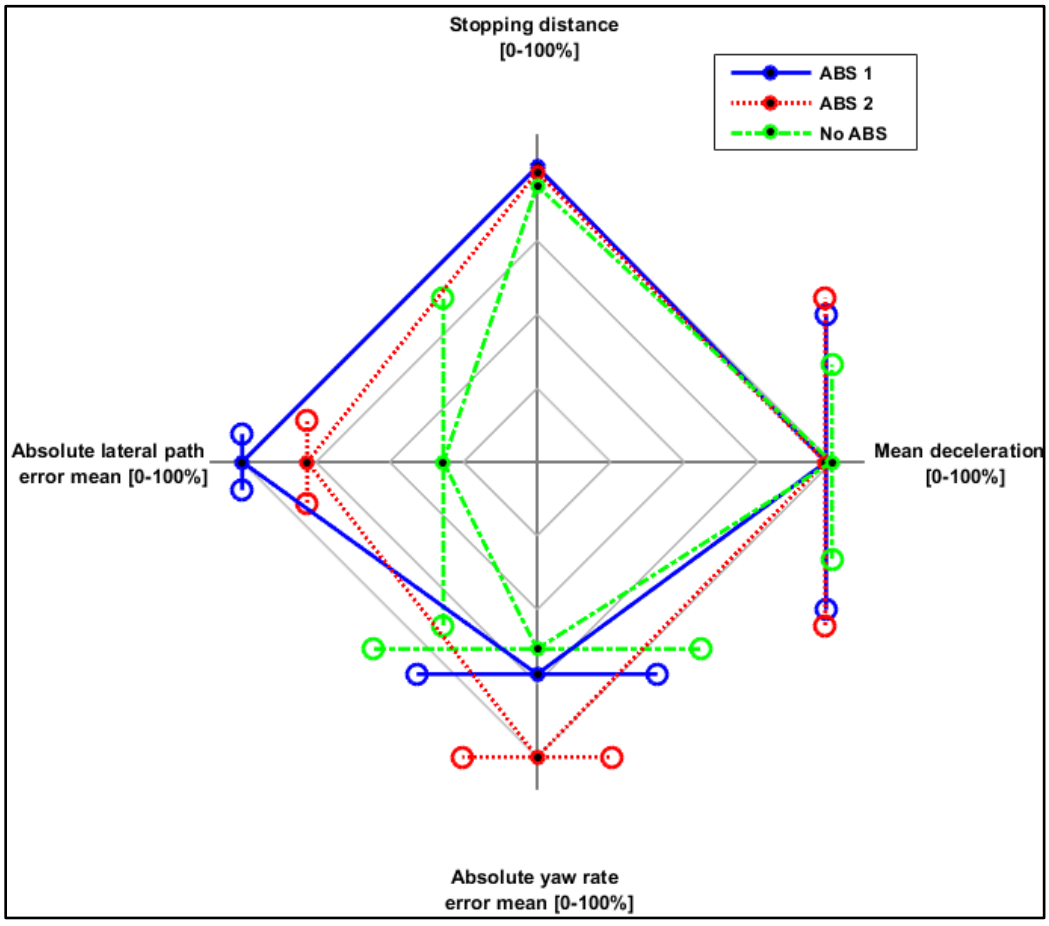

Figure 4-11 Comparing ABS performance for brake-in-turn on low friction surface

4.6.3 *Split-mu braking results*

Figure 4-12 shows the split-mu braking results. As is the case for the brake-in-turn simulations, the advantage of having ABS is evident on the split-mu surface. The yaw rate error of the vehicles equipped with ABS is negligible when compared to the yaw rate error of the vehicle without ABS. The ABS equipped vehicles also managed to stop in a shorter time than the vehicle without ABS.

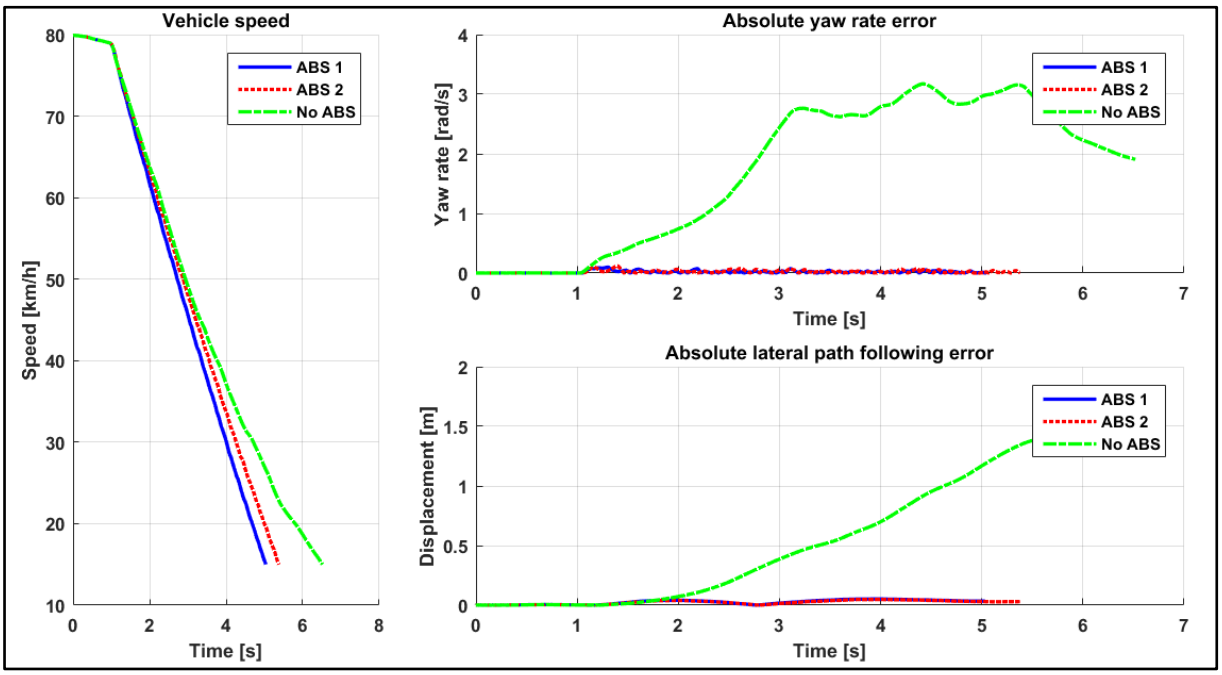

Figure 4-12 Split-mu braking results

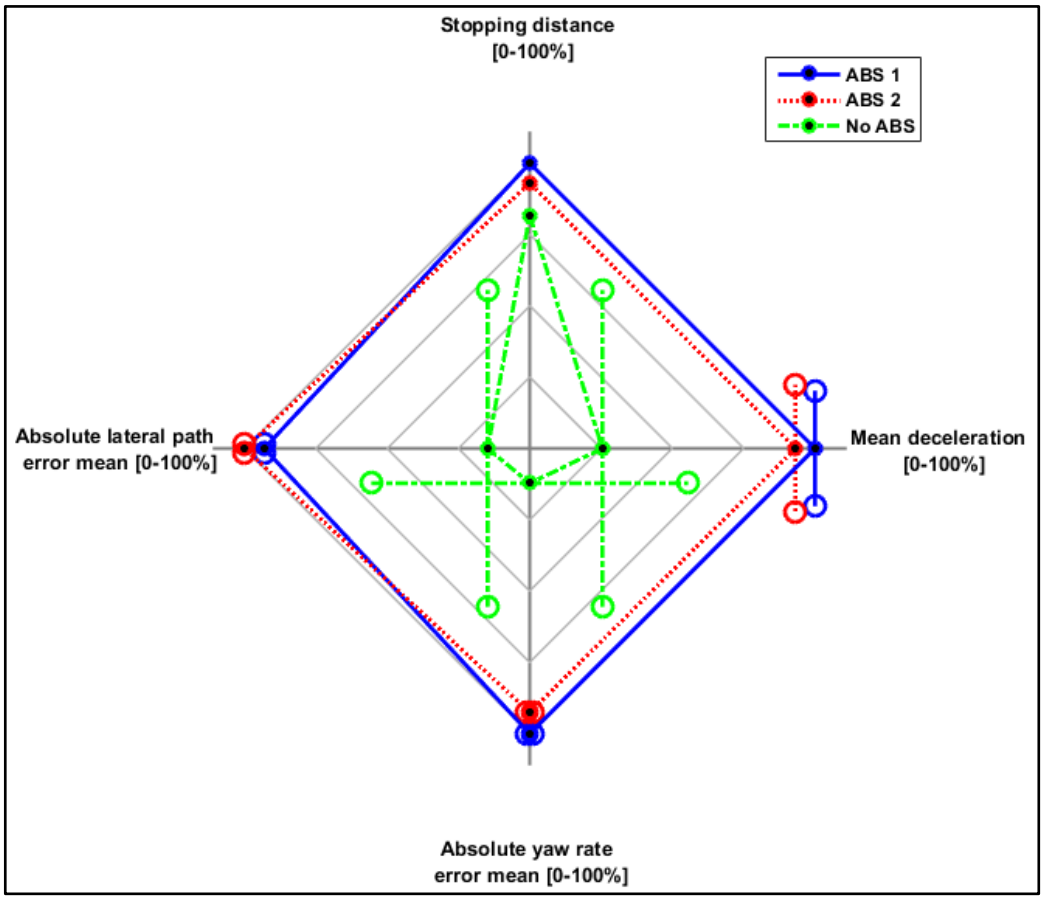

Figure 4-13 Comparing ABS performance on split-mu surface

Comparing the simulation results in Figure 4-13 shows the significant advantage ABS braking has under split-mu conditions. The ABS enabled simulations outperformed the conventional braking system significantly with all four the metrics investigated. Similarly, the variations in each of those metrics were significantly less for the ABS simulations compared to that of the conventional system.

4.6.4 *Discussion of the proposed performance evaluation technique*

The proposed performance evaluation technique provides a quick and concise way of comparing the braking performance of vehicles with different braking configurations. In many of the radar plots shown throughout Section 4.6, it is sometimes difficult to identify the ABS algorithm that performed the best. A contributing factor to this is that in all of the discussed cases, the ABS algorithms' performance was compared with a conventional braking system's performance. The advantage of using the proposed evaluation technique is that it scales the comparison of the variation for each metric automatically. To illustrate this, Figure 4-14 is a reproduction of Figure 4-13, but with the conventional brake system omitted from the comparison. It is clear in Figure 4-14 that ABS algorithm 1 outperforms ABS algorithm 2 in three of the four metrics, with the standard deviation of the mean deceleration and the absolute yaw rate mean error lower than that of ABS algorithm 2.

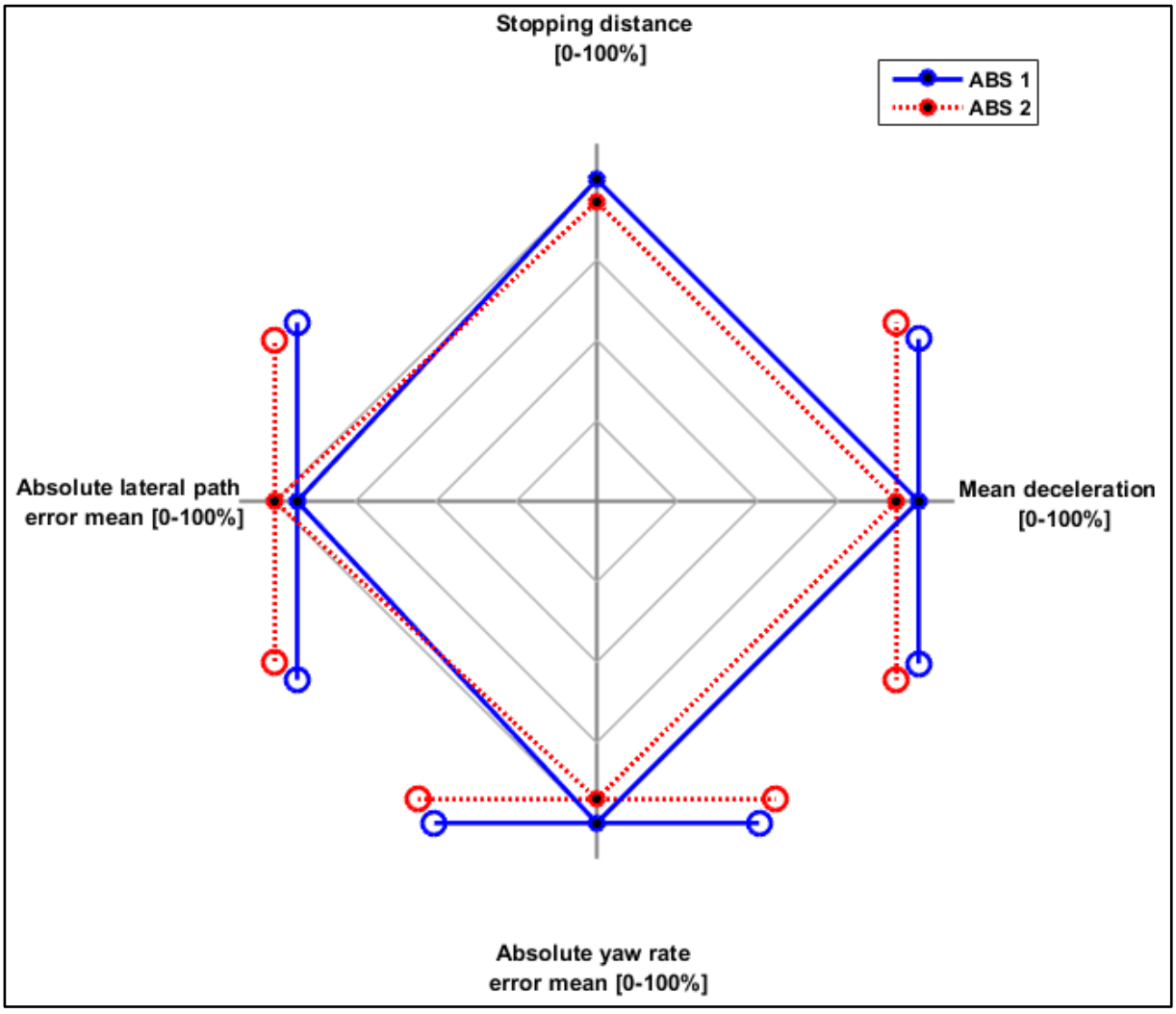

Figure 4-14 Comparison of ABS performance on split-mu surface

The performance evaluation technique was illustrated throughout Section 4.6 by comparing different braking system configurations' performance with one another for the same test. The same comparison technique can however be used for a single brake system

configuration, but with multiple tests compared on the same radar plot. This may give some insight into the braking performance of the brake system with different manoeuvres, but it is recommended that the surface friction coefficient of the tests compared on the same radar plot be kept close to one another. Failure to do so may result in unrealistic comparisons for all four metrics and their standard deviations.

Finally, the proposed evaluation technique is intended as a first step in the process of evaluating the performance of braking systems. It may be used to identify braking systems that perform inadequately when compared to the other systems the designer is considering. If it becomes difficult to decide which of the systems' performance is best, the designer is encouraged either to add additional metrics, or to delve deeper into the actual performance of the vehicle by investigating the test or simulation results in the time domain.

4.7 Application of performance evaluation technique on rough roads

To illustrate the application of the performance evaluation technique on rough roads, two simulations were run using the measured road profile of the Belgian paving shown in Section 3.2.1. Rather than modifying the ABS algorithm, the suspension configuration was changed. The vehicle model was braked from 80km/h with the suspension in the 'Ride Comfort' mode and with the suspension in the Handling mode. The simulation results are shown in Figure 4-15. The performance evaluation technique is applied to the simulation results and the comparison is shown in Figure 4-16.

The results shown in Figure 4-15 show that the stopping time is influenced by the suspension configuration. Although the Belgian paving is concrete and is simulated in a dry condition, the braking time is significantly longer compared to the results on the high friction smooth road shown in Figure 4-4. The comparison in Figure 4-16 shows that the 'Ride Comfort' suspension setting outperforms the Handling suspension setting on the Belgian paving when comparing stopping distance and average deceleration. The lateral path error and yaw rate error are very similar, as one would expect in a straight line brake simulation.

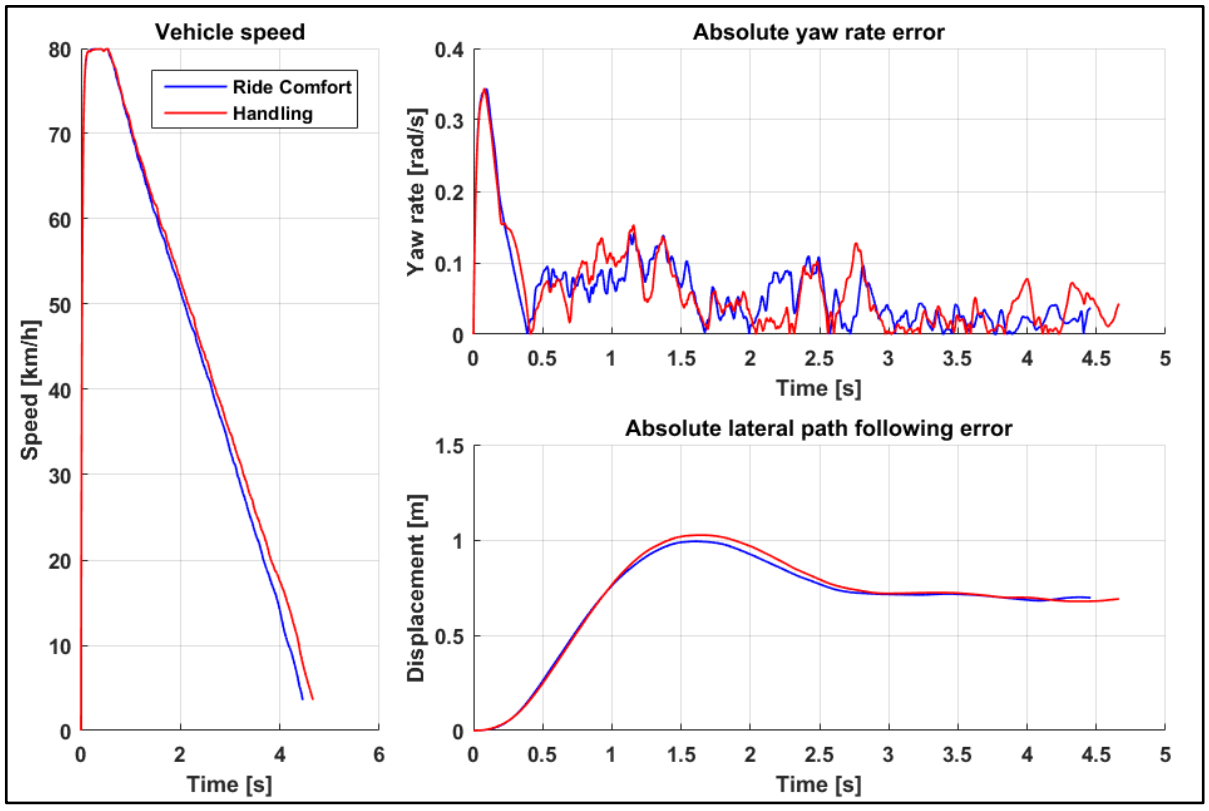

Figure 4-15 Belgian paving braking simulation results

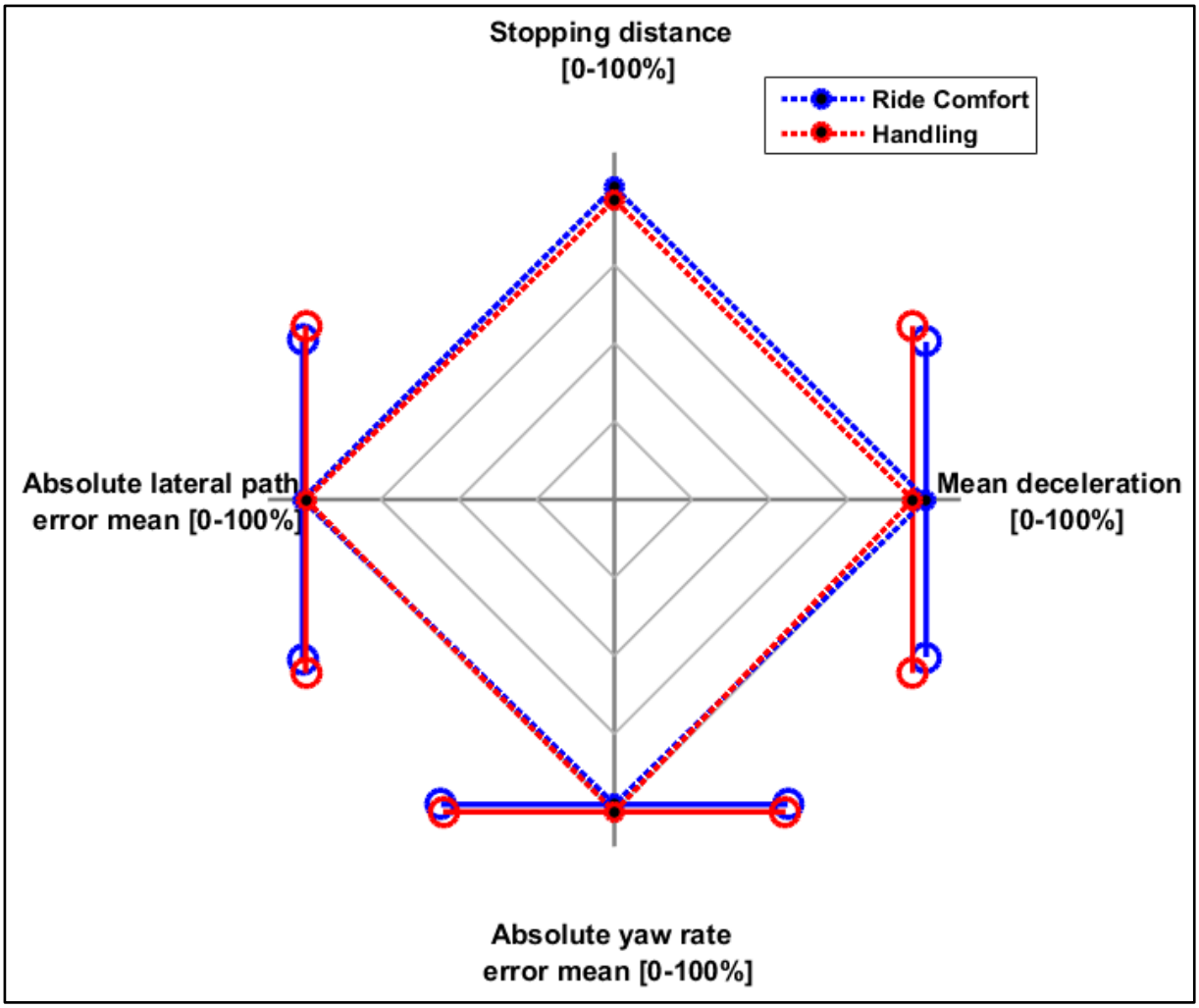

Figure 4-16 Comparison of ABS performance on Belgian paving

4.8 Conclusion

The aim of this chapter was to formulate an evaluation technique that can be used to clearly and concisely compare the performance of various antilock brake systems with one another taking both stopping ability and directional stability into account. An extensive literature review was performed and several examples of existing metrics used were critically discussed. The requirements as stipulated by SAE International was also investigated. The optimal utilisation of the friction available to the driver, as limited by the tyre's friction force generation characteristics, was discussed to illustrate the compromise that ABS aims to achieve optimally.

Five braking scenarios were chosen to represent the requirements of SAE International of ABS equipped vehicles on smooth roads. These five scenarios were simulated with two different ABS algorithms and with a vehicle equipped with a conventional brake system using an experimentally validated vehicle model. Significant differences in the performance of these systems were noted.

The proposed evaluation technique defined four metrics to evaluate the braking performance of a vehicle, namely:

a) Stopping distance and its standard deviation (if more than one test is carried out for the same algorithm)
b) Mean and standard deviation of vehicle deceleration during the braking manoeuvre

c) Mean and standard deviation of absolute vehicle yaw rate error during the braking manoeuvre
d) Mean and standard deviation of absolute lateral path following error during the braking manoeuvre

These metrics were normalised, with the best performing brake system for each metric being assigned a value of 100%. The metrics were then illustrated on a radar plot to enable quick and clear comparisons. The proposed evaluation technique provides a clear and logical method in which the performance of ABS algorithms can be compared on any road surface, be it smooth or rough, wet or dry.

4.9 Next steps

Question c) of the research questions in Section 2.3 has now been addressed. At this point, the investigation has all the tools needed to address the remaining research questions of Section 2.3. The first step at attempting to improve the braking performance of a vehicle on an undulating road is aimed at improving the inputs to the ABS control algorithm.

Chapter 5

ABS algorithm inputs

If you're not accurate, you'll cause untold trouble.

- David O. Selznick (1902–1965), American film producer

5.1 Introduction

The basic premise of any ABS control algorithm was discussed in Section 2.2.3. Of all the states the control engineer can measure on a vehicle, ABS algorithms base all their decisions on a single measurement and several assumptions. The brake pressure is modulated with pump, dump and hold states. The state of each brake is determined by the triggering of longitudinal slip and wheel angular acceleration thresholds. Both the longitudinal slip and wheel angular acceleration rely on the accurate measurement of wheel speed and knowledge of the tyre rolling radius.

Section 2.2.4 briefly discussed the influence of the rolling radius on the performance of ADAS systems that rely on the estimation of longitudinal tyre slip. The definitions of the kinematic and kinetic rolling radius of Section 2.2.4 are repeated here as Equations (5.1) and (5.2), respectively:

$$r_{kinematic} = distance\ travelled / total\ wheel\ rotation\ angle\ in\ radians \tag{5.1}$$

$$M_y = F_x r_{kinetic} \tag{5.2}$$

Upadhyaya et al. (1988), Kiss (2003) and Pacejka (2005) investigated the rolling radius of tyres when used in off-road conditions (Upadhyaya et al., 1988, Kiss, 2003) and over discrete obstacles (Pacejka, 2005). The investigations were however limited to quasi-static or low speed situations. The aim of this section is to investigate the rolling radius of a pneumatic tyre on both undulating and smooth hard roads and to look at the use of this rolling radius to determine longitudinal slip, specifically for application to ADAS systems intended for use on off-road vehicles such as SUVs. It was found that the overwhelming approach in the literature is to assume the rolling radius to be a constant parameter that can be determined under quasi-static conditions, but that there is little consensus among researchers as to how to define the rolling radius. Seldom is there a distinction made between a kinematic rolling radius, used to relate the kinematics of a rolling wheel, and a kinetic rolling radius, which is used to relate the kinetics of torques applied to a wheel and the resulting longitudinal forces.

The approach in this chapter is to evaluate the validity of some common assumptions relating to the rolling radius found in the scientific literature and then to propose some improved strategies to estimate the contact patch velocity and other related states and parameters.

5.1.1 *Kinematic rolling radius*

Before commencing with a detailed discussion on a pneumatic tyre rolling radius, it is important to define kinematics as opposed to kinetics. Kinematics is the branch of dynamics that describes the motion of particles or bodies by referring only to the displacements, velocities, and accelerations of those particles or bodies. Kinetics on the other hand is the study of the relations between unbalanced forces and moments and the resulting changes in motion (Meriam and Kraige, 2012).

The kinematic rolling radius of a tyre is used during the parameterisation and the simulation stages of longitudinal tyre modelling. The longitudinal force generating property of a tyre is usually parameterised as a function of longitudinal tyre slip (Gillespie, 1992). The longitudinal tyre slip is calculated with Equation (2.2), which is repeated as Equation (5.3) for the sake of continuity. Equation (5.4) defines the kinematic rolling radius

$$\lambda = \frac{|v - v_{cp}|}{v} \tag{5.3}$$

$$v_{cp} = \omega \times r_{kinematic}$$
$$\therefore r_{kinematic} = v_{cp}/\omega \tag{5.4}$$

5.1.1.1 Definition of zero conditions for kinematic rolling radius

The kinematic rolling radius in Equation (5.4) is assumed to be constant (the rigid disc assumption) and is defined under specified zero conditions. Two of the most common zero conditions are (Upadhyaya et al., 1988):

a) when there is a driving torque applied to propel the vehicle across a surface while delivering zero net traction, and
b) when the vehicle is pushed with zero axle torque. This is also the condition under which the Society of Automotive Engineers (SAE) defines the effective radius (Miller et al., 2001).

In both of these cases the kinematic rolling radius is defined with Equation (5.1) (Upadhyaya et al., 1988).

5.1.1.2 Problems with the definition of the kinematic rolling radius

The problem with kinematic rolling radius under quasi-static conditions, such as those described above, is that the tyre deforms when driving. This deformation is due to numerous factors, such as rough roads, load transfer during vehicle manoeuvres, wear, and excitation of the wheel hop frequency. Adcox et al. (2012) investigated the interaction between the tyre torsional dynamics and ABS control algorithms and found a significant increase in the stopping distance when the torsional dynamics were excited. It is possible that the reason for the increase in stopping distance is attributable to the definition of the rolling radius used to determine contact patch slip.

5.1.1.3 Challenges with measurement of the parameters and implementation

As shown in Equation (5.3), calculation of the longitudinal slip requires information of the vehicle speed (also known as the reference velocity) and the contact patch velocity. It is relatively easy to measure the reference velocity if a Global Positioning System (GPS) is fitted to the vehicle. A GPS is often not available on a commercial vehicle and typically has inadequate accuracy and sampling frequency or latency (delay) and hence the reference velocity is estimated from measured wheel speeds. Penny and Els (2016) discussed the use of an algorithm utilising the measured wheel speed and static rolling radius to estimate reference velocity.

The direct measurement of the contact patch velocity is even more complicated than measuring or estimating the reference velocity and as a result it is usually estimated. To estimate the contact patch velocity, it is commonly assumed that the wheel is a rigid body. The kinematic relationship given in Equation (5.4) is then used to calculate the contact patch velocity (Meriam and Kraige, 2012).

Measurement of the wheel speed is usually done with proximity switches and a pulse ring. This technique is universally implemented on commercial vehicles for ABS wheel speed measurement (Bosch, 2005).

The torsional dynamics of the tyre may contribute to a significant error when assuming the wheel is a single rigid body and measuring wheel speed on the wheel hub (Botha et al., 2015). This is especially true for soft, high aspect ratio tyres often used on off-road vehicles with coarse tread patterns and low inflation pressures. An alternative method for measuring the longitudinal slip of a tyre directly, using Digital Image Correlation (DIC), was proposed by Botha and Els (2014).

Care must also be taken when choosing a wheel speed filtering approach (Adcox et al., 2012, Penny and Els, 2016), especially on rough terrains. Delays (latency) in the wheel speed measurement may significantly influence the performance of ABS systems. Sensor vibration on rough terrains may also have a detrimental effect on the wheel speed measurement and control system designers are encouraged to ensure the rigidity of the sensor and elimination of its resonant frequencies. Errors may also be introduced when the tyres are used at different inflation pressures, different tyre brands are used, or when there is significant tread wear present on the tyres.

5.1.2 *Kinetic rolling radius*

The kinetic rolling radius is used to convert applied torque (either through applying friction brakes or torque from the drive shaft) to an effective longitudinal force, Figure 5-1 shows a combined free body and kinetic diagram of the forces and moments acting on a wheel with a pneumatic tyre (from Equation (5.6)). The moment induced by the vertical force acting an offset distance from the geometric centre of the wheel is assumed to be the rolling resistance, as defined by Gillespie (1992). Further rolling resistance effects may be attributed to rubber hysteresis effects, but these effects are lumped into the $F_z\rho_{rr}$ term. Also indicated in Figure 5-1 are the angular velocity and wheel centre velocity of Equations (5.3) and (5.4). By considering the wheel rotating about the axle, the system reduces to planar motion and Euler's extension of Newton's Second Law from particles to rigid bodies (Equation (5.5)) may be used (Meriam and Kraige, 2012). .

$$\sum M_O = I_O\alpha \tag{5.5}$$

$$\begin{aligned} &F_x r_{kinetic} - F_z\rho_{rr} - M_y = I_O\alpha \\ &\therefore r_{kinetic} = \frac{I_O\alpha + F_z\rho_{rr} + M_y}{F_x} \end{aligned} \tag{5.6}$$

This rolling radius is thus a kinetic relationship and not the same as the kinematic rolling radius used in Equation (5.4). The kinetic rolling radius is generally not used explicitly in ABS algorithms, but is often used in simplified tyre models when simulating ABS braking.

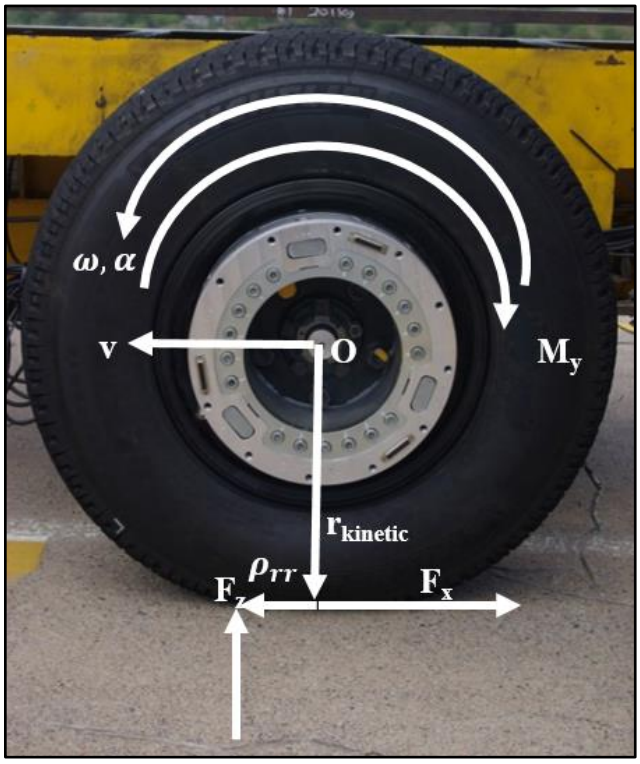

Figure 5-1 Forces and moments acting on a braked tyre

5.1.3 *Approach*

The first step in the investigation is to compare the kinematic and the kinetic rolling radius. The following research questions are investigated:

a) How does the dynamic kinematic rolling radius measured experimentally compare with the static kinematic rolling radius defined under the abovementioned zero-conditions?
b) Is it valid to use a static or quasi-static definition of the rolling radius to determine contact patch velocity?
c) Can the wheel be approximated as a rigid body so that the kinetic rolling radius can be used to convert the applied brake torque to the applied brake force?

An experimental setup that uses a wheel force transducer to measure the applied forces and moments (to determine the kinetic rolling radius) and a dual-camera vision-based measurement system that measures the contact patch velocity (to determine the kinematic rolling radius) was developed in an attempt to answer these research questions. The tests were conducted on the Land Rover Defender braking on a smooth paved road and on the Belgian paving at Gerotek Test Facilities (Armscor Defence Institutes SOC, 2016). The experimental results thus include the effects that would be experienced by the tyre in a real world situation and not laboratory conditions.

5.2 Experimental setup

From Equations (5.3), (5.4) and (5.6), it is evident that the following states need to be measured in order to determine the two roll radii of interest:

a) Wheel angular velocity and angular acceleration
b) Longitudinal velocity of wheel centre
c) The forces and moments acting on the wheel

In addition to the abovementioned states, the mass and inertia parameters are also required. The Michelin LTX A/T2 235/85R16 (Michelin, 2016) has a measured mass of 19kg and inertia

about the spin axis of 3.1 kg.m^2, including the rim. All the tests were performed at 200kPa tyre pressure on the front left tyre of the vehicle. Data was recorded while the vehicle was braked from approximately 45km/h on both a smooth road and a Belgian Paving test track. The tests were repeated several times to confirm repeatability. Data acquisitioning was performed on a Helios Single Board Computer (Diamond Systems Corporation, 2016) (from this point on referred to simply as the Data Acquisitioning System or DAQ) at a sampling rate of 1000Hz. The experimental setup is shown in Figure 5-2.

To compare the kinematic rolling radius of definition (b) of Section 5.1.1 with the kinematic rolling radius experienced during a braking test, Equation (5.4) is rearranged as shown in Equation (5.7):

$$r_{kinematic} = \frac{v_{CP}}{\omega} \tag{5.7}$$

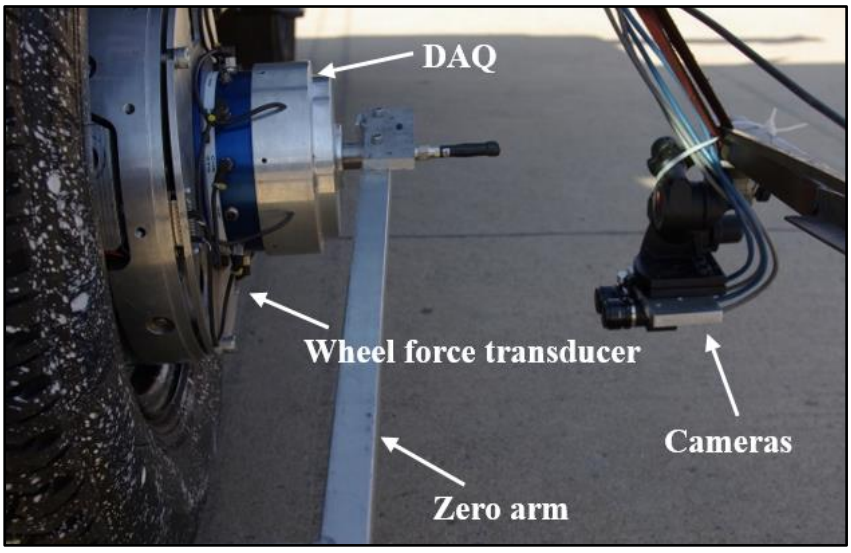

Figure 5-2 Experimental setup

From Equation (5.7) it is evident that contact patch velocity and wheel angular velocity are to be measured to determine the kinematic rolling radius. Wheel angular velocity is measured with inductive proximity switches. Sixty (60) indentations were machined in the brake disc. When the wheel rotates, a square wave related to the angular velocity of the wheel is generated and converted to a voltage with a frequency to voltage converter. A disadvantage of this measurement approach to angular velocity is possible poor performance at lower angular velocities and high angular acceleration (e.g. at wheel lockup). The frequency to voltage converter may also introduce a slight delay in the measurement. Vehicle speed was measured with a NovAtel SPAN-CPT Single Enclosure GNSS/INS Receiver (NovAtel Inc., n.d.). The SPAN-CPT makes use of both the GPS and GLONASS systems (NovAtel Inc., n.d.).

The contact patch velocity, v_{CP}, is measured directly using Digital Image Correlation (DIC) (Botha and Els, 2014). DIC is a mathematical measurement technique used to track changes in an image. There are several algorithms available, but the basic approach remains the same. Regions in successive images are matched, effectively tracking these regions. These regions are often simplified to several key points. Initially key points are identified using their uniqueness and ease of tracking from one image to the next. After identifying these key points, they are matched from one image to the next. There are several feature descriptors in the literature, the Scale-Invariant Feature Transform (SIFT) feature descriptor is used in this study (Botha and Els, 2014, Lowe, 2004). The SIFT algorithm finds unique points in an image. It identifies these key points using a feature vector which describes local

gradients around each key point. These feature vectors are used to identify the key points in different images and therefore allows them to be tracked across images, as shown in Figure 5-3. A time sequence of images is then recorded at a predefined frequency. Thus, if points are tracked across consecutive images the velocity of these points can also be determined.

A calibrated two-camera setup was mounted on the outside of the left front wheel of the test vehicle (see Figure 5-2). The two-camera system is capable of measuring 3D geometry. However, this requires textured surfaces to be able to match features between the two different camera views. The road surface normally contains sufficient texture, but the tyre normally has a monotonous colour and thus few features to track. Texture was added by spraying the sidewall of the tyre with white paint or using a white marker to make arbitrary marks or spots as can be seen in Figure 5-3.

Points are tracked over an area encompassing both the tyre and road. The interface between the tyre and road are first determined. Points that lie below this interface are classified as points on the road. Points above and close to the interface are classified as tyre points. A Random Sample Consensus (RANSAC) algorithm (Fischler and Bolles, 1981) is used to determine the average velocities of the tyre and road using all points, while removing outliers.

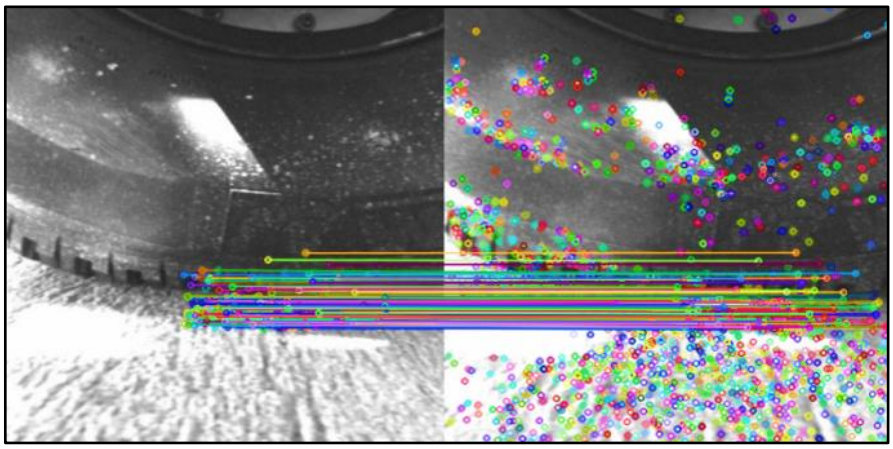

Figure 5-3 Tracking key points in the contact patch across two consecutive frames

This allows for the linear velocity of the tyre at the contact patch and vehicle speed to be measured directly, thus enabling the rolling radius to be determined from Equation (5.7). The camera frames are synchronised with the other captured data using trigger pulses. A frame is taken at half the frequency of the other captured data (due to the physical limitations of the cameras). This allows the camera data to be easily synchronised with other measurements.

Figure 5-4 shows the result of the classification algorithm applied to the DIC data in 2D format. A 3D format image containing the clustering results is shown in Figure 5-5. Points classified as lying on the tyre are indicated as green and points on the road are blue. The remaining points are classified as outliers and are magenta and cyan. This shows that the algorithm classifies the points correctly with no errors in either the tyre or road set.

To calculate the kinetic rolling radius used in the force balance in Equation (5.6), the wheel forces and moments shown in Figure 5-1 need to be measured along with the wheel's angular acceleration. A wheel force transducer (WFT) developed by Becker and Els (2012) was used to measure the forces and moments acting on the wheel. The WFT consists of six single component load cells arranged in the rim of the wheel. The wheel's rotation angle is measured with an encoder that is held stationary with a zero arm, attached to the vehicle axle. The wheel rotation angle is used to convert the forces measured by the single

component load cells to forces and moments oriented along the tyre coordinate system. The static wheel load was approximately 650kg. The measured wheel angular velocity's time derivative is used to calculate wheel angular acceleration.

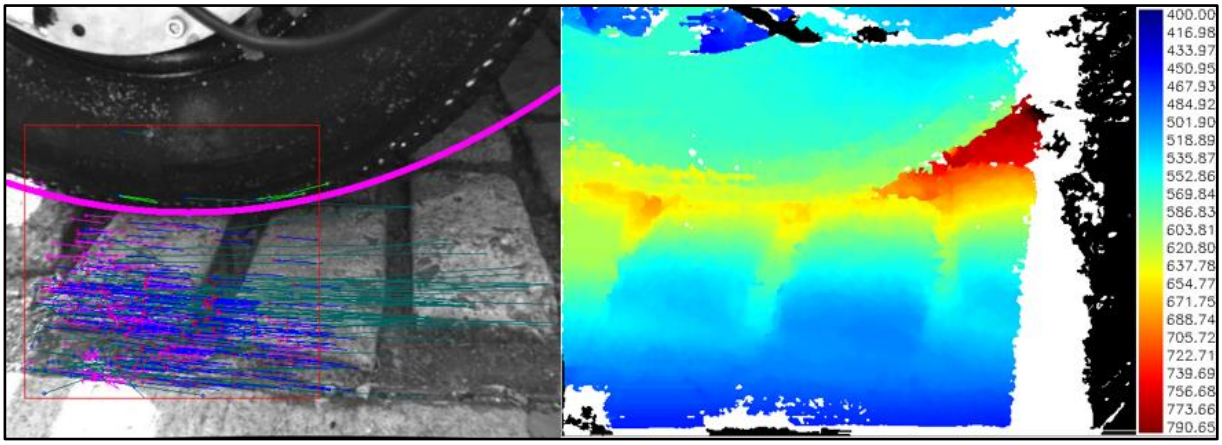

Figure 5-4 Clustering of key points into ground and outlier points in the 2D image. The colour scale indicates distance from cameras.

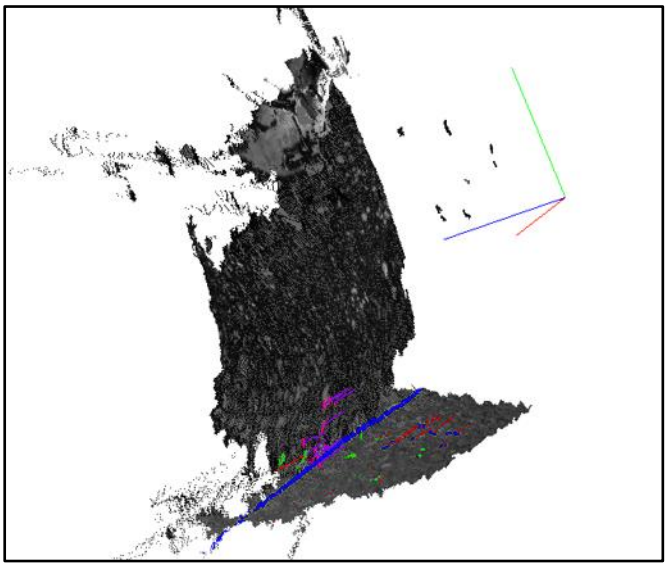

Figure 5-5 Clustering of points into tyre, ground and outlier points in a 3D point cloud

The WFT data is captured on a DAQ that is mounted to the WFT. Two DAQs are thus used, one in the vehicle that measures wheel and vehicle speed and the other mounted to the WFT. A trigger pulse is generated by the DAQ on the vehicle. The trigger pulse is used to synchronise the data sets captured on the two DAQs and the camera images.

5.3 Experimental results

The experimental results for both the kinematic and kinetic roll radii are now discussed.

5.3.1 *Kinematic rolling radius*

The zero condition definition of Section 5.1.1.1 (b) is used to determine the kinematic rolling radius under quasi-static conditions. This kinematic rolling radius is used as the benchmark for comparative purposes. A mark is made on the ground directly below the wheel centre on the road and on the tyre and the vehicle is pushed until the wheel has made a full rotation and another mark is made on the road. The distance between the two marks is then measured and the kinematic rolling radius defined by Equation (5.1) is calculated. This benchmark kinematic rolling radius was found to be 0.3875m.

The kinematic rolling radius is calculated with Equation (5.7) and the results for braking on a smooth road from 12m/s are shown in Figure 5-6. In Figure 5-6(a) the vehicle speed as measured with a GPS is compared to the speed as measured with the cameras and a close correlation is evident. The DIC technique therefore accurately measures road speed. Figure 5-6(b) shows the kinematic rolling radius as calculated with Equation (5.7) from the DIC data.

Figure 5-7 indicates the kinematic rolling radius while braking on the Belgian Paving. From Figure 5-6 and Figure 5-7 it may be seen that the rolling radius reduces towards the end of the test run and eventually becomes zero, which is an unrealistic value. Some of the initial reduction in rolling radius may be due to load transfer during braking. Further reduction in the rolling radius is a numerical issue. This is due to Equation (5.7), where a small contact patch velocity will reduce the result of Equation (5.7) to zero. At these low speeds, a small, unaccounted delay error in the frequency to voltage converter may also significantly influence the results.

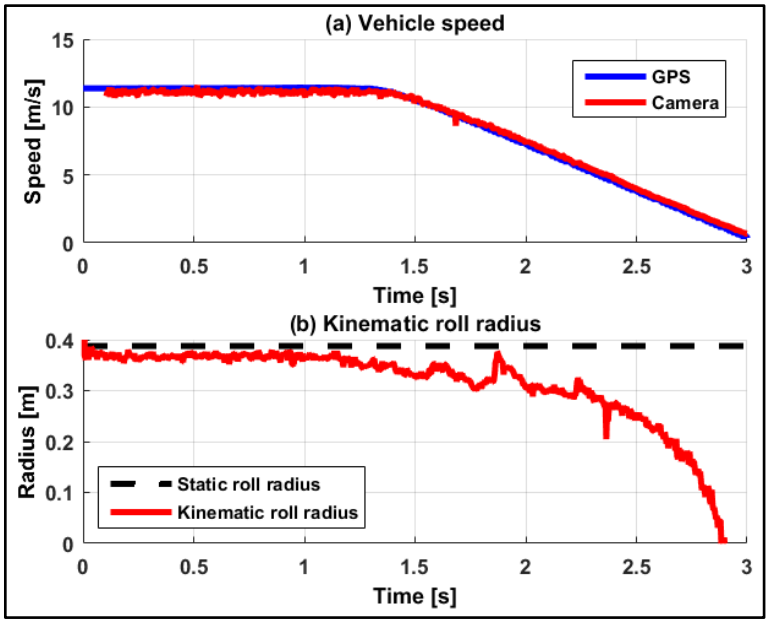

Figure 5-6 (a) Vehicle speed comparison as measured with a GPS and the DIC technique and (b) the calculated kinematic rolling radius on a smooth road

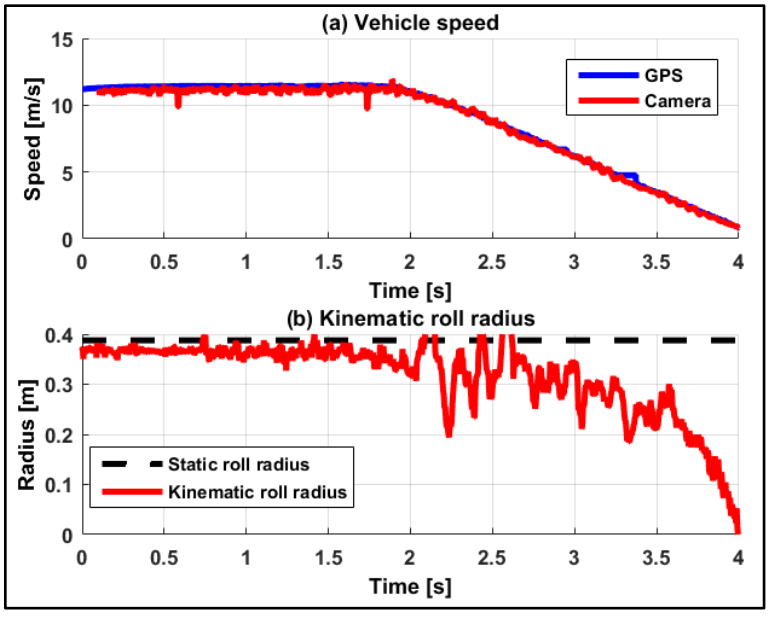

Figure 5-7 (a) Vehicle speed comparison as measured with a GPS and the DIC technique and (b) the calculated kinematic rolling radius on Belgian paving

Rather than comparing the kinematic rolling radius as shown in Figure 5-6 and Figure 5-7, Figure 5-8a compares the contact patch velocity calculated with Equation (5.4) and Figure 5-8b shows the absolute error between the measured and estimated contact patch velocity. As stated in the Section 5.1, Equation (5.4) relies on assuming the wheel to be a rigid body. Figure 5-8 indicates that the contact patch velocity, predicted by Equation (5.4), is a good approximation when compared to the velocity measured with DIC, with the error less than 1m/s for the duration of the test on the smooth road. Defining the rolling radius with definition b) in Section 5.1.1 gives an accurate and smooth result. On the Belgian paving (shown in Figure 5-9), however, a more noticeable difference is observed between the contact patch velocity as estimated with Equation (5.4) and the DIC measured contact patch velocity. There are significant differences between the DIC measured contact patch velocity and that of Equation (5.4) when looking at the peaks between 2 and 3 seconds in Figure 5-9a. This filtering effect may be due to the filtering of the wheel speed signal present during the frequency to voltage conversion and may account for the poor performance of ADAS systems on rough roads. The absolute difference between the measured and estimated contact patch velocity on the Belgian paving, shown in Figure 5-9b, is however less than 2m/s, even for the portion of the test where the wheel starts slipping significantly.

An example of the error made by using definition b) in Section 5.1.1 to define the kinematic rolling radius is clearly visible in Figure 5-8 and Figure 5-9. During the first portion of both figures, before braking commences, the contact patch velocity calculated with Equation (5.4) gives a higher speed than the DIC measured contact patch velocity. Since Equation (5.4) is a linear relationship, the error margin will increase at higher speeds and significant errors may be made. Using definition b) in Section 5.1.1.1 to define the kinematic rolling radius does not take tyre wear, different inflation pressures, and the weight transfer of the vehicle into account. However, the error between the contact patch velocity measurement with the stereovision cameras and the estimation with zero condition definition b) is not as large as expected.

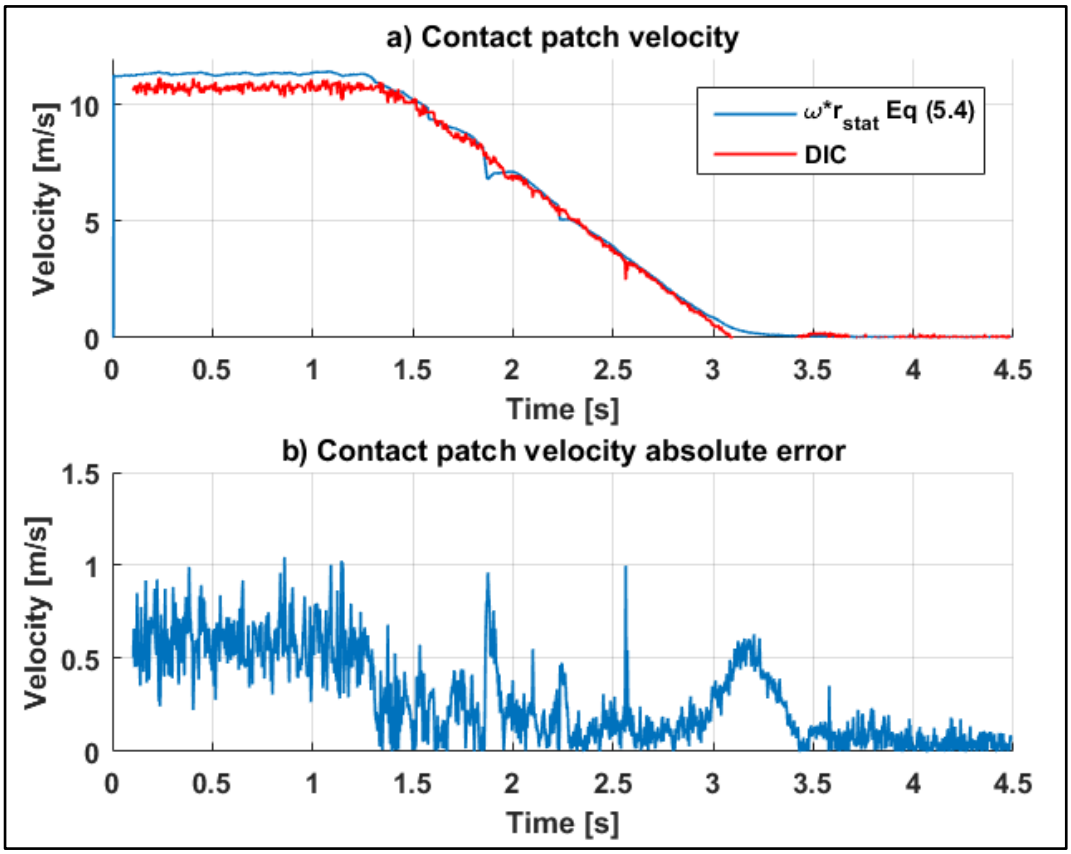

Figure 5-8 Contact patch velocity on a smooth road

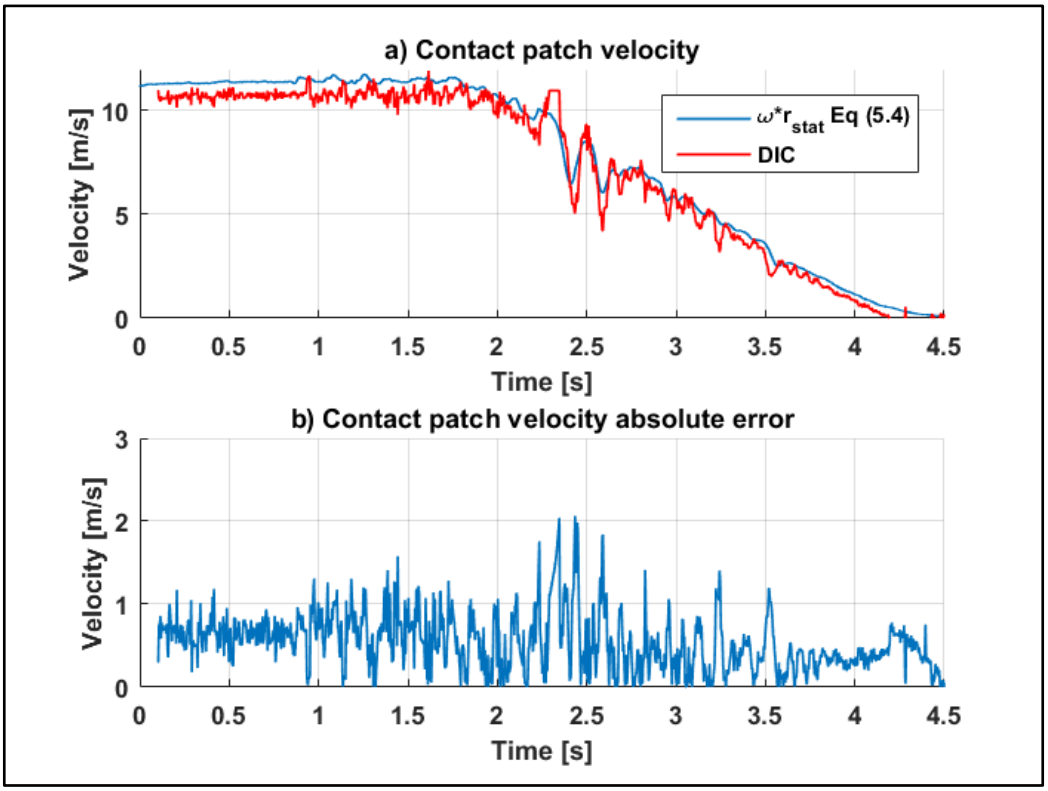

Figure 5-9 Contact patch velocity on Belgian paving

5.3.2 *Kinetic rolling radius*

Figure 5-10 shows the resulting brake force and moment and the corresponding vehicle speed for a test run on the Belgian paving. Initially, for the first second, the variation in vertical force is small, seen in Figure 5-10a). The variation then suddenly increases as the vehicle drives from the run-up area, which is smooth concrete, onto the undulating Belgian paving. Instants when ground contact is lost may be seen when the vertical force reduces to zero. At approximately two seconds, the brake torque is increased (Figure 5-10b) and a corresponding increase in the longitudinal force and brake torque can be seen. At this stage, the vehicle speed starts to decrease.

The kinetic rolling radius of the wheel was calculated by rearranging Equation (5.6) as:

$$\therefore r_{kinetic} = \frac{I_O \alpha + F_z \rho_{rr} + M_y}{F_x} \tag{5.8}$$

The rolling resistance included in the $F_z\rho$ term was determined by measuring the moment about the wheel axle when performing a coast-down test while the vehicle was not in gear. The coast-down tests were performed on both the smooth road and on the Belgian Paving and the root mean square (RMS) of the rolling resistance moment was calculated. The RMS rolling resistance moment was included as the $F_z\rho$ term in Equation (5.8). Table 5-1 shows the RMS rolling resistance moments.

Table 5-1 RMS rolling resistance on smooth road and Belgian paving

ROAD	RMS ROLLING RESISTANCE [N.m]
Smooth road	18.1
Belgian paving	38.0

The resulting kinetic rolling radius is shown in Figure 5-11 and it immediately becomes evident that the rigid disc (or rigid body) assumption allowing the use of Equation (5.8) is invalid. Bearing in mind that the tyre has dimensions 235/85R16 (and thus a maximum unloaded diameter of 805.9mm), the kinetic rolling radius is not expected to exceed 403mm.

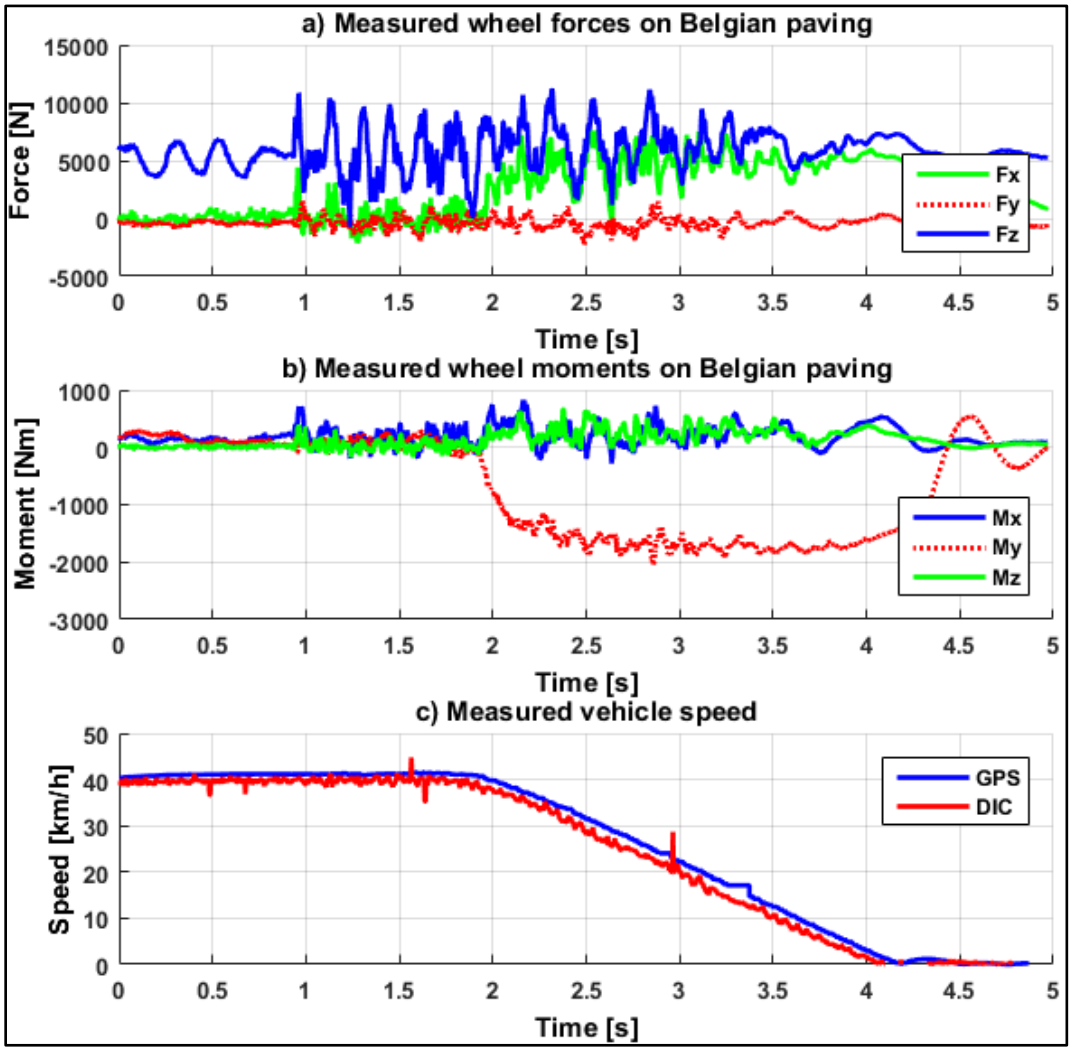

Figure 5-10 Measured forces (a), moments (b) and vehicle speed (c) on Belgian Paving

The tyre is fitted to a 16" rim, which means the rim radius is at 0.203m and rolling radius values below that indicates contact between the rim and the road surface and tyre damage should occur. This did not happen. Even on the smooth road, the kinetic rolling radius lies almost exclusively above 400mm. On the Belgian paving Equation (5.7) becomes unstable since the measured brake force is sometimes very close to zero as the tyre traverses the cobblestones. Additional noise is added to the system because the angular acceleration of the wheel was not measured and α has to be derived from the measured angular velocity. It is evident that the assumption of a rigid disc to approximate the forces acting on a wheel is invalid under these conditions.

To improve the kinetic rolling radius results, the measured forces, moments and wheel angular acceleration were zero-phase filtered with a 50Hz low pass Butterworth filter. Zero-phase filtering processes the input data in both the forward and reverse directions, resulting in zero-phase distortion. Butterworth filters have a magnitude response that is maximally flat in the passband and monotonic overall. A compromise between this smoothness and the roll-off steepness results in reduced roll-off steepness. 50Hz was chosen as a cut-off frequency, because it is known that the tyre natural frequencies of interest lie below this cut-off frequency (wheel hop frequency is typically at about 15Hz and the tyre torsional frequency without preload on the tyre is known to lie at 28.4Hz, measured by Bosch et al. (2016)). Filtering markedly improved the kinetic rolling radius estimate on the smooth road, but it had a negligible effect on the results on the Belgian paving. The filtered results are also indicated in Figure 5-11 and Figure 5-12. The filtering still did not improve the kinetic rolling radius results sufficiently to justify the use of a rigid disc to model the tyre.

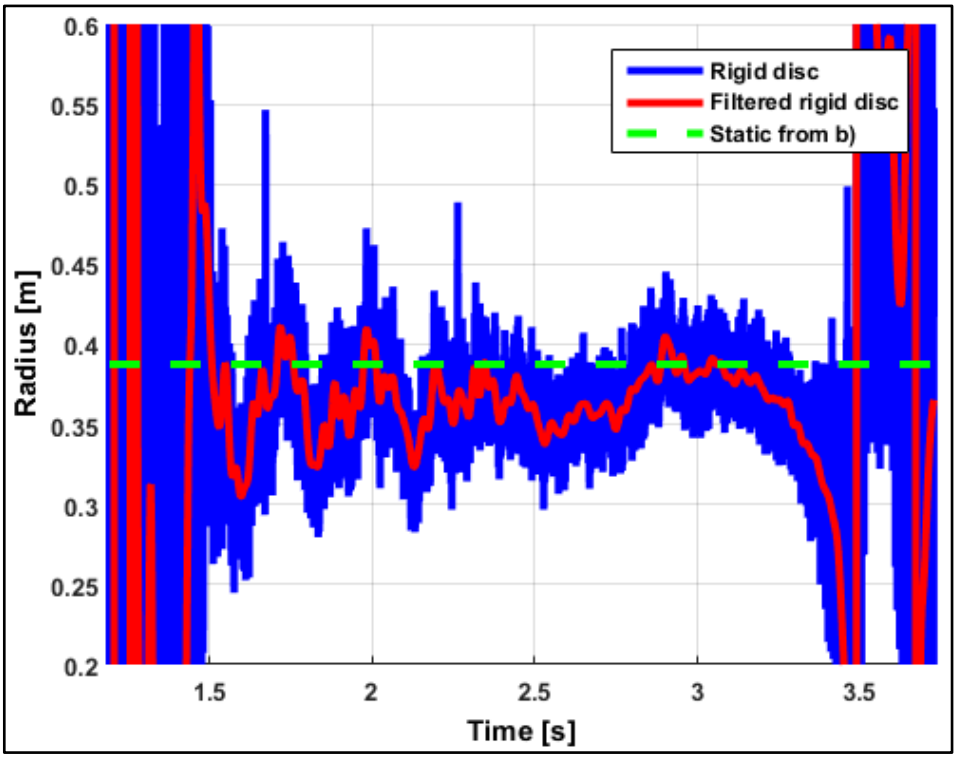

Figure 5-11 Rigid body calculation of kinetic rolling radius on smooth road (Note that only the braking portion of the test run is shown)

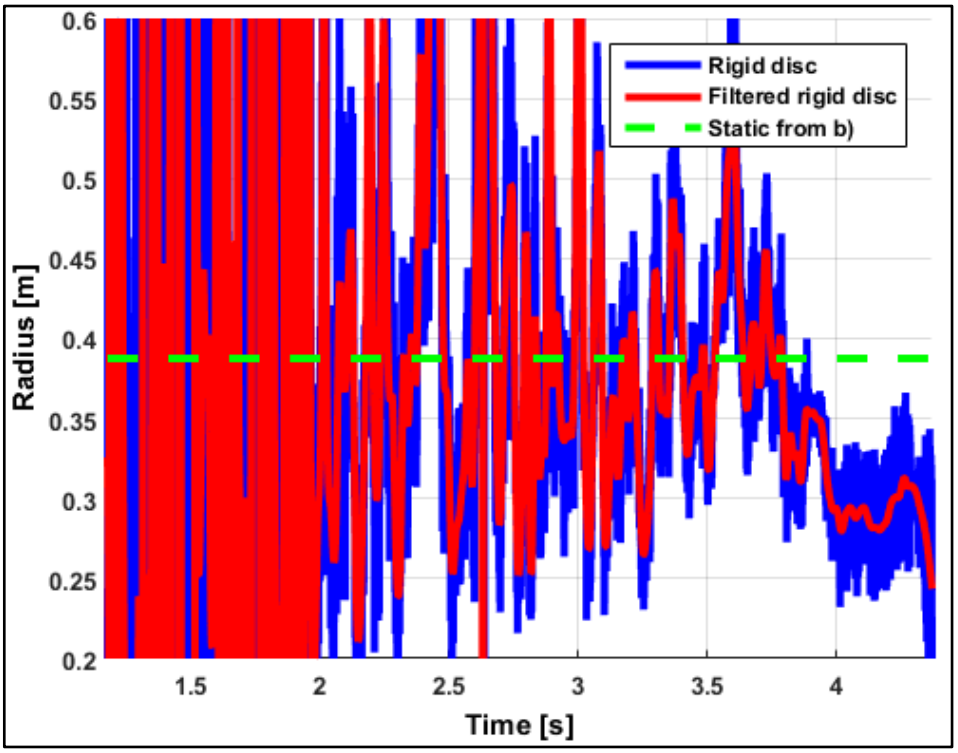

Figure 5-12 Rigid body calculation of rolling radius on Belgian paving (Note that only the braking portion of the test run is shown)

Figure 5-13 and Figure 5-14 show the Fast Fourier Transform (FFT) magnitudes for the vertical and longitudinal tyre force and brake moment on the smooth road and the Belgian Paving, respectively. When comparing the results shown in Figure 5-13 and Figure 5-14 it becomes evident that the frequency content excited by the Belgian Paving is significantly more than on the smooth road, as expected. A definite peak is seen in the vertical tyre

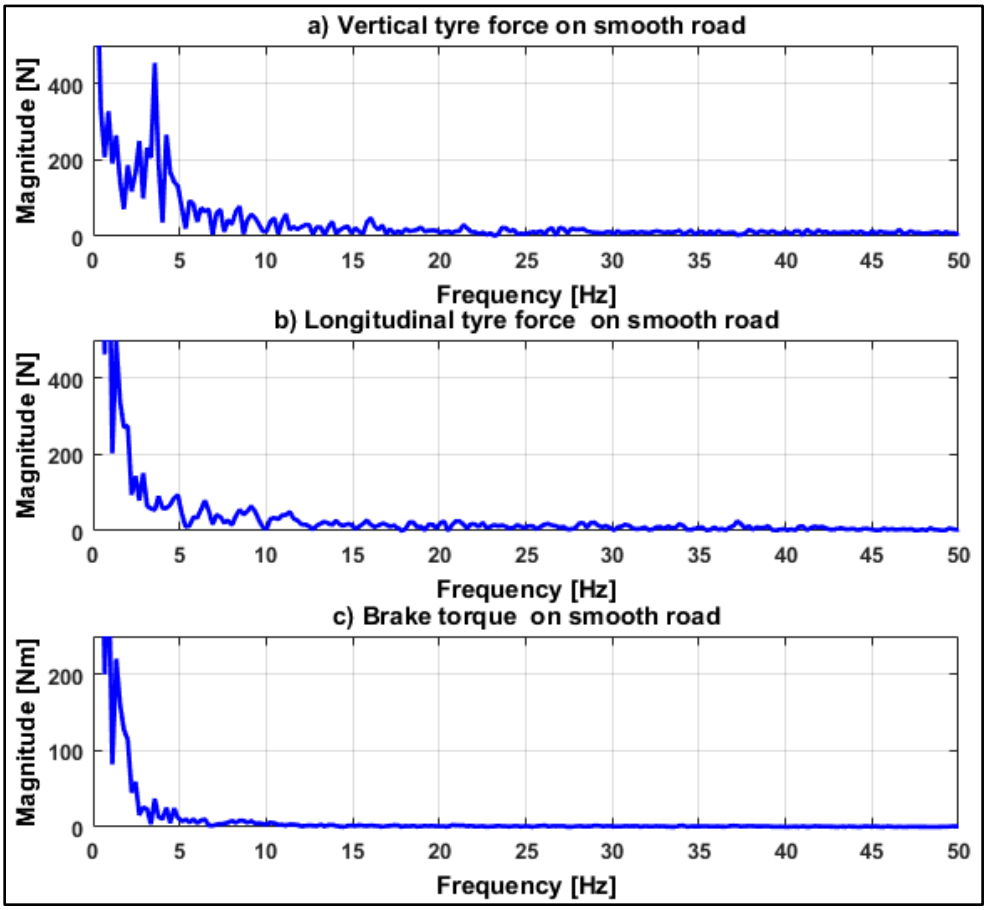

Figure 5-13 FFT magnitudes of measured forces on smooth road

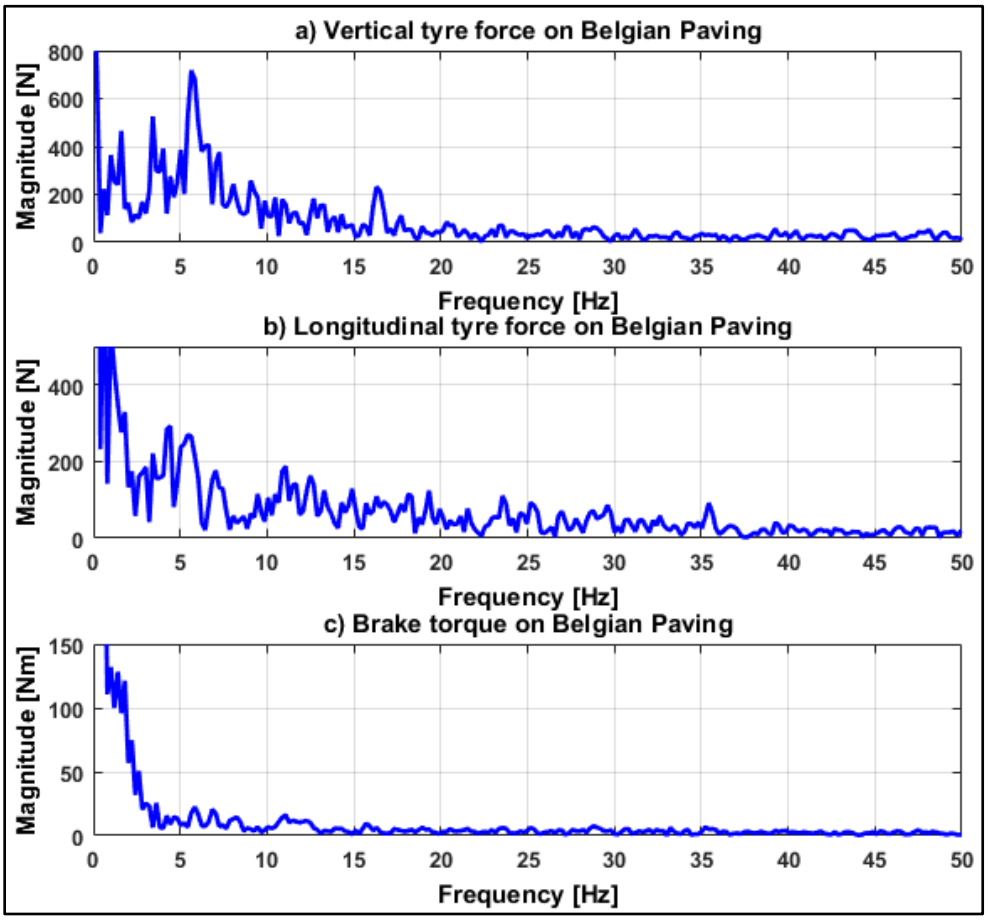

Figure 5-14 FFT magnitudes of measured forces on Belgian Paving

force on the smooth road at approximately 4Hz. This corresponds to the pitch natural frequency of the vehicle and hence the load transfer between front and rear axles during braking. The same peak at 4Hz is present in Figure 5-14, but an additional peak is seen at 5.6Hz. The peak at 5.6Hz was evident on all the runs on the Belgian Paving, but not on the smooth road. It may thus be concluded that the 5.6Hz peak was excited by the terrain input, but that the 4Hz peak is independent of the terrain. In Figure 5-13 and Figure 5-14 a small peak may be seen at 16Hz, this corresponds to the wheel hop natural frequency. There is some evidence of a peak at around 35Hz on the longitudinal tyre force FFT magnitudes. This corresponds with the tyre's torsional natural frequency and justifies the use of 50Hz as a low-pass filtering cut-off frequency.

The dynamic behaviour of the tyre under dynamic conditions renders the rigid disk assumption for the kinetic definition of the roll radius invalid. This can lead to the underperformance of ADAS systems that rely on the constant rolling radius assumption.

5.4 Conclusions

The aim of this chapter was to determine the validity of using constant kinematic and kinetic roll radii of a pneumatic tyre on both undulating and smooth hard roads. The overwhelming approach in the literature is to assume the rolling radius to be a constant parameter that can be determined under quasi-static conditions. No distinction is made between a kinematic rolling radius, used to relate the kinematics of a rolling wheel, and a kinetic rolling radius, which is used to relate the kinetics of torques applied to a wheel and the resulting longitudinal forces. To answer the research questions posed in Section 5.1.3:

a) How does the dynamic kinematic rolling radius measured experimentally compare with the static kinematic rolling radius defined under the abovementioned zero-conditions? Is it safe to use a static or quasi-static definition of the rolling radius to determine contact patch velocity?

The rolling radius defined by Equation (5.1), under the condition of zero applied torque, is a valid assumption when used on a smooth, hard road surface. It may be used to estimate contact patch velocity and thus longitudinal slip under these conditions. This conclusion is supported by the success of modern driver assist systems, such as traction control and ABS, when driving on smooth hard roads.

The rolling radius defined by Equation (5.1) gives acceptable results when used to estimate contact patch velocity on hard, undulating surfaces such as a Belgian paving. There are some differences in the peaks contact patch velocity as seen in Figure 5-9. This may contribute to the poor performance of ADAS systems on rough roads. Some signal conditioning and filtering may be necessary for the wheel speed measurement that may account for the differences in the peak values.

It must however be noted that the contact patch velocity determined with the static rolling radius gives acceptable results on the rough road, with an absolute error of less than 2m/s on the Belgian paving, and thus does not fully explain why ABS algorithms' performance deteriorates when active on a rough road. The reduction in performance of these systems must thus also be attributed to other physical phenomena, probably associated with the tyre transient behaviour. Another possible explanation is given by Adcox et al. (2012) . Their investigation looked at the filtering (specifically the cut-off frequency of a low pass filter) of the wheel speed signal that is used to determine the wheel's angular acceleration. ABS algorithms often use both longitudinal slip thresholds and angular acceleration thresholds to modulate brake pressure. It is possible that the noise induced by deriving angular acceleration form wheel speed and the filtering of the wheel speed that is required has a larger influence on the ABS algorithm's performance than originally expected. The

reference velocity used to determine the wheel slip is also determined from the wheel speeds. Improving the wheel speed measurement on rough roads may also provide the ABS algorithm with more reliable inputs.

b) Can the wheel be approximated as a rigid body so that the kinetic rolling radius can be used to convert the applied brake torque to the applied brake force?

The assumption that the wheel is a rigid disc is invalid when converting an applied torque to a generated longitudinal force, even on a smooth road. The dynamics of the tyre need to be taken into account. This explains the poor performance seen by single point-follower contact methods employed by many semi-empirical tyre models when simulating tyres on rough roads. Zero-phase low-pass filtering the measured tyre forces and brake moment improved the kinetic rolling radius calculation, but not sufficiently to justify the assumption that the wheel may be approximated as a rigid disc.

A frequency domain analysis was performed and several observations were made. The vehicle's pitch natural frequency is at approximately 4Hz and is excited during braking on any hard terrain. The wheel hop natural frequency may also be seen in the FFT magnitude of the vertical tyre force at 16Hz. A small peak in the 35 to 40Hz range was seen on the longitudinal tyre force FFT magnitude plots; this corresponds to the tyre's torsional natural frequency.

It is of the utmost importance that designers working in the field of ADAS take note of the identified problems and refrain from using semi-empirical curve fit methods that rely on rigid body assumptions to model the complex tyre dynamics. This is especially true for rough road and off-road applications.

The scope of this chapter was limited to investigating the rolling radius of a single tyre on hard terrain and this has barely scratched the surface of this hotly debated topic. Extending the approach used in this paper to the same tyre on deformable terrains such as sand and mud and on low friction terrains such as snow and ice may give more insight. Continuing the work on hard terrains at different tyre inflation pressures may also open up new areas of investigation.

5.5 Next steps

Chapter 2 identified the two main factors that influence the performance of ABS systems. Chapter 5 investigated the ABS algorithm inputs and found that, in general, the assumptions made with regard to the longitudinal slip calculation are valid for off-road applications. Chapter 6 investigates tyre force generation and related phenomena that may contribute to the worsened braking performance on rough roads.

Chapter 6

The influence of tyre force generation on the braking performance

Design and technology should be the subject where mathematical brainboxes and science whizzkids turn their bright ideas into useful products.

- Sir James Dyson (1947-), British inventor

6.1 Introduction

The literature survey of Chapter 2 indicated that one of the main contributing factors in decreasing the braking performance on an undulating road is the large variation of tyre normal force. On a smooth road, tyre normal force variation during braking is mainly due to the load transfer from the rear to the front axle. This load transfer is purely due to the deceleration of the vehicle. On an undulating road, the presence of wheel hop excitation significantly increases the normal force variation. The wheel hop excitation is superimposed on the load transfer effect.

Using the dynamic tyre normal force as an indication of the vehicle's road holding capability is an established approach in the literature. It is the basic principle of groundhook control logic and although there are many variations of the groundhook control strategy, its aim is the reduction of the dynamic tyre force and thus improving both handling and road damage (Guglielmino et al., 2008). The dynamic tyre force is reduced by connecting the unsprung mass to a hypothetical reference on the ground with a controllable suspension damper, limiting the vertical motion of the tyre.

More specific to the braking performance on a rough road, Alleyne (1997) investigated the improvement in braking performance by integrating active suspension components with ABS. The work done by Alleyne (1997) made use of the Magic Formula tyre model and his investigations were limited to smooth road braking manoeuvres. Nevertheless, load transfer from the rear to the front axle was taken into account. By controlling the normal load on the axles with the active suspension, the braking distance was decreased by up to 9 percent.

Niemz and Winner (2006) reduced the stopping distance of a passenger car by controlling semi-active dampers. A 1.5 percent improvement was achieved on a road with unevenness similar to that of a German autobahn. The control algorithm, called the MiniMax control algorithm, switched the damping between high and low in an effort to reduce the wheel load variation. The control algorithm determines whether the dynamic vertical load needs to be increased or decreased, based either on an estimate of the actual dynamic wheel load or from ABS phase feedback from the ABS algorithm. It is assumed that if the ABS algorithm is in a pump phase, vertical load needs to be decreased and vice versa for the dump phase. The damper velocity and the change in wheel dynamic load is used to determine the switching required, as shown in Table 6-1.

Table 6-1 MiniMax control algorithm decision making matrix

Damper stage / Damper switching	Compression	Rebound
Hard to Soft	Decrease in wheel load	Increase in wheel load
Soft to Hard	Increase in wheel load	Decrease in wheel load

The work of Niemz and Winner (2006) was furthered by Reul and Winner (2009), who included the dynamic wheel load information in the ABS algorithm, modifying the braking force operating point – effectively adjusting the set points the ABS algorithm uses to determine whether brake pressure needs to be increased, maintained, or decreased. Reul and Winner (2009) summarise the strategies for improving the braking process as:

- Increasing the mean friction coefficient. This can be done by minimising the oscillation of the longitudinal tyre slip.
- Maximising the front wheel load during the initial part of the braking process.

The first observation that increasing the mean friction coefficient by reducing the longitudinal slip oscillation is similar to an optimal slip controller, which, as discussed in detail in Chapter 4, may negatively affect the vehicle's directional stability. The second observation is a better approach, as the front wheels are usually equipped with larger and better brakes, resulting in improved braking performance.

The conclusions drawn from the work of Niemz and Winner (2006) and Reul and Winner (2009), although based on uneven roads such as public highways and not as severely undulating as off-road terrains, shows that controlling the damper settings may yield improved braking performance. The influence of the suspension stiffness was not investigated. Since the experimental vehicle is equipped with the $4S_4$ suspension, the influence of suspension stiffness and damping can be investigated on severely undulating roads.

6.2 The influence of suspension configuration on braking distance

The possible improvements that could be achieved by modifying the vehicle's suspension characteristics were investigated by varying the gas volumes and damping scale factors of the $4S_4$ suspension in the simulation environment. As stated in Section 3.1, a lower gas volume results in higher suspension stiffness and a higher damping scale factor indicates higher damping being present. The gas volume and damping scale factors were varied for the front and rear suspension separately. Four discrete gas volumes and four discrete damping scale factors were used, to give a better indication of the influence each of these parameters have on the braking performance. As a result, 256 combinations were simulated for each road profile. Although all of these configurations are not currently feasible on the $4S_4$, the aim of the initial investigation is to identify a trend in the influence of the suspension configuration on the braking performance. The influences of four variables are thus being investigated, namely:

1. Gas volume (or suspension stiffness)
2. Damping scale factor (or suspension damping)
3. The influence of different front and rear suspension characteristics
4. Different road profiles

The 256 simulations for the various gas volumes and damping scale factors are repeated on each of these tracks, resulting in a 768 simulations. The vehicle was braked from 80km/h.

The ABS algorithm discussed in Section 2.2.3 was used with the thresholds given in Table 6-2.

Table 6-2 ABS algorithm thresholds

THRESHOLD	VALUE	UNIT
A	25	[rad/s^2]
α_{max}	5	[rad/s^2]
α_{min}	-100	[rad/s^2]
λ_{max}	0.2	[-]

Presenting multi-variable data logically and concisely that enables easy comparison between suspension configurations was a challenge. Rather than representing each suspension configuration as a single data point, a configuration is represented as a line in 3D space, as shown in Figure 6-1. In Figure 6-1, the left vertical plane (labelled 'Front') represents the front suspension configuration. The vertical axis is the damping scale factor and the horizontal axis the suspension gas volume. A point on the 'front' plane thus represents the damping and stiffness of the front $4S_4$ struts. Similarly, the 'Right' plane represents the damping and stiffness of the rear $4S_4$ struts. Connecting the two points (one in the 'Front' plane and one in the 'Rear' plane) shows the $4S_4$ configuration for the vehicle. The colour of the line indicates the braking distance (in metre) of that specific configuration. The configuration shown in Figure 6-1 is the 'Ride Comfort' setting. For the initial investigation, only the braking distance was used as a metric to evaluate braking performance. A more detailed analysis is done on the simulations resulting in the best and worst stopping distances.

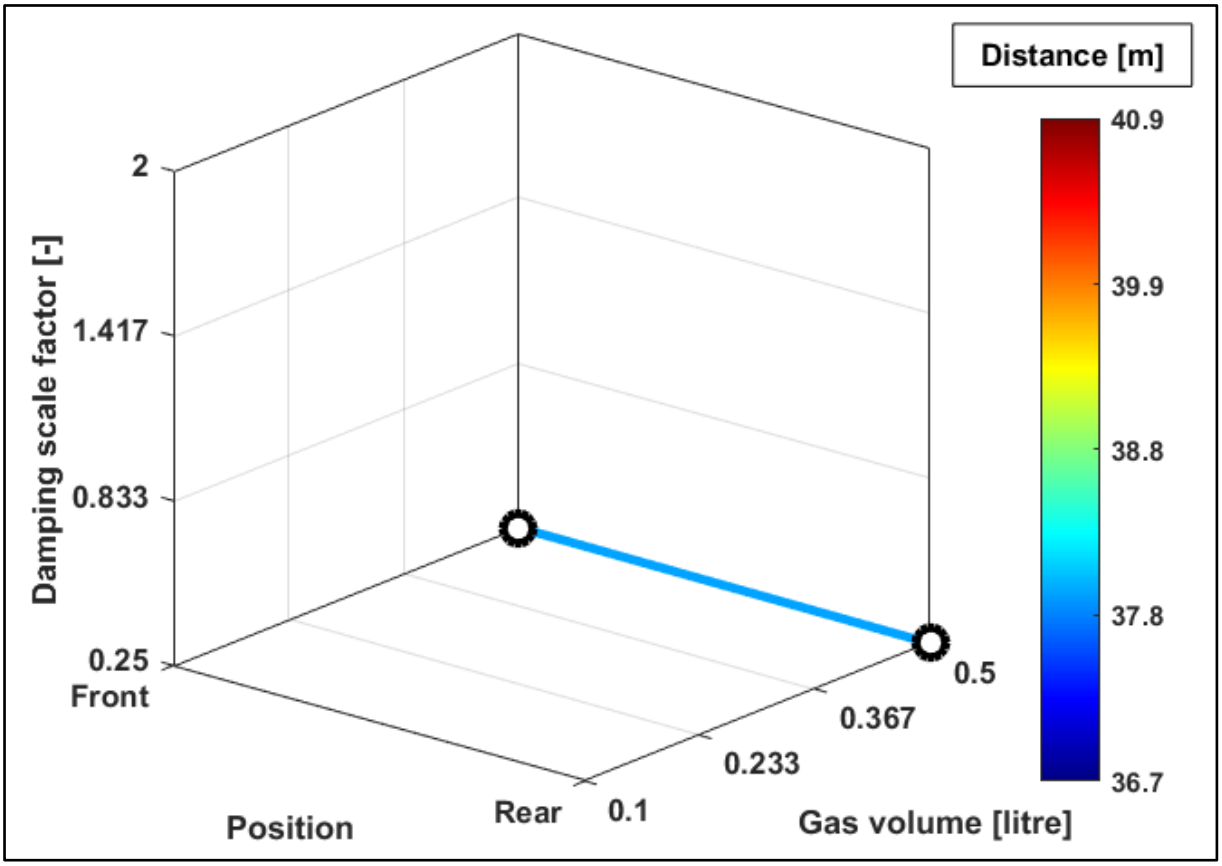

Figure 6-1 Example of visualising brake distance

6.2.1 *Parallel corrugations braking simulation results*

Figure 6-2 shows the braking distance for the 256 brake simulations on the parallel corrugations. The braking distance was taken as the distance from the moment the driver stepped on the brake pedal (this was at 0.5s of simulation time for all the simulations). Figure 6-2 shows that, in general, lower damping with larger gas volumes resulted in shorter braking distances. The shortest braking distance was 36.7m and the longest stopping distance was 40.9m, a difference of 4.2m or 10.2%. The best and worst simulation results are shown in Figure 6-3 and their suspension configurations are given in Table 6-3. The best and worst suspension configurations are plotted with dashed lines, but they are obscured in Figure 6-2. See Figure 6-14 for more detail.

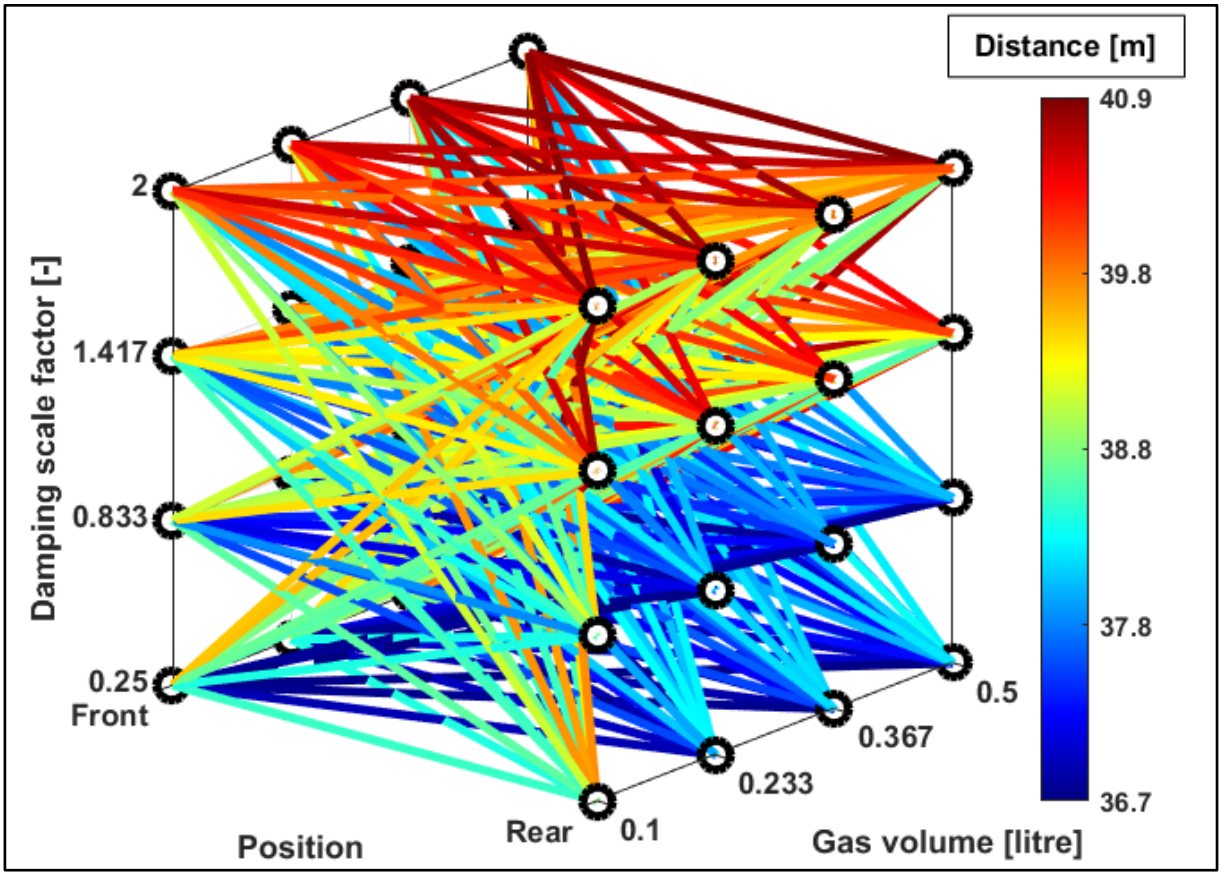

Figure 6-2 Braking distance for all suspension configurations on parallel corrugations

Table 6-3 Best and worst suspension configurations on parallel corrugations

PARAMETER	BEST	WORST
Front gas volume	0.1ℓ	0.5ℓ
Rear gas volume	0.233ℓ	0.233ℓ
Front damping scale factor	0.25	0.833
Rear damping scale factor	0.833	2

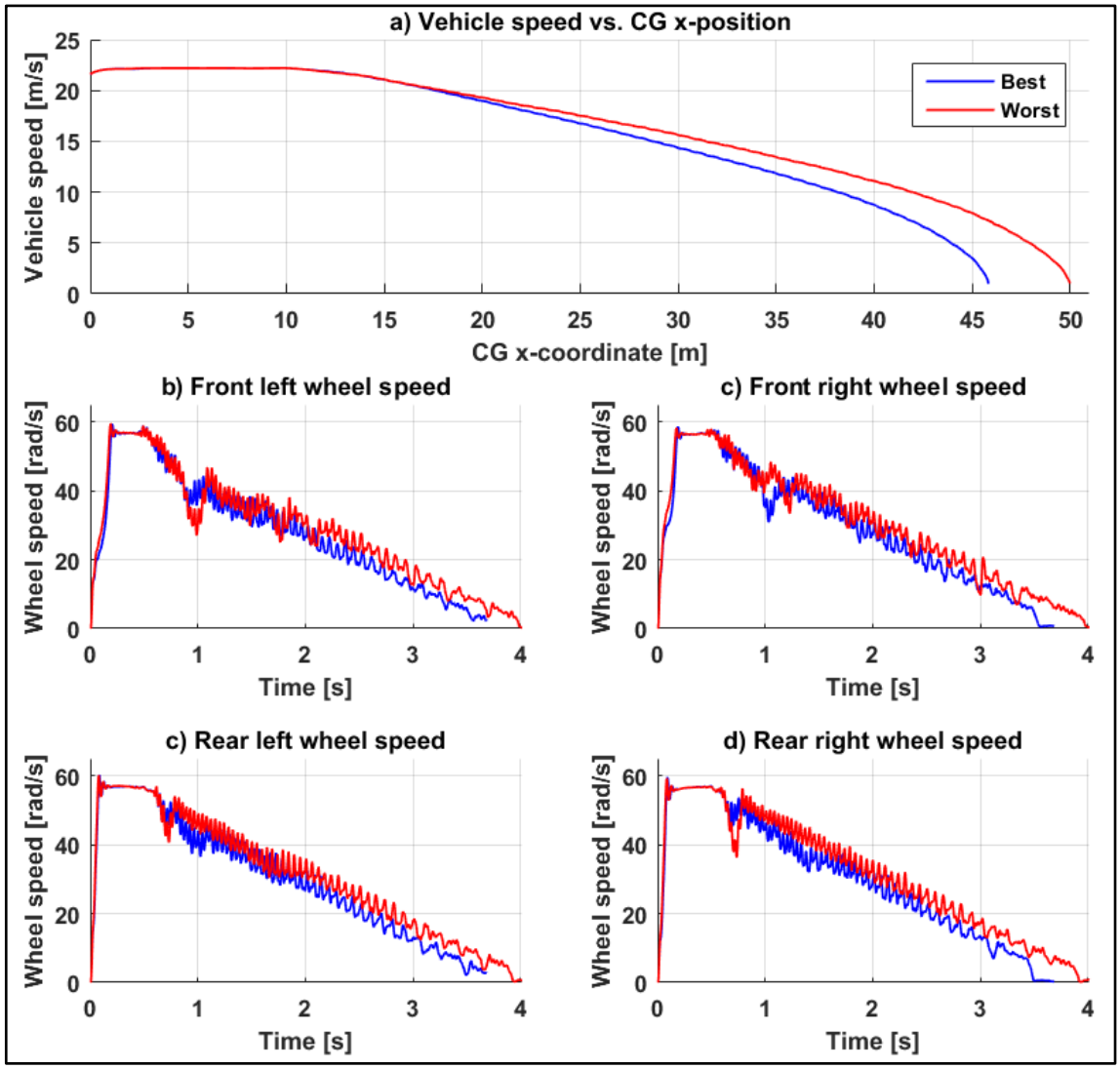

Figure 6-3 Time domain comparison of best and worst brake simulation results on parallel corrugations

Figure 6-4 shows two histograms comparing best and worst-case scenarios' tyre normal forces for the front and rear axles. The datasets shown in the histograms have been normalised so that the number of data points in the two datasets being compared are the same. It is evident in Figure 6-4 that the worst-case scenario's front tyre normal force has a significant number of points (the red histogram in Figure 6-4a) to the left of the blue histogram. This indicates that the load on the front axle was lower in the worst-case scenario. Since the experimental vehicle is equipped with larger brakes in the front, a lower load on the front axle may significantly influence the braking performance. The worst-case scenario's rear tyre normal force histogram in Figure 6-4b also has a small peak below 2000N that is larger than that of the best-case scenario histogram.

The distribution of the suspension strut forces was also analysed in an attempt to identify a reason for the significant influence the suspension configuration has on the braking performance. Figure 6-5 shows the histograms of the suspension forces. The histogram datasets have been normalised so that they contain the same number of data points. The front strut force distribution (Figure 6-5a) of the worst-case scenario is seen to be much wider than that of the best-case scenario. The rear strut force distributions also differ, but not as significantly as the front strut force distributions. Minimising the front strut force variation may lead to a shorter stopping distance on the parallel corrugations.

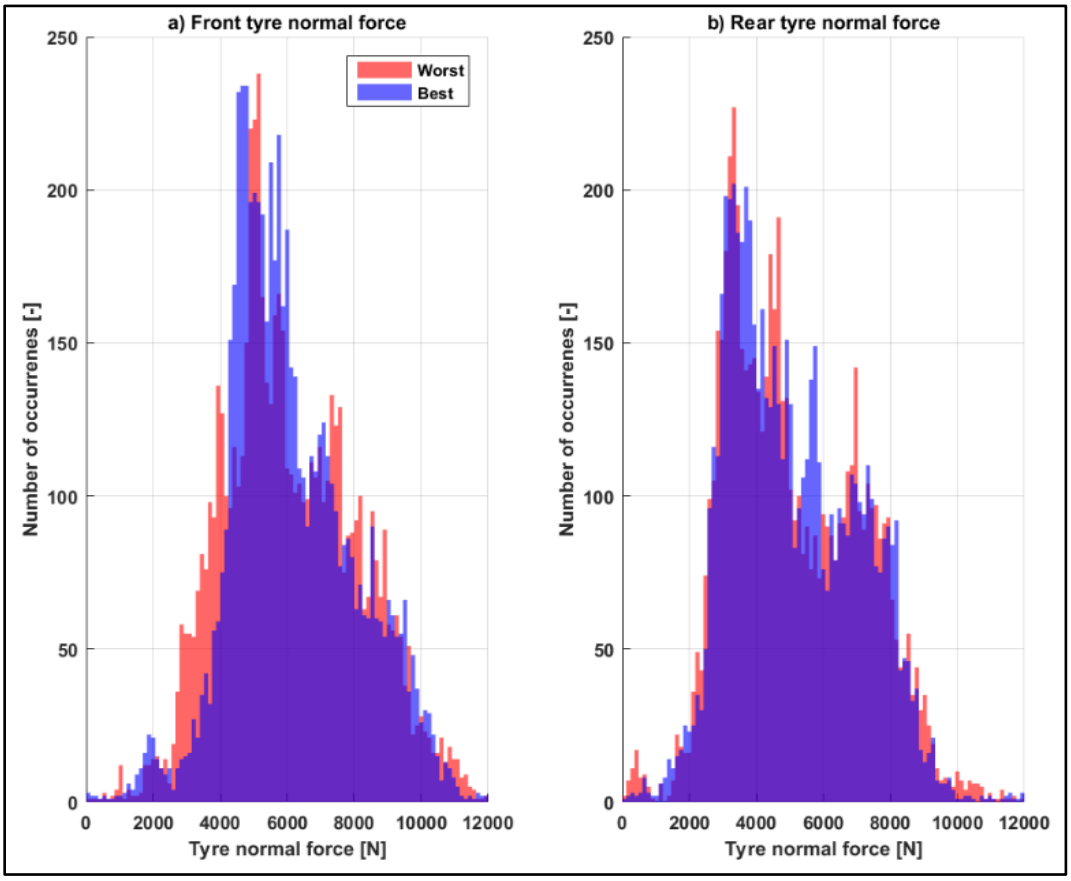

Figure 6-4 Histogram of average front (a) and rear (b) tyre normal forces for best and worst simulation results on parallel corrugations

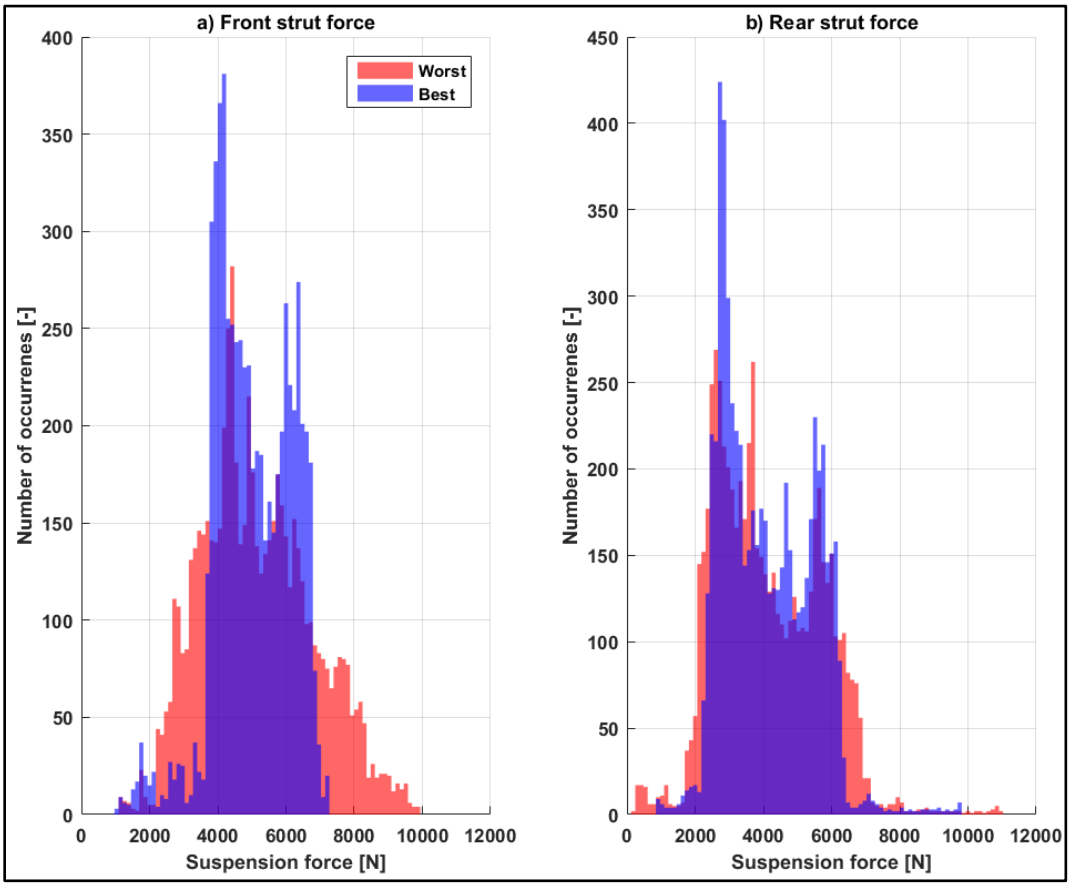

Figure 6-5 Histogram of average front (a) and rear (b) suspension strut forces for best and worst simulation results on parallel corrugations

6.2.2 *Angled corrugations braking simulation results*

Figure 6-6 shows the braking distance for the 16 brake simulations on the angled corrugations. Figure 6-6 shows that the four simulations with the shortest distance were all for the case where the rear $4S_4$ struts were set to the lowest damping scale factor and largest gas volume. Dashed lines are used to indicate the best and worst suspension configurations in Figure 6-6, also refer to Figure 6-14 for an unobscured view. The shortest stopping distance was 37.5m and the longest stopping distance was 41.6m, a difference of4.1m or 5.5%. The best and worst simulation results are shown in Figure 6-7. Similar to the results on the parallel corrugations, lower damping and lower suspension stiffness settings resulted in shorter stopping distances in general.

As was done during the analysis of the simulation results on the parallel corrugations, the tyre normal force distributions and the suspension strut force distributions are compared. Figure 6-8 shows tyre normal force distribution and Figure 6-9 the suspension strut force distribution.

Table 6-4 Best and worst suspension configurations on angled corrugations

PARAMETER	BEST	WORST
Front gas volume	0.233ℓ	0.367ℓ
Rear gas volume	0.5ℓ	0.1ℓ
Front damping scale factor	0.25	2
Rear damping scale factor	0.25	2

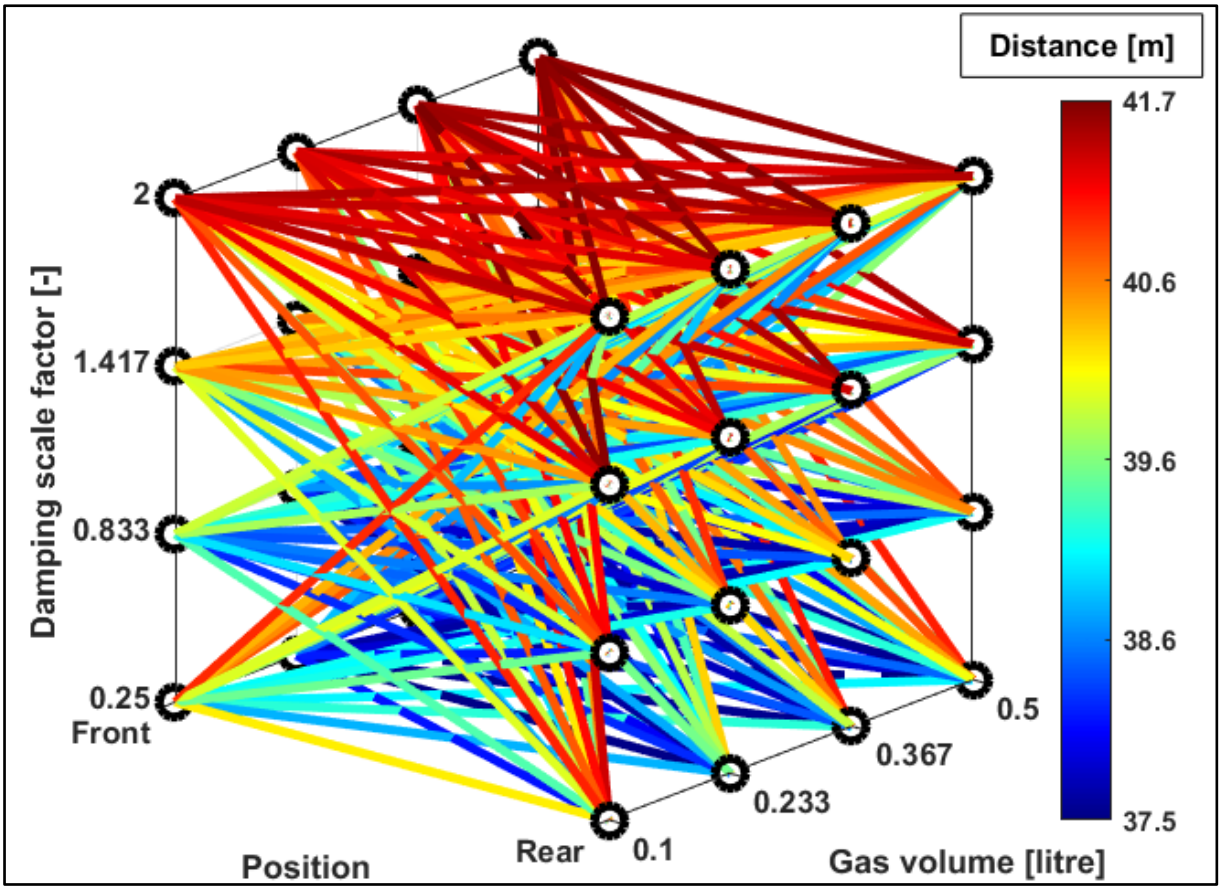

Figure 6-6 Braking distance for all suspension configurations on angled corrugations

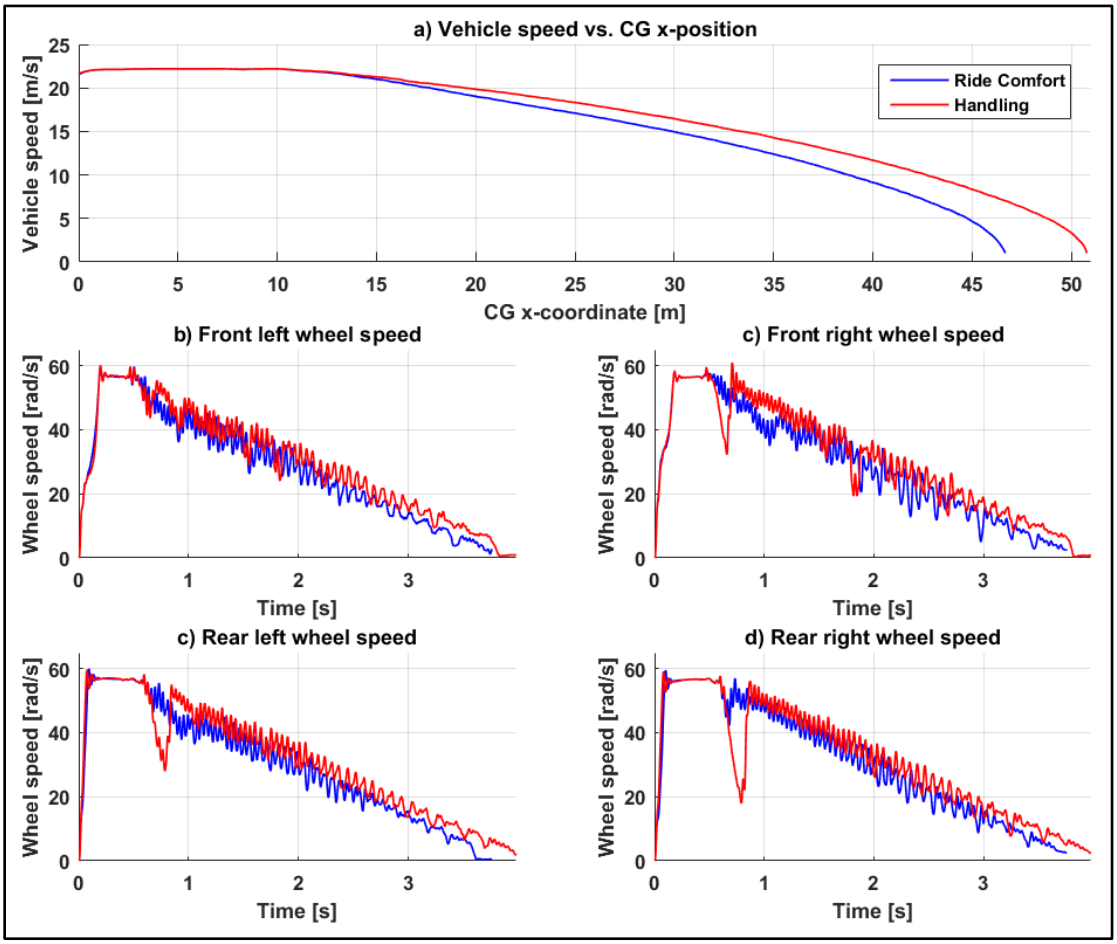

Figure 6-7 Time domain comparison of best and worst brake simulation results on angled corrugations

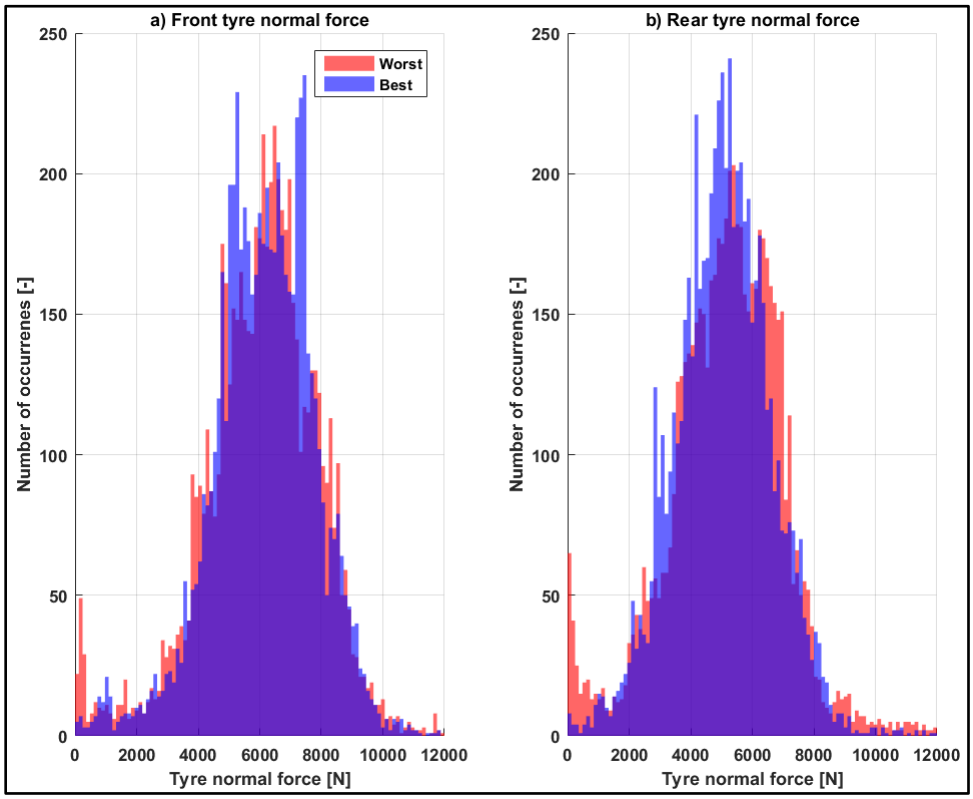

Figure 6-8 Histogram of average front (a) and rear (b) tyre normal forces for best and worst simulation results on angled corrugations

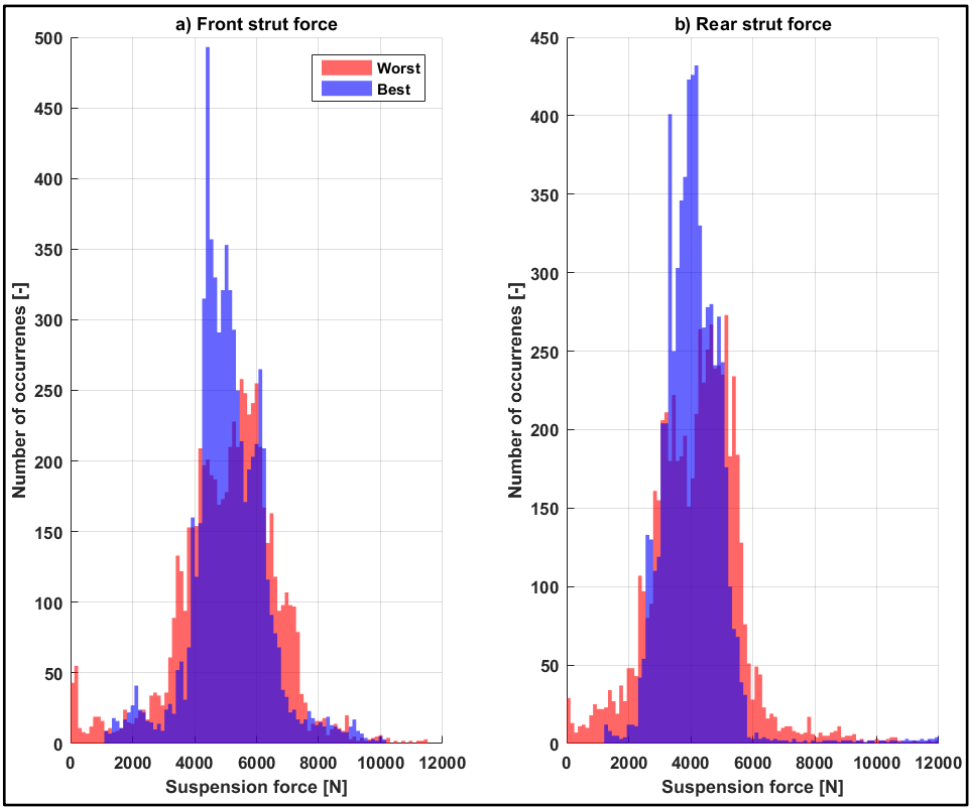

Figure 6-9 Histogram of average front (a) and rear (b) suspension strut forces for best and worst simulation results on angled corrugations

As was seen in Section 6.2.1, the force histograms reveal interesting results. The tyre normal force histograms show peaks at lower values for the worst-case scenarios when compared to the best-case scenarios. Figure 6-8 shows that for significant portions of the simulations, the tyre force is close to or at zero, indicating loss of contact with the road. The suspension strut force histograms also show significantly wider distributions for the worst-case suspension configuration, as was the case for the parallel corrugations simulation results. The rear suspension force histogram also shows a significant difference between the two configurations, in contrast with the parallel corrugations results.

6.2.3 *Belgian paving braking simulation results*

Figure 6-10 shows the braking distance results for the 256 suspension configurations on the Belgian paving. As seen in Sections 6.2.1 and 6.2.2, higher damping results in longer stopping distances. The shortest stopping distance was 44.5m and the longest stopping distance was 50.1m, a difference of 5.6m or 7.0%. The best and worst configurations are indicated with dashed lines in Figure 6-10 and the corresponding suspension configurations are given in Table 6-5. Figure 6-11 compares the best and worst simulation results. The wheel speeds shown in Figure 6-11 show that the wheels are more prone to lockup and lockup for longer periods for the worst-case scenario. This is an interesting observation, as the ABS algorithm used for the simulations is unchanged.

Table 6-5 Best and worst suspension configurations on Belgian paving

PARAMETER	BEST	WORST
Front gas volume	0.1ℓ	0.1ℓ
Rear gas volume	0.1ℓ	0.233ℓ
Front damping scale factor	0.25	2
Rear damping scale factor	0.25	2

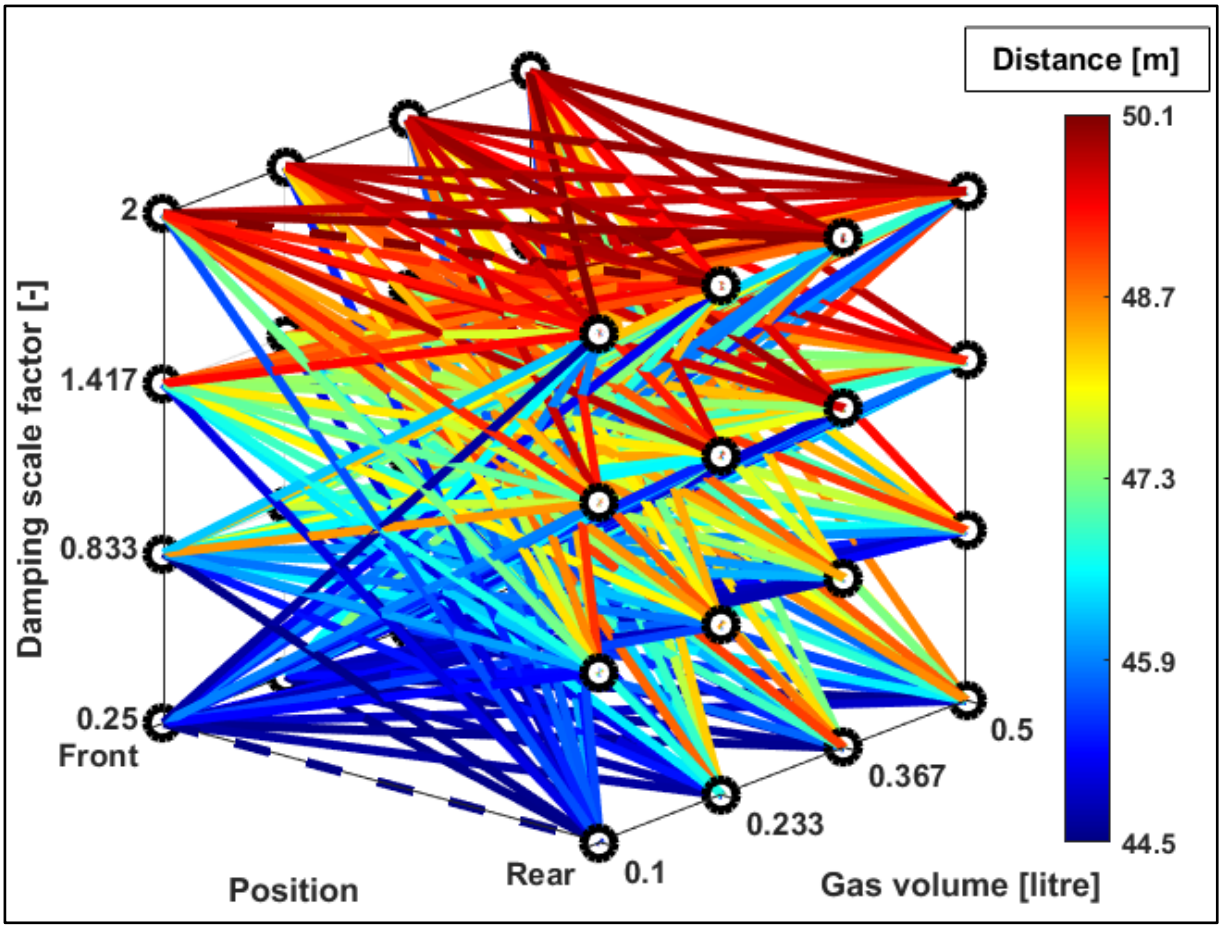

Figure 6-10 Braking distance for all suspension configurations on Belgian paving

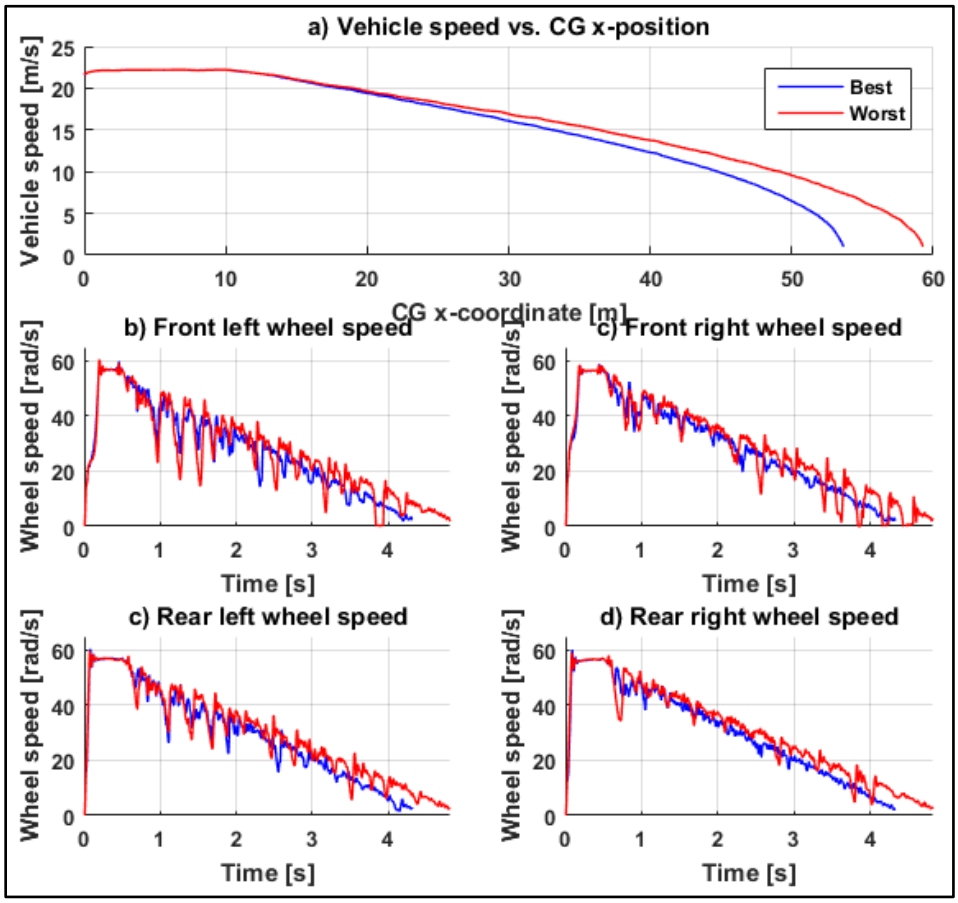

Figure 6-11 Time domain comparison of best and worst brake simulation results on the Belgian paving

Figure 6-12 shows histograms of the tyre normal forces. The tyre normal force variation is very different for the two suspension configurations, with the ideal configuration having a noticeably 'thinner' histogram, i.e. a lower standard deviation. This is the case for the front and rear tyre normal force histograms and the suspension force histograms shown in Figure 6-13. A significant number of data points in Figure 6-12 are at zero, indicating loss of contact with the road surface on the front and rear axle. The simulated results follow a trend already established in Sections 6.2.1 and 6.2.2. The best-case scenarios have lower force variations on both the front and rear axles.

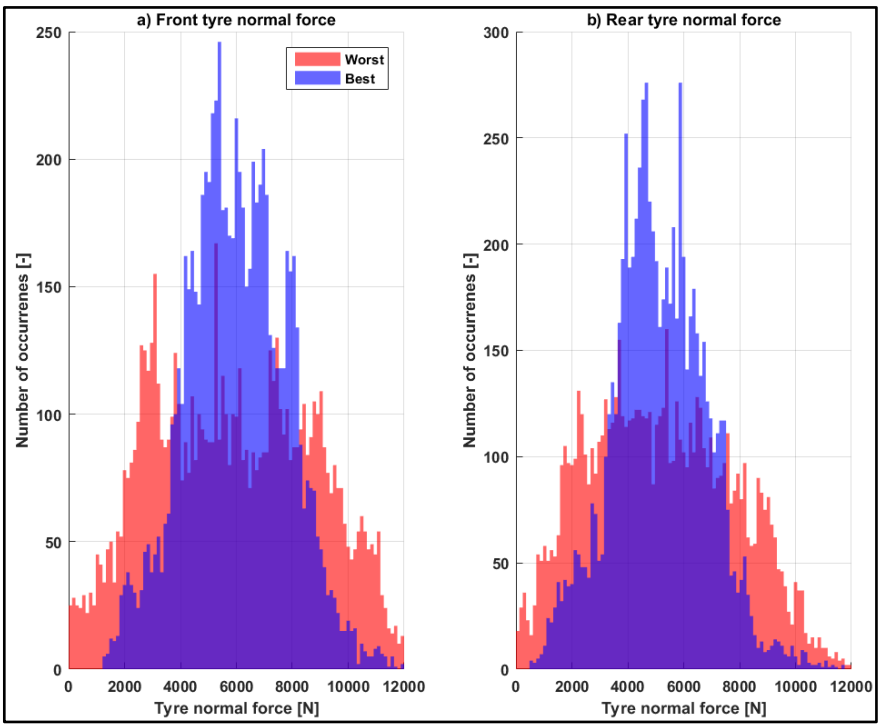

Figure 6-12 Histogram of average front (a) and rear (b) tyre normal forces for best and worst simulation results on Belgian paving

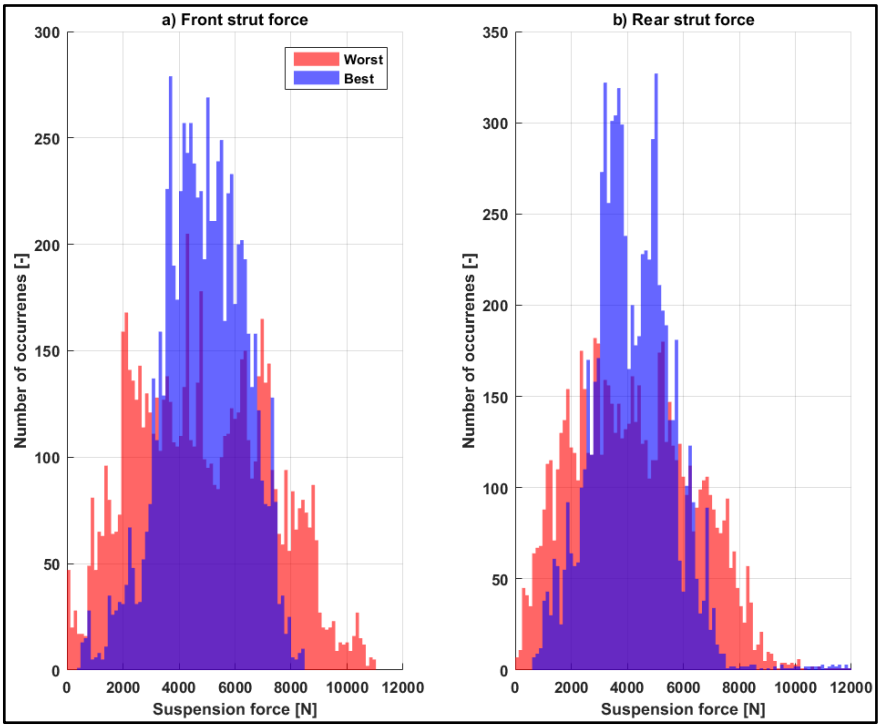

Figure 6-13 Histogram of average front (a) and rear (b) suspension strut forces for best and worst simulation results on Belgian paving

6.2.4 *Discussion of results*

The best and worst suspension settings for the three road profiles are shown in Figure 6-14. The three suspension configurations resulting in the shortest stopping distance on all three investigated road profiles all have lower damping compared to the worst suspension settings. The ideal suspension stiffness settings all have different requirements on the different road profiles. There is not a single, 'better than all other possible configurations', configuration that presents itself as the ideal suspension configuration for all the investigated scenarios. As shown in Figure 6-5, Figure 6-9 and Figure 6-13, there is a correlation between the suspension strut force variation and the stopping distance.

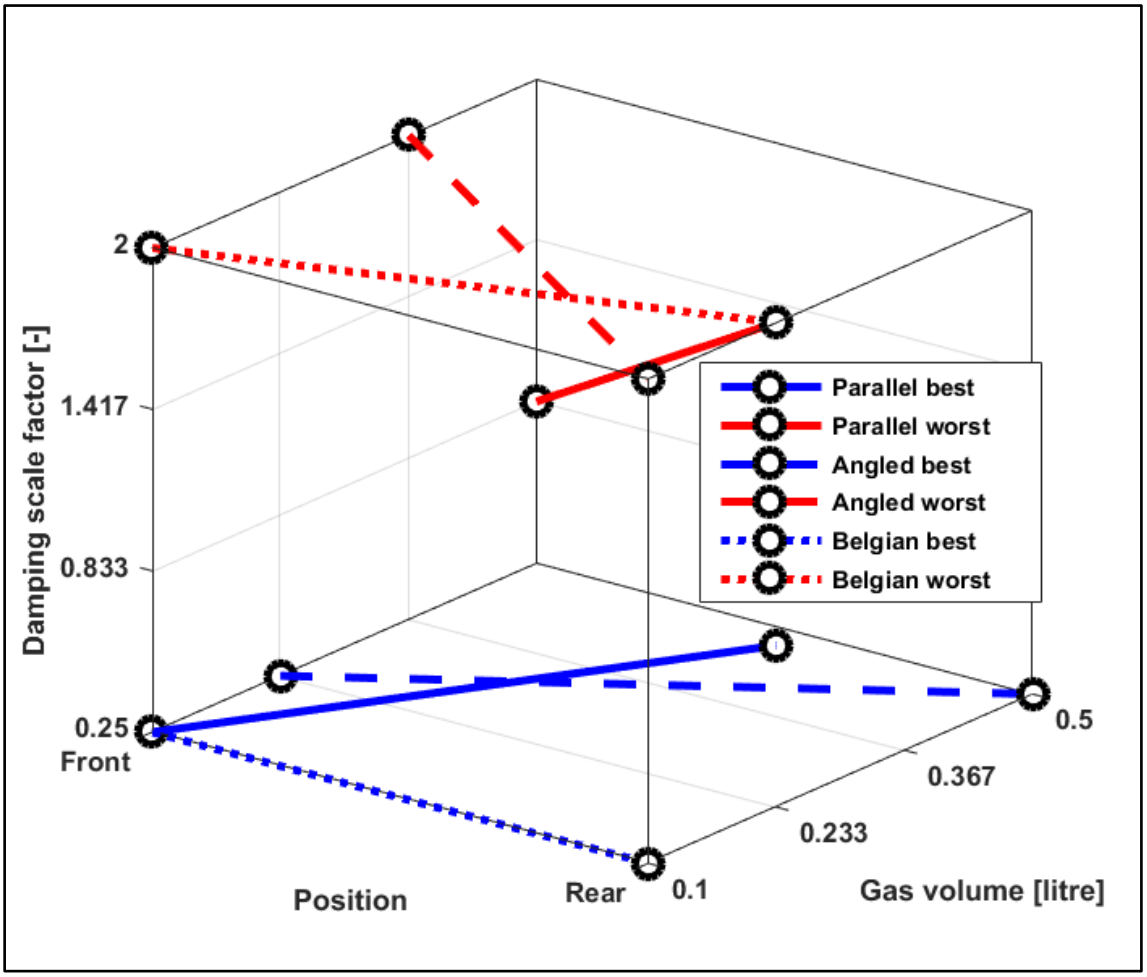

Figure 6-14 Summary of best and worst suspension configurations on all road profiles investigated

Because the low damping $4S_4$ settings resulted in the shortest stopping distances, a sensitivity analysis was done on the four configurations with the lowest damping possible on the physical $4S_4$ – that is for the largest and smallest gas volumes in the front and rear. The braking simulations were repeated for each of the four configurations five times with different braking points on the three road profiles. The sensitivity analysis results are given in Table 6-6 and show that the braking point influences the stopping distance. On all three road profiles, the difference between the best and worst suspension configurations is approximately 2%. This is in contrast to the much more significant differences in stopping distance reported in Sections 6.2.1, 6.2.2, and 6.2.3, where a difference of up to 10.2% was seen on the parallel corrugations. Considering that on a rough road that the 'Ride Comfort' $4S_4$ mode will be the default configuration, there seems to be very little to gain by selecting a different suspension setting. The standard deviations seen for each configuration indicated that, while the braking point does influence the stopping distance, the results are acceptably repeatable.

Table 6-6 Braking simulation sensitivity analysis results

	PARALLEL CORRUGATIONS				ANGLED CORRUGATIONS				BELGIAN PAVING			
Front Gas VOLUME [ℓ]	**0.1**	**0.1**	**0.5**	**0.5***	**0.1**	**0.1**	**0.5**	**0.5***	**0.1†**	**0.1**	**0.5**	**0.5***
Rear Gas Volume [ℓ]	**0.1**	**0.5**	**0.1**	**0.5***	**0.1**	**0.5**	**0.1**	**0.5***	**0.1†**	**0.5**	**0.1**	**0.5***
Run 1 Stopping Distance [m]	39.0	36.7	39.8	40.0	40.2	39.4	39.5	39.3	44.5	46.0	46.2	45.4
Run 2 Stopping Distance [m]	39.8	38.7	40.0	39.8	38.9	37.5	38.6	40.1	44.0	44.8	45.2	44.6
Run 3 Stopping Distance [m]	38.8	38.5	39.1	39.9	38.4	38.7	39.0	38.6	44.2	45.8	44.1	45.2
Run 4 Stopping Distance [m]	38.1	38.5	38.7	40.1	38.3	37.9	38.4	39.0	45.1	44.9	45.0	44.8
Run 5 Stopping Distance [m]	38.4	39.4	38.2	39.4	37.6	38.2	38.0	38.9	46.6	46.7	45.5	48.0
Average [m]	**38.8**	**38.3**	**39.2**	**39.8**	**38.7**	**38.3**	**38.7**	**39.2**	**44.9**	**45.6**	**45.2**	**45.6**
Standard Deviation [m]	**0.59**	**0.87**	**0.67**	**0.22**	**0.86**	**0.64**	**0.53**	**0.52**	**0.92**	**0.70**	**0.67**	**1.24**

* This is the 'Ride Comfort' setting of the $4S_4$

† This was the configuration with the shortest stopping distance on the Belgian paving (see Figure 6-14)

Matters become even more complicated upon deeper investigation of the simulation results. Dividing the vehicle speed into intervals and plotting the results reveals that the ideal suspension configuration varies from one speed interval to the next. As the vehicle speed reduces, the road excitation frequency changes. This is especially the case on a track such as the parallel corrugations where the undulations are spaced evenly at a constant spatial frequency. Figure 6-15, Figure 6-16, and Figure 6-17 show the stopping distance for all the simulated suspension configurations in 20km/h intervals from 80km/h to 0km/h for the parallel corrugations, angled corrugations, and Belgian paving, respectively. The blue portion of the figures moves, depending on the speed interval. In general, lower damping is still seen to dominate shorter stopping distances.

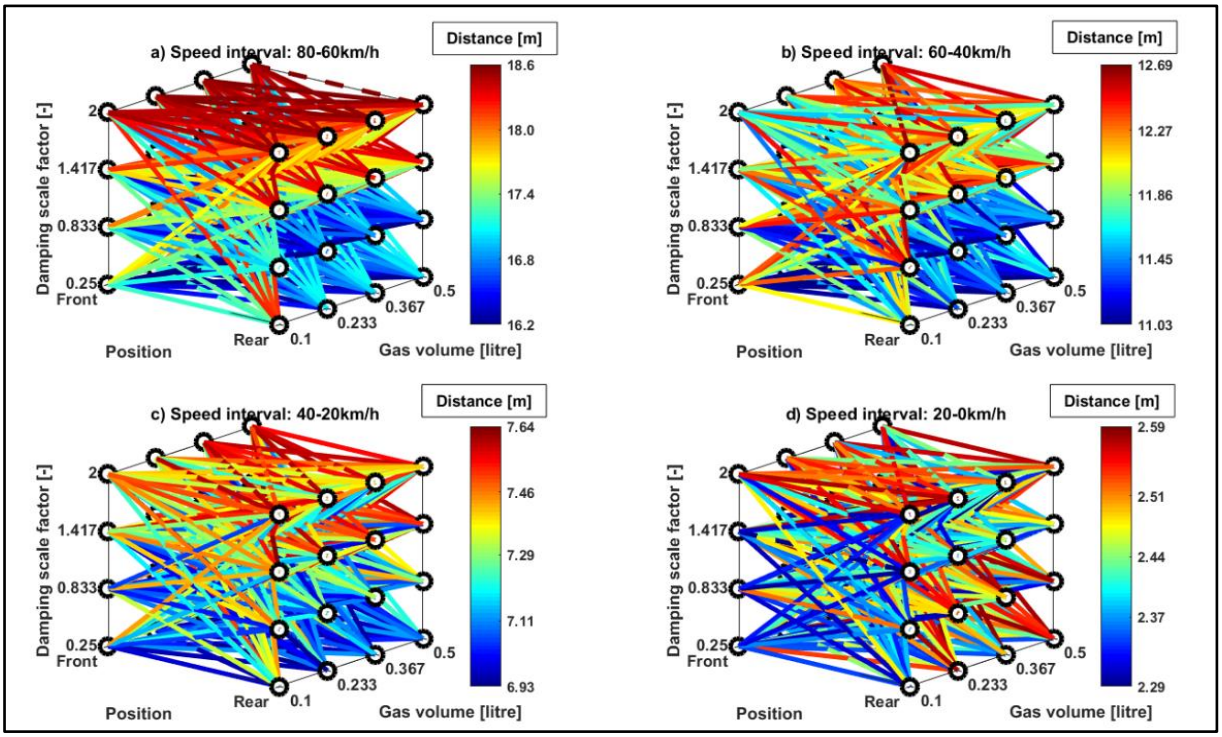

Figure 6-15 Stopping distance in 20km/h intervals on the parallel corrugations

.

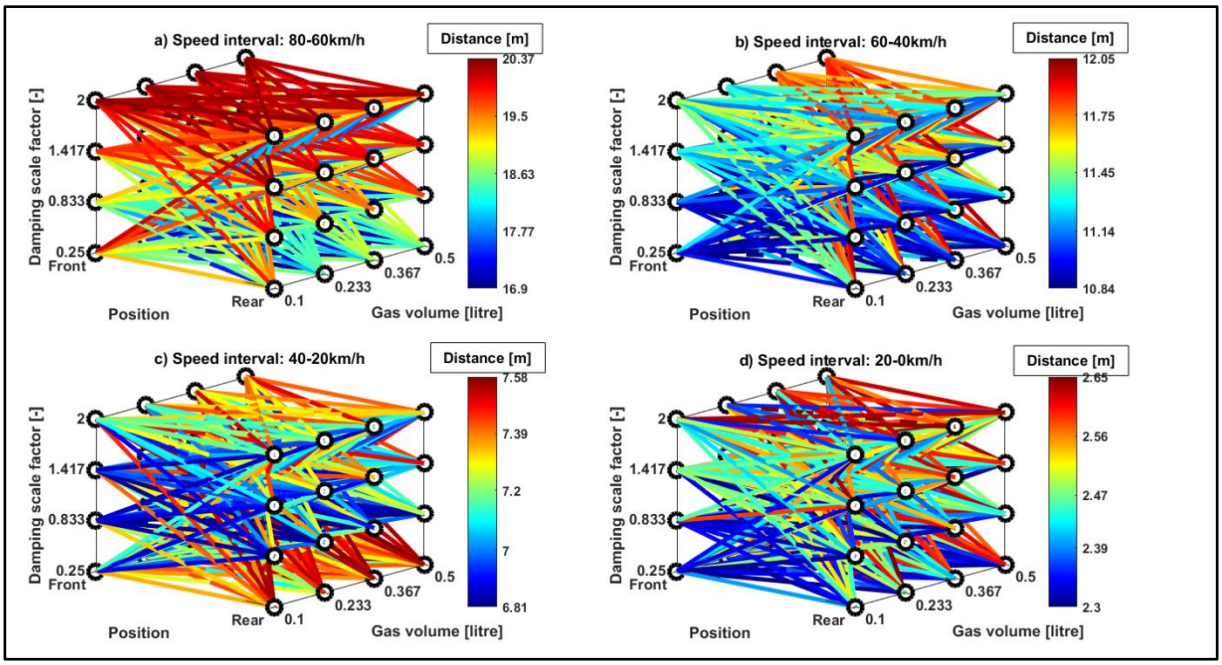

Figure 6-16 Stopping distance in 20km/h intervals on the angled corrugations

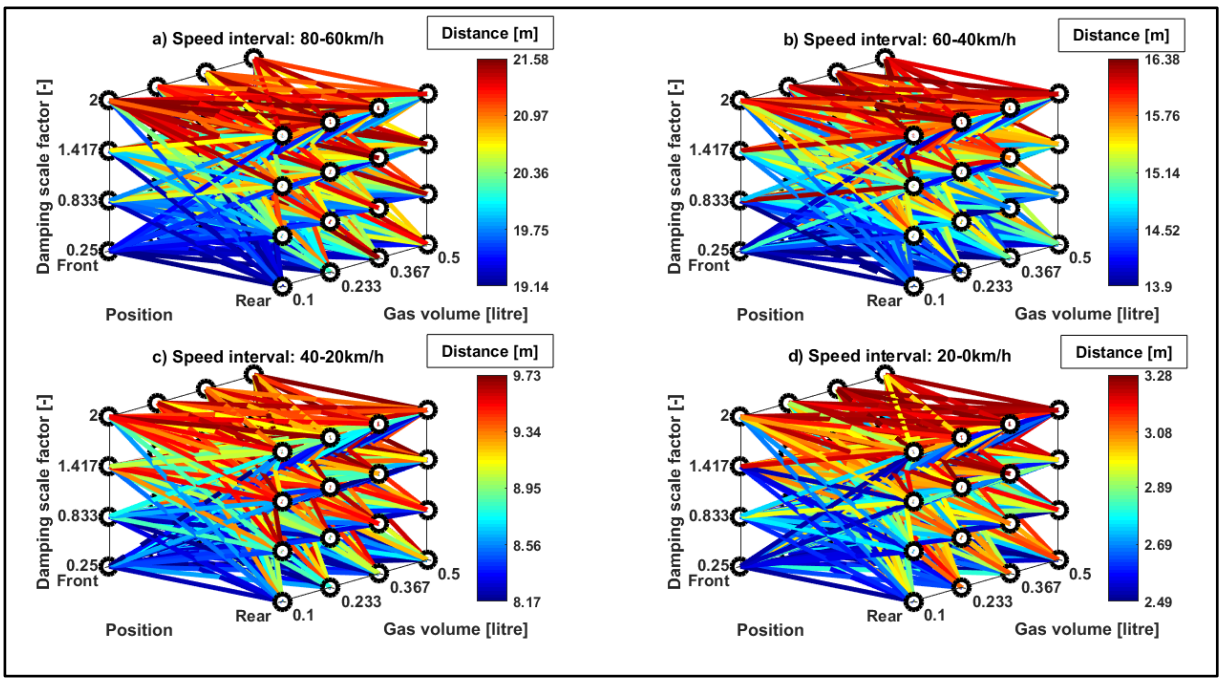

Figure 6-17 Stopping distance in 20km/h intervals on the Belgian paving

6.3 Conclusion

Stopping distances are significantly influenced by suspension stiffness and damping. The simulation results show that there is not a single simple answer to improving the ABS braking performance of a vehicle by changing the suspension settings. Each of the undulating roads used for the investigation resulted in different ideal suspension configurations and different worst suspension configurations. This is reflected in Figure 6-14, which shows the best and worst suspension configurations for all three road profiles. The shortest braking distance was achieved when the tyre normal force variation was minimised, as expected. Lower tyre normal force variation was also accompanied by reduced suspension strut force variation, as expected. It is also expected that the reduction in tyre normal force variation will provide

the driver with more control over the heading of the vehicle, although this was not investigated explicitly.

What is evident throughout the simulation results in Figure 6-2, Figure 6-6, and Figure 6-10 is that lower damping overall resulted in improved braking performance – this is also reflected in Figure 6-14. This contradicts what was found in the literature where higher damping improved the braking performance. It must be noted that the lowest damping characteristic used in this investigation is the lowest damping identified by Thoresson et al. (2009b). This damping setting is not the lowest physically possible, it is limited by wheel hop constraints that were imposed on the optimal damping scale factor identification algorithm (used to optimise the suspension characteristics for the 'Ride Comfort' $4S_4$ mode). Thoresson et al. (2009b) states that the inclusion of the wheel hop constraint is to reduce loss of contact between the wheels and the road surface, as this may cause the vehicle to become unstable. The wheel hop constraint had a larger effect on the lower limit of the damping scale factor's than the objective function. Damping scale factors lower than that investigated may thus lead to even further improved braking results, but at the risk that the vehicle becomes unstable in other situations. The suspension stiffness also significantly influences the braking performance, but the ideal suspension stiffness in the front and rear depends on the road input and the vehicle speed.

The results summarised in Section 6.2.4 show the suspension configurations that, on average, performed the best and the worst for the entire braking simulation. These suspension configurations were shown in Section 6.2.4 not to be the best configuration for 20km/h speed intervals from the initial speed of 80km/h down to stopping. The possibility thus exists that even shorter stopping distances are achievable by changing the suspension configuration during braking. This requires some method of intelligently identifying and selecting the ideal suspension configuration.

Chapter 7

Improving the braking performance: The WiSDoM algorithm

I have been aware from the outset … that the deep analysis of something, which is now called Kalman filtering, were of major importance. But even with this immodesty I did not quite anticipate all the reactions to this work.

- Rudolf E. Kálmán (1930-2016), Hungarian-American electrical engineer

7.1 Introduction

The simulation results of Chapter 6 indicate that a reduction in suspension force variation may result in shorter stopping distances on rough roads. The suspension force variation is influenced by the type of road excitation and the vehicle speed. A semi-active suspension, combined with an intelligent method of selecting the ideal suspension configuration for a specific road condition and vehicle speed, is a potential solution that may cost-affectively address the problem. Chapter 7 proposes a solution to the increased and varying stopping distances seen in the simulation results of Chapter 6 by combining brake control and suspension control.

The aim of the proposed control system is to minimise the dynamic suspension strut force variation. The proposed approach is to estimate the wheel hop of the unsprung masses and then use the estimated wheel hop to predict a simplified pitch-bounce model's response to the road excitation. Knowledge of the wheel hop can then be used to predict the suspension force variation on the road currently being traversed and the ideal suspension configuration may then be identified and selected. The proposed approach is shown in Figure 7-1. The assumptions made and models used in the proposed approach are also shown in Figure 7-1. The assumptions are discussed in more detail in the subsequent sections. It is also of paramount importance that the proposed algorithm can estimate wheel hop in real-time and can predict the suspension forces faster than real-time.

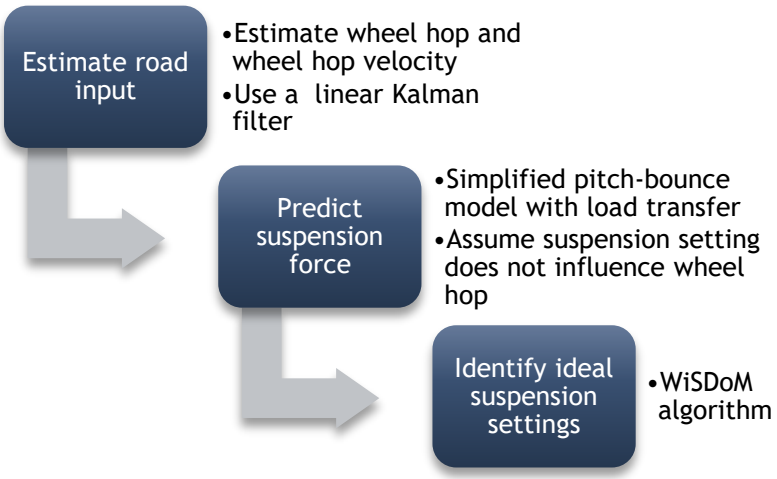

Figure 7-1 Proposed approach to reduce suspension force variation and assumptions made at each step

7.2 Identify road input

The road input is identified by estimating the wheel hop using a linear Kalman Filter (KF). Kalman filtering is also known as linear quadratic estimation. As shown in Figure 7-1, several assumptions are being made and limitations are applied to the wheel hop estimation step of the proposed approach. The most important assumption is that the road input does not change as the vehicle drives along. The information used to estimate the wheel hop is thus *a priori* information. It is assumed that the vehicle does not make use of sensing technology that can measure the road profile while the vehicle is moving. Readily available and accessible sensors are used for input to the estimation algorithm. Ideally, the direct measurement of wheel hop would have simplified matters greatly. Using advanced measurement techniques such as DIC (see Section 5.2) the absolute wheel hop can be measured directly. This, however, is deemed to be sensing technology that is not available for commercial application yet.

Measurements containing inaccuracies are observed over time and through Bayesian inference and estimating a joint probability distribution over the variables, a more precise estimate of the unknown variables is found. The KF tracks the estimated state and the variance of the estimate. A recursive process containing two steps is followed. The first step is predicting estimates of the state variables and their uncertainties. The second step makes use of the observed noisy measurements to update the estimated states with a weighted average. Estimates with higher certainty are assigned a larger weighting (Kalman, 1960). The basic KF algorithm is given in Equations (7.1) to (7.9).

The algorithm assumes that the states of the next time step develop from the states at the current time step, where $\boldsymbol{x}_k$ is the state vector at time step *k*, $\boldsymbol{F}$ is the state transition matrix, $\boldsymbol{B}$ is the control matrix, $\boldsymbol{u}_k$ is the control vector and $\boldsymbol{w}_k$ is the process noise. The process noise has covariance $\boldsymbol{Q_k}$ at time step *k*. An observation of some of the states in $\boldsymbol{x}_k$ is made, according to Equation (7.2), where $\boldsymbol{z}_k$ is the observation vector, $\boldsymbol{H}$ is the observation model, and $\boldsymbol{v}_k$ is the observation noise. The observation noise has covariance $\boldsymbol{R_k}$ at time step *k*. The subscript $k|k-1$ indicates that the *a priori* information up to, but not including, time step *k* is used and this is found in the prediction step of the algorithm. The subscript $k|k$ is the updated estimate using information up to and including time step *k*.

$$\boldsymbol{x}_k = \boldsymbol{F}\boldsymbol{x}_{k-1} + \boldsymbol{B}\boldsymbol{u}_k + \boldsymbol{w}_k \tag{7.1}$$

$$\boldsymbol{z}_k = \boldsymbol{H}\boldsymbol{x}_k + \boldsymbol{v}_k \tag{7.2}$$

The first step is the prediction step, predicting the state estimate and its covariance:

$$\widehat{\boldsymbol{x}}_{k|k-1} = \boldsymbol{F}\widehat{\boldsymbol{x}}_{k-1|k-1} + \boldsymbol{B}\boldsymbol{u}_k \tag{7.3}$$

$$\boldsymbol{P}_{k|k-1} = \boldsymbol{F}\boldsymbol{P}_{k-1|k-1}\boldsymbol{F}^{\boldsymbol{T}} + \boldsymbol{Q_{k-1}} \tag{7.4}$$

The next step is updating the measurement residual $\boldsymbol{z}_k$ and its covariance $\boldsymbol{S_k}$:

$$\widetilde{\boldsymbol{y}}_k = \boldsymbol{z}_k - \boldsymbol{H}\widehat{\boldsymbol{x}}_{k|k-1} \tag{7.5}$$

$$\boldsymbol{S}_k = \boldsymbol{H}\boldsymbol{P}_{k|k-1}\boldsymbol{H}^{\boldsymbol{T}} + \boldsymbol{R_k} \tag{7.6}$$

The optimal Kalman gain is then calculated:

$$\boldsymbol{K}_k = \boldsymbol{P}_{k|k-1}\boldsymbol{H}^{\boldsymbol{T}}\boldsymbol{S_k^{-1}} \tag{7.7}$$

Finally, the state estimate and its covariance is updated:

$$\hat{\boldsymbol{x}}_{k|k} = \hat{\boldsymbol{x}}_{k|k-1} + \boldsymbol{K}_k \tilde{\boldsymbol{y}}_k \tag{7.8}$$

$$\boldsymbol{P}_{k|k} = (I - \boldsymbol{K}_k \boldsymbol{H}) \boldsymbol{P}_{k|k-1} \tag{7.9}$$

7.2.1 *Estimator and observer model*

One limitation of the KF is that it applies only to linear systems. The estimator model has been formulated in such a way that it is linear. The estimator model used is a pitch-bounce model, a half vehicle model that consists of four DOFs: front and rear wheel hop, body hop, and body pitch. The states of interest are the unsprung mass displacements (wheel hop) and velocities. Since the suspension may be in different states and because the suspension stiffness and damping characteristics are highly nonlinear, the estimator and observer models are formulated as kinematic models. The state vector is given in Equation (7.10). The suspension displacements are used as observations with high certainty. To reduce drift and to drive the unsprung mass displacements to zero, the unsprung mass displacement is given as a zero measurement with high uncertainty. The observation vector is given in Equation (7.11).

$$\boldsymbol{x}_k = \langle z_1 \quad \dot{z}_1 \quad z_2 \quad \dot{z}_2 \quad z_3 \quad \dot{z}_3 \quad \theta_y \rangle_k^T \tag{7.10}$$

$$\boldsymbol{z}_k = \langle z_3 - z_1 - l_f \theta_y \quad z_3 - z_2 + l_r \theta_y \quad z_1 \quad z_2 \rangle_k^T \tag{7.11}$$

The estimator model uses the previous time step's information and the time integral of the state's derivatives to determine the state estimate at the current time step. The unsprung and sprung mass displacement and velocity updates are given in Equation (7.12) and (7.13). *i* in Equations (6.12) and (6.13) represents the subscript 1, 2, or 3, as shown in Figure 7-2.

$$z_{i_k} = z_{i_{k-1}} + \dot{z}_{i_{k-1}} \Delta t + \frac{1}{2} \ddot{z}_{i_{k-1}} \Delta t^2 \tag{7.12}$$

$$\dot{z}_{i_k} = \dot{z}_{i_{k-1}} + \ddot{z}_{i_{k-1}} \Delta t \tag{7.13}$$

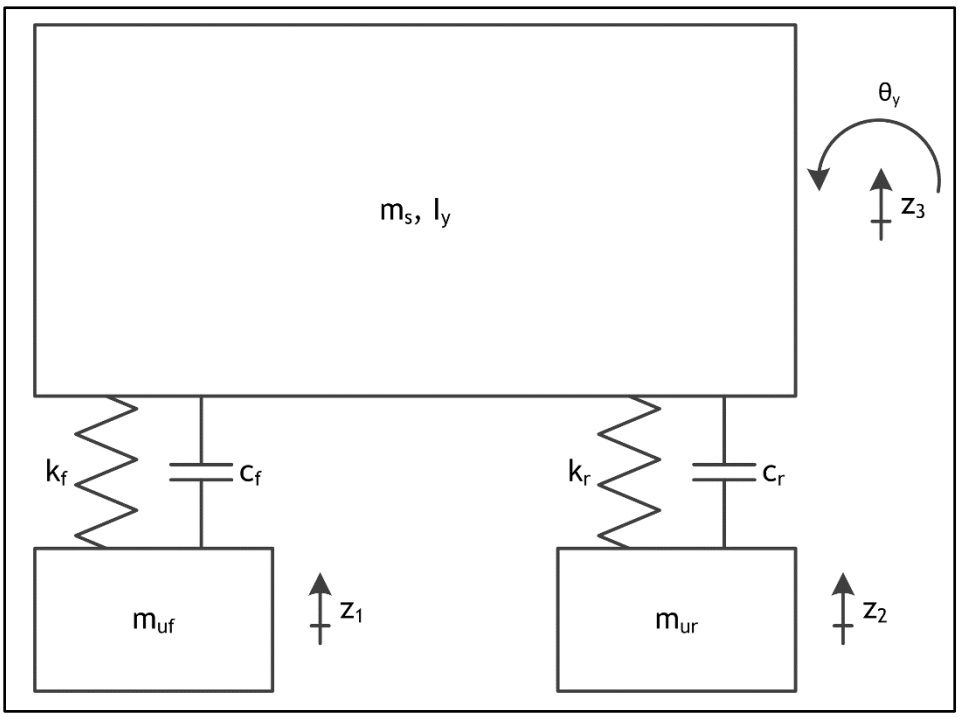

Figure 7-2 Pitch-bounce model used as estimator model

The pitch angle is updated with Equation (7.14):

$$\theta_{y_k} = \theta_{y_{k-1}} + \dot{\theta}_{y_{k-1}} \Delta t \tag{7.14}$$

The control vector comprises of the measured vertical accelerations of the sprung and unsprung masses and the pitch rate of the sprung mass:

$$\boldsymbol{u}_k = \langle \ddot{z}_1 \quad \ddot{z}_2 \quad \ddot{z}_3 \quad \dot{\theta}_y \rangle^T \tag{7.15}$$

The complete estimator and observer models are given in Equations (7.16) and (7.17):

$$\boldsymbol{x}_k = \boldsymbol{F}\boldsymbol{x}_{k-1} + \boldsymbol{B}\boldsymbol{u}_k$$

$$\boldsymbol{x}_k = \begin{bmatrix} 1 & \Delta t & 0 & 0 & 0 & 0 & 0 \\ 0 & 1 & 0 & 0 & 0 & 0 & 0 \\ 0 & 0 & 1 & \Delta t & 0 & 0 & 0 \\ 0 & 0 & 0 & 1 & 0 & 0 & 0 \\ 0 & 0 & 0 & 0 & 1 & \Delta t & 0 \\ 0 & 0 & 0 & 0 & 0 & 1 & 0 \\ 0 & 0 & 0 & 0 & 0 & 0 & 1 \end{bmatrix} \boldsymbol{x}_{k-1} + \begin{bmatrix} 0.5\Delta t^2 & 0 & 0 & 0 \\ \Delta t & 0 & 0 & 0 \\ 0 & 0.5\Delta t^2 & 0 & 0 \\ 0 & \Delta t & 0 & 0 \\ 0 & 0 & 0.5\Delta t^2 & 0 \\ 0 & 0 & \Delta t & 0 \\ 0 & 0 & 0 & \Delta t \end{bmatrix} \boldsymbol{u}_k \tag{7.16}$$

$$\boldsymbol{z}_k = \boldsymbol{H}\boldsymbol{x}_k$$

$$\boldsymbol{z}_k = \begin{bmatrix} -1 & 0 & 0 & 0 & 1 & 0 & -l_f \\ 0 & 0 & -1 & 0 & 1 & 0 & l_r \\ 1 & 0 & 0 & 0 & 0 & 0 & 0 \\ 0 & 0 & 1 & 0 & 0 & 0 & 0 \end{bmatrix} \boldsymbol{x}_k \tag{7.17}$$

7.2.2 *State estimation results*

The parameters used for the state estimator model are given in Table 7-1.

Table 7-1 Estimator model parameters

PARAMETER	VALUE	UNIT
l_f	1.4465	[m]
l_r	1.3275	[m]

The wheel hop estimation algorithm is first evaluated in simulation. The ADAMS (MSC Software, 2016) vehicle model is driven over the parallel corrugations, angled corrugations and the Belgian paving at constant speed. The KF algorithm is then applied to the simulated results. Figure 7-3, Figure 7-4 and Figure 7-5 compare the results of the KF wheel hop estimation with the simulated results over the parallel corrugations, angled corrugations and Belgian paivng. Very little numerical integration drift is present. There is a slight discrepancy initially in the wheel hop estimation, but the estimation algorithm converges relatively quickly to values very close to the actual simulated results. A comparison of the wheel hop estimation results is also done in the frequency domain.

A mirrored and scaled single-sided FFT is performed on the estimated and simulated wheel hop. The results are shown in Figure 7-6. Comparing the FFT magnitudes, one may see that the wheel hop estimation very accurately captures the wheel hop dynamics up to at least 25Hz. There are some discrepancies at very low frequencies, as shown in Figure 7-6e and Figure 7-6f, where the frequencies below 1Hz are not as accurately captured. This is due to the high uncertainty zero measurements used to drive the wheel hop estimation to oscillate about zero. The wheel hop estimation results obtained by simulation are however acceptable, although experimental validation is needed to remove all doubt. More on this in Section 7.3.2.

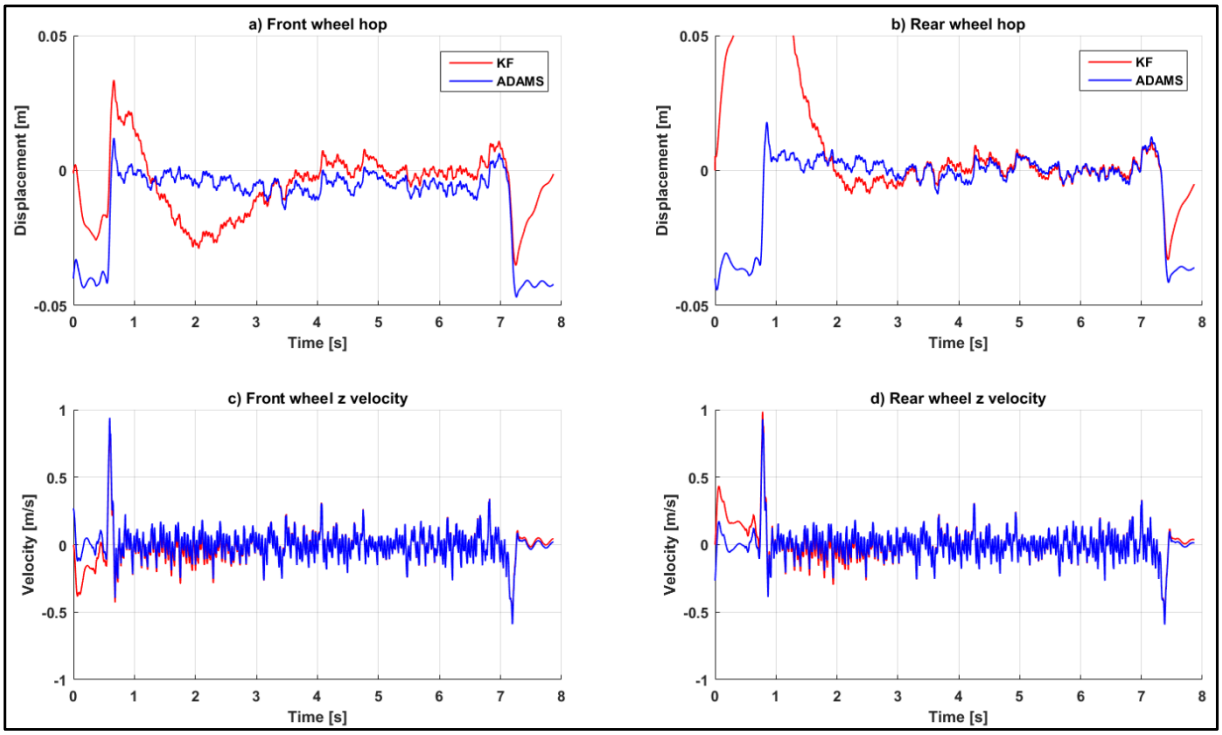

Figure 7-3 Comparison of simulated and estimated front (a) and rear (b) wheel hop on parallel corrugations

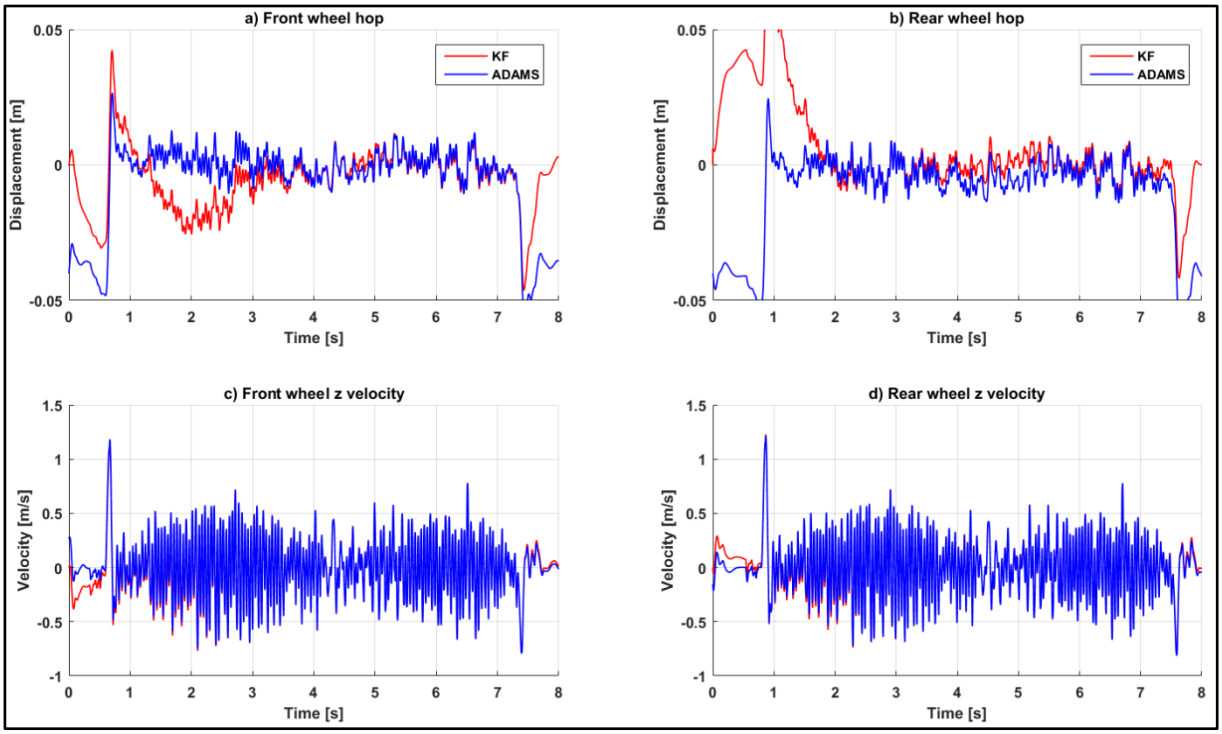

Figure 7-4 Comparison of simulated and estimated front (a) rear (b) wheel hop on angled corrugations

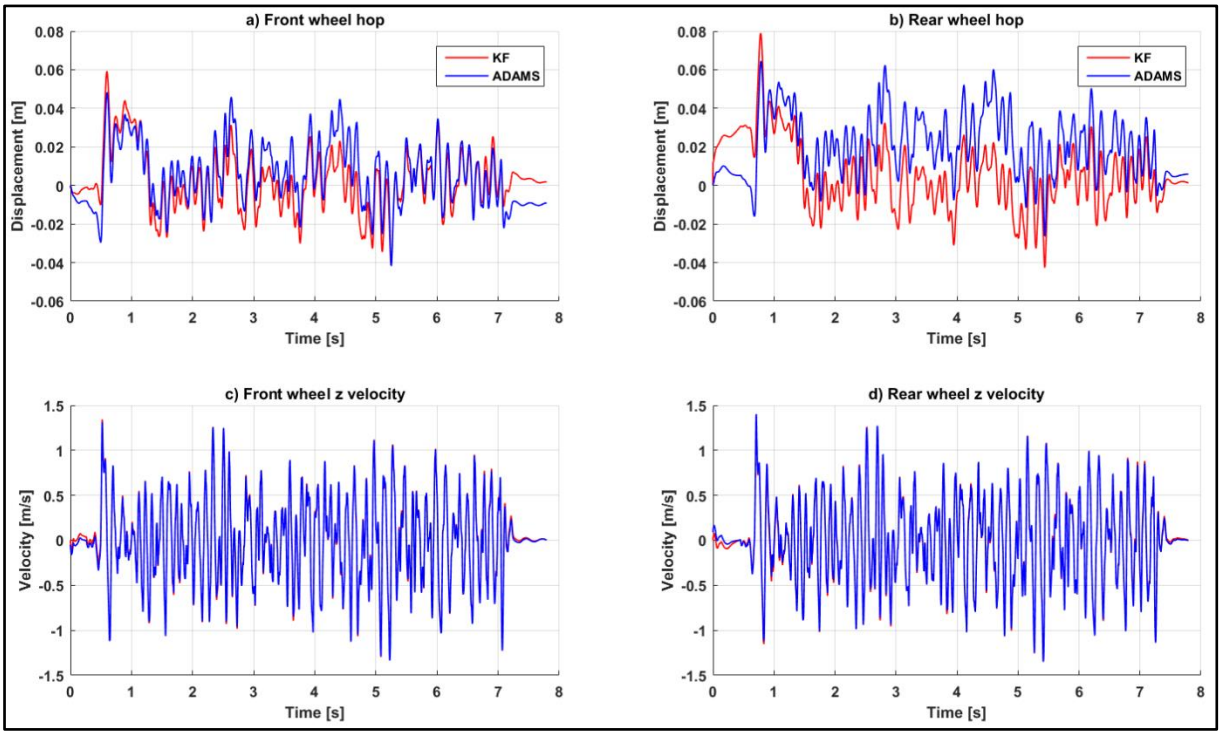

Figure 7-5 Comparison of simulated and estimated front (a) rear (b) wheel hop on Belgian paving

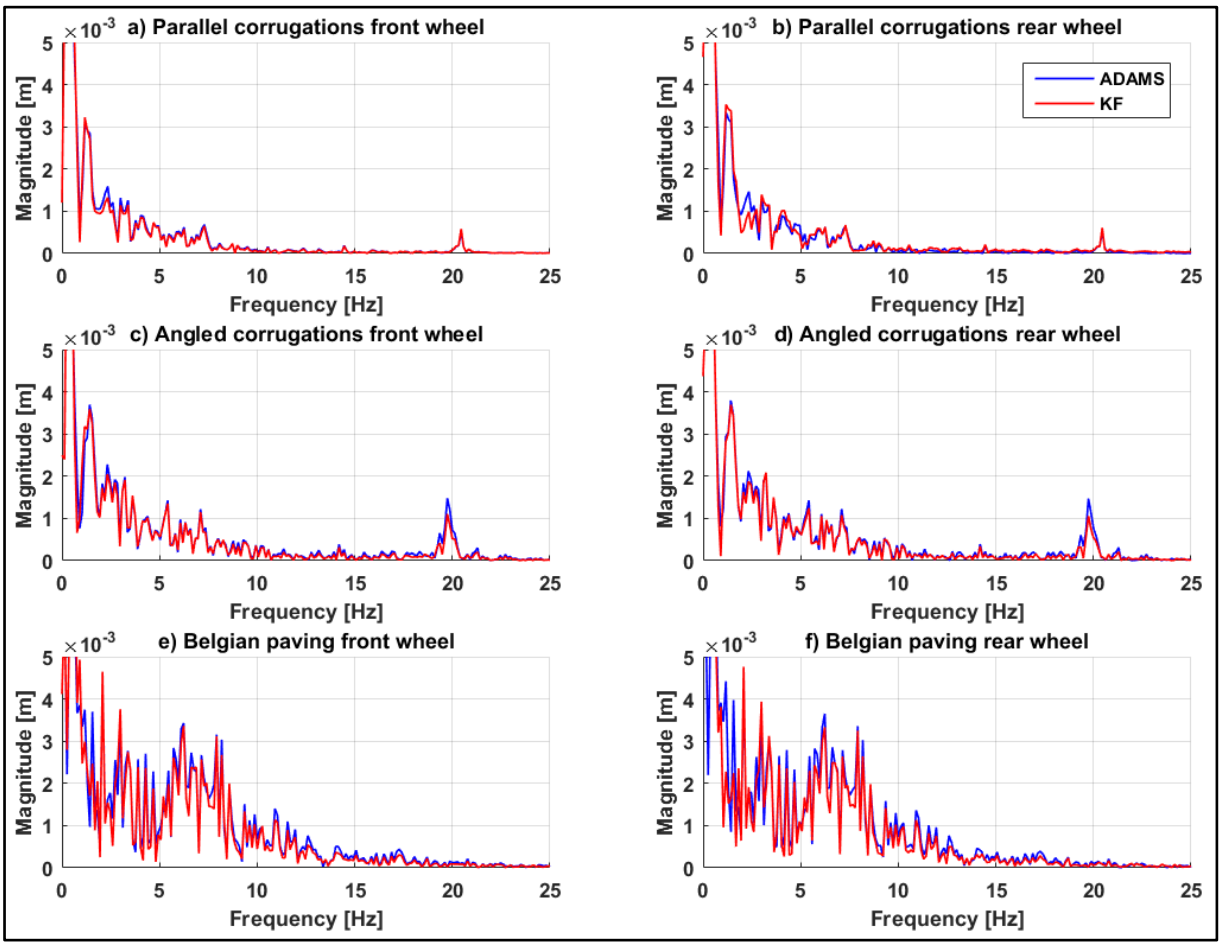

Figure 7-6 Mirrored and scaled single-sided FFT magnitude comparison of wheel hop estimation

7.3 Predicting suspension force

The estimated wheel hop displacement and velocity may now be used as input to a model that predicts the suspension forces. As shown in Figure 7-1, the predicted suspension force variation will be used to select the suspension configuration that will result in the lowest suspension force variation. The pitch-bounce model of Figure 7-2 (see Equations (7.23) and (7.24)) is used as the predictor model, but now the suspension strut forces and the effect of load transfer during braking is included.

The system of differential equations needs to be integrated from an initial time to some final time with predetermined initial conditions. The solver used for the integration is MATLAB's (MathWorks, 2016) implementation of the explicit Runge-Kutta (4,5) formula, the Dormand-Prince pair. It computes the solution to the system of differential equations with knowledge of only the solution at the previous time step. The solver is intended to solve nonstiff systems. A nonstiff solver is suitable to the task at hand, as the frequency bandwidth of interest is from the body pitch natural frequency up to and including the wheel hop natural frequency (which is typically below 20Hz). The body pitch natural frequency depends on the suspension mode and varies from 1.25Hz to 2.7Hz, depending on the gas volume selected on the $4S_4$. The natural frequencies present in the pitch-bounce model are thus within relatively close proximity to one another and a stiff solver is not necessary.

7.3.1 *Predictor pitch-bounce model*

The predictor model differs slightly from the pitch-bounce model of Equations (7.12) to (7.14), because the true spring and damping characteristics of the $4S_4$ are used. The predictor model is thus a nonlinear model. Equations (7.23) and (7.24) are rewritten as a first order differential equation, to be solved with the Runge-Kutta solver. The predictor model's equations are given in Equations (7.18) to (7.24). The load transfer during braking is included in Equations (7.21) and (7.22). Note that braking will induce a negative acceleration in the x-direction by the sign convention used throughout this project.

$$z_f = z_3 - l_f\theta_y - z_{1\_UKF} \tag{7.18}$$

$$\dot{z}_f = \dot{z}_3 - l_f\dot{\theta}_y - \dot{z}_{1\_UKF} \tag{7.19}$$

$$z_r = z_3 + l_r\theta_y - z_{2\_UKF} \tag{7.20}$$

$$\dot{z}_r = \dot{z}_3 + l_r\dot{\theta}_y - \dot{z}_{2\_UKF} \tag{7.21}$$

$$F_{susp\_front} = f_{4S_{4_{front}}}(z_f, \dot{z}_f) - \frac{m_s h_{PC}}{l_f + l_r}\ddot{x} \tag{7.22}$$

$$F_{susp\_rear} = f_{4S_{4_{rear}}}(z_r, \dot{z}_r) + \frac{m_s h_{PC}}{l_f + l_r}\ddot{x} \tag{7.23}$$

$$\begin{Bmatrix} \dot{z}_3 \\ \ddot{z}_3 \\ \dot{\theta}_y \\ \ddot{\theta}_y \end{Bmatrix} = \begin{bmatrix} 0 & 1 & 0 & 0 \\ 0 & 0 & 0 & 0 \\ 0 & 0 & 0 & 1 \\ 0 & 0 & 0 & 0 \end{bmatrix} \begin{Bmatrix} z_3 \\ \dot{z}_3 \\ \theta_y \\ \dot{\theta}_y \end{Bmatrix} + \begin{bmatrix} 0 & 0 \\ \frac{1}{m_s} & \frac{1}{m_s} \\ 0 & 0 \\ -\frac{l_f}{I_y} & \frac{l_r}{I_y} \end{bmatrix} \begin{Bmatrix} F_{susp\_front} \\ F_{susp\_rear} \end{Bmatrix} \tag{7.24}$$

7.3.2 *Suspension force prediction results*

The wheel hop estimates of Section 7.3.1 are now used as inputs to the pitch-bounce predictor model. The ADAMS simulated and predicted suspension forces for the parallel

corrugation track, angled corrugation track and the Belgian paving are shown in Figure 7-7, Figure 7-8, and Figure 7-9, respectively. Although there are some slight discrepancies between the predicted and simulated forces, the results show that the suspension forces can be very accurately predicted on the three tracks of interest when using simulation results. These discrepancies may be attributed to the fact the estimated wheel hop used for the prediction is not precisely the same as the actual wheel hop and that a simplified pitch-bounce model is used.

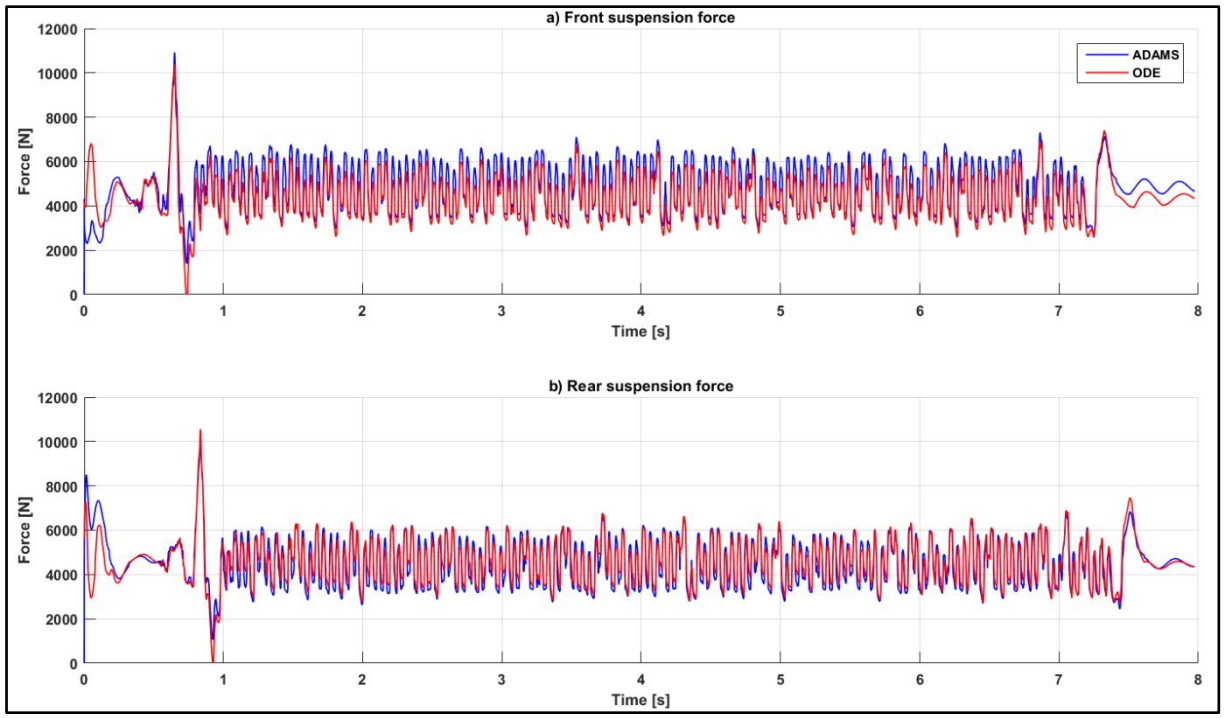

Figure 7-7 Parallel corrugation track suspension prediction results

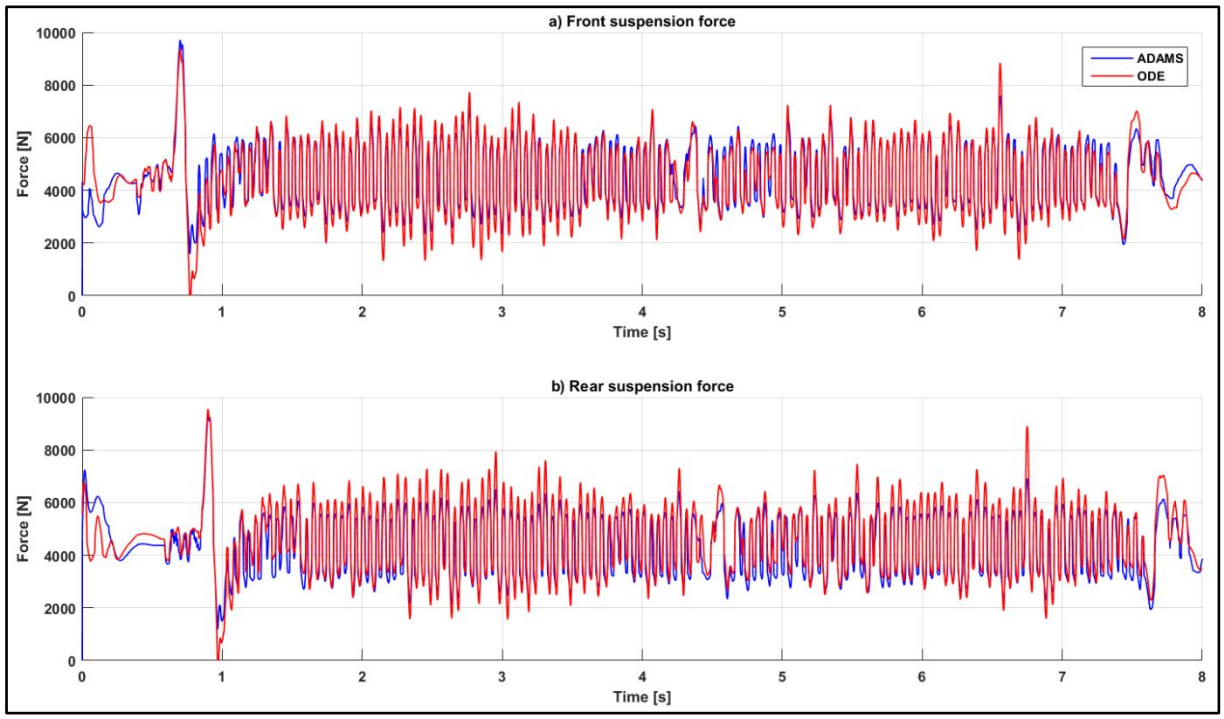

Figure 7-8 Angled corrugation track suspension prediction results on Ride Comfort suspension mode

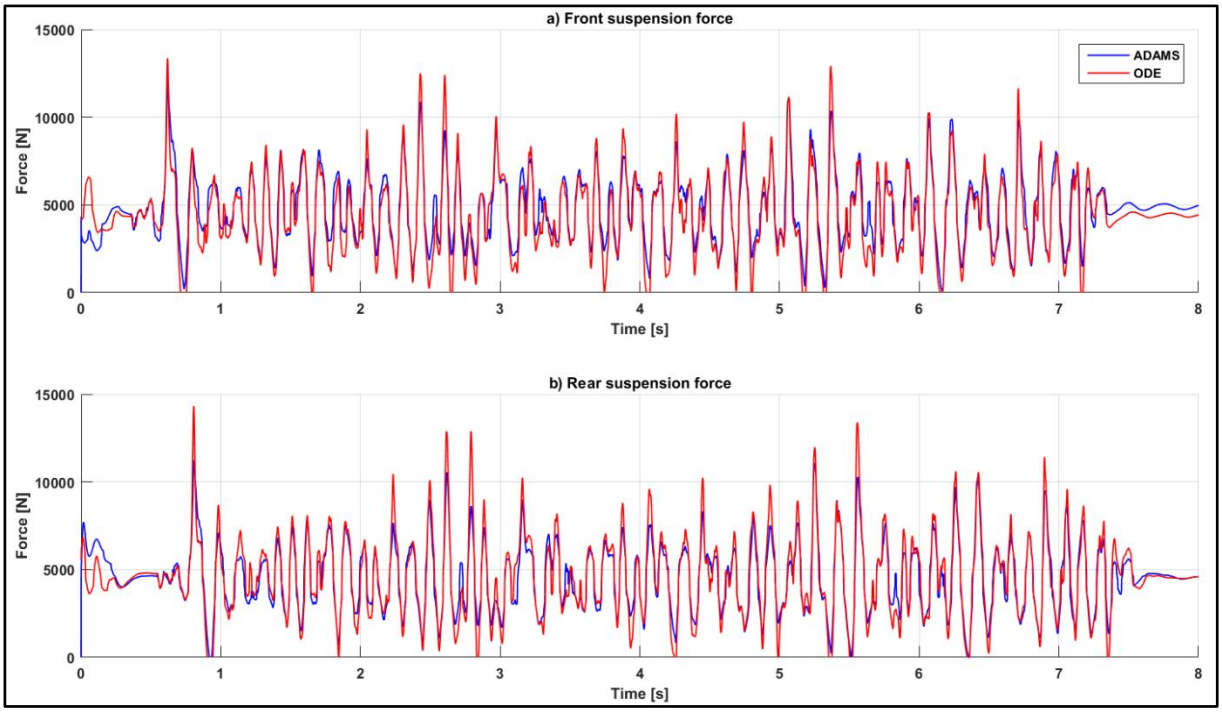

Figure 7-9 Belgian paving suspension prediction results on Ride Comfort suspension mode

Although the application of the wheel hop estimation and suspension force prediction results to measurements generated in the simulation environment looks very promising, experimental validation is required to remove all doubt. Experiments were conducted at Gerotek Testing Facilities (Armscor Defence Institutes SOC) to validate the proposed algorithm. Direct measurement of the absolute wheel hop is very difficult, and hence it was decided to use the measured suspension forces for validation purposes. The measured states are listed in Table 7-2.

Table 7-2 Measured states and sensors used

MEASURED STATES	SENSOR
Front right unsprung mass vertical acceleration	10g accelerometer
Rear right unsprung mass vertical acceleration	10g accelerometer
Front right suspension strut pressure	400bar pressure transducer
Rear right suspension strut pressure	250bar pressure transducer
Front right suspension relative displacement	Linear variable differential transformer (LVDT)
Rear right suspension relative displacement	Linear variable differential transformer (LVDT)
Sprung mass CG vertical acceleration	4g accelerometer
Sprung mass pitch rate	Gyroscope

Data was captured on a HBM eDAQlite (HBM) at a sampling frequency of 2000Hz. The HBM eDAQlite has built in anti-aliasing filters and no further signal processing of the measured data was performed. The vehicle was driven at a constant speed (approximately 30 to 35km/h) over the Belgian paving. The velocity was held constant by driving the vehicle in first gear at the engine speed limit, but some speed fluctuation is inevitable. Figure 7-10 shows the measured data on the Belgian paving. The measured strut pressures were used to calculate the strut forces. The pressure transducers were located between the main strut piston and the floating pistons separating the hydraulic fluid from the gas accumulators. The strut forces calculated from the pressure transducers thus include the force due to the gas accumulators and the damper packs, but excludes the force due to strut friction.

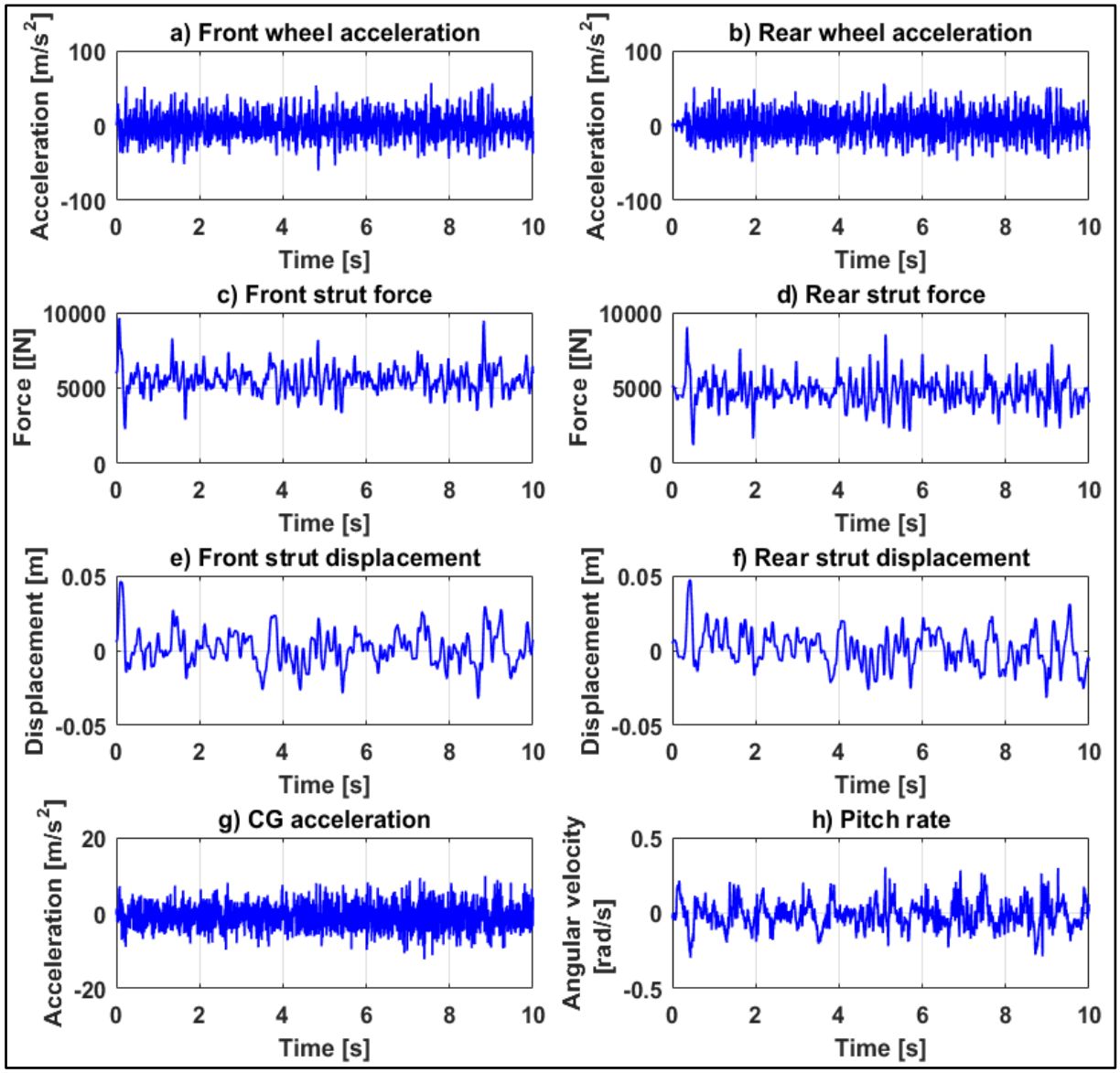

Figure 7-10 Example of measured data on Belgian paving

The measured data is given as inputs to the estimation algorithm, which estimates the wheel hop. The estimated wheel hop is used as excitation for the pitch-bounce predictor model and the resulting strut forces are compared with the measured strut forces. The estimated wheel hop is shown in Figure 7-11 and the predicted suspension force is shown in Figure 7-12. The results show that, although the force prediction is not as accurate as the simulation results, useful results are obtained. Discrepancies may be attributed to inaccuracies in the wheel hop estimation, the use of a simplified vehicle model for prediction and the fact that the friction in the suspension struts are not measured with the pressure transducers. Despite these inaccuracies, the predicted forces may be used to make an informed selection of the suspension configuration that will hopefully lead to a reduction in the braking distance.

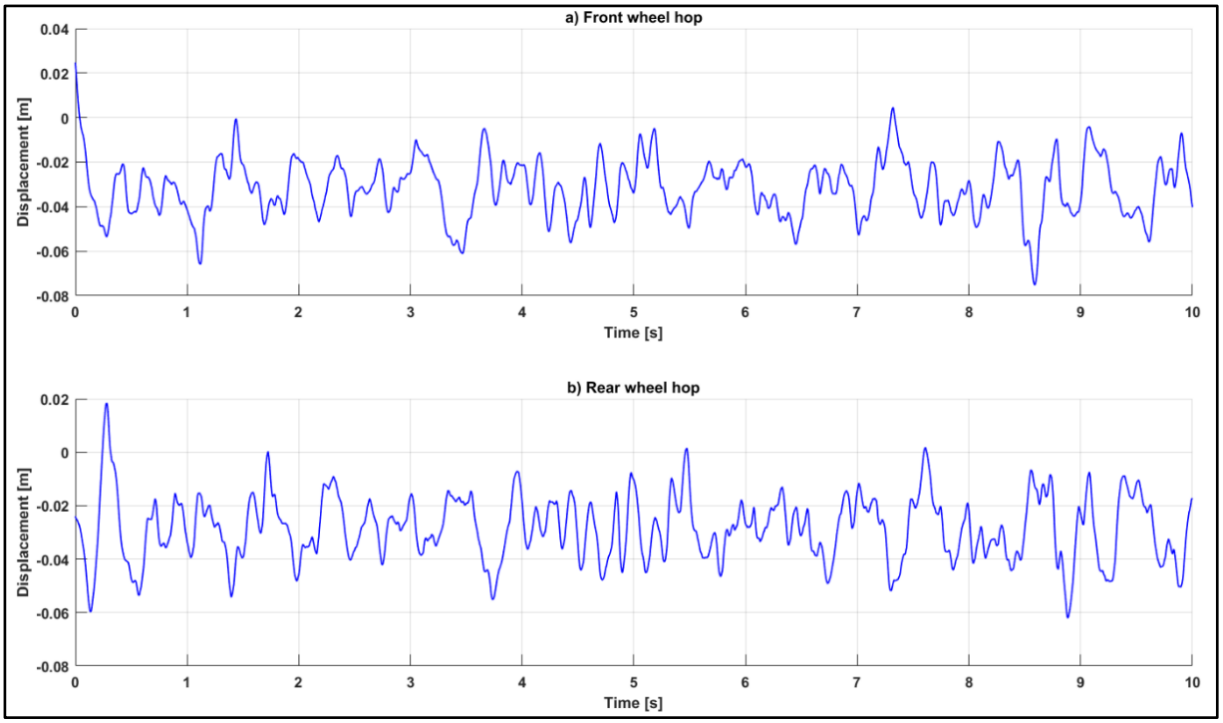

Figure 7-11 Estimated wheel hop with measured data as input

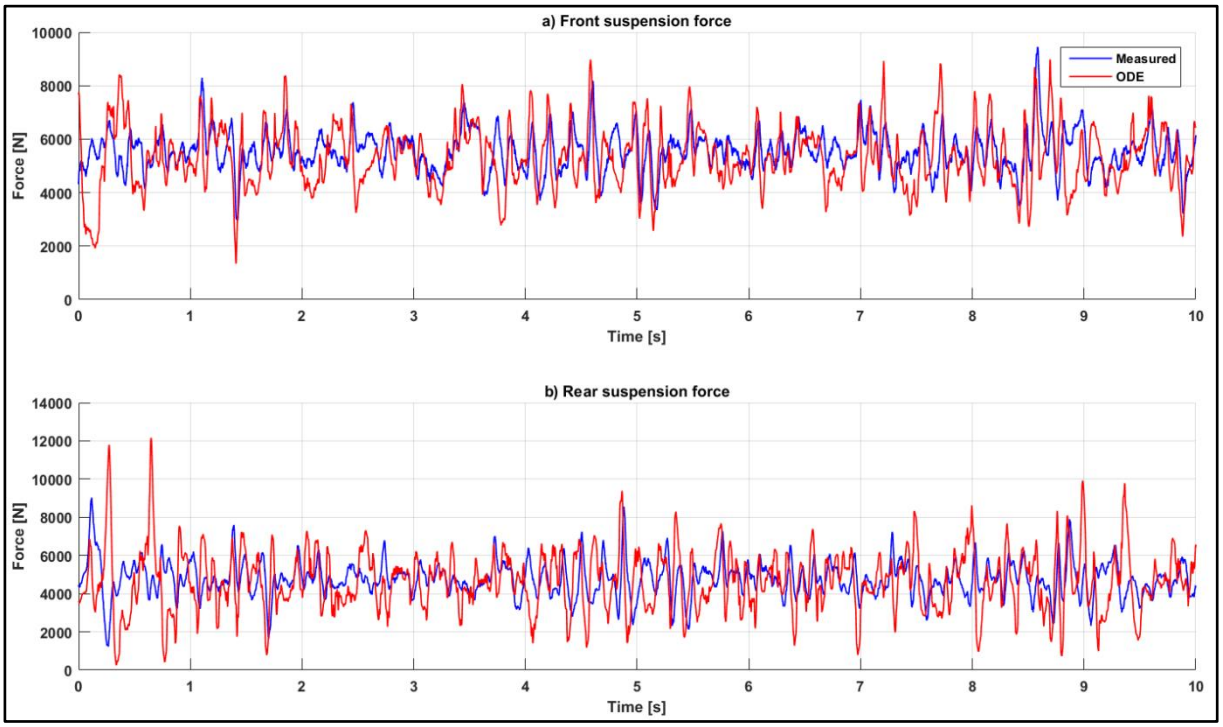

Figure 7-12 Predicted suspension force using experimentally estimated wheel hop as input

7.4 Suspension configuration selection

The final step of the algorithm to reduce the dynamic force variation of the suspension struts is selecting the ideal configuration. The simulation results of Section 6.2 showed that, in general, lower damping in the front and rear suspension struts results in improved braking. The suspension stiffness has a significant influence on reducing the stopping distance, but the ideal suspension stiffness varies, depending on the road excitation and the vehicle speed. The results shown in Section 6.2 showed that reducing the strut force variance on correlated with shorter stopping distances.

The suspension configuration selection algorithm will thus aim to reduce the strut force standard deviation (standard deviation is the square root of the variance). A smaller standard deviation indicates that the data points in the population are close to the mean of the population. This is in agreement with the literature reviewed in Section 2.2.4, which indicated that the variation in tyre normal force reduces the average longitudinal force generated due to the run-in effect. Standard deviation is defined in Equation (7.25):

$$\sigma = \sqrt{\frac{1}{N-1}\sum_{i=1}^{N}|A_i - \bar{A}|^2} \tag{7.25}$$

where $\bar{A}$ is the mean of the population:

$$\bar{A} = \frac{1}{N}\sum_{i=1}^{N} A_i \tag{7.26}$$

The results shown in Section 6.2 showed the strut force variations for the entire braking simulation. It is however pointless to wait until the vehicle has come to a halt to decide on the optimal suspension configuration. A running standard deviation of a selection of points (the sample) thus has to be determined. The sample size selection is governed by the frequency bandwidth of interest. As mentioned in Section 7.3, the lowest frequency of interest is assumed to be the body pitch natural frequency, which is approximately 1.25Hz. This value was determined by linearizing the suspension stiffness about the static equilibrium point. A frequency of 1.25Hz equates to a time period of 800ms, which at a 0.5ms solver step size, results in a sample size of 1600 data points.

Because dynamic load transfer occurs during braking, it was further decided to include a weighting in the calculation of the standard deviation. The aim of the weighting is to increase the importance of the minimisation of the standard deviation of the force acting on the axle with the highest load. The weighting is determined by comparing the mean forces acting on the front and rear axles, with Equation (7.26), also with a sample size of 1600 and is updated dynamically. The forces used to determine the weighting is obtained from the force prediction model with the current $4S_4$ setting. The weighting, or ratio of the two means is then multiplied or divided with the sample, as shown in Equations (7.27) to (7.29). If load is transferred to the front axle, the ratio will be larger than one and the front axle sample will be larger in magnitude. The rear axle sample will be accordingly reduced. A ratio smaller than one will have the opposite effect.

$$\varphi = {\bar{F}_{front}}\Big/{\bar{F}_{rear}} \tag{7.27}$$

$$F_i = \varphi F_{i,front} + \varphi^{-1} F_{i,rear}, \qquad for\ i = 1,2,3,\dots,N \tag{7.28}$$

$$\sigma_{weighted} = \sqrt{\frac{1}{N-1}\sum_{i=1}^{N}\left|F_i - \bar{F}_{weighted}\right|^2} \tag{7.29}$$

The $4S_4$ setting with the lowest weighted standard deviation is then chosen as the ideal suspension configuration setting. The suspension configuration selection algorithm is dubbed Weighted Standard Deviation Minimisation, or WiSDoM. The WiSDoM algorithm is shown schematically in Figure 7-13. The next step is to apply the WiSDoM algorithm to the simulation model and investigate the results.

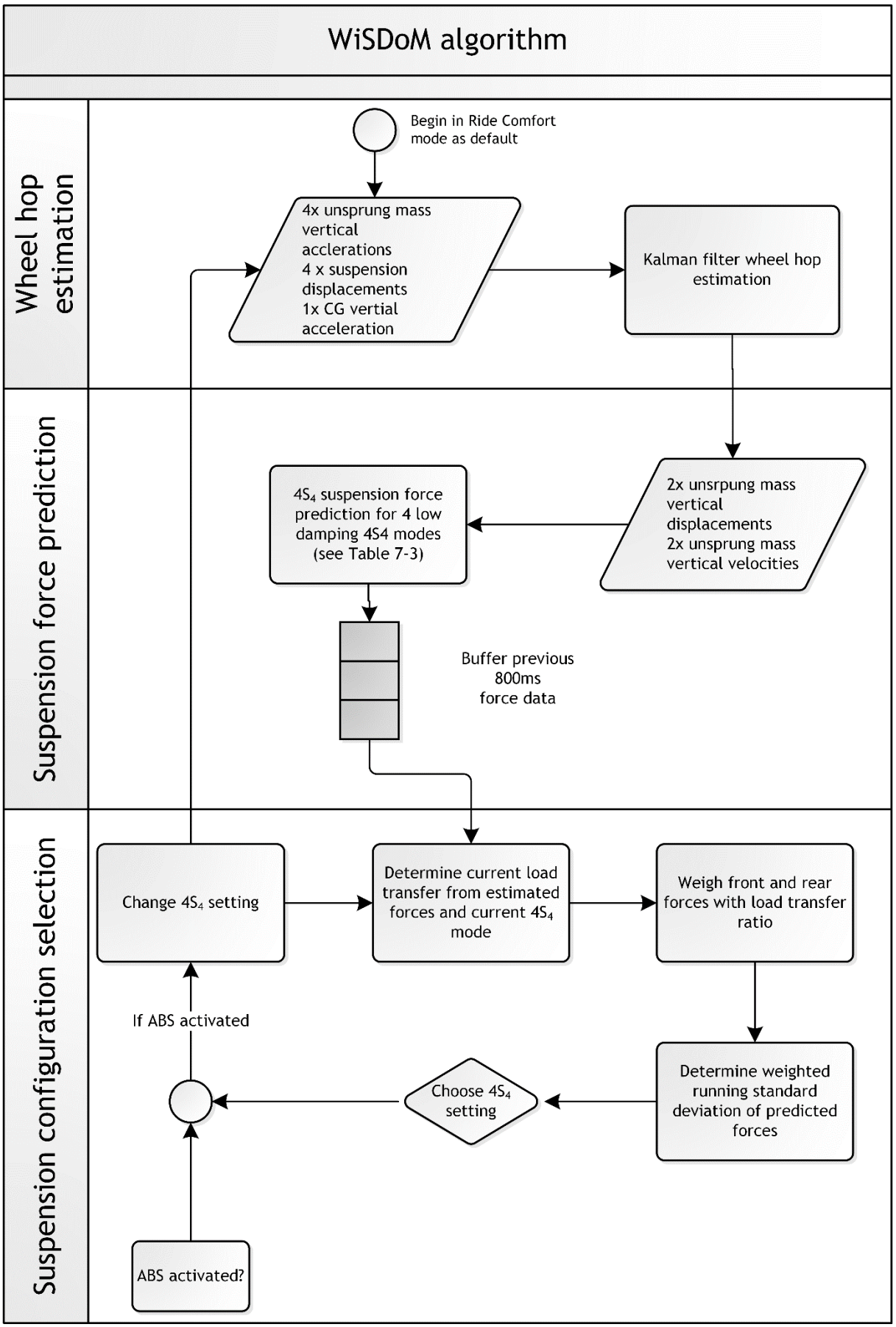

Figure 7-13 Suspension setting selection algorithm

7.5 Simulation results

The WiSDoM algorithm is implemented on the simulation model. A 50ms zero-order hold is imposed on the output of the WiSDoM algorithm. This is done to emulate the 50ms response time of the solenoid valves in the $4S_4$ valve blocks. Simulations are run on the three road profiles, with the $4S_4$ initially set to the 'Ride Comfort' mode. The 'Ride Comfort' mode will in all likelihood be the suspension mode the vehicle is operated in on a rough road. Examples of the simulation results are shown in Figure 7-14 for the parallel corrugations, Figure 7-15 for the angled corrugations, and Figure 7-16 for the Belgian paving. The suspension modes are explained in Table 7-3.

The simulations were repeated for ten different braking points on each road profile to give an indication of the robustness and repeatability of the algorithm. The braking performance of the vehicle with the $4S_4$ passively set to the 'Ride Comfort' mode is also simulated with the same braking points. The 'Ride Comfort' mode simulations will serve as the baseline against which the WiSDoM results are evaluated. The stopping distances of the simulations are given in Table 7-4

Table 7-3 Key to suspension modes in Figure 7-14, Figure 7-15, and Figure 7-16

KEY	FRONT GAS VOLUME [ℓ]	REAR GAS VOLUME [ℓ]	FRONT DAMPING SCALE FACTOR [-]	REAR DAMPING SCALE FACTOR [-]
1	0.1	0.1	0.25	0.25
2	0.1	0.5	0.25	0.25
3	0.5	0.1	0.25	0.25
4	0.5	0.5	0.25	0.25

Table 7-4 Stopping distances of Ride Comfort simulations and WiSDoM simulations

	PARALLEL CORRUGATIONS		ANGLED CORRUGATIONS		BELGIAN PAVING	
RUN	**Ride Comfort**	**WiSDoM**	**Ride Comfort**	**WiSDoM**	**Ride Comfort**	**WiSDoM**
1	40.0	38.3	39.3	37.6	44.6	44.0
2	39.8	39.1	40.1	38.9	45.2	44.3
3	39.9	37.8	38.6	37.7	44.8	44.0
4	40.1	38.3	39.0	38.4	48.0	45.4
5	39.4	38.5	38.2	37.3	46.2	43.2
6	39.9	39.3	38.9	39.0	46.4	45.3
7	39.9	38.7	39.2	38.5	46.6	48.0
8	39.8	38.6	38.4	36.9	45.9	44.0
9	39.7	39.3	39.1	38.4	48.2	47.0
10	39.9	39.7	39.1	37.8	48.5	45.9
AVERAGE	39.8	38.8	39.0	38.0	46.4	45.1
STANDARD DEVIATION	0.16	0.56	0.51	0.66	1.33	1.43

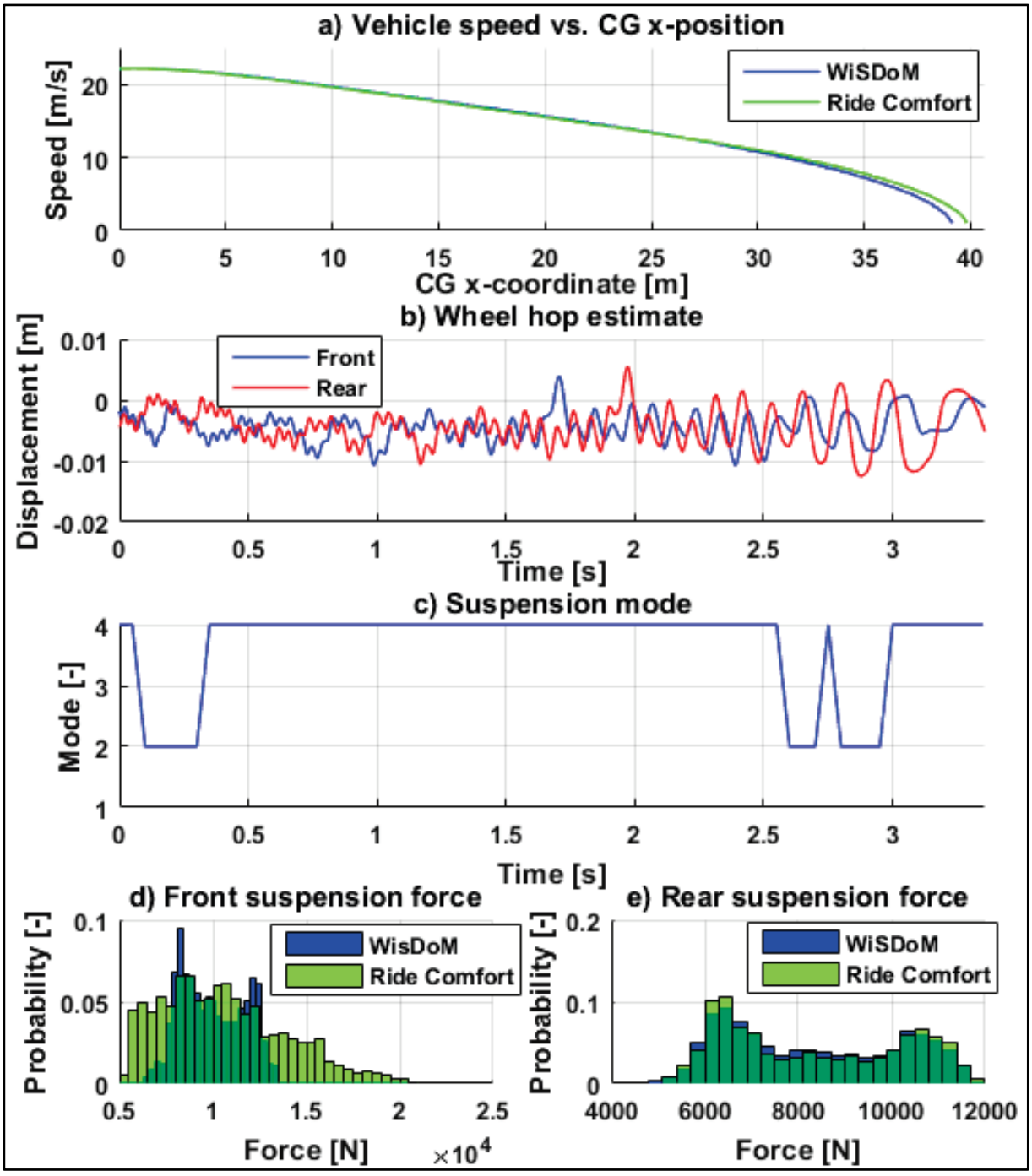

Figure 7-14 Parallel corrugation WiSDoM brake results

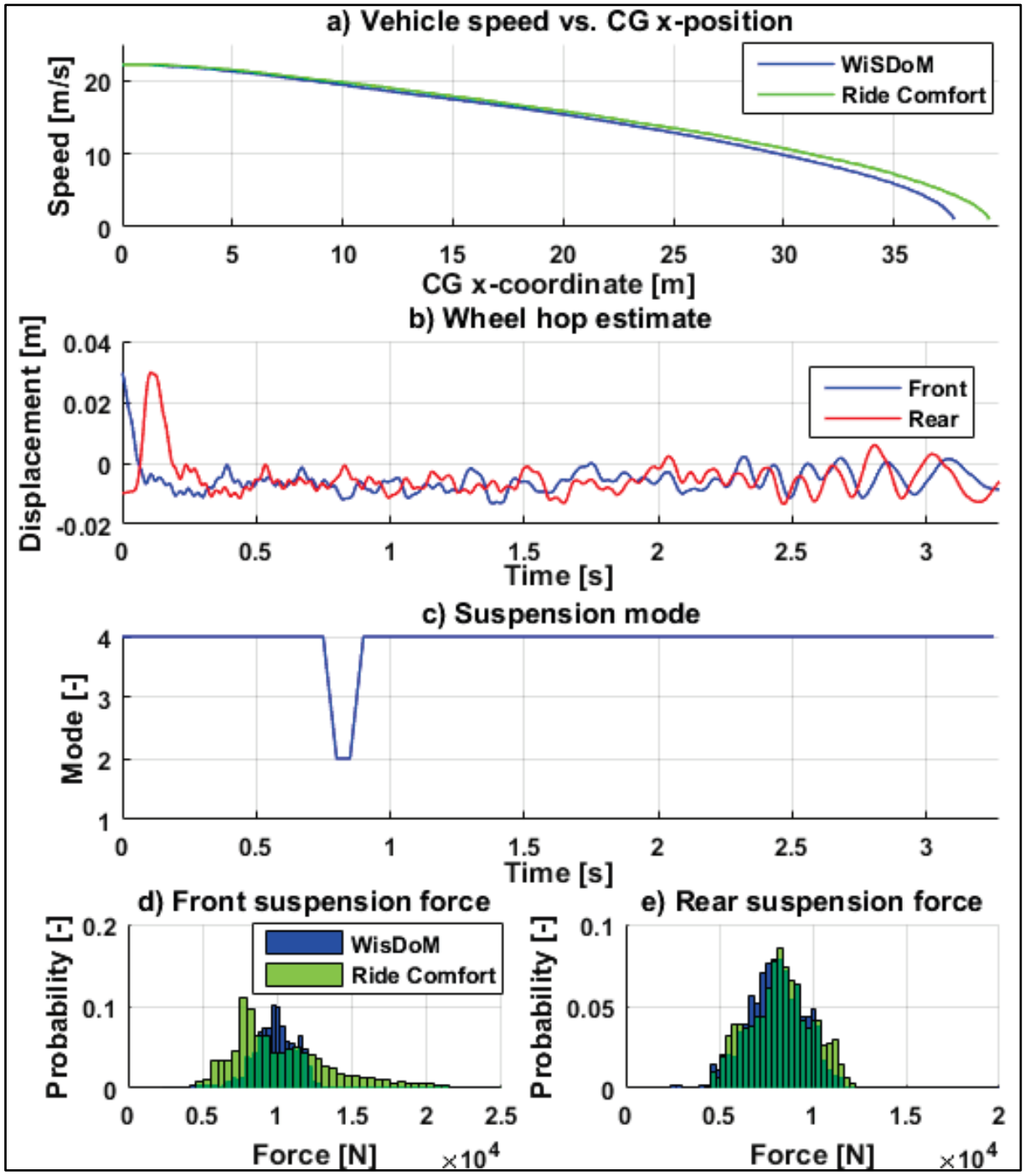

Figure 7-15 Angled corrugations WiSDoM brake results

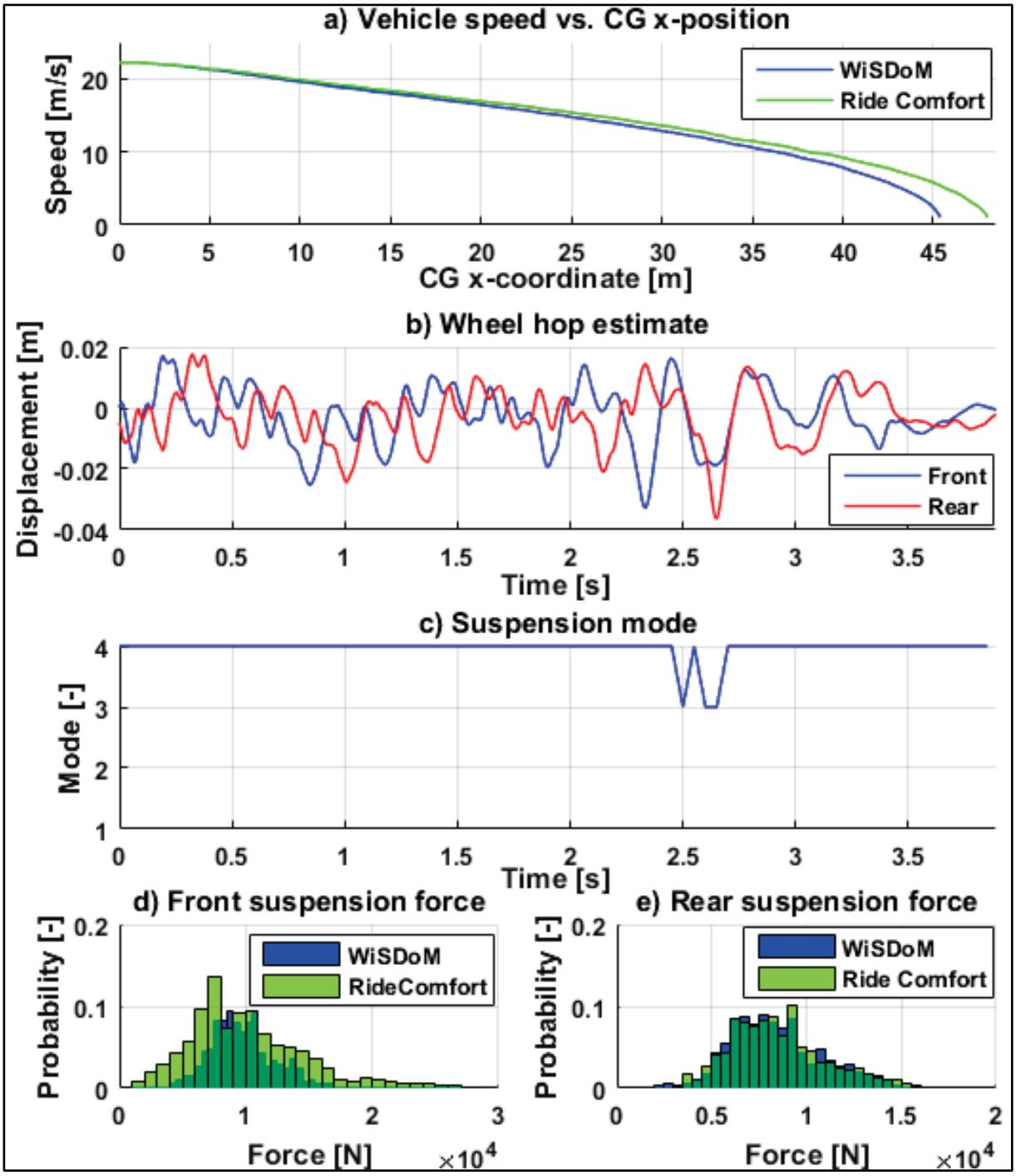

Figure 7-16 Belgian paving WiSDoM brake results

7.6 Discussion of results

The braking performance evaluation technique of Chapter 4 is used to compare the WiSDoM braking results with the 'Ride Comfort' passive suspension mode results as baseline. Figure 7-17 compares the parallel corrugations simulation results, Figure 7-18 the angled corrugation simulation results, and Figure 7-19 the Belgian paving simulation results.

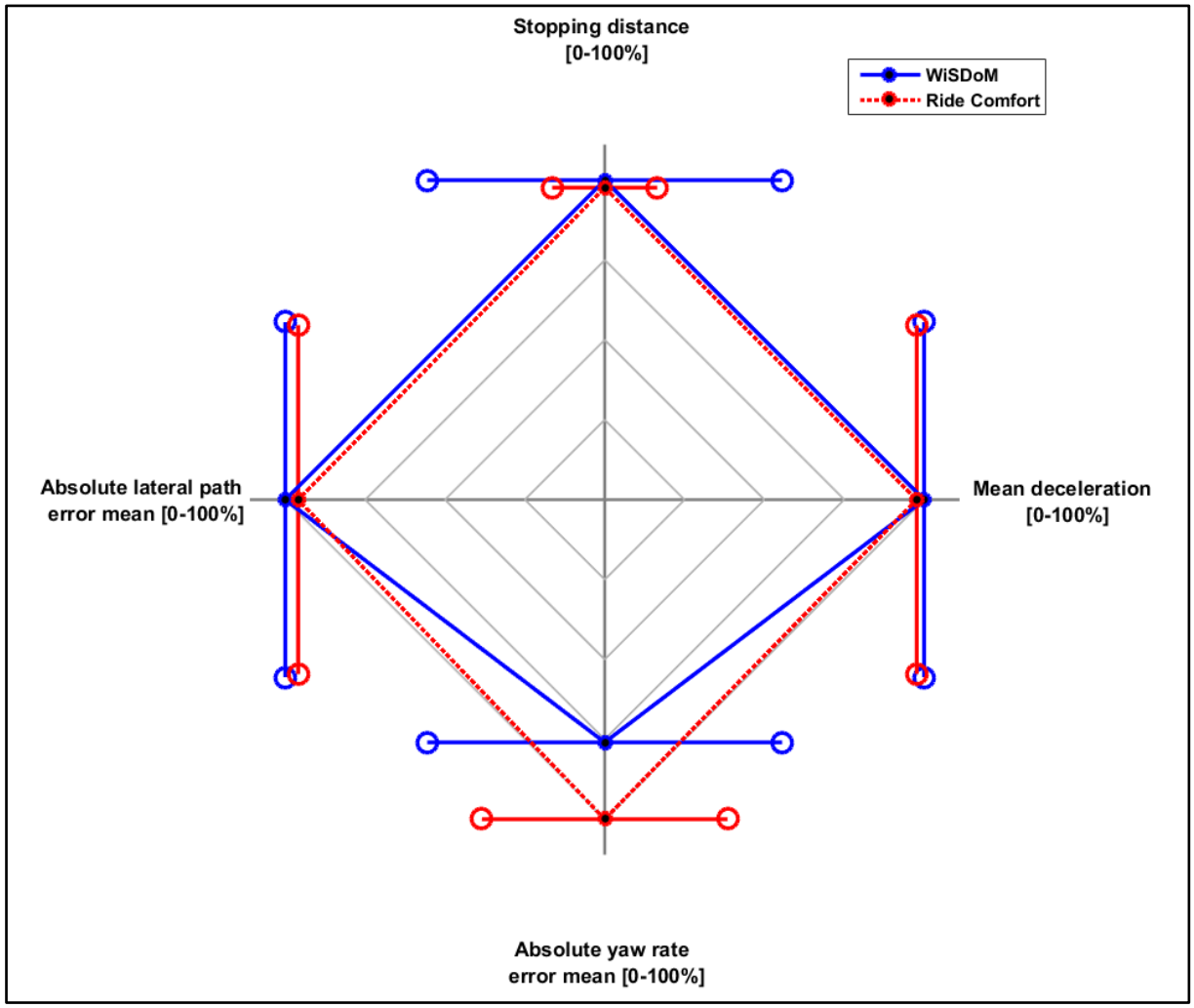

Figure 7-17 Radar plot comparing WiSDoM and 'Ride Comfort' mode simulation results on parallel corrugations

As seen in Table 7-4, the stopping distance with the WiSDoM algorithm on the parallel corrugations improved on average with 1.0m, a difference of 2.7%, compared to the 'Ride Comfort' results. The standard deviation of the 'Ride Comfort' stopping distance, was however, significantly less: 0.16m compared to 0.56m. The improvement in stopping distance by the WiSDoM algorithm is thus almost two standard deviations from the average stopping distance in 'Ride Comfort' mode. The WiSDoM algorithm also improved the mean deceleration, as is expected if the stopping distance is shortened. The lateral path following error was also reduced. The only metric of Figure 7-17 where the 'Ride Comfort' mode outperforms the WiSDoM algorithm on the parallel corrugation, is the absolute yaw rate error. The difference between the two suspension configurations is approximately 27%, a significant difference. Upon closer inspection, the yaw rate errors were found to be 1.8deg/s for the WiSDoM algorithm and 1.3deg/s for the 'Ride Comfort' mode. The corresponding lateral path offset errors were 0.08m for the WiSDoM algorithm and 0.084 for the 'Ride Comfort' mode. These are insignificant differences. Considering that the brake manoeuvre is in a straight line, both the lateral path error and yaw rate error differences may be considered negligible. The WiSDoM algorithm thus improves the stopping distance of the vehicle on the parallel corrugations when compared with the 'Ride Comfort' mode, without affecting the controllability or steerability.

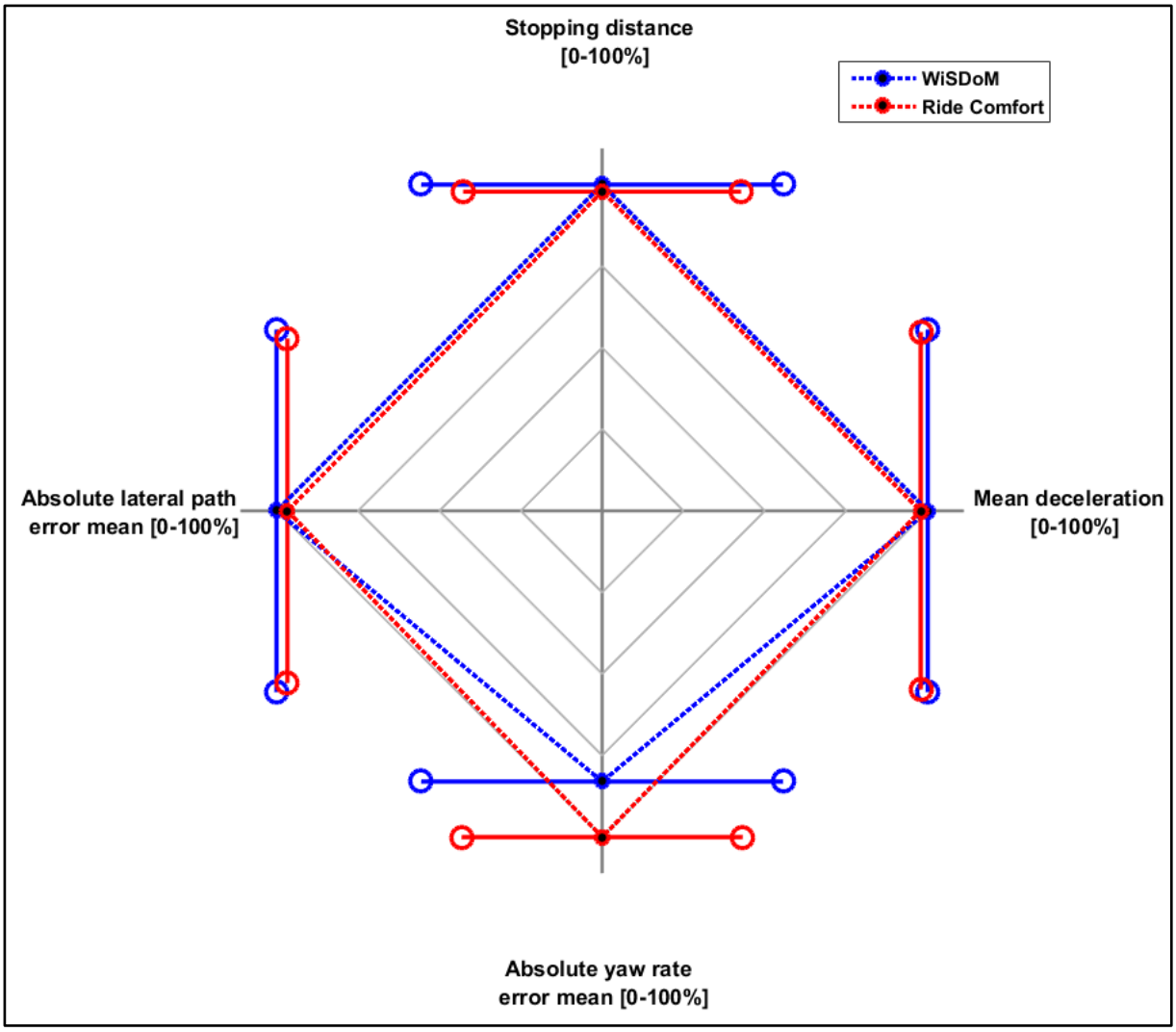

Figure 7-18 Radar plot comparing WiSDoM and 'Ride Comfort' mode simulation on the angled corrugations

Figure 7-18 compares the braking performane of the WiSDoM algorithm and the 'Ride Comfort' mode on the angled corrugations. The average stopping distance with the WiSDoM algorithm is 38.0m, an improvement of 1.0m over the 'Ride Comfort' mode average. The standard deviation with the WiSDoM algorithm is 0.66m, compared to 0.51 for the 'Ride Comfort' mode. The improvement is thus approximately 1.5 standard deviations. The average lateral path errors are 0.08m for both sets of simulations and the yaw rate errors are 2.1deg/s and 1.7deg/s. It may thus be concluded that the WiSDoM algorithm improves the stopping distance without significantly influencing the stability of the vehicle.

The comparison of the braking performance on the Belgian paving, shown in Figure 7-19, was scaled, because the differences are small. The radar plot in Figure 7-19 scales the axes between 90 and 100%, with 100% being the best of the simulated values, as discussed in Chapter 4. The stopping distance on the Belgian paving was improved on average by 1.3m, or 2.8%, with the WiSDoM algorithm. The standard deviation of the stopping distance was 1.43m with the WiSDoM algorithm, compared to 1.33m for the 'Ride Comfort' mode results. The average stopping distance thus improved by one standard deviation when the WiSDoM algorithm was activated. The mean deceleration also improved, as is expected when the stopping distance improves. The lateral path error was unchanged at 0.1m. The enlarged scale of the axes in Figure 7-19 over exaggerates the differences. The yaw rate error was also unchanged. The stopping distance on the Belgian paving was thus improved on average by a significant value, without reducing the stability of the vehicle, by applying the WiSDoM algorithm.

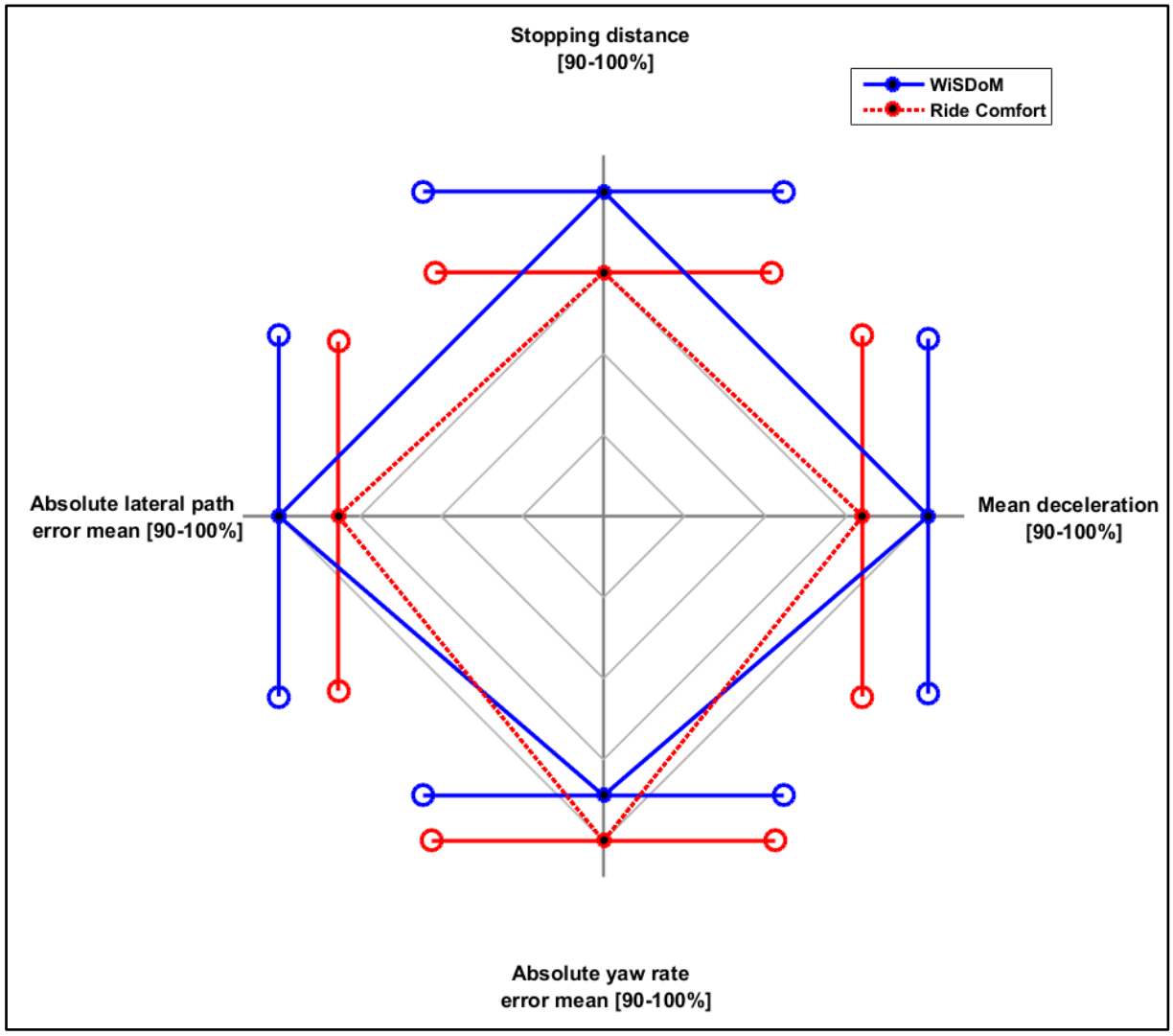

Figure 7-19 Radar plot comparing WiSDoM and 'Ride Comfort' mode simulation results on Belgian paving

The final comparison of this chapter is between the braking results on a smooth road with the WiSDoM algorithm activated and with the suspension left passively in 'Ride Comfort' mode. This is done to ensure that the braking performance on a smooth road is not negatively affected by activating the WiSDoM algorithm. The comparison is shown in Figure 7-20.

Only a single simulation was done, as different braking points on a smooth road will not change the simulation results. The stopping distance with the WiSDoM algorithm activated was 28.5m, compared to 28.3m with the suspension left passively in 'Ride Comfort' mode, a difference of 0.9%. The average deceleration during the tests were 8.9m/s^2 and 9.1m/s^2 for the two tests, very close to the friction limit on typical paved roads. The path offset errors were 0.1m for the WiSDoM algorithm and 0.09m for the 'Ride Comfort' mode. The yaw rate errors were 2.6deg/s and 1.5deg/s, negligible errors. The WiSDoM algorithm thus performs slightly worse than the 'Ride Comfort' mode on a smooth road. This can be avoided by fine-tuning the wheel hop detection algorithm. Additionally, a cut-off limit can be placed on the unsprung mass vertical acceleration. Below the acceleration limit, the WiSDoM algorithm may be deactivated.

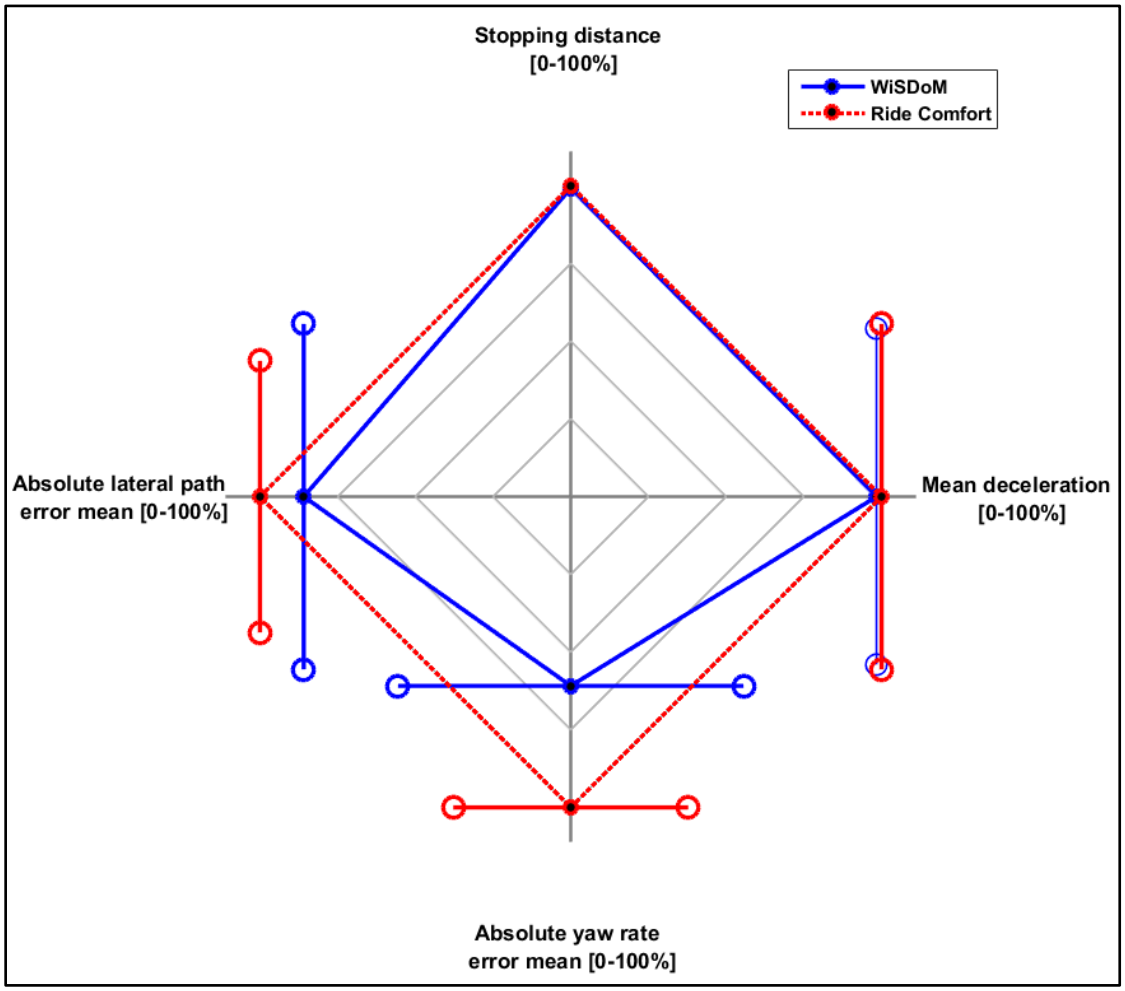

Figure 7-20 Radar plot comparing WiSDoM and 'Ride Comfort' mode simulation results on a smooth road

7.7 Conclusion

This chapter set out to improve the braking performance of the vehicle on the three rough roads investigated in Chapter 6. A control strategy that estimates the vertical wheel hop, predicts the suspension forces for the lowest damping setting, and then selects the ideal suspension configuration was proposed.

Wheel hop estimation was done with a linear Kalman filter relying on easily measureable vehicle states. The wheel hop estimation results compared favourably with simulated results. The suspension force was predicted with a simplified pitch-bounce model that takes the estimated wheel hop as input. The predicted forces were compared with experimentally measured forces and an acceptable correlation was obtained.

Finally, the ideal suspension configuration was selected, based on the predicted suspension forces. The ideal configuration selection was based on the weighted running standard deviation of the suspension force. A dynamic weighting based on the load transfer from the rear to the front axle was used.

The control strategy's effectiveness was investigated by doing several braking simulations on the three off-road road profiles with different starting positions. The results were compared with braking simulations performed with the same starting positions, but with the suspension passively set to the default 'Ride Comfort' mode. The results showed that, on average, the developed control strategy outperformed the baseline mode when considering the stopping distance. This improvement in stopping distance did not significantly compromise the stability of the vehicle during braking.

Chapter 8

Conclusions and recommendations

8.1 Conclusion

The aim of this project was to improve the braking performance of a vehicle on rough roads. An initial experimental investigation indicated that the stopping distance of a vehicle increases significantly when braking on a rough road such as a Belgian paving. Four research questions were formulated:

a) *What are the causes of the unsatisfactory stopping time and distance when braking on a rough road and how can they be addressed?*
b) *Can the off-road braking of a vehicle be modelled mathematically?*
c) *What are the criteria used to evaluate the on-road braking performance of a vehicle and can the off-road braking performance of a vehicle be evaluated using the same criteria?*
d) *Can the off-road braking performance be improved without compromising the on-road performance?*

Two main factors that were identified that may possibly influence the worsened braking performance on a rough road, namely the inputs to the ABS algorithm and the physical phenomena related to the tyres' force generation properties. These two factors were identified through an extensive literature survey, in an attempt to address research question a). The literature did not reveal any method in which these factors had been addressed successfully in the past, and further investigation was deemed necessary.

The first step in investigating these two factors and addressing the four research questions was the development of a very detailed multi-body dynamics model of the experimental vehicle in ADAMS (MSC Software, 2016). An ABS algorithm modelled on the Bosch algorithm was included in the model. An experimentally validated FTire tyre model was used. The vehicle model was validated experimentally with very good correlation between measured and modelled responses. The validation results confirmed that the vehicle's braking performance can indeed be modelled mathematically, answering research question b).

The next step taken was addressing research question c). There is a significant amount of literature on various ABS algorithms and strategies, the majority of which focuses on braking on smooth roads, with varying friction coefficients, with passenger vehicles. No single, quantifiable metric exists in the literature that takes all of the aspects of ABS braking (as defined by the SAE) into account. A quantifiable evaluation technique comprising four metrics was developed that can be applied to on-road and off-road braking. The developed evaluation technique has the added advantage that it can be represented visually and allows the control system design engineer to easily identify the algorithms giving the best performance. This addresses research question c).

Equipped with an experimentally validated model and an ABS performance evaluation technique, the validity of some assumptions used in ABS algorithms and the influence of tyre force generation on the braking performance was investigated. ABS algorithms rely on the assumptions regarding the kinematic rolling radius to estimate longitudinal wheel slip. The

validity of assuming the kinematic rolling radius is constant, defined under specified zero conditions, was investigated experimentally and found to be a valid assumption. The assumption of a constant kinematic rolling radius thus does not contribute to the degradation of braking performance on a rough road.

The influence of tyre force generation on the braking performance was investigated next. The influence of tyre force generation was investigated by performing several simulations on three different rough roads with various suspension configurations. The suspension configuration was found to have a significant influence on the braking performance. The significant tyre normal force variation experienced on rough roads was found to significantly contribute to the unsatisfactory braking performance. This concurs with the limited available literature. The tyre normal force variation correlated with suspension force variation. No single suspension configuration was identified that could improve the stopping distance on rough roads. The ideal suspension configuration varied across the three road profiles used and it changed as the vehicle speed decreased during braking. Lower damping in general resulted in shorter stopping distances on the three rough roads. This partially answers research question a).

Further improvement of the braking performance was sought based on the tyre force generation investigation. A three step algorithm, called the Weighted Standard Deviation Minimisation algorithm (WiSDoM), which attempts to reduce the suspension force variation was developed. The three steps were:

1. Estimating wheel hop with a linear Kalman filter that takes the unsprung mass vertical accelerations, sprung mass CG vertical acceleration, sprung mass pitch rate, and suspension displacements as input. The resulting wheel hop estimates correlated closely with the simulated wheel hop.
2. Predicting the suspension forces based on the wheel hop estimates with a simplified pitch-bounce model that includes load transfer from the rear to the front axle. The four $4S_4$ suspension configurations with the lowest damping and various gas volumes are used to predict the suspension forces. The predicted forces were compared with measured forces, with acceptable correlation.
3. Selecting the ideal suspension configuration with a weighted running standard deviation of the predicted forces. The weighting was based on the load transfer from the rear to the front axle, with the axle with the higher load given a heavier weighting factor. The weights were updated dynamically based on the longitudinal deceleration. The running window was chosen as 800ms, based on the frequencies of interest.

The performance of the algorithm was evaluated by doing ten simulations on each of the three road profiles with different braking points. The performance was compared to the braking performance from the same braking points if the vehicle suspension was set to the default ‘Ride Comfort’ mode. The WiSDoM algorithm improved the vehicle’s stopping distance on all three road profiles between 2.6% and 2.8%, without negatively affecting the stability of the vehicle during braking.

The ease and relatively low cost associated with implementation of the WiSDoM algorithm must also be noted. This was one of the aims of the proposed algorithm, as stated in Chapter 7. The sensors needed to measure the states of interest are relatively cheap and are already found on higher-end vehicles available on the market. Many of these vehicles are already equipped with air suspension, allowing for easy switching between different spring characteristics.

Another advantage of estimating the wheel hop rather than the road profile is that a tyre model is not needed. If the road profile were estimated and used as a perturbation to the

predictor model, a tyre model capable of running in real-time would have been needed, adding additional complexity to the algorithm.

8.2 Recommendations

Several recommendations may be made, based on the results contained in this thesis.

The first is that the inputs to the ABS algorithm must be studied in more detail, specifically experimentally. The results contained in Chapter 5 showed that the assumption of a static rolling radius is valid. Chapter 5 did however not investigate the estimation of the vehicle speed. The vehicle speed, or reference speed, is usually estimated from the wheel speeds. The experimental results of Chapter 5 showed that the wheel speed contains significant noise due to the road input. Some method of filtering away some of the noise without inducing significant delays may improve the braking results even further. Application of an estimation strategy using a Kalman filter or one of its derivatives may improve the reference speed estimation.

The WiSDoM algorithm can be studied and improved further. The effect of the sample size (currently 800ms) on the standard deviation calculation can be investigated. The efficacy of the WiSDoM algorithm must be done experimentally. Although extensive simulations were done to prove the performance and robustness of the algorithm, the final proof lies in experimental demonstration.

References

ABE, M. 2015. *Vehicle handling dynamics: theory and application*, Butterworth-Heinemann.

ADCOX, J., AYALEW, B., RHYNE, T., CRON, S. & KNAUFF, M. 2012. Interaction of anti-lock braking systems with tire torsional dynamics. *Tire Science and Technology,* 40**,** 171-185.

ADCOX, J., AYALEW, B., RHYNE, T., CRON, S. & KNAUFF, M. 2013. Experimental investigation of tire torsional dynamics on the performance of an anti-lock braking system. ASME 2013 International Design Engineering Technical Conferences and Information in Engineering Conference, 2013 Portland, Oregon August 4-7, 2013. ASME.

ALLEYNE, A. 1997. Improved Vehicle Performance Using Combined Suspension and Braking Forces. *Vehicle System Dynamics,* 27**,** 235-265.

ALY, A. A., ZEIDAN, E.-S., HAMED, A. & SALEM, F. 2011. An Antilock-Braking Systems (ABS) Control: A Technical Review. *Intelligent Control and Automation,* 02**,** 186-195.

ARMSCOR DEFENCE INSTITUTES SOC. 2016. *Gerotek Test Facilities* [Online]. Available: http://www.armscordi.com/SubSites/Gerotek1/Gerotek01_landing.asp [Accessed 12 July 2016].

BABULAL, Y., STALLMANN, M. J. & ELS, P. S. 2015. Parameterisation and modelling of large off-road tyres for on-road handling analyses. *Journal of Terramechanics,* 61**,** 77-85.

BAKKER, E., PACEJKA, H. B. & LIDNER, L. 1989. A new tire model with an application in vehicle dynamics studies. *SAE paper,* 890087**,** 101-113.

BECKER, C. M. & ELS, P. S. 2012. Wheel force transducer measurements on a vehicle in transit. *12th European Regional Conference of the ISTVS*. Pretoria, South Africa.

BECKER, C. M. & ELS, P. S. 2014. Profiling of rough terrain. *International Journal of Vehicle Design,* 64**,** 240-261.

BLUNDELL, M. & HARTY, D. 2004. *The multibody systems approach to vehicle dynamics*, Elsevier.

BOSCH, H.-R. B., HAMERSMA, H. A. & ELS, P. S. 2016. Parameterisation, validation and implementation of an all-terrain SUV FTire tyre model. *Journal of Terramechanics,* 67**,** 11-23.

BOSCH, R. 2005. *Driving Stability Systems*, Sae Soc Of Automotive Eng.

BOTHA, T. R. 2011. *High speed autonomous off-road vehicle steering*. MEng (Mechanical), University of Pretoria.

BOTHA, T. R. & ELS, P. S. 2014. Tire Longitudinal Slip-Ratio Measurement Using a Camera. ASME 2014 International Design Engineering Technical Conferences and Computers and Information in Engineering Conference, 2014. American Society of Mechanical Engineers, V003T01A043-V003T01A043.

BOTHA, T. R., SHYROKAU, B., ELS, P. S. & HOLWEG, E. 2015. Kinematic analysis of a tyre rolling over rough terrain using digital image correlation. *In:* PAOLUZZI, R. (ed.) *13th ISTVS European Conference*. Rome, Italy: ISTVS.

BRADLEY, J. & ALLEN, R. 1931. The behaviour of rubber-tyred wheels. *The automotive engineer,* 21.

BREUER, B. & BILL, K. H. 2008. *Brake technology handbook*.

BUDYNAS, R. G. & NISBETT, J. K. 2008. *Shigley's Mechanical Engineering Design Eighth Edition in SI Units,* New York, NY, McGraw-Hill Education (Asia).

DAY, T. D. & ROBERTS, S. G. 2002. A simulation model for vehicle braking systems fitted with ABS. SAE Technical Paper.

DIAMOND SYSTEMS CORPORATION. 2016. *Helios PC/104 SBC* [Online]. Available: http://www.diamondsystems.com/products/helios [Accessed 20 July 2016].

DUKKIPATI, R. V., PANG, J., QATU, M. S., CHEN, G. S. & SHUGUANG, Z. 2008. *Road vehicle dynamics*.

ELS, P. S. 2006. *The ride comfort vs. handling compromise for off-road vehicles*. PhD (Mechanical Engineering), University of Pretoria.

ELS, P. S., UYS, P. E., SNYMAN, J. A. & THORESSON, M. J. 2006. Gradient-based approximation methods applied to the optimal design of vehicle suspension systems using computational models with severe inherent noise. *Mathematical and Computer Modelling,* 43**,** 787-801.

FIALA, E. 1954. Seitenkrafte am rollenden Luftreifen. *ZVD I,* 96**,** Nr. 29.

FISCHLER, M. A. & BOLLES, R. C. 1981. Random sample consensus: a paradigm for model fitting with applications to image analysis and automated cartography. *Communications of the ACM,* 24**,** 381-395.

FMVSS 2013. 571.135 Standard No. 105; Hydraulic and electric brake systems. *In:* REGULATION, C. O. F. (ed.). Code of Federal Regulations.

GILLESPIE, T. D. 1992. *Fundamentals of Vehicle Dynamics,* Warrendale, PA, Society of Automotive Engineers, Inc.

GIPSER, M. 2007. FTire – the tire simulation model for all applications related to vehicle dynamics. *Vehicle System Dynamics,* 45**,** 139-151.

GUGLIELMINO, E., SIRETEANU, T., STAMMERS, C. W., GHITA, G. & GIUCLEA, M. 2008. *Semi-active suspension control: improved vehicle ride and road friendliness*, Springer Science & Business Media.

HAMERSMA, H. A. & ELS, P. S. 2014. Longitudinal vehicle dynamics control for improved vehicle safety. *Journal of Terramechanics,* 54**,** 19-36.

HBM. *Somat eDAQlite* [Online]. Available: https://www.hbm.com/en/2226/somat-edaqlite-modular-rugged-mobile-data-acquisition-system/ [Accessed 2 February 2017].

HEIDRICH, L., SHYROKAU, B., SAVITSKI, D., IVANOV, V., AUGSBURG, K. & WANG, D. 2013. Hardware-in-the-loop test rig for integrated vehicle control systems. *IFAC Proceedings Volumes,* 46**,** 683-688.

INTERNATIONAL ORGANISATION OF STANDARDISATION 1999. ISO 3888-1:1999 Passenger Cars -- Test track for a severe lane-change manoeuvre -- Part 1: Double lane-change. Geneva, Switzerland.

INTERNATIONAL ORGANISATION OF STANDARDISATION 2016. ISO 8608:2016 Mechanical vibration - Road surface profiles - Reporting of measured data. Geneva, Switzerland.

IVANOV, V., SAVITSKI, D., AUGSBURG, K. & BARBER, P. 2015. Electric vehicles with individually controlled on-board motors: Revisiting the ABS design. Mechatronics (ICM), 2015 IEEE International Conference on, 6-8 March 2015 2015a. 323-328.

IVANOV, V., SAVITSKI, D. & SHYROKAU, B. 2015b. A Survey of Traction Control and Antilock Braking Systems of Full Electric Vehicles With Individually Controlled Electric Motors. *Institute of Electrical and Electronics Engineers (IEEE) Transactions on Vehicular Technology,* 64**,** 3878-3896.

JAISWAL, M., MAVROS, G., RAHNEJAT, H. & KING, P. D. 2010. Influence of tyre transience on anti-lock braking. *Proceedings of the Institution of Mechanical Engineers, Part K: Journal of Multi-body Dynamics,* 224**,** 1-17.

KALMAN, R. E. 1960. A new approach to linear filtering and prediction problems. *Journal of basic Engineering,* 82**,** 35-45.

KAPP, M. & ELS, P. S. 2015. *Robust High Speed Autonomous Steering of an Off-Road Vehicle*. University of Pretoria.

KAT, C. J., JOHRENDT, J. L. & ELS, P. S. 2012. Computational Efficiency and Accuracy Comparison of Leaf Spring Modelling Techniques. *Proceedings of the Asme International Design Engineering Technical Conferences and Computers and Information in Engineering Conference, Vol 6***,** 605-613.

KIENHÖFER, F. W., MILLER, J. I. & CEBON, D. 2008. Design concept for an alternative heavy vehicle ABS system. *Vehicle System Dynamics,* 46**,** 571-583.

KISS, P. 2003. Rolling Radii of a Pneumatic Tyre on Deformable Soil. *Biosystems Engineering,* 85**,** 153-161.

LEE, K. C., JEON, J. W., HWANG, D. H. & KIM, Y. J. 2003. Performance evaluation of Antilock Brake Controller for pneumatic brake system. *2003 Ieee Industry Applications Conference, Vols 1-3*, 301-307.

LOWE, D. G. 2004. Distinctive image features from scale-invariant keypoints. *International journal of computer vision,* 60, 91-110.

MATHWORKS. 2016. *MATLAB and Simulink* [Online]. Available: http://www.mathworks.com/ [Accessed 20 July 2016].

MAURICE, J. P. & PACEJKA, H. B. 1997. Relaxation Length Behaviour of Tyres. *Vehicle System Dynamics,* 27, 339-342.

MERIAM, J. L. & KRAIGE, L. G. 2012. *Engineering mechanics: dynamics*, John Wiley & Sons.

MICHELIN. 2016. *Michelin LTX A/T2* [Online]. Available: http://www.michelinman.com/US/en/tires/products/ltx-a-t-2.html# [Accessed 20 Jul 2016].

MILLER, S. L., YOUNGBERG, B., MILLIE, A., SCHWEIZER, P. & GERDES, J. C. 2001. Calculating longitudinal wheel slip and tire parameters using GPS velocity. American Control Conference, 2001. Proceedings of the 2001, 2001. IEEE, 1800-1805.

MSC SOFTWARE. 2016. *Adams* [Online]. MSC Software Corporation. Available: http://www.mscsoftware.com/product/adams [Accessed 18 July 2016].

NIEMZ, T. & WINNER, H. 2006. Reduction of braking distance by control of active dampers. *FISITA World Automotive Congress*. Yokohama, Japan.

NOVATEL INC. n.d. *SPAN-CPT Single Enclosure GNSS/INS Receiver* [Online]. Available: http://www.novatel.com/products/span-gnss-inertial-systems/span-combined-systems/span-cpt/ [Accessed 20 July 2016].

PACEJKA, H. 2005. *Tire and vehicle dynamics*, Elsevier.

PENNY, W. C. W. & ELS, P. S. 2016. The test and simulation of ABS on rough, non-deformable terrains. *Journal of Terramechanics,* 67, 1-10.

REUL, M. & WINNER, H. 2009. Enhanced braking performance by integrated ABS and semi-active damping control. Proceedings of the 21st International Technical Conference on Enhanced safety of vehicles, Stuttgart, Germany, 2009. 09-0204.

SAE 2014. Antilock Brake System Review. SAE International.

SAVITSKI, D., IVANOV, V., AUGSBURG, K., SHYROKAU, B., WRAGGE-MORLEY, R., PU TZ, T. & BARBER, P. 2015. The new paradigm of an anti-lock braking system for a full electric vehicle: experimental investigation and benchmarking. *Proceedings of the Institution of Mechanical Engineers, Part D: Journal of Automobile Engineering*.

SAVITSKI, D., IVANOV, V., SHYROKAU, B., PUTZ, T., DE SMET, J. & THEUNISSEN, J. 2016. Experimental Investigations on Continuous Regenerative Anti-Lock Braking System of Full Electric Vehicle. *International Journal of Automotive Technology,* 17, 327-338.

SCHMEITZ, A. J. C., BESSELINK, I. J. M. & JANSEN, S. T. H. 2007. Tno Mf-Swift. *Vehicle System Dynamics,* 45, 121-137.

SIEGERT, E., VON GLASNER, E.-C., GEIßLER, H., VAN ZANTEN, A., BERG, P., BECKER, R., PFÄFFLE, J., SOWA, P., CZINCZEL, A., SCHMIDT, G., GERSTENMAIER, J., KNUST, A., KÜHNER, K., REINKE, K.-H., STEGMAIER, A., MEIßNER, M. & SIGL, A. 1999. *Driving-safety Systems,* Stuttgart, Germany, Robert Bosch GmbH.

SMALLWOOD, K. 2013. *The First Car Accident* [Online]. Available: http://www.todayifoundout.com/index.php/2013/07/the-first-car-accident [Accessed 12 July 2016].

STALLMANN, M. J. & ELS, P. S. 2014. Parameterization and modelling of large off-road tyres for ride analyses: Part 2-Parameterization and validation of tyre models. *Journal of Terramechanics,* 55, 85-94.

STALLMANN, M. J., ELS, P. S. & BEKKER, C. M. 2014. Parameterization and modelling of large off-road tyres for ride analyses: Part 1-Obtaining parameterization data. *Journal of Terramechanics,* 55, 73-84.

THORESSON, M. J. 2007. *Efficient gradient-based optimisation of suspension characteristics for an off-road vehicle*. PhD (Mechanical Engineering), University of Pretoria.

THORESSON, M. J., BOTHA, T. R. & ELS, P. S. 2014. The relationship between vehicle yaw acceleration response and steering velocity for steering control. *International Journal of Vehicle Design,* 64, 195-213.

THORESSON, M. J., UYS, P. E., ELS, P. S. & SNYMAN, J. A. 2009a. Efficient optimisation of a vehicle suspension system, using a gradient-based approximation method, Part 1: Mathematical modelling. *Mathematical and Computer Modelling,* 50**,** 1421-1436.

THORESSON, M. J., UYS, P. E., ELS, P. S. & SNYMAN, J. A. 2009b. Efficient optimisation of a vehicle suspension system, using a gradient-based approximation method, Part 2: Optimisation results. *Mathematical and Computer Modelling,* 50**,** 1437-1447.

UPADHYAYA, S., CHANCELLOR, W. & WULFSOHN, D. 1988. Sources of variability in traction data. *Journal of terramechanics,* 25**,** 249-272.

VAN DER WESTHUIZEN, S. F. & ELS, P. S. 2015. Comparison of different gas models to calculate the spring force of a hydropneumatic suspension. *Journal of Terramechanics,* 57**,** 41-59.

VIRES SIMULATIONSTECHNOLOGIE GMBH. 2016. *OpenCRG - managing the road surface ahead* [Online]. Available: http://www.opencrg.org/ [Accessed 7 March 2017].

WAN, M. 2000. *Technology development during the past 100 years* [Online]. Autozine. Available: http://www.autozine.org/Misc/Article/tech_history/tech_history.htm [Accessed 12uly 2016].

ZEGELAAR, P. W. A. & PACEJKA, H. B. 1997. Dynamic Tyre Responses to Brake Torque Variations. *Vehicle System Dynamics,* 27**,** 65-79.

Appendix A – Tyre test trailer ADAMS model

The success of this project relies on the accurate modelling of the vehicle and its subsystems and their components. None of these are more important than the tyre and its interaction with the road. As such, an FTire (Gipser, 2007)model was parameterised and experimentally validated. The parameterisation and validation process is outlined in Figure A.1. This process consists of extensive laboratory and field testing.

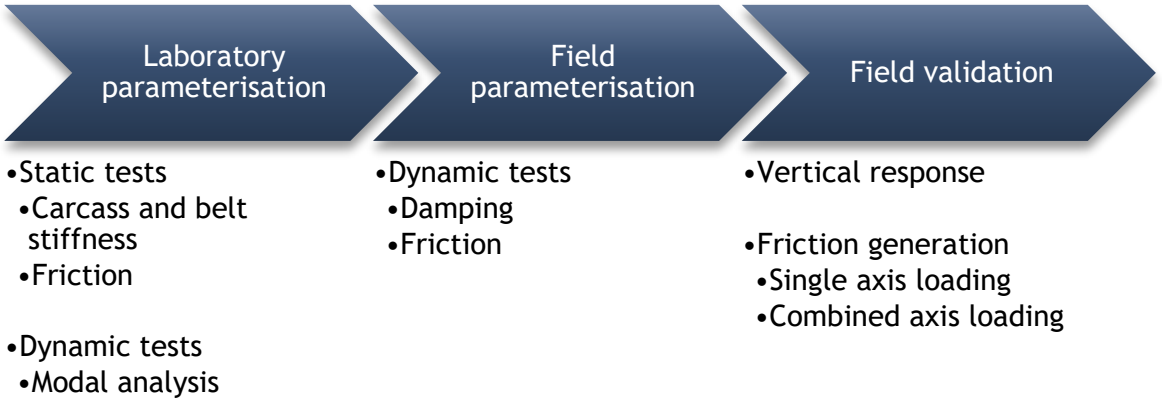

Figure A.1 Tyre parameterisation and validation process

The validation results are presented in Section 3.2.2 and the development of an ADAMS (MSC Software, 2016) model of the tyre test trailer for validation purposes is mentioned, but detail is omitted for the sake of brevity. This Appendix provides some more detail of the modelling of the tyre test trailer.

A.1 The tyre test trailer

The Vehicle Dynamics Group at the University of Pretoria built the tyre test trailer during the course of 2016. It consists of two truck trailer axles with static load ratings of 11ton. The axle closest to the towing vehicle is the test axle and the other is a stabilisation axle. Each axle is equipped with OEM supplied air springs, dampers and axle lifts. The air spring pressures are controlled with on-off valves through pulse width modulation, allowing adjustment of the static load on the test axle. The test axle has adjustable hubs that allow for the continuous variation of the test tyre slip angles and for discrete variation of the camber angles. An OEM supplied, air brake system is used to brake the test tyres. The tyre tester is thus capable of determining the lateral, longitudinal and combined force generation properties of tyres.

Lateral force validation tests are performed by slowly sweeping the tyre slip angles while towing the vehicle at a constant speed. Similarly, longitudinal force validation is done by gradually increasing the brake pressure of the test axle until lockup occurs. The brakes are then released and the process repeated. Combined loading tests are performed by incrementally changing the slip angle, waiting for a small period until the lateral force is presumed to have stabilised, and then brake pressure is gradually increased until lockup

occurs. The brakes are then released and the slip angle adjusted to the next discrete value. The process is then repeated.

Numerous sensors are used to measure the states of interest on the tyre test trailer. The most important of these sensors are the wheel force transducers developed by Becker and Els (2012). The WFTs are used on both the test tyres and record the tyre forces and moments in and about all the Cartesian coordinates. The wheel rotation speeds of both the test tyres and of one of the wheels on the stabilising axle are measured with proximity switches. Measurement of the actual slip angle is done with encoders located on the test axle kingpins. The air spring pressures and brake line pressures are measured with pressure transducers. Data is recorded on Diamond Systems Helios PC/104 form factor Single Board Computers (Diamond Systems Corporation, 2016).

A.2 ADAMS model architecture

Validation of the tyre model properties is done with an ADAMS (MSC Software, 2016) model of the test axle. A simplified model of the axle was built; the architecture is shown schematically in Figure A.2. The model is run in co-simulation with MATLAB/Simulink (MathWorks, 2016). This allows easy input of the experimentally measured states to the model.

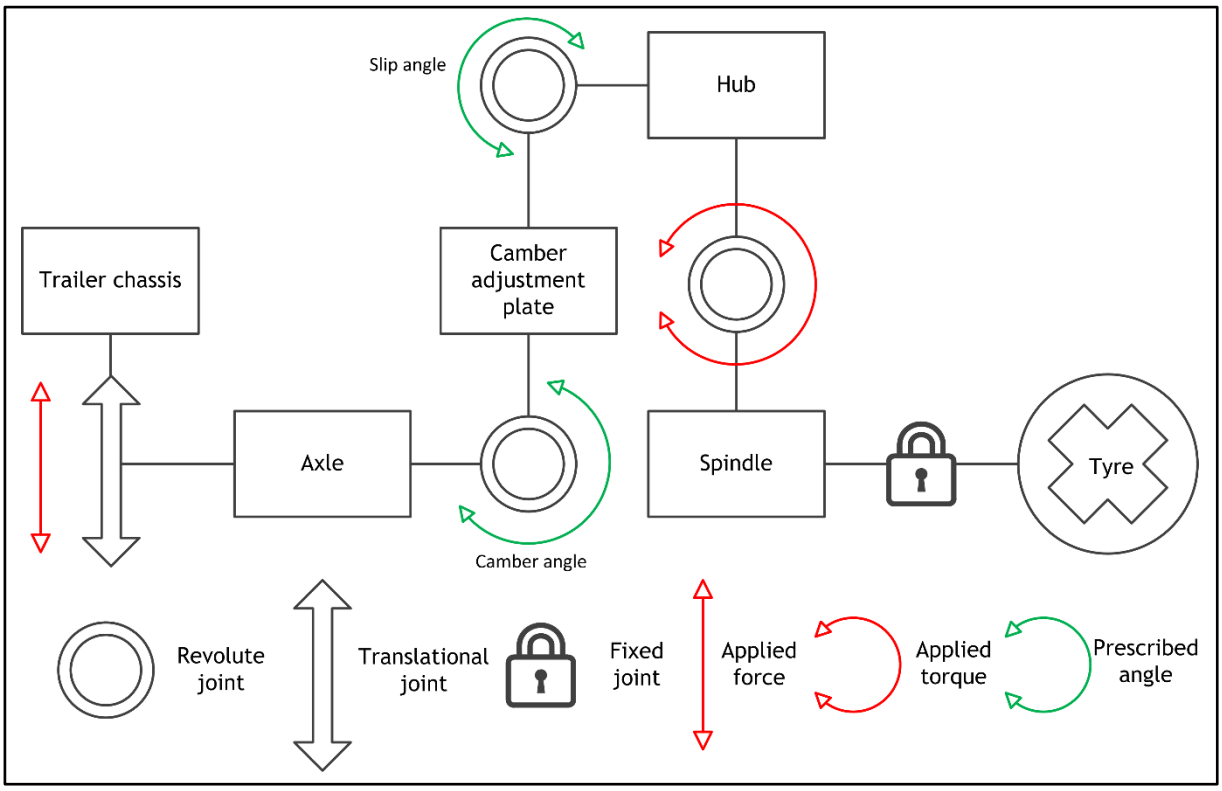

Figure A.2 Test axle model architecture

Two actuator inputs are shown in Figure A.2, the applied force and the applied torque. The applied torque given as input to the model is the WFT measured moment about the tyre spin axis. The force that is applied to the axle is a controlled value from Simulink (MathWorks, 2016). The input is based on feedback from the vertical tyre force output from the ADAMS (MSC Software, 2016) model. A PID controller is used to control the modelled vertical force by adjusting the force acting on the axle. The measured camber and slip angle values are directly applied to the revolute joints between the axle and the camber adjustment plate and the camber adjustment plate and the hub, respectively.

A.3 Results

The measured and simulated results for lateral, longitudinal, and combined load tests are shown to illustrate the tyre test trailer model's performance. Figure A.3 shows the results for a lateral test, Figure A.4 for a longitudinal test, and Figure A.5 for a combined load test. All three figures show the input control variables and the resulting force of interest. The vertical force feedback control may be seen in part b) of all three figures to very accurately follow the measured force. During the tyre model parameterisation in Section 3.2.2, the tyre test trailer model was used to fine tune the friction characteristics of the tyres until they matched those measured in the field tests.

van bestaande navorsing

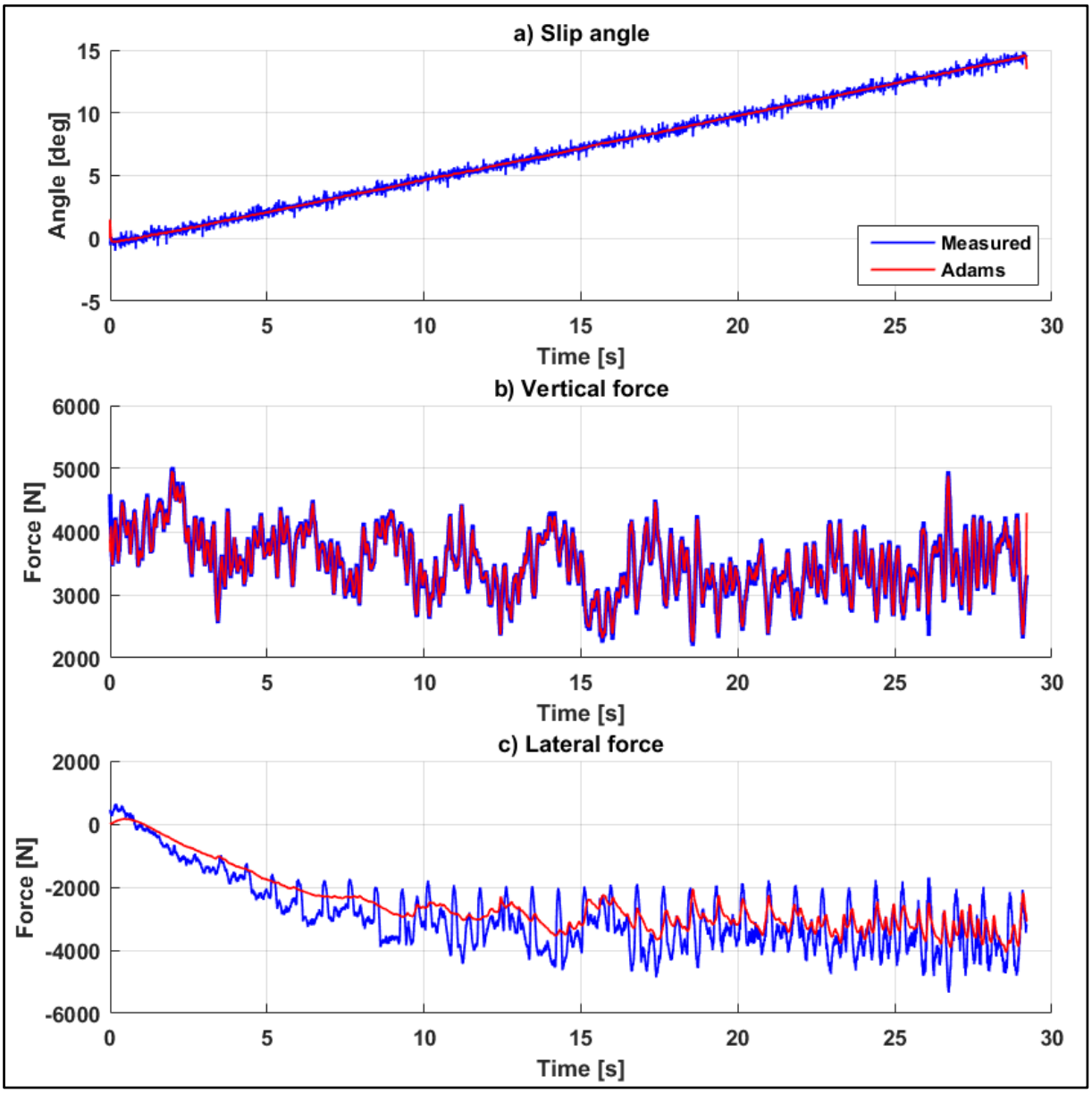

Figure A.3 Lateral simulation results

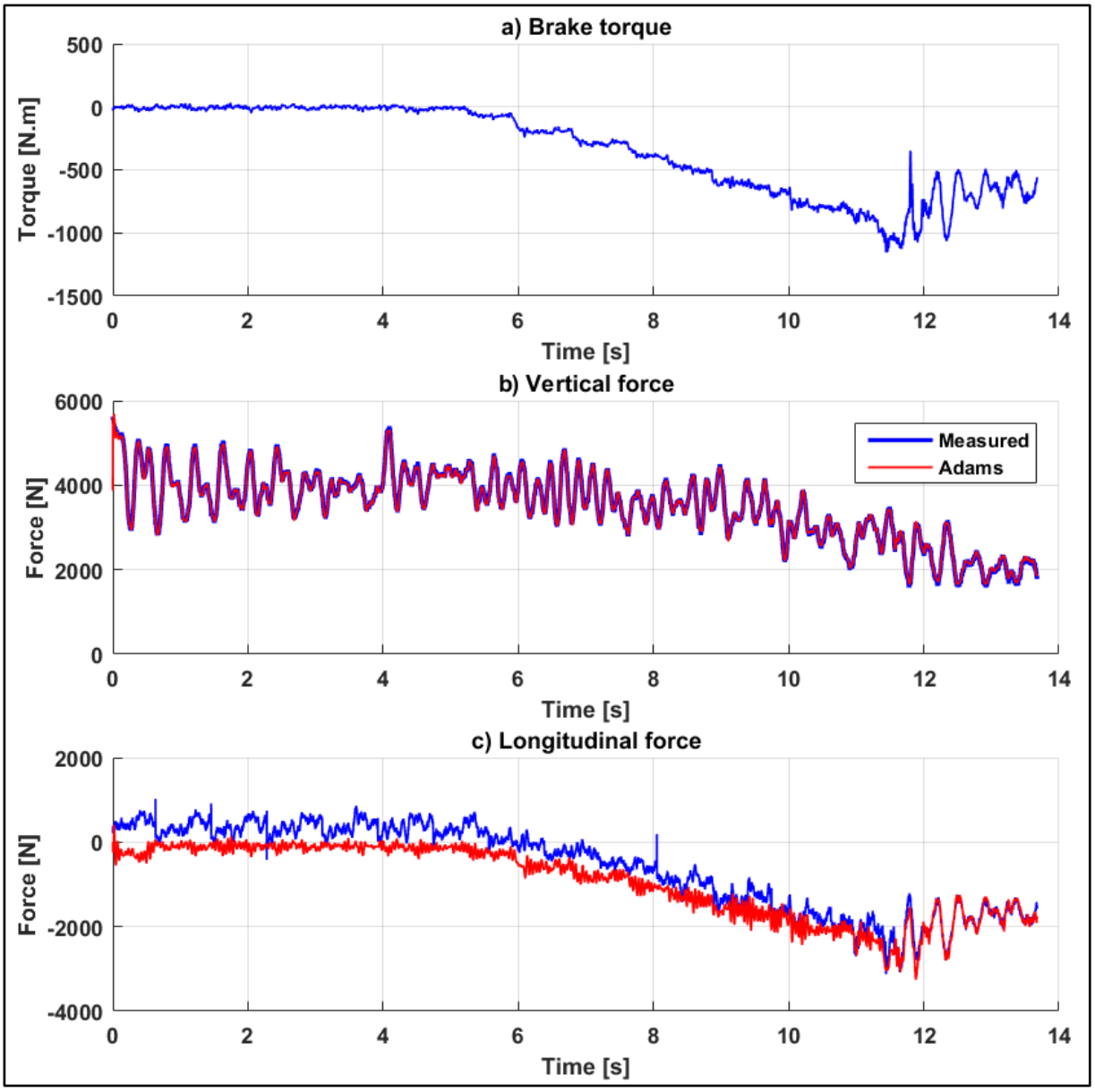

Figure A.4 Longitudinal simulation results

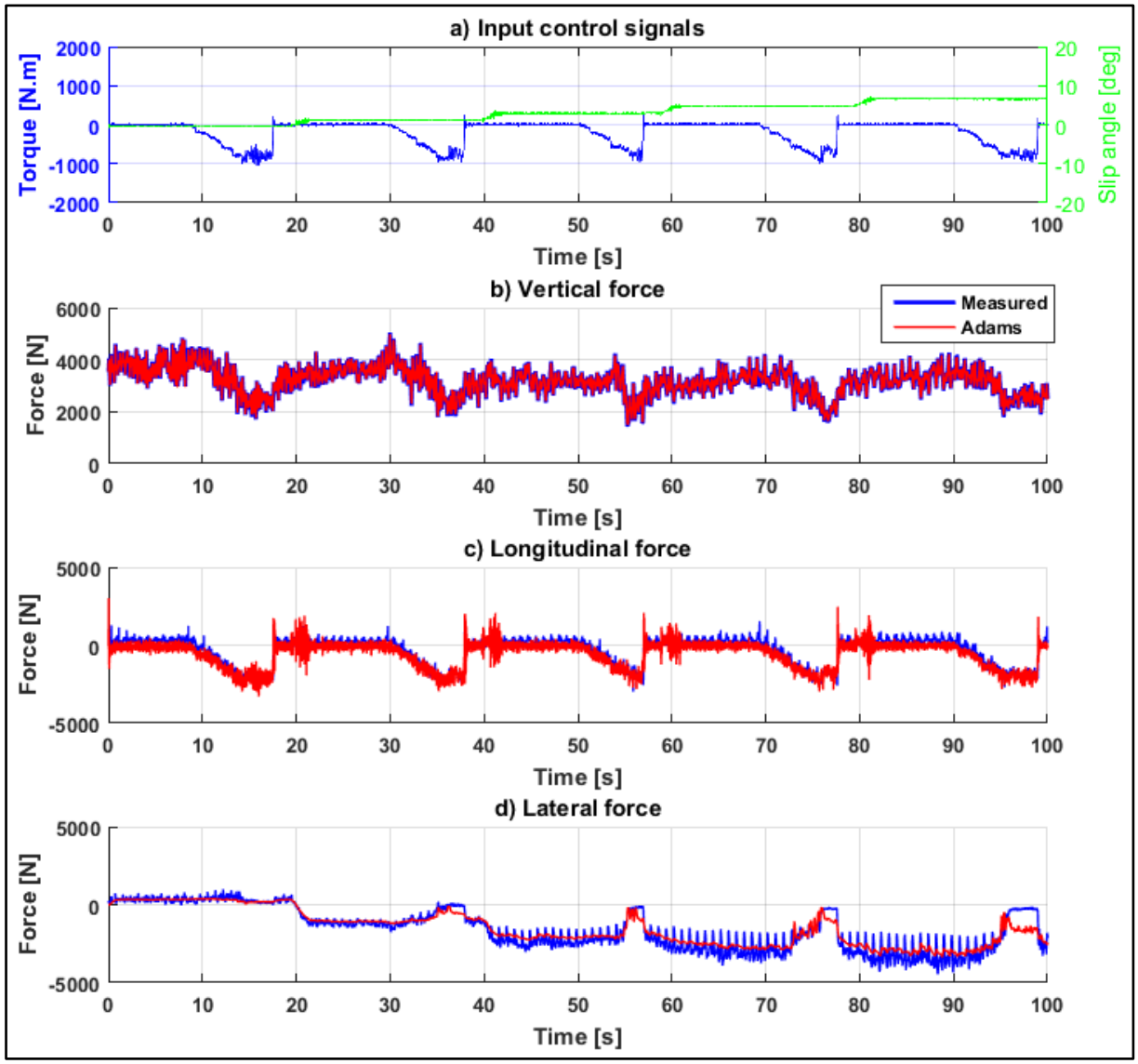

Figure A.5 Combined loading simulation results